NEW LOW MOMENTUM-TRANSFER MEASUREMENTS OF THE $p(e, e'p)\pi^0$ CROSS SECTION TO ACCESS THE COULOMB QUADRUPOLE AMPLITUDE OF THE $\Delta(1232)$ RESONANCE

by

David James Anez

Submitted in partial fulfillment of the
requirements for the degree of
Doctor of Philosophy

at

Dalhousie University
Halifax, Nova Scotia
August 2014

Dedicated to my son John, whose timing was impeccable.

Table of Contents

List of Tables

vii

List of Figures

xv

Abstract

Deviation of the proton's wave function from pure spherical symmetry, referred to as proton deformation, has been a topic of continued interest for the last few decades, as its examination may lead to be a better understanding of proton structure, especially with regard to the roles of virtual pions in that structure and their interplay with the quark core. In the low momentum transfer region, this deformation can be explored by examining the electromagnetic transitions between the proton and the $\Delta(1232)$.

In March 2011, Experiment E08-010 in Hall A at Jefferson Lab measured $p(e, e'p)\pi^0$ reaction cross sections with energies near the $\Delta(1232)$ resonance. Measurements were made at three low momentum transfer values between the electron and proton, Q^2 = 0.045, 0.090, and 0.125 $(\mathrm{GeV}/c)^2$, using an 1160 MeV electron beam and Hall A's two high resolution spectrometers. Each momentum transfer value included multiple cross section measurements to exploit the dependence of the recoil proton's polar and azimuthal angles on the cross section.

The goal of these measurements was to extract the magnetic dipole and the Coulomb quadrupole transition amplitudes, as well as their ratio, the CMR, in a region sensitive to the effects of the pion cloud contribution. These values were extracted from the cross sections using a model-independent multipole extraction method. The results were compared to model predictions, which found reasonable agreement for the two higher momentum transfer values, where previous measurements had previously existed, but none of the models were able to properly predict the behavior of the momentum transfer dependency of the data. These measurements thus provide new experimental impetus for the current theoretical models to revisit how the pion cloud dynamics influence proton deformation in this particularly sensitive low momentum transfer region.

Lists of Abbreviations Used

ADC	Analog-to-Digital Converter
Al	Aluminum
BCM	Beam Current Monitor
BeO	Beryllium Oxide
BPM	Beam Position Monitor
C	Carbon
CEA	Cambridge Electron Accelerator
CEBAF	Continuous Electron Beam Accelerator Facility
CGLN	Chew, Goldberger, Low, and Nambu
CH_2	Methylene
ChEFT	Chiral Effective Field Theory
CLAS	CEBAF Large Acceptance Spectrometer
CMR	Coulomb-to-Magnetic Ratio
CODA	CEBAF Online Data Acquisition
CQM	Constituent Quark Model
CRL	CODA Readout Language
DAQ	Data Acquisition
DESY	Deutches Elektronen Synchrotron
DMT	Dubna, Mainz, and Taipei
EDTM	Electronic Dead-Time Module
ELSA	Elektronen-Stretcher Anlage
EMR	Electric-to-Magnetic Ratio
eP	Electron-Proton
EPICS	Experimental Physics and Industrial Control System
FC	Faraday Cup
FEL	Free Electron Laser
FPP	Focal Plane Polarimeter
FWHM	Full-Width Half-Maximum

GH	Gail-Hemmert
HAND	Hall A Neutron Detector
HQM	Hypercentral Quark Model
HRS	High Resolution Spectrometer
HRSe	Electron High Resolution Spectrometer
HRSh	Hadron High Resolution Spectrometer
HRS-L	Left High Resolution Spectrometer
HRS-R	Right High Resolution Spectrometer
LD_2	Liquid Deuterium
LEGS	Laser Electron Gamma Source
LH_2	Liquid Hydrogen
LHRS	Left High Resolution Spectrometer
MAID	Mainz Unitary Isobar Model
MAMI	Mainz Microtron
MCC	Machine Control Center
MCEEP	Monte-Carlo for $(e, e'p)$
MDE	Model Dependent Extraction
MIT	Massachusetts Institute of Technology
NINA	Daresbury Nuclear Physics Laboratory
PMT	Photo-Multiplier Tube
PS	Phase Space
QCD	Quantum Chromodynamics
QED	Quantum Electrodynamics
QQDQ	Quadrupole-Quadrupole-Dipole-Quadrupole
RF	Radio Frequency
RHRS	Right High Resolution Spectrometer
ROC	Read-Out Controller
SAID	Partial Wave Analysis calculations from George Washington University group
SMR	Scalar-to-Magnetic Ratio
SRC	Short-Range Correlations
TDC	Time-to-Digital Converter

TME	Truncated Multipole Expansion
TO	Target Operator
VDC	Vertical Drift Chamber
XS	Cross Section
Y	Yield

Acknowledgements

Chapter 1

Introduction

The main goal of this experiment was to measure the Coulomb, or scalar, quadrupole transition amplitude for the pion electroproduction reaction in the Δ (1232) resonance region with low momentum transfer between the proton and the electron.

Many experiments in the last few decades have conclusively proven that the proton is not spherical, but instead has some sort of "deformation", as evidenced by non-spherical components in the nucleon wave function [1]. These deformations may originate from several possible sources, such as the non-central color hyperfine interaction between constituent quarks at short-range or an asymmetric coupling of a pion cloud to the quark core at long-range.

Experiment E08-010, which was performed at the Thomas Jefferson National Accelerator Facility (Jefferson Lab) in the spring of 2011, took measurements of the $p(e, e'p)\pi^0$ reaction using the two high resolution spectrometers (HRS) in Hall A at the facility. From these measurements, the ratio of the Coulomb quadrupole amplitude to the magnetic dipole amplitude (CMR) was extracted for three different momentum transfer values. These measurements will help bridge the gap in the world data in the very low momentum transfer region as well as overlap previous results, validating the world data in that region. They can be used to constrain theoretical models concerning the "shape" of the nucleon and help to explore the source of the nucleon's "deformation".

1.1   Constituent Quark Model

Prior to the discovery of quarks and the development of quantum chromodynamics (QCD), it was believed that the proton and neutron were fundamental particles. Though they have since been demoted to composite particles made of still-smaller quarks, there was initially no reason to believe these quark distributions were not spherical.

It was not until 1979 that the idea of a non-spherical nucleon[1] was first developed [2], in which a non-spherical component to the particle's wave function results in a "deformation" to its "shape"[2].

To better understand the source of this deformation, a simplified nuclear model called the constituent quark model (CQM) can be used. In the CQM, the nucleon is modeled as a collection of three "heavy" quarks, where the mass of each quark is one-third the mass of the nucleon. These effective masses are a result of the gluon-field self-energy "dressing" of the core up and down quarks of the standard model, as well as by the inclusion of sea quarks produced by this gluon field. Using the CQM, the general form of the nucleon's wave function can be determined from the spin-orbit couplings of the individual quarks

Each quark has an intrinsic spin angular momentum, S, of 1/2. These spins can combine to form a total spin of either 1/2 or 3/2. If there is no orbital angular momentum, L, this total spin becomes the composite particle's total angular momentum, J, with the 1/2 corresponding to the nucleon and the 3/2 corresponding to the Δ.

However, L need not be zero. Due to parity conservation, $L = 2$ is also a possibility[3]. This results in additional combinations of spin and orbital angular momenta that can also result in the overall spin of the nucleon or Δ.

Wave functions for both the nucleon and the Δ can then be constructed as linear combinations of the two coupling possibilities, with the $L = 0$ term being the spherical component and the $L = 2$ term being the non-spherical component [3].

$$|N(939)\rangle = a_S \left|\left(S = \frac{1}{2}, L = 0\right) J^\pi = \frac{1}{2}^+\right\rangle + a_D \left|\left(S = \frac{3}{2}, L = 2\right) J^\pi = \frac{1}{2}^+\right\rangle \quad (1.1)$$

$$|\Delta(1232)\rangle = b_S \left|\left(S = \frac{3}{2}, L = 0\right) J^\pi = \frac{3}{2}^+\right\rangle + b_D \left|\left(S = \frac{1}{2}, L = 2\right) J^\pi = \frac{3}{2}^+\right\rangle \quad (1.2)$$

A natural way to measure an object's deviation from spherical is to measure its quadrupole moment. Unfortunately, while the nucleon may have an intrinsic

---

[1]The proton and neutron are collectively known as the nucleon.

[2]Quotation marks are used when referring to "deformation" and "shape", since there are no unique quantum mechanical definitions for these classical terms. However, since these terms are used in the literature to discuss these topics, they will be used here as well.

[3]$L = 1$ is also a possibility if parity isn't conserved, something not dealt with in this experiment.

quadrupole moment, due to angular momentum selection rules, particles with a spin of 1/2 have no spectroscopic quadrupole moment [3]. That is, the nucleon's quadrupole moment cannot be measured using simple Coulomb scattering. Instead, the quadrupole moment of the nucleon's transition to a higher spin particle, such as the Δ (1232)[4], is measured.

The proton can be excited to a Δ (1232) electromagnetically with real photons or virtual photons via an interaction with another charged particle, such as an electron. Due to angular momentum coupling restrictions, only three electromagnetic transitions can excite a proton to a Δ: the magnetic dipole ($M1$), the electric quadrupole ($E2$), and the scalar or Coulomb quadrupole ($C2$).

In the CQM, the $L = 0$ component of the nucleon's wave function can be visualized with all three quarks in an s-state energy level, with two quarks spin up and one quark spin down, resulting in the total spin of 1/2. Likewise, the $L = 0$ component of the Δ's wave function has all three quarks in the s-state energy level with spins in the same direction, resulting in the total spin of 3/2, as visualized in Figure 1.1 [3].

The magnetic dipole transition, then, is simply a spin flip of the nucleon's odd quark, leaving all three quarks with spins in the same direction, resulting in a Δ (1232). This is the dominant transition observed between the nucleon and the Δ [4].

The $L = 2$ components can be visualized as one of the quarks being elevated to a d-state energy level. This means that the two quadrupole transitions can be thought of as quark transitions between the s-state and d-state energy levels without a spin flip, as visualized in Figure 1.2 [3]. These transitions are known as the color hyperfine interaction [5], which is thought to be the source of deformation for the quark core.

By measuring the strength of the quadrupole transitions, the strength of the $L = 2$ component of the nucleon's wave function can be indirectly measured, along with the nucleon's "deformation", meaning its deviation from pure $L = 0$ spherical symmetry.

The transitions discussed so far are all one-body interactions. That is, the incoming photon only interacts with one quark, as seen in Figure 1.3. The one-body quadrupole operator can be written as [3]:

$$\hat{Q}_{[1]} = \sqrt{\frac{16\pi}{5}} \sum_{i=1}^{3} e_i r_i^2 Y_0^2(\vec{r_i}) = \sum_i e_i \left(3z_i^2 - r_i^2\right) \tag{1.3}$$

---

[4]Specifically, this thesis is referring to the Δ^+.
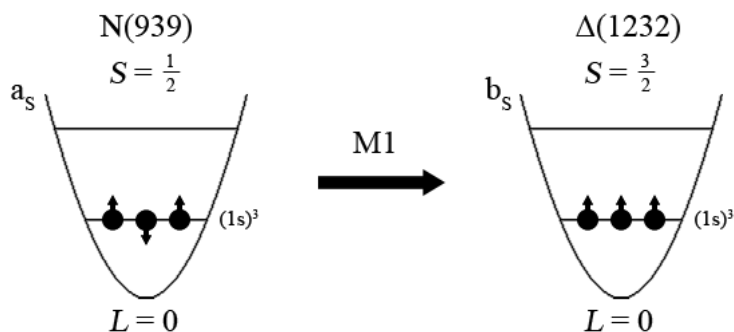
Figure 1.1: Cartoon model of the Constituent Quark Model of the nucleon and Δ, showing how the $M1$ transition is a spin flip of the odd quark. Figure reproduced from Reference [3].
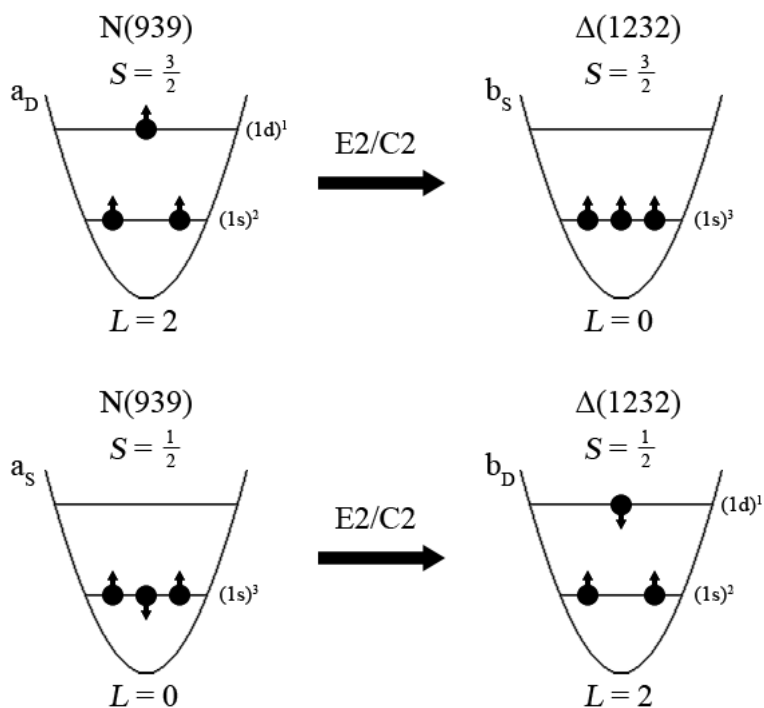
Figure 1.2: Cartoon model of the quadrupole transitions between the nucleon and the Δ, based on CQM, showing how the $E2$ and $C2$ transitions involve movement between quark energy levels. Figures reproduced from Reference [3].
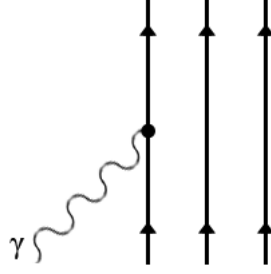
Figure 1.3: Cartoon diagram of an example one-body transition, in which a photon interacts directly with a quark. Figure reproduced from Reference [3].
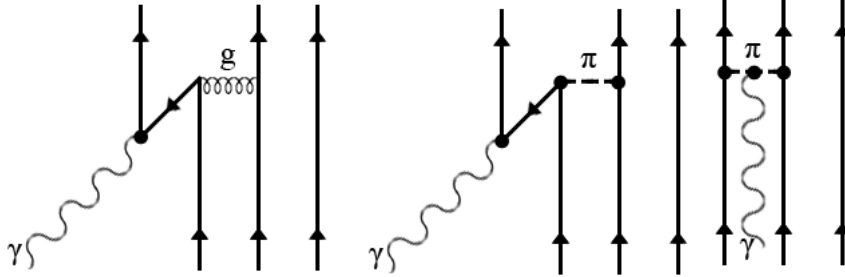
Figure 1.4: Cartoon diagrams of potential two-body transitions, in which photons interact with quarks and other particles including gluons and mesons. Figures reproduced from Reference [3].

Multiple-particle transitions are also possible, such as those in Figure 1.4. For example, a photon and a meson could interact with a quark simultaneously, resulting in a quadrupole transition without a change in the orbital angular momentum of the quark [3].

$$\hat{Q}_{[2]} = B \sum_{i \neq j=1}^{3} e_i \left(3\sigma_{iz}\sigma_{jz} - \vec{\sigma}_i \cdot \vec{\sigma}_j \right) \tag{1.4}$$

These mesons, which are predominantly pions, can be visualized as existing in a cloud surrounding the quark core. In this case, it can be imagined that it is not the quark core but this pion cloud that is deformed, as shown in Figure 1.5.

Indeed, at low energies, the incoming photon's effective wavelength may be too large to interact with the quark core directly; instead, it interacts with the pion cloud, much in the same way that ultraviolet photons tend to interact with an atom's valence electrons while relatively higher energy gamma rays interact with the atom's nucleus.
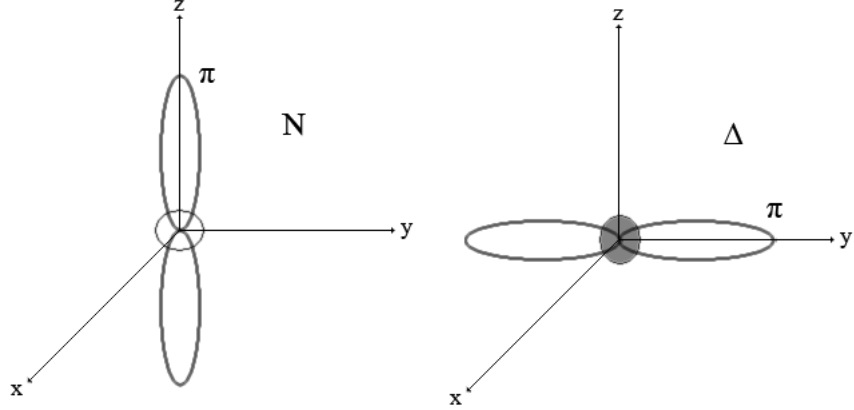
Figure 1.5: Cartoon pion cloud configurations of the nucleon and the Δ, showing how the pion cloud and quark core can both be deformed, but deformed in different configurations. Figure reproduced from Reference [3].

This possibility could explain the discrepancy between CQM-based calculations and experimental results for the CMR in the region of low momentum transfer, since the CQM does not take into account the pion cloud, and it is the pion cloud with which low momentum photons are likely interacting [6].

1.2 Kinematics

In this experiment, the goal was to measure the Coulomb quadrupole transition amplitude. Since that amplitude can only be measured using virtual photons, the target protons were excited using an electron beam. The electronic vertex is well known through quantum electrodynamics (QED), so no unnecessary complications were added by using electrons, as opposed to beams of nucleons or mesons, where the strong interaction would be involved [7].
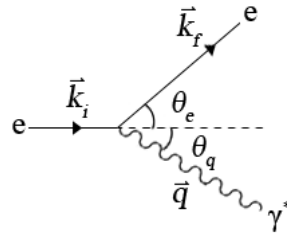
Figure 1.6: Diagram of the electronic vertex in the lab frame. The incoming beam electron emits the virtual photon and then scatters away.

In this reaction, the incoming electron has an energy E and a momentum $\vec{k}_i$. The interaction with the target proton causes the electron to scatter away with energy E' and momentum $\vec{k}_f$, as shown in Figure 1.6, with an angle θ_e relative to the incoming electron's original direction, known as the "beamline". These quantities are used to determine the physical position and momentum setting of the electron detector.

The resulting change in the electron's energy and momentum is imparted to the virtual photon, which is described with energy ω and momentum $\vec{q}$, with an angle θ_q relative to the beamline. Combined, ω and $\vec{q}$ give a 4-momentum q, which is usually converted to $Q^2 = -q^2 = -(\omega^2 - \vec{q}^2)$. Q^2 is inversely related to the wavelength of the probing virtual photon and is usually referred to simply as the "momentum transfer" or "momentum transfer squared". Q^2 is the first of the kinematic variables that makes up the phase space for this experiment.

The scattered electron angle θ_e is related to Q^2 through

$$Q^2 \approx 4EE' \sin^2 \frac{\theta_e}{2}, \tag{1.5}$$

with the assumption that the electron's mass is much lower than its energy and $c = 1$. This allows the value of Q^2 in the experiment to vary only by changing the angle and momentum setting of the electron detector.

The virtual photon then interacts with the proton at the hadronic vertex, where the experimentally-relevant interactions take place. If the energy transfer ω is between 300 and 400 MeV, the proton may be excited to a Δ^+ (1232); but the Δ^+ is short-lived and promptly decays, primarily[5] to a nucleon and a pion, with a 2:1 ratio between p-π^0 and n-π^+ [8].

This experiment specifically looked at the $p(e, e'p)\pi^0$ reaction, in which the proton target is initially stationary in the lab frame, and the recoil proton's momentum is given as $\vec{p}_f$, which makes an angle θ_{pq} with the $\vec{q}$-vector, as shown in Figure 1.7. Using θ_{pq} and θ_q, the angle of the recoil proton relative to the beamline, θ_p, can be determined, which is needed to set the angle of the proton/hadron detector.

The recoil pion is not directly observed, but its energy, E_π, and momentum, $\vec{p}_\pi$, can be determined from missing mass calculations. Using the angles and momenta of the

---

[5]There is also a small probability, approximately 0.5%, of the Δ decaying directly to a proton and a photon.
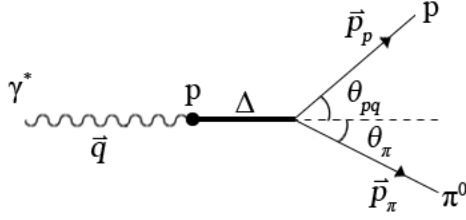
Figure 1.7: Diagram of the hadronic vertex in the lab frame. The virtual photon interacts with a stational target proton, exciting it to a Δ, which then decays into a recoil proton and recoil π^0.
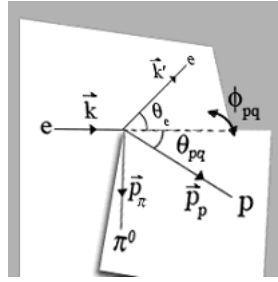
Figure 1.8: Three-dimensional diagram of the scattering and reaction planes, including the azimuthal angle between them.

detected particles, along with the conservation of energy and momentum, the energy, mass, and momentum that appear to be missing from the reaction be calculated. If the missing mass corresponds to the mass of the pion, it confirms the identity of the third recoil particle.

The vectors $\vec{k}_i$ and $\vec{k}_f$ form the scattering plane, while $\vec{p}_f$ and $\vec{p}_\pi$ form the reaction plane. Seen in Figure 1.8, the angle between these planes is ϕ_{pq}, the azimuthal angle, which can play an important role in extracting transition amplitude information.

It is often easier to examine the hadronic vertex from the center-of-mass frame, shown in Figure 1.9, where the target proton has a non-zero momentum, p_i^*, and collides with the virtual photon head-on.

In this frame, the system has no net momentum, so a Δ can be created if the total energy of the system, W, is close to the Δ's rest mass of 1232 MeV. W is also known as the intrinsic mass, is the square root of the Mandelstam variable s, and is the second of the kinematic variables used to define the experiment's phase space.

Following the collision in this center-of-mass frame, the resulting recoil proton and pion are ejected with equal momentum in exactly opposite directions. The angle
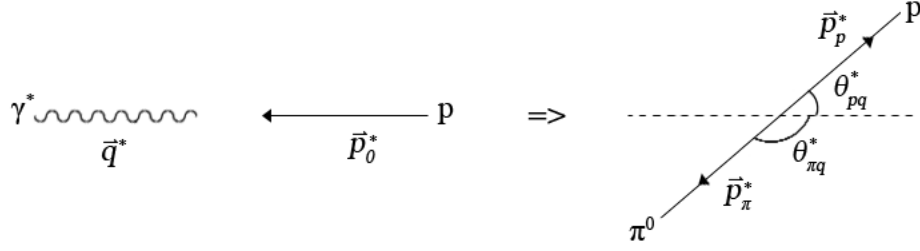
Figure 1.9: Diagram of the hadronic vertex in the center-of-mass frame. The virtual photon collides head-on with the non-stational target proton, exciting the proton into a Δ, which then decays into the proton and the π^0, which scatter away in exactly opposite directions.

between the recoil proton and the direction of the virtual photon, $\hat{q}$, is θ_{pq}^*, which is the third phase space kinematic variable.

In the literature, the pion center-of-mass angle, $\theta_{\pi q}^*$, is generally used rather than the proton angle. This is easily rectified as the two angles are $180°$ apart.

1.3 Multipole Amplitudes

Since the Δ cannot be detected directly, information about the transition amplitudes between the nucleon and the Δ must be collected from the Δ's decay products, the nucleon and the pion. Since many possible reaction mechanisms can result in the production of a nucleon and a pion, it is necessary to differentiate between the various possible transition amplitudes.

The general notation for the (complex) transition amplitudes in which a nucleon and pion are produced is $X_{\ell\pm}^I$, where X denotes the type of excitation, I is the isospin of the excited intermediate state, ℓ is the orbital angular momentum of the system, and the $\pm$ indicates whether the spin of the intermediate state is the result of the nucleon's spin being added to or subtracted from ℓ: $J = \ell \pm 1/2$ [9].

The intrinsic spin of the Δ, nucleon, and pion are $S = 3/2$, $1/2$, and 0, respectively. This indicates that the decay of the Δ into the nucleon and pion must have an orbital angular momentum of either $\ell = 1$ or $\ell = 2$. Parity conservation further limits this to $\ell = 1$, since the intrinsic parities of the Δ, nucleon, and pion are $+$, $+$, and $-$, respectively.

In the $p(e, e'p)\pi^0$ reaction, where the isospin of the Δ is $I = 3/2$, the $\pm$ must be

γN-Multipoles	Initial State		Excited State			Final State		πN-Multipoles
C, E, M	L_γ^π	s_N^π	J_R^π	$N^* I_{2I2J} \Delta$		s_N^π	I_π^π	$L_{\ell\pm}, E_{\ell\pm}, M_{\ell\pm}$
$C0$	0^+	$1/2^+$	$1/2^+$	P_{11}	P_{31}	$1/2^+$	1^+	L_{1-}
$C1, E1$	1^-	$1/2^+$	$1/2^-$	S_{11}	S_{31}	$1/2^+$	0^-	L_{0+}, E_{0+}
		$1/2^+$	$3/2^-$	D_{13}	D_{33}	$1/2^+$	2^-	L_{2-}, E_{2-}
$M1$	1^+	$1/2^+$	$1/2^+$	P_{11}	P_{31}	$1/2^+$	1^+	M_{1-}
		$1/2^+$	$3/2^+$	P_{13}	P_{33}	$1/2^+$	1^+	M_{1+}
$C2, E2$	2^+	$1/2^+$	$3/2^+$	P_{13}	P_{33}	$1/2^+$	1^+	L_{1+}, E_{1+}
		$1/2^+$	$5/2^+$	F_{15}	F_{35}	$1/2^+$	3^+	L_{3-}, E_{3-}
$M2$	2^-	$1/2^+$	$3/2^-$	D_{13}	D_{33}	$1/2^+$	2^-	M_{2-}
		$1/2^+$	$5/2^-$	D_{15}	D_{35}	$1/2^+$	2^-	M_{2+}

Table 1.1: Various transition amplitudes, reproduced from Reference [9]. The γN multipoles form the excited intermediate state, which then decays with the πN multipoles. The highlighted section contains the amplitudes of interest.

$+$, and therefore the three electromagnetic transitions of interest correspond to the following multipole amplitudes [9]:

$$M1 \leftrightarrow M_{1+}^{3/2}$$
$$E2 \leftrightarrow E_{1+}^{3/2}$$
$$C2 \leftrightarrow S_{1+}^{3/2}$$

Occasionally in the literature, the scalar multipole, $S_{\ell\pm}$, is used interchangeably with the longitudinal multipole, $L_{\ell\pm}$, with the relation $\omega^* S_{\ell\pm} = |\vec{q}^*| L_{\ell\pm}$, where ω^* is the photon energy and $\vec{q}^*$ is the photon momentum [10], both in the center-of-mass frame.

In addition to the three multipoles of interest, there are a multitude of background amplitudes due to the existence of other possible reaction mechanisms. The presence of these additional amplitudes makes extraction of the desired multipoles difficult, especially because these background terms are at roughly the same magnitude as the two non-dominant resonant amplitudes E_{1+} and S_{1+} [11].

Table 1.1 contains some of the multipole amplitudes that may be present in the pion electroproduction reaction [9]. The resonant amplitudes are highlighted.

As will be discussed later, the non-dominant S_{1+} and E_{1+} multipoles can still have potential measurable influence on some observables through interference with the dominant M_{1+} multipole [1]. For that reason, it is convenient to refer to the

strength of the smaller amplitudes with respect to the magnetic dipole. These relative strengths are referred to as the electric-to-magnetic ratio (EMR) and the Coulomb-to-magnetic ratio (CMR) (or SMR for scalar-to-magnetic ratio), and are given as [1]:

$$EMR = R_{EM}^{3/2} = Re\left(\frac{E_{1+}^{3/2}}{M_{1+}^{3/2}}\right) \tag{1.6}$$

$$CMR = R_{CM}^{3/2} = Re\left(\frac{S_{1+}^{3/2}}{M_{1+}^{3/2}}\right) \tag{1.7}$$

The ultimate goal of this experiment is to obtain the CMR for three different momentum transfer values.

1.4 Response Functions

The extraction of the wanted multipole values from the experiment begins with the unpolarized differential cross section.

There are a few different methods of expressing the formalism related to response functions which will be presented here. For the purposes of this thesis, and to ensure consistency, we follow the conventions which have been clearly defined and delineated by J. J. Kelly in the manual written to supported his computer code "epiprod" – which was developed to convert various theoretical model inputs into physics lab observables for electroproduction of pions. [12]

For the $p(e, e'p)\pi^0$ reaction, the five-fold differential cross section is given as [11]:

$$\frac{d^5\sigma}{dk_f d\Omega_e d\Omega^*} = \Gamma_\gamma \bar{\sigma}[1 + hA + \mathbf{\Pi} \cdot \mathbf{S}] \tag{1.8}$$

where the cross section is differentiable in final electron energy (k_f), electron solid angle (Ω_e), and proton solid angle (Ω^*)[6]. h is the helicity, A is the beam analyzing power, S is the spin direction for the recoil nucleon, and $\mathbf{\Pi} = \mathbf{P} + h\mathbf{P'}$ is the recoil polarization.

Since this experiment did not deal with polarization, only the first term in the brackets of Equation 1.8 survives, and the differential cross section reduces to

---

[6]In many cases, the *pion* solid angle is used instead, though in the cm frame, the two terms are interchangeable.

$$\frac{d^5\sigma}{dk_f d\Omega_e d\Omega^*} = \Gamma_\gamma \bar{\sigma} \tag{1.9}$$

where

$$\Gamma_\gamma = \frac{\alpha}{2\pi^2} \frac{k_f}{k_i} \frac{k_\gamma}{Q^2} \frac{1}{1-\epsilon} \tag{1.10}$$

is the virtual photon flux for the initial (final) electron momentum k_i (k_f)[12]. In that equation, α is the fine-structure constant, and

$$\epsilon = \left(1 + 2\frac{q^2}{Q^2} \tan^2 \frac{\theta_e}{2}\right)^{-1} \tag{1.11}$$

is the transverse polarization of the virtual photon, where q is the photon momentum in the lab frame. Further,

$$k_\gamma = \frac{W^2 - m_p^2}{2m_p} \tag{1.12}$$

is the laboratory energy a real photon would need to excite the same reaction, and m_p is the proton mass.

$$\bar{\sigma} = \nu_0[\nu_L R_L + \nu_T R_T + \nu_{LT} R_{LT} \cos\phi + \nu_{TT} R_{TT} \cos 2\phi] \tag{1.13}$$

is referred to as the unpolarized cross section. While there is no established standard for the values of the coefficients Equation 1.13, in this document they are as follows [12]:

$$
\begin{aligned}
\nu_0 &= \frac{p_f^*}{k_\gamma^*} \\
\nu_L &= \epsilon \\
\nu_T &= 1 \\
\nu_{LT} &= \sqrt{2\epsilon(1+\epsilon)} \\
\nu_{TT} &= \epsilon
\end{aligned}
\tag{1.14}
$$

where

$$p_f^* = \sqrt{\frac{(W^2 + m_p^2 - m_\pi^2)^2}{4W^2} - m_p^2} \tag{1.15}$$

is the center of mass proton momentum in the final state[7], and

$$k_\gamma^* = \frac{W^2 - m_p^2}{2W} \tag{1.16}$$

is the center of mass momentum a real photon needs for the same transition[8].

R_L, R_T, R_{LT}, and R_{TT} are known as the unpolarized response functions[9]. They can be thought of as independent partial cross sections and can be related to the individual multipole amplitudes through several different methods.

One method is to construct the response functions from a series of structure functions, also known as the Chew, Goldberger, Low, and Nambu (CGLN) amplitudes [9].

$$R_L = |F_5|^2 + |F_6|^2 + 2\cos\theta\,\mathrm{Re}\left\{F_5^* F_6\right\} \tag{1.17}$$

$$R_T = |F_1|^2 + |F_2|^2 + \frac{1}{2}\sin^2\theta\left(|F_3|^2 + |F_4|^2\right)$$

$$- \mathrm{Re}\left\{2\cos\theta F_1^* F_2 - \sin^2\theta\left(F_1^* F_4 + F_2^* F_3 + \cos\theta F_3^* F_4\right)\right\} \tag{1.18}$$

$$R_{LT} = -\sin\theta\,\mathrm{Re}\left\{\left(F_2^* + F_3^* + \cos\theta F_4^*\right)F_5 + \left(F_1^* + F_4^* + \cos\theta F_3^*\right)F_6\right\} \tag{1.19}$$

$$R_{TT} = \sin^2\theta\left(\frac{1}{2}\left(|F_3|^2 + |F_4|^2\right) + \mathrm{Re}\left\{F_1^* F_4 + F_2^* F_3 + \cos\theta F_3^* F_4\right\}\right) \tag{1.20}$$

These structure functions can themselves then be constructed directly from the

---

[7]This is often referred to in the literature as k or k_W, but since the lab frame final momentum was p_f, for consistency here it is p_f^*.

[8]This is often referred to in the literature as q_0, but since the lab frame energy was k_γ, for consistency here it is k_γ^*.

[9]In the literature, the "R"-designated response functions are sometimes referred to as the *reduced* response functions. These are the full response functions, usually designed with a W, with the $\sin\theta$ terms already included.[12]

multipole amplitudes[10] [9].

$$F_1 = \sum_{\ell \geq 0} \left\{ (\ell M_{\ell+} + E_{\ell+}) P'_{\ell+1} + [(\ell+1) M_{\ell-} + E_{\ell-}] P'_{\ell-1} \right\} \tag{1.21}$$

$$F_2 = \sum_{\ell \geq 1} [(\ell+1) M_{\ell+} + \ell M_{\ell-}] P'_\ell \tag{1.22}$$

$$F_3 = \sum_{\ell \geq 1} \left[(E_{\ell+} - M_{\ell+}) P''_{\ell+1} + (E_{\ell-} + M_{\ell-}) P''_{\ell-1} \right] \tag{1.23}$$

$$F_4 = \sum_{\ell \geq 2} (M_{\ell+} - E_{\ell+} - M_{\ell-} - E_{\ell-}) P''_\ell \tag{1.24}$$

$$F_5 = \sum_{\ell \geq 0} \left[(\ell+1) L_{\ell+} P'_{\ell+1} - \ell L_{\ell-} P'_{\ell-1} \right] \tag{1.25}$$

$$F_6 = \sum_{\ell \geq 1} [\ell L_{\ell-} - (\ell+1) L_{\ell+}] P'_\ell \tag{1.26}$$

An additional step can be included, where helicity amplitudes are constructed from the CGLN amplitudes [12]:

$$H_1 = -\frac{1}{\sqrt{2}} \sin\theta \cos\frac{\theta}{2} (F_3 + F_4) \tag{1.27}$$

$$H_2 = \sqrt{2} \cos\frac{\theta}{2} \left[(F_2 - F_1) + \frac{1}{2}(1 - \cos\theta)(F_3 - F_4) \right] \tag{1.28}$$

$$H_3 = \frac{1}{\sqrt{2}} \sin\theta \sin\frac{\theta}{2} (F_3 - F_4) \tag{1.29}$$

$$H_4 = \sqrt{2} \sin\frac{\theta}{2} \left[(F_1 + F_2) + \frac{1}{2}(1 + \cos\theta)(F_3 + F_4) \right] \tag{1.30}$$

$$H_5 = \cos\frac{\theta}{2} (F_5 + F_6) \tag{1.31}$$

$$H_6 = \sin\frac{\theta}{2} (F_6 - F_5) \tag{1.32}$$

The response functions are then built from them [12]:

$$R_L = |H_5|^2 + |H_6|^2 \tag{1.33}$$

$$R_T = \frac{1}{2}(|H_1|^2 + |H_2|^2 + |H_3|^2 + |H_4|^2) \tag{1.34}$$

$$R_{LT} = -\text{Re}\{H_5^*(H_4 - H_1) + H_6^*(H_3 + H_2)\} \tag{1.35}$$

$$R_{TT} = \text{Re}\{H_3^* H_2 - H_4^* H_1\} \tag{1.36}$$

---

[10]In some of the literature, F_5 and F_6 are constructed with the S_{l+} multipoles instead of the L_{l+} multipoles. This can result in the formation of F_5' and F_6' terms instead, and involves conversions in the response functions. Regardless, the equations as presented in this document are consistent with themselves as written [12].

Using these response functions and Equations 1.13, the unpolarized cross section can be calculated. That cross section will be in units of µb/sr, and is referred to as the two-fold cross section in the center-of-mass frame.

Multiplying this unpolarized cross section by the virtual photon flux, Γ_γ, results in a five-fold cross section, still in the center-of-mass frame, and in units of µb/MeV/sr^2.

An additional step could be to multiply this five-fold cross section by the Jacobian [9],

$$\frac{d\Omega_\pi^{cm}}{d\Omega_p^{lab}} = \frac{p_f^2 W}{|p_f^*|\,|\gamma W|p_f| - E_p|q|\cos\theta_{pq}|} \tag{1.37}$$

which transforms the equation from the solid pion angle in the center-of-mass frame to the solid proton angle in the lab frame, where p_f is the recoil proton momentum in the lab frame, p_f^* is the recoil proton in the center-of-mass frame, γ is the relativistic correction factor, E_p is the recoil proton energy in the lab frame, and θ_{pq} is the angle between the recoil proton and the virtual photon.

1.5 World Data

The first pion electroproduction experiments took place in 1969 at Harvard's Cambridge Electron Accelerator (CEA) [13]. It was during these experiments that the dominance of the M_{1+} transition amplitude was first discovered. Further experiments took place at the Deutches Elektronen Synchrotron (DESY) between 1970 and 1972 [14] and the Daresbury Nuclear Physics Laboratory (NINA) in 1971 [15].

The current increase in research activity began in 1997, when pion electroproduction experiments at the Elektronen-Stretcher Anlage (ELSA) in Bonn produced rather unusual results [16]. That same year, pion photoproduction experiments were undertaken at Brookhaven's Laser Electron Gamma Source (LEGS) [17] and the Mainz Microtron (MAMI) [18]. Jefferson Lab's Hall C did additional pion electroproduction experiments in 1998 [19], as did MIT-Bates in 2000 [20] and Mainz in 2001 [21].

In 2002, Jefferson Lab's Hall B, as part of the CEBAF Large Acceptance Spectrometer (CLAS) collaboration, ran a series of experiments with full angular acceptance [22], hoping to obtain a comprehensive measurement of the amplitudes in
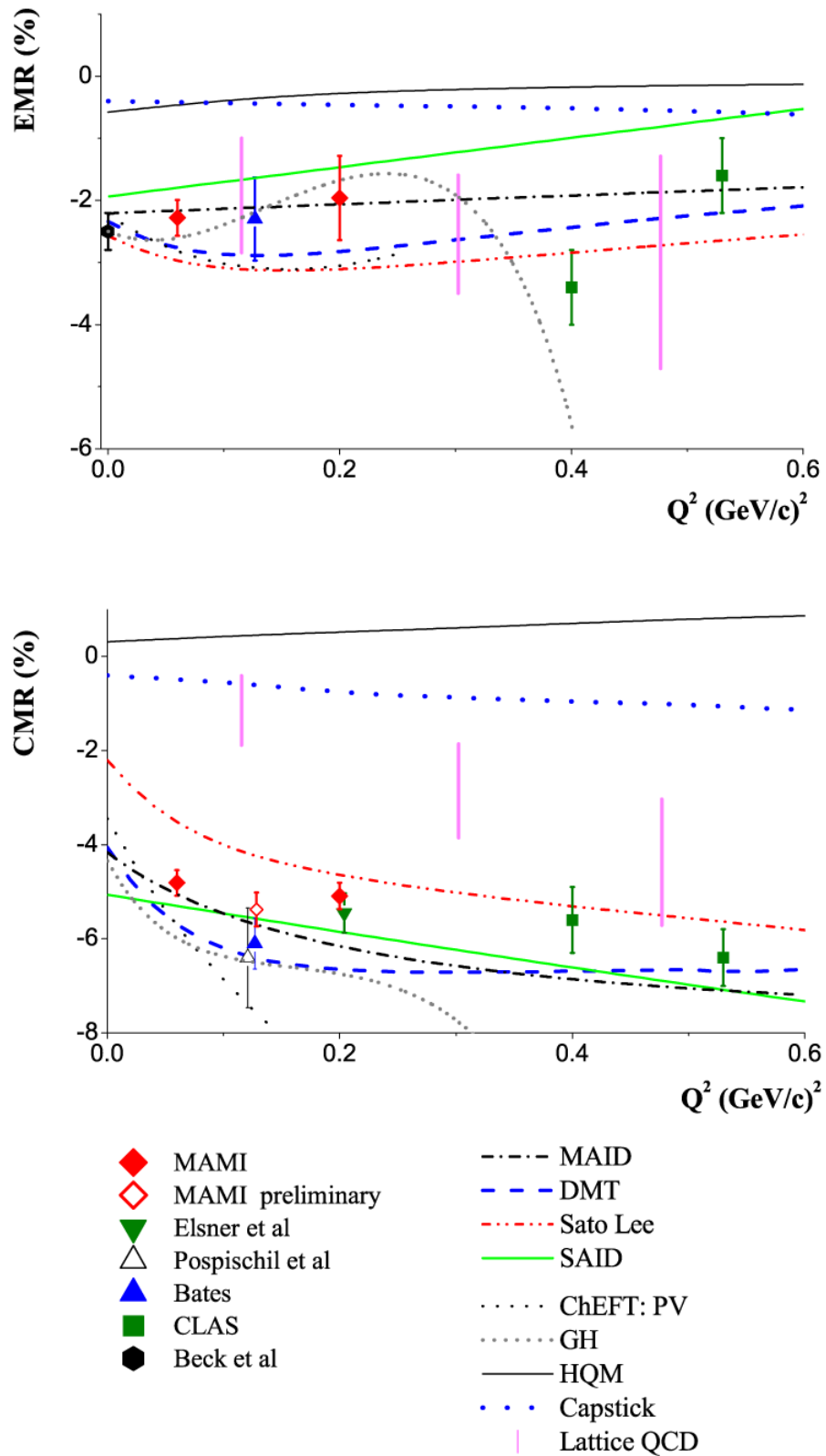
Figure 1.10: The EMR and CMR world data at $Q^2 < 0.6$ $(\text{GeV}/c)^2$, showing experimental data and model predictions for this region. Figure taken directly from the experiment proposal [1].
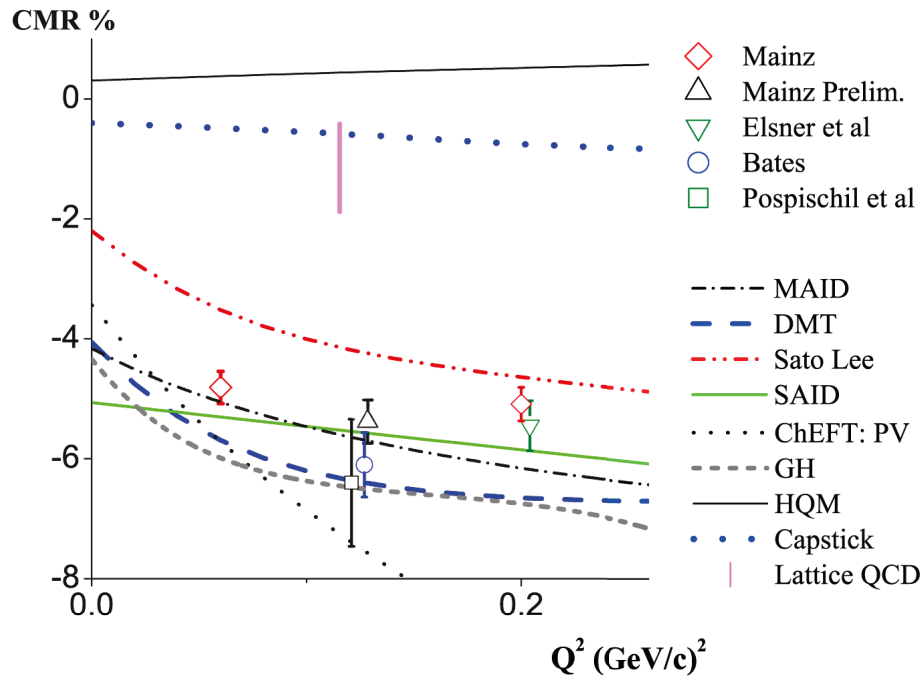
Figure 1.11: The CMR world data and model predictions for low Q^2. Figure taken directly from the experimental proposal [1] and modified to remove the projected experimental values.

question. However, their experiments lacked polarization measurements of the recoil protons, which are necessary for a complete analysis. The missing polarization measurements were later taken by Jefferson Lab's Hall A in 2003 [7, 10, 11, 23].

In 2004, further pion electroproduction measurements were made at MIT-Bates, utilizing the out-of-plane spectrometer (OOPS) [24]. In 2005 [25] and 2006 [26], a series of experiments at Mainz explored the area around $Q^2 = 0.2$ (GeV/c)^2 [27] as well as getting the then-lowest measurements at $Q^2 = 0.060$ (GeV/c)^2 [26].

Altogether, these experiments produced the world data on the EMR and CMR, displayed in Figure 1.10, conclusively proving that the nucleon is indeed deformed, as a spherical nucleon would have EMR and CMR values of 0. However, while many pion electroproduction experiments varied over a wide range of Q^2 values, it was felt that more CMR data could be collected in the low Q^2 region, shown in Figure 1.11, where the pion cloud is expected to have a significant influence on the CMR values [1]. The purpose of this experiment was to further explore this region.

Prior to this experiment, the lowest Q^2 value for which the CMR had been measured was $Q^2 = 0.060$ $(\text{GeV}/c)^2$ [21]. The experiment reported in this thesis went lower, to $Q^2 = 0.045$ $(\text{GeV}/c)^2$, made possible by the spectrometer configuration in Jefferson Lab's Hall A, where the positioning of the electron arm can reach as low as $\theta_e = 12.5°$ [28].

Further, the CMR data collected in the vicinity of $Q^2 = 0.125$ $(\text{GeV}/c)^2$ has shown a curious dip. This experiment took high precision measurements at that value to help validate and clarify the previous measurements.

Data was also taken at $Q^2 = 0.090$ $(\text{GeV}/c)^2$ to bridge the gap between previous measurements.

1.6 Models

In addition to data from experiments, the plots in Figures 1.10 and 1.11 also include predictions from a variety of models.

Two commonly-used models are both phenomenological, MAID [29, 30] and SAID [31, 32]. Both models are computational, using scattering amplitudes with parameterizations, but MAID is derived from the Mainz Unitary Isobar Model and SAID is derived from a phase shift analysis of the world data.

A dynamical model used is the Dubna Mainz Taipei (DMT) model. It has the same resonance terms as the MAID model, but different background terms [33].

There are also models based more directly on the underlying QCD, such as chiral effective field theory [34] and lattice QCD [35]. Lattice QCD is of particular interest, as it attempts to take QCD to the lower energy regions where traditional perturbation methods are no longer valid. This has met with little success in the area of understanding nucleon deformation, since the theoretical predictions are far from the experimental data for the EMR and CMR, as can be seen in Figure 1.11, where the Lattice QCD results are represented by a vertical line near the top of the graph.

This failure may be explained by a dynamical model created by T. Sato and T.-S. H. Lee [6]. They propose to theoretically treat the nucleon as a "bare" quark core surrounded by a pion cloud. This can be seen in Figure 1.12, where the dashed lines show the transition amplitudes for the quark core contribution only, and the solid lines show the amplitudes for the full calculation, quark core plus pion cloud.
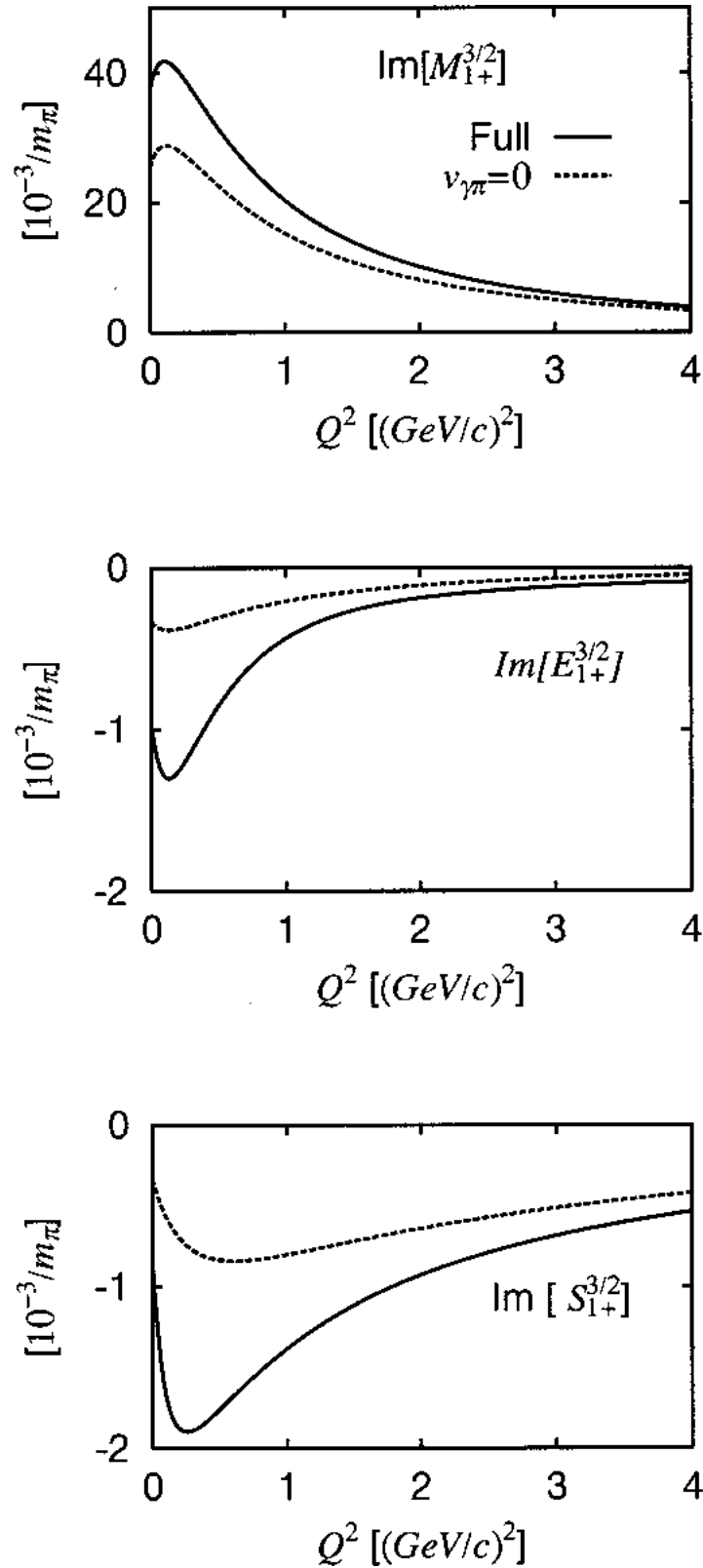
Figure 1.12: The Sato-Lee model predictions for the imaginary parts of the magnetic dipole and electric and Coulomb quadrupole amplitudes. The dotted line represent the model results from the core quarks alone, while the solid line represents the model results from the full nucleon, including the pion cloud contribution. Figure taken directly from Reference [6]

With this approach, the authors believe they can compare the "full" nucleon to the experimental data while comparing the "bare" core to lattice QCD results, hopefully finding a way to link QCD to this low energy region.

1.7   Multipole Extraction

Using the equations from Section 1.4, constructing a cross section from multipole amplitudes is relatively straightforward, but attempting to do the reverse and extract multipole values from a cross section measurement is more difficult.

One method for extracting multipoles is referred to as the Truncated Multipole Expansion (TME) [36], which starts by assuming that only the $\ell = 0$ and $\ell = 1$ multipoles contribute to the response functions. This transforms the response function equations to:

$$
\begin{aligned}
R_L \sqrt{\frac{\omega_{cm}^2}{Q^2}} = & |L_{0+}|^2 + 4|L_{1+}|^2 + 4\mathrm{Re}\{L_{1+}^* L_{1-}\} + 2\cos\theta \mathrm{Re}\{L_{0+}^*(4L_{1+} + L_{1-})\} \\
& + 12\cos^2\theta(|L_{1+}|^2 + \mathrm{Re}\{L_{1+}^* L_{1-}\}) \tag{1.38}
\end{aligned}
$$

$$
\begin{aligned}
R_T = & |E_{0+}|^2 + \frac{1}{2}|2M_{1+} + M_{1-}|^2 + \frac{1}{2}|3E_{1+} - M_{1+} + M_{1-}|^2 \\
& + 2\cos\theta \mathrm{Re}\{E_{0+}^*(3E_{1+} + E_{1+} - M_{1-})\} \tag{1.39} \\
& + \cos^2\theta(|3E_{1+} + M_{1+} - M_{1-}|^2 - \frac{1}{2}|2M_{1+} + M_{1-}|^2 - \frac{1}{2}|3E_{1+} - M_{1+} - M_{1-}|^2)
\end{aligned}
$$

$$
\begin{aligned}
R_{LT} \sqrt{\frac{\omega_{cm}^2}{Q^2}} = & -\sin\theta \mathrm{Re}\{L_{0+}^*(3E_{1+} - M_{1+} + M_{1-}) - (2L_{1+}^* - L_{1-}^*)E_{0+} \\
& + 6\cos\theta(L_{1+}^*(E_{1+} - M_{1+} + M_{1-}) + L_{1-}E_{1+})\} \tag{1.40}
\end{aligned}
$$

$$
R_{TT} = 3\sin^2\theta(\frac{3}{2}|E_{1+}|^2 - \frac{1}{2}|M_{1+}|^2 - \mathrm{Re}\{E_{1+}^*(M_{1+} - M_{1-}) + M_{1+}^* M_{1-}\}) \tag{1.41}
$$

The TME then assumes that any term without the dominant M_{1+} amplitude is small enough to safely ignore, which reduces the equations to:

$$R_L \approx 0 \tag{1.42}$$

$$R_T \approx \frac{5}{2}|M_{1+}|^2 + 2\cos\theta\mathrm{Re}\{E_{0+}^*M_{1+}\} - \frac{3}{2}\cos^2\theta|M_{1+}|^2 \tag{1.43}$$

$$R_{LT} \approx \sin\theta\mathrm{Re}\{L_{0+}^*M_{1+}\} - 6\cos\theta(L_{1+}^*M_{1+}) \tag{1.44}$$

$$R_{TT} \approx -3\sin^2\theta(\frac{1}{2}|M_{1+}|^2 + \mathrm{Re}E_{1+}^*M_{1+} + M_{1+}^*M_{1-}\}) \tag{1.45}$$

From this point, algebraic manipulation of the equations using data collected at different polar and azimuthal angles can allow the extraction of some combinations of multipole amplitudes.

For this method to be reliable, the background, non-resonant terms must remain small, so that the argument of only including terms involving the resonant M_{1+} remains an appropriate assumption, and there is concern that in the low momentum region this may not hold true.

Another method often used is the Model Dependent Extraction (MDE) [36], where the background amplitudes are supplied by one or more of the theoretical models. These values are then fixed while the resonant terms are allowed to vary in an attempt to fit the resulting cross section to the experimental results. This process can be quite time-intensive, especially if correlations between the resonant terms are required, with processing time growing exponentially as the number of resonant terms grows. The MDE results also include a model dependency, which is often mitigated by using multiple models together, but the error due to model dependence can be difficult to quantify[37].

A third method, the one used in this analysis, is a model-independent extraction[37], where all of the multipole amplitudes are randomly chosen, and the resulting calculated cross section is compared with the experimental cross section. This is done numerous times, with patterns developing which indicate values of the multipoles that best correspond to the experimental results. The multipole results are automatically correlated with one other, and while also time-intensive, the process should take less time than the MDE with the same number of response functions.

Chapter 2

The Experiment

The experiment E08-010 took place in Hall A, shown in Figures 2.1 and 2.2, at the Thomas Jefferson National Accelerator Facility (Jefferson Lab) in Newport News, Virginia, between February 27th and March 7th, 2011.

Dubbed "N-Delta", it was part of a family of four experiments that ran together that spring. These experiments shared calibrations and introduced compromises that had to be taken into account prior to the experimental run.

2.1 Continuous Electron Beam Accelerator Facility

The electron accelerator facility at Jefferson Lab is known as the Continuous Electron Beam Accelerator Facility (CEBAF). Originally, the entire complex shared that name, but as the overall facility grew in size, incorporating other areas of research such as the Free Electron Laser (FEL), the complex was renamed while retaining "CEBAF" for the accelerator itself.

The accelerator facility consists of the injector site, the linear accelerators (linacs), the recirculation arcs, and the three experimental halls, as seen in Figure 2.3.

The electron beam is produced in the injector, where a gallium-arsenide (GaAs) cathode is illuminated by a 1497 MHz gain-switched 180 nm diode laser [28]. Before the electrons leave the injector site, they can be accelerated by a set of cryomodules to a maximum initial energy of approximately 63 MeV[1].

This beam is then fed into the north linac, where twenty cryomodules can add up to 560 MeV of additional energy to the beam. The electrons then enter the east recirculation arc, which curves them into the south linac, also with twenty crymodules which accelerate the electrons further.

---

[1]When the accelerator first opened, the maximum initial energy was approximately 45 MeV, as seen Figure 2.3, due to a cryomodule field gradient of 5 MeV/m. That has since been upgraded to 7 MeV/m for all cryomodules, increasing all maximum energies beyond the original values seen in the diagram.

Hall A Spectrometers and Beamline Transport Assembly
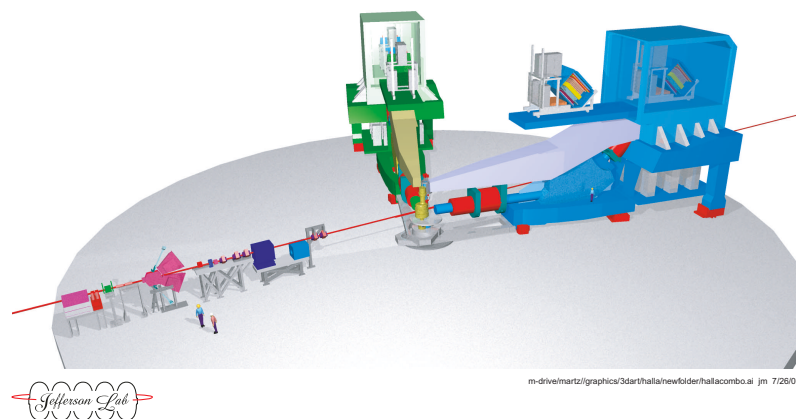
Figure 2.1: Three-dimensional diagram of Jefferson Lab's Hall A, showing the two High Resolution Spectrometers, with two human figures for scale. Figure taken directly from the Hall A website [42].
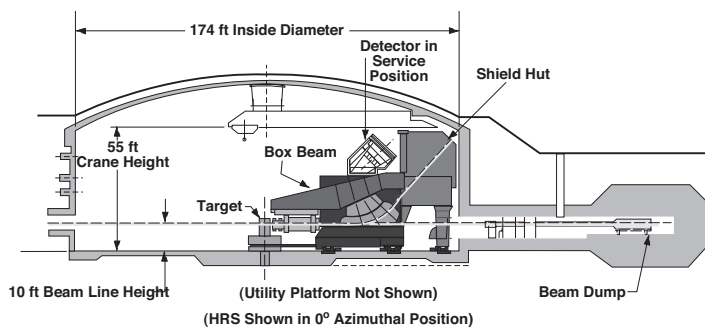
Figure 2.2: Schematic of Jefferson Lab's Hall A, showing details of the Hall and one of the High Resolution Spectrometers. Figure taken directly from Reference [28].
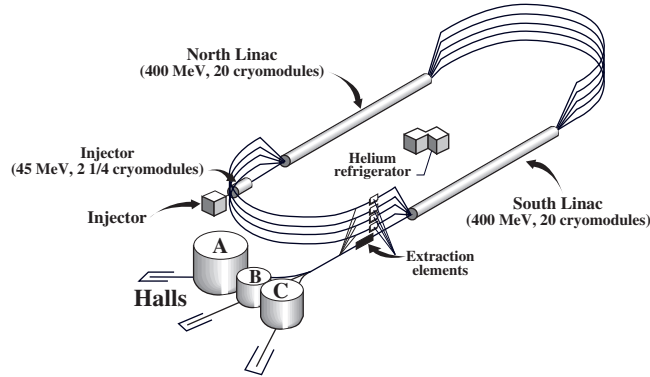
Figure 2.3: Diagram of the Continuous Electron Beam Accelerator Facility at Jefferson Lab. Upgrades since this diagram was created include an injector energy of 63 MeV and a linac energy of 560 MeV. Figure taken directly from Reference [28].

Following the south linac, the electron beam passes through a switcher, which can send it to one or more of the three Halls or into the west recirculation arc for another loop through the accelerator system. With each loop or "pass", the electrons can gain up to approximately 1 GeV, with a maximum of 5.7 GeV after five passes[2].

As the beam energy required by the N-Delta experiment was a little over 1 GeV itself, only one pass was needed. Higher beam energy for other experiments running that spring were achieved by simply including additional passes.

2.2 The Beamline

When the electron beam has been accelerated to the desired energy, it is passed into a hall's beamline by the switcher. For Hall A, this beamline consists of stainless steel tubing kept under vacuum that directs the beam into the Hall, where it passes several devices designed to track the beam's energy, position, current, and polarization.

2.2.1 Beam Energy

The beam's energy is measured by two separate methods, the Arc method and the eP method. The Arc method involves a careful measurement of the precise amount of curvature the beam experiences as it traverses the series of magnetic dipole magnets which "arc" the beam into the Hall. This precise determination is done using wire beam-position-scanners at various positions through the arc, and therefore cannot be

---

[2]Recent renovations to the accelerator system have increased the maximum energy to 12 GeV.
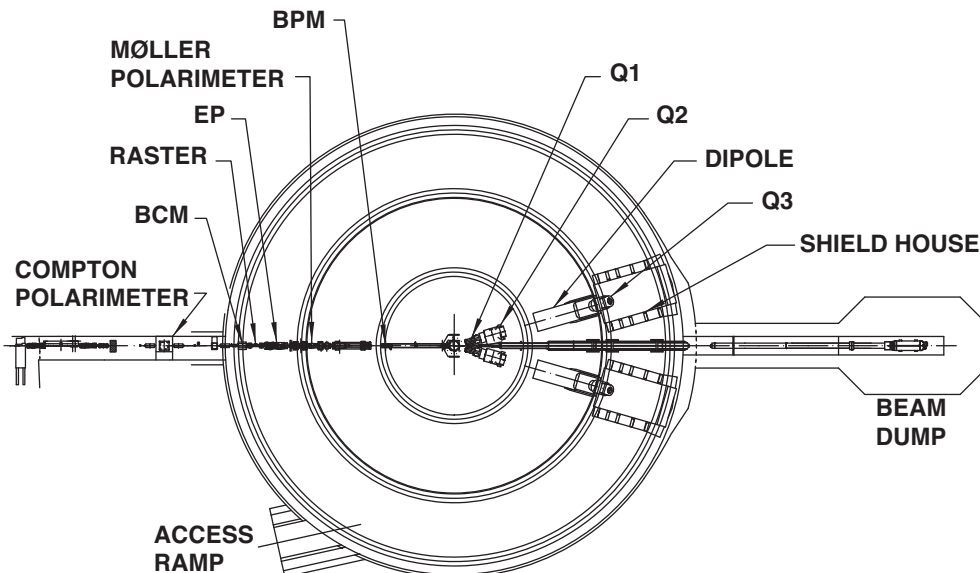
Figure 2.4: Diagram of Hall A and its beamline, showing the relative locations of the polarimeters, the BPM, the BCM, the energy measurment devices, the magnets, and the beam dump. Figure taken directly from Reference [28].
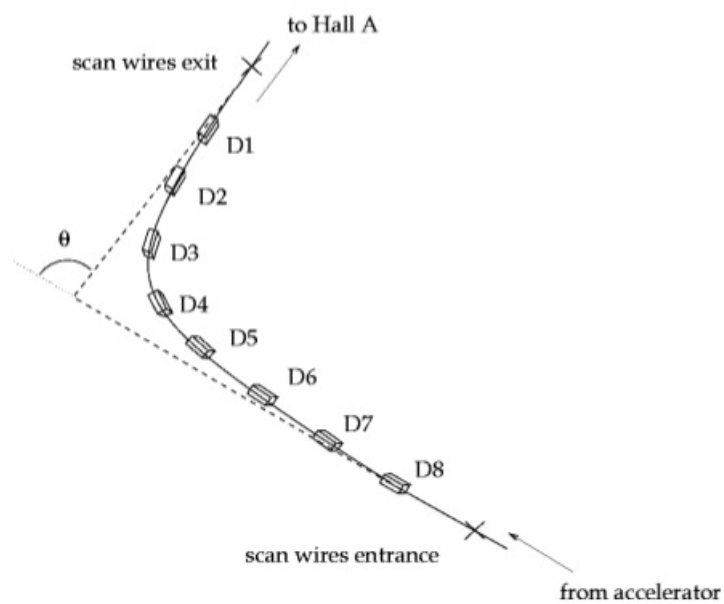
Figure 2.5: Diagram of the Arc beam energy method. Figure taken directly from Reference [38].
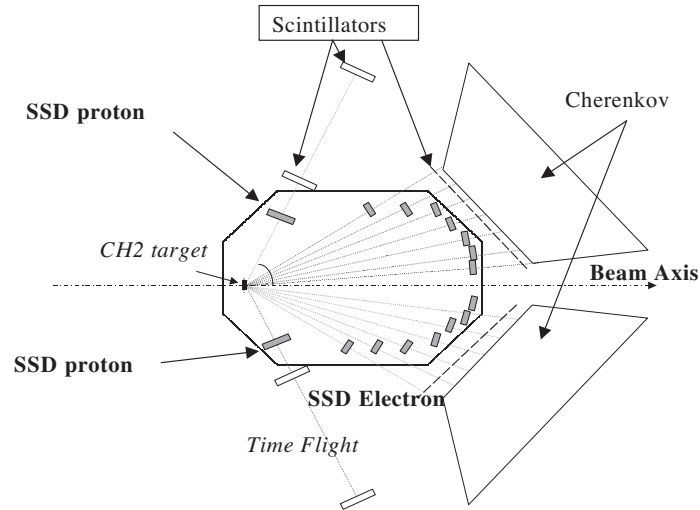
Figure 2.6: Diagram of the eP beam energy method, showing the CH_2 target and the dedicated detectors. Figure taken directly Reference [28].

done when the experiment is active, instead requiring some dedicated time to make the position scans. The eP method inserts a CH_2 strip into the beamline and measures the scattering electron angle using a series of dedicated detectors. The eP method is also invasive to the beam and cannot be used when an experiment is active and can be used to independently verify the measurements from the Arc method [28].

Beam energy measurements are routinely taken and were found to be sufficiently consistent that no additional calibration was necessary for the N-Delta experiment.

2.2.2   Beam Position

The beam's position is determined using two beam position monitors (BPM) located 7.524 m and 1.286 m upstream of the target [28]. Details of that calibration process are included in Section 3.2.

In addition to overall positioning, the beam also undergoes a process called "rastering". Because a direct electron beam can be intense enough to boil liquid targets and possibly melt some of the solid targets, the beam is quickly and repeatedly scanned over a small rectangular pattern to keep it from resting too long on a single location.

To check the size and positioning of the beam and raster, a special run called a "spot++" is performed using the beryllium oxide (BeO) target. During the run, the

beam illuminates a spot on the target, which can be seen using cameras installed inside the target chamber. After the run, a small program can be used to produce a set of plots similar to those in Figure 2.7 to examine the reconstructed beam position and raster size. For this experiment, the raster size was typically approximately 3 mm by 2 mm.

2.2.3   Beam Current

One of the most important quantities in any experiment is the beam current, since it directly factors into the luminosity, which is necessary for cross section calculations.

The beam current monitor (BCM) system in Hall A consists of several detectors working together to give an accurate measurement of the beam current during an experiment.

The Faraday Cup (FC) and the 0L02 cavity are near the injector end of the beamline [28]. The Faraday Cup is the most accurate measurement, but it is destructive, so no beam may be sent into the hall while it is active. The 0L02 cavity's measurement is non-destructive, but tends to drift over time, so it needs to be periodically recalibrated relative to the Faraday Cup. Typically the 0L02 cavity is not used during an actual experimental run, as it is located too far from the Hall to accurately reflect the current at the target.

Instead, measurements are made from two BCM cavities located in the Hall. They are both upstream of the target but are designated "upstream" and "downstream" based on their locations relative to each other. The BCM cavities measure induced voltage differences which are recorded in the data stream through the scalers. Each cavity is recorded using three different multipliers: x1, x3, and x10. x10 has the highest resolution but becomes unusable at high currents.

Additionally, there is a detector between the BCM cavities called the Unser coil. It tends to drift more than the other devices and was not used for this experiment or its analysis.

2.2.4   Beam Polarization

There are also two polarimeters in the beamline designed to measure the polarization of the beamline, the Compton polarimeter and the Møller polarimeter. Neither was
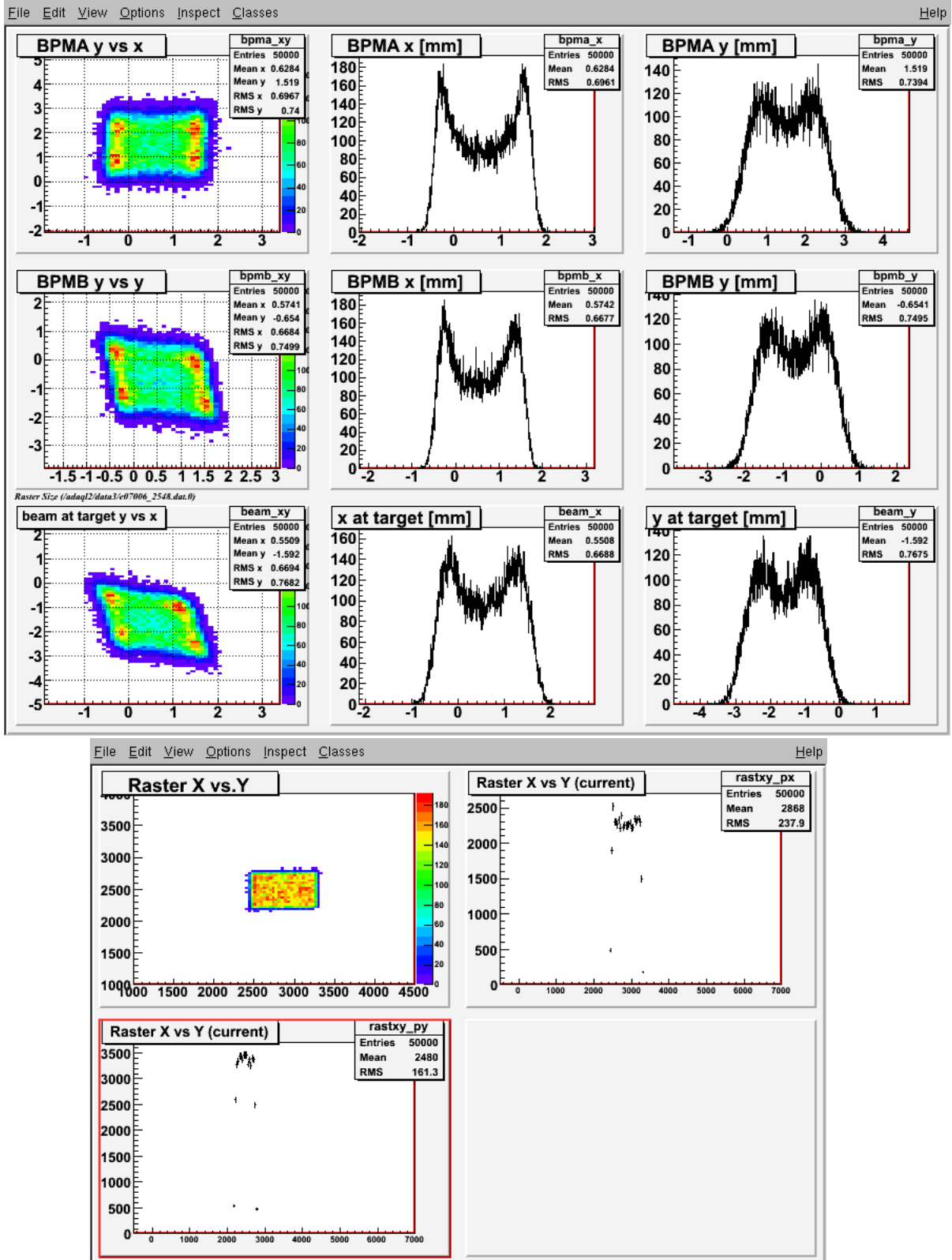
Figure 2.7: Example spot++ images from run 2548, showing the reconstructed beam positioning and rastering. Figure taken directly from Reference [39].

used during this experiment, as beam polarization information was not required.

2.3   The Target

The Hall A target system consists of a scattering chamber and a target ladder [28].

The scattering chamber has several ports for vacuum pumps, visual inspection, electrical feedthroughs, as well as beam entrance and exit ports, ensuring that the beam interacts with as little material as possible aside from the target. The target chamber vacuum was maintained at less than 0.13 mPa throughout the experiment, with values typically around 0.05 mPa [39].

The target ladder inside the scattering chamber, seen in Figure 2.8, was designed to hold numerous targets, both cryogenic and solid, and can be manipulated remotely, which allows different targets to move into position without opening the Hall or the target chamber.

The target ladder configuration used in this experiment contained three cryogenic loops: a liquid hydrogen loop (LH_2), a liquid deuterium loop (LD_2), and a gaseous helium loop, although the helium would not be introduced into the system until after the experiment ended. The cryogenic targets were continuously monitored from a station in the counting house above the Hall, where pressure and temperature could be manipulated to maintain target density.

The liquid deuterium target was maintained at a temperature of 22 K and a pressure of approximately 160 kPa, while the hydrogen target was maintained at a temperature of 19 K and a pressure of approximately 210 kPa throughout the experiment [39], resulting in a near-constant density of 0.0725 g/cm^3. All three cryogenic targets consisted of a pair of "cigar-shaped" aluminum loops, as seen in Figure 2.8. One loop is 4 cm long, which is useful for high currents, since a smaller loop is less likely to undergo density changes due to the beam. The other is a 15 cm loop, which allows for more interaction between the beam and the target material, which produces more events in less time but also contributes more background events, producing a noisier signal, and must be run at a lower current to avoid target boiling.

Accounting for the location of the beam, curvature of the endcaps, expansion of the cell due to pressure, and contraction of the aluminum due to the cold, it was determined that the effective length for the 4 cm target was 3.860 ± 0.004 cm and
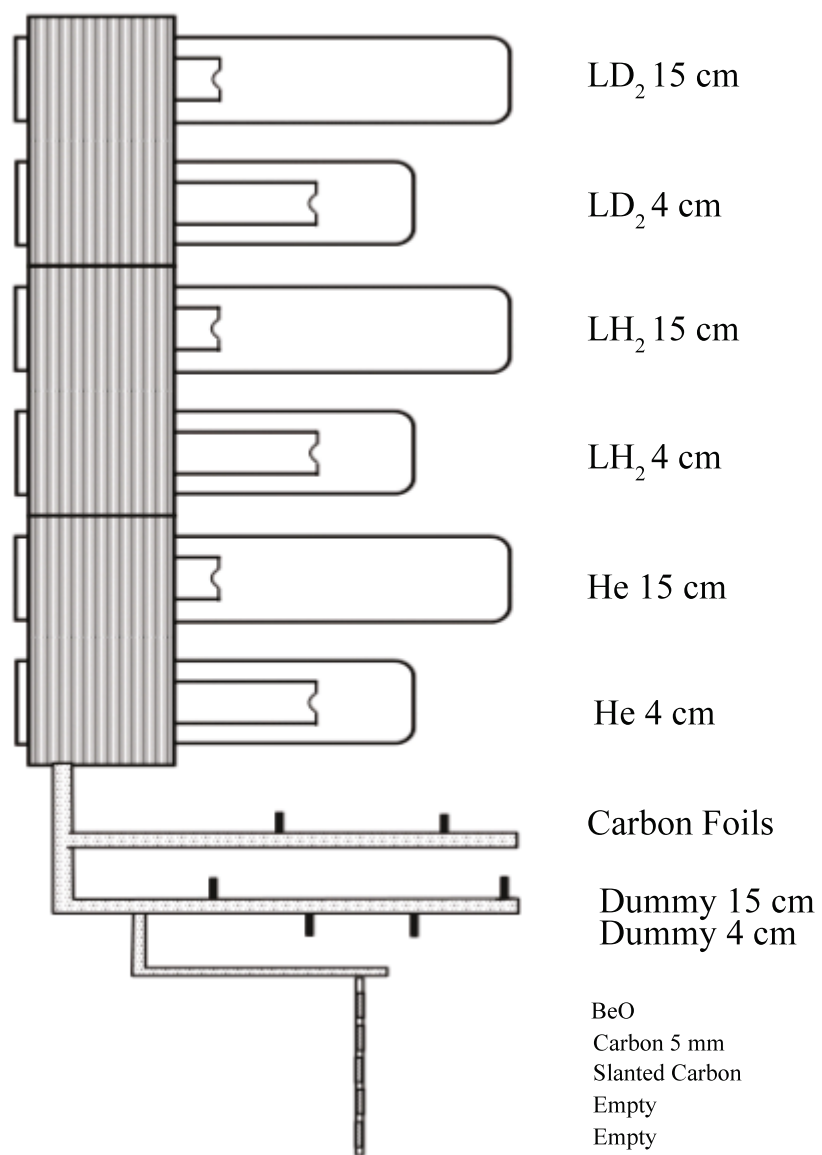
Figure 2.8: Side view of the Hall A target ladder. Figure taken directly from Reference [10] and modified to reflect the target configuration during the experiment.

LH$_2$ (cm)	Entrance Window (cm)	Exit Window (cm)	Side Wall (cm)
14.80 ± 0.02	0.0081 ± 0.0004	0.0207 ± 0.0055	No data
3.860 ± 0.004	0.0145 ± 0.0004	0.0149 ± 0.0008	0.0141 ± 0.0014

Table 2.1: Thickness of the liquid hydrogen cryotargets and their cell walls, from Reference [40]. The effective lengths of the LH$_2$ targets were calculated by Adam Blomberg.

14.80 ± 0.02 cm for the 15 cm target.

In addition to the cyrotargets, there were also several solid targets used prior to and during the experiment for calibration purposes and determination of background contributions.

Directly beneath the cryogenic loops was an "optics" target made of a set of carbon foils, spread out over 15 cm along the beamline. This target is usually a set of seven foils [38], which is then used for mispointing calibrations; in this experiment, thirteen foils were used, and it was felt that it would be too difficult to resolve the individual foils during the calibration process, so the beryllium oxide (BeO) target was chosen for that purpose instead.

Beneath the carbon foils were two "dummy" aluminum targets, designed to mimic the entrance window and end-cap of the cryogenic targets, one with the aluminum foils 15 cm apart and one with foils 4 cm apart. Both targets were made of an aluminum alloy with a density of 2.810 g/cm^3 [41]. These dummy targets could be used to examine background radiation introduced into the data stream by the aluminum in the cryotarget cells.

Beneath the dummy targets was a single beryllium oxide (BeO) foil, usually used only for visual inspection of the beam. For this experiment, the BeO target was also used for mispointing calibration purposes and raster checks.

There were also two additional carbon foil targets located under the BeO, one 5 mm thick and the other slanted to provide a different illumination geometry on the focal plane. Neither of these targets were used in this experiment, but they were used in other experiments in the spring run period.

Further information about the solid targets is available in Table 2.2.

During the experiment, the target operator (TO) had the assigned task of using a computer in the counting house to move the target ladder to the desired position,

Target Name	Material	Purity	Thickness (g/cm^2)
Optics	C	99.5%	0.025 ± 0.001 each
15 cm dummy	7075 T-6 Al		0.2750 ± 0.0003 (u)
			0.2790 ± 0.0003 (d)
4 cm dummy	7075 T-6 Al		0.1140 ± 0.0002 (u)
			0.1160 ± 0.0002 (d)
BeO	BeO	99.0%	0.149 ± 0.001
Carbon	C	99.95%	0.8918 ± 0.0008
Slanted Carbon	C	99.9%	0.0419 ± 0.0005

Table 2.2: Information about the Hall A solid targets, taken from [40].

as well as to monitor the temperature and pressure of the cryotargets, adjusting the liquid helium coolant flow to keep the liquid targets from freezing or boiling.

2.4   High Resolution Spectrometers

The two high resolution spectrometers, seen in Figure 2.9, are the central pieces of Hall A. They both contain four superconducting magnets in a quadrupole-quadrupole-dipole-quadrupole (QQDQ) configuration [28], seen in Figure 2.10, designed to direct incoming charged particles to the detectors. The design was optimized for angular and momentum acceptance, position and angular resolution, target acceptance, and angular range.

While both spectrometers can be configured to detect a variety of particles, in this experiment one was used to detect the scattered electrons, designated here as HRSe or RHRS, and the other, designated here as HRSh or LHRS, was used to detect the recoil protons. The basic hardware configuration for both spectrometers is virtually identical.

The basic detector package consists of two vertical drift chambers, three scintillator layers, a gas Cherenkov detector, and a set of lead-glass shower counters [28]. Depending on the particular experiment, other components could be added or removed. For example, as the polarization of the recoil proton was required for another experiment, the Focal Plane Polarimeter (FPP) was added to the LHRS, as seen in Figure 2.9.

Table 2.3 lists the operating specifications for the HRS detectors.
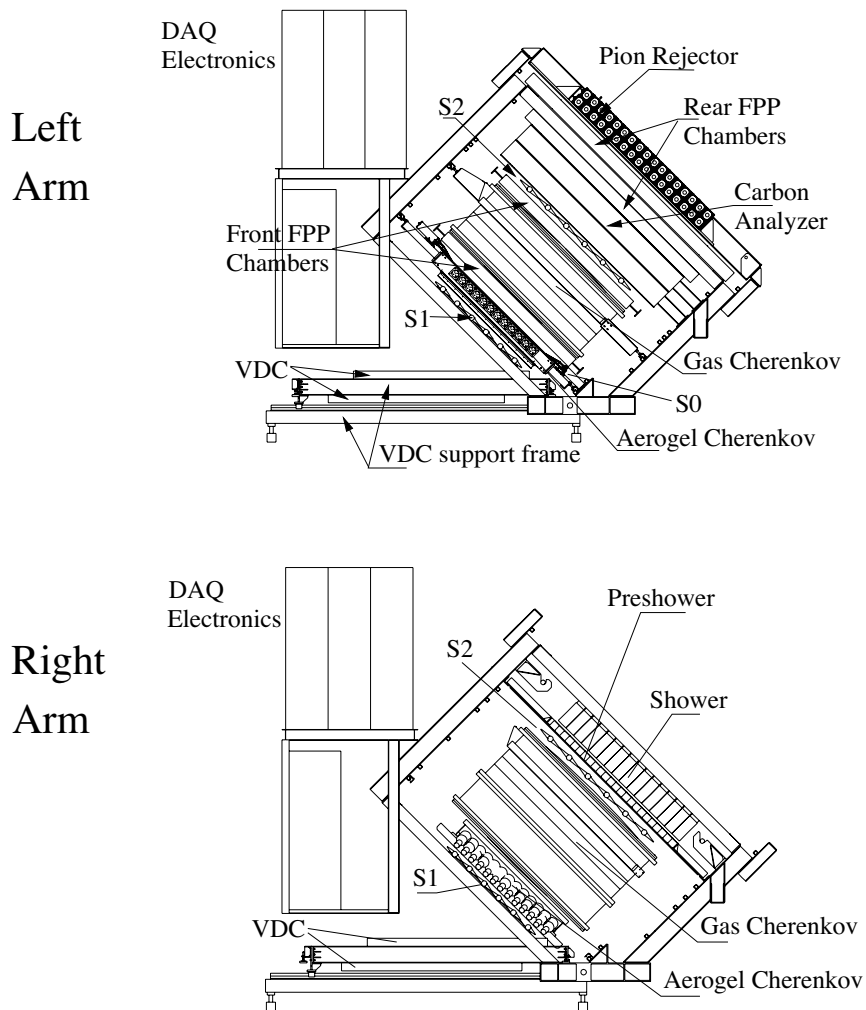
Figure 2.9: Example side view of the Hall A detector packages, showing the various detectors. Figure taken directly from Reference [28].

Configuration	QQD$_n$Q vertical bend
Bend Angle	45°
Optical Length	23.4 m
Momentum Range	0.3 - 4.0 GeV/c
Momentum Acceptance	$\|\delta$p/p$\|$<4.5%
Momentum Resolution (FWHM)	1×10^{-4}
Dispersion (D)	12.4 cm/%
Radial Linear Magnification (M)	2.5
D/M	5.0
Angular Range	
HRS-L	12.5 - 150°
HRS-R	12.5 - 150°
Angular Acceptance	
Horizontal	$\pm$28 mr
Vertical	$\pm$60 mr
Angular Resolution	
Horizontal	0.6 mr
Vertical	2.0 mr
Solid Angle	
(rectangular approximation)	6.7 msr
(elliptical approximation)	5.3 msr
Transverse Length Acceptance	$\pm$5 cm
Transverse Position Resolution	1 mm
Transverse Position Resolution (FWHM)	1.5 mm
Spectrometer Angle Determination Accuracy	0.1 mr

Table 2.3: Main design characteristics of the Hall A high resolution spectrometers, including resolution and acceptances [28, 42].
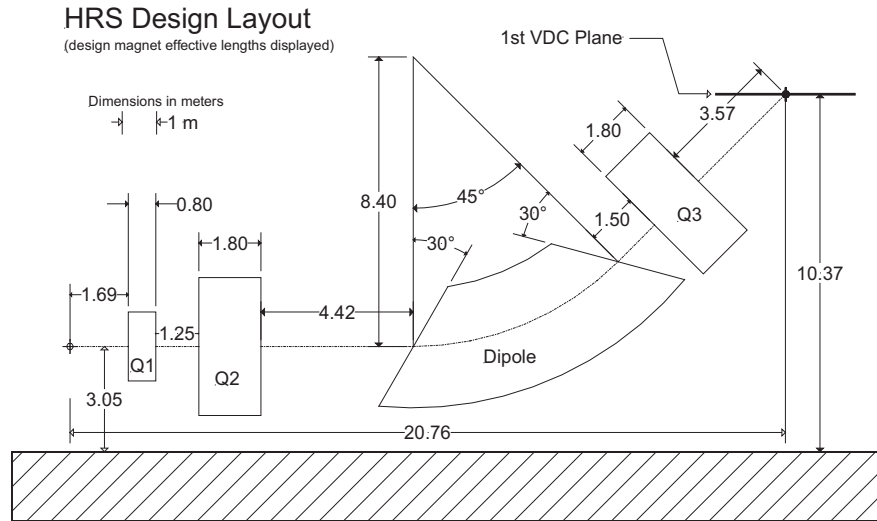
Figure 2.10: Side view of the Hall A spectrometer magnets. Figure taken directly from Reference [28].

2.4.1 Vertical Drift Chambers

The vertical drift chambers (VDC) consist of two gas-filled chambers with two layers of 368 wires in each [28].

The two chambers, labeled "1" and "2", are 335 mm apart and lay horizontally relative to the Hall floor. As the spectrometer magnets bend the scattered and recoil particles to an angle of 45 degrees, relative to the floor, the VDCs end up angled at 45 degrees relative to the incoming particles. The two layers of wires in each chamber, labeled "U" and "V", are 26 mm apart and set at right angles to each other for optimal tracking [28].

The wires themselves are 4.24 mm apart, with a constant voltage of approximately 4 kV in a gas mixture of 62% argon and 38% ethane, which is kept in constant circulation [28].

When a particle passes through the gas contained within the chambers, it triggers a cascade of charged particles, which are attracted or repelled by the voltage in the wires, creating a detectable signal whose strength is related to the distance between the incoming particle and the wire.

Using the pattern of affected wires in the four layers, a trajectory for the detected particle can be determined. If more than one possible trajectory is available, typically one is singled out as the "golden" track based on a χ^2 minimization algorithm in the
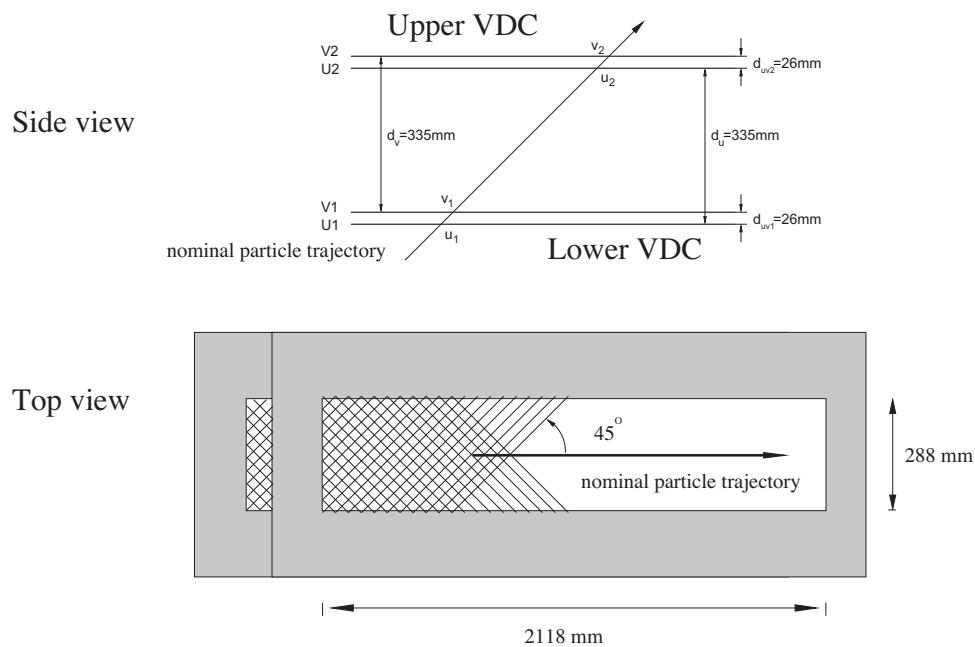
Figure 2.11: Schematic of the VDCs. Figure taken directly from Reference [28].
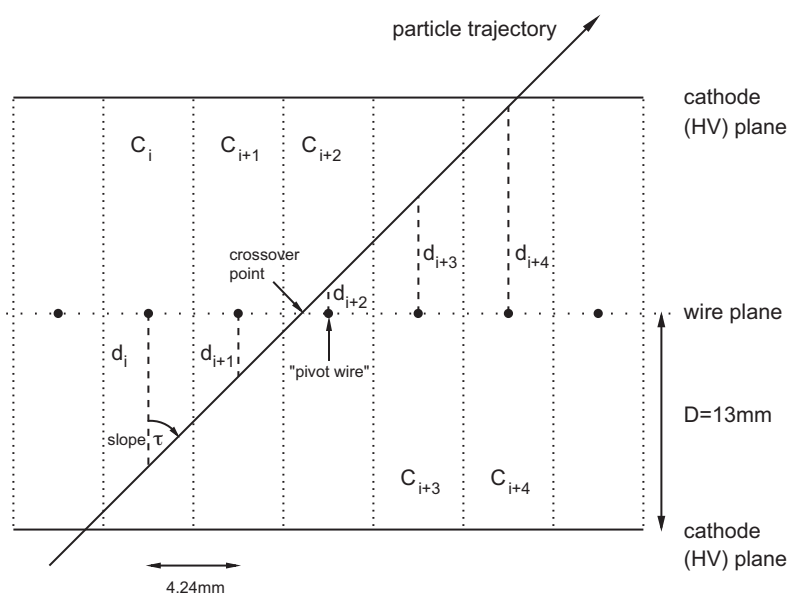
Figure 2.12: Schematic of drift chamber particle detection. Figure taken directly from Reference [28].

analyzing software [43].

The calibration of the VDCs is covered in Section 3.3.

2.4.2   Scintillators

Within the detector hut are three layers of scintillating materials designed for triggering and timing. The primary layers are labeled "S1" and "S2", with the third layer labeled "S0", which is typically used for a scintillator efficiency check.

The S1 layer is made up of six 5 mm thick BICRON 408 plastic scintillator bars. Each bar has an active area 35.5 cm wide and 29.5 cm tall, with a 10 mm overlap between the bars [28].

The S2 layer was originally identical to the S1 layer, but later rebuilt as "S2m" with sixteen 5 cm thick EJ-230 fast plastic scintillator bars, each 43.2 cm wide and 14 cm tall with no overlap between the bars [28].

The S0 layer is made of a single 10 mm thick BICRON 408 plastic scintillator with an active area of 170 cm long by 25 cm wide. While the S1 and S2 bars have horizontal orientations, the single S0 bar in each arm is oriented vertically [28].

The primary purpose of the scintillators is triggering the data acquisition (DAQ) system. Each bar has two photo-multiplier tubes (PMTs), one on each end, and these PMTs send any signals from detected particles to the electronics. The electronics first look for a coincidence between the two PMTs from a single bar, and then look for a coincidence between the S1 and S2 layers. If two signals arrive within a predetermined timing window, the electronics determine that a particle has been detected and produces a pulse known as a "trigger". For the right arm, the trigger was called "T1" and for the left arm, "T3".

If these two triggers occur within a "coincidence window", a third signal, "T5" is produced, known as the "coincidence trigger", which indicates that an experimentally-relevant event may have occurred.

To determine how efficient the S1 and S2 layers are, the S0 layer can be used as an efficiency trigger. Since most events that trigger the S1 or S2 layers also have to pass through the S0 layer, the electronics keep track of how often two of the three layers are triggered without triggering all three. If the S0 layer triggers but only one of S1 or S2, this produces a trigger called "T2" in the right arm and "T4" in the left

arm. By comparing the rates of T2 (T4) with T1 (T3), an efficiency of the triggering system can be calculated. More information about this process is in Section 4.2.5.

The scintillators are also used for timing purposes. Typically the length of the wires connecting the PMTs with the electronics are carefully exploited so that the signal from the PMTs on one side of one scintillator layer, such as the right side of the S2 layer, always arrives at the electronics last. This sets the timing of every other signal relative to that one side, allowing for a relatively simple coincidence timing calculation between the two arms.

In this experiment, the wire lengths were not adjusted properly, and the coincidence timing was more complicated. More information about this is available in Section 3.5.

2.4.3 Cherenkov Detectors

The typical HRS configuration includes a gas Cherenkov detector, usually with CO_2 at atmospheric pressure [47]. As the particles travel through the gas, they may emit Cherenkov radiation if their speeds exceed the speed of light in the gas. The light is bounced around inside the detectors by a series of mirrors and can be picked up by one or more of the 10 PMTs connected to the detector. The Cherenkov detectors are typically used as part of the trigger efficiency setup, where they play the same role as the S0 plane, or for particle identification, since the gas can be adjusted such that desired or undesired particles can be quickly identified by the Cherenkov radiation and filtered at the electronics level.

For example, if a particular reaction will produce a large number of unwanted pions and muons in addition to electrons, the gas can be adjusted such that only the faster electrons produce Cherenkov radiation. Then, if the Cherenkov system detects a particle, that particle must be an electron, resulting in particle identification without computer involvement.

During the spring experimental run, the gas Cherenkov detector in the left arm was moved out of the way to make room for the focal plane polarimeter (FPP). This was not detrimental to the experiment, since both the wanted protons and unwanted pions in the LHRS were too slow to trigger the detector in that arm.

There was talk prior to the experiment of possibly using an aerogel Cherenkov

HRS-L
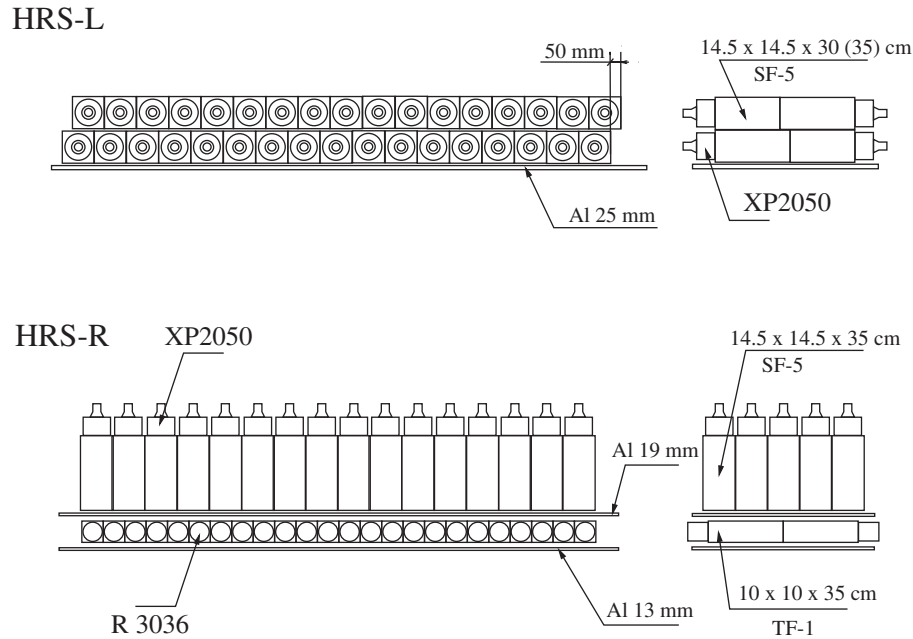
Figure 2.13: Schematics of the shower counters. Figure taken directly from Reference [10].

detector which would be able to separate the protons and pions, but that detector had been out of service for so long that it was felt it would not be worth the effort to recommission it.

While the Cherenkov detector in the right arm was examined in a parallel analysis of this experiment for post-experiment particle identification, it was not ultimately used.

2.4.4 Shower Counters

After the particles have passed through the rest of the detectors, they pass through two layers of lead-glass shower counters. In the left arm, the two layers are referred to as the pion rejectors, while in the right arm they are called the preshower and shower counters.

Each of the pion rejector layers contains 34 blocks of SF5 glass in two rows of 17. Each block is 14.7 cm by 35.0 cm by 14.7 cm. The pre-shower layer is made of 48 TF1 glass blocks in two rows of 24, with each block 10.0 cm by 35.0 cm by 10.0 cm. The shower layer is made of 75 SF5 glass blocks in five rows of 15, with each block 15.0 cm by 15.0 cm by 32.5 cm [28].

The shower counters contain no timing information and only report energy deposition, which is useful for particle identification. Like the RHRS Cherenkov detector, a parallel analysis examined the shower counters, ultimately deciding to use data only from the preshower counters for particle identification.

2.5 Data Acquisition

Data acquisition was performed using a combination of hardware and software, in both the counting house and the Hall itself.

All data signals produced by the various detector systems were read in by either analog-to-digital converters (ADC), time-to-digital converters (TDC), or scaler counters. Timing information was stored in the TDCs, model 1877, with a 0.5 ns time resolution. These modules were common stop, meaning that the last signal detected was the first signal in the read-out. The ADC modules were model 1885 and measured signal strength, proportional to energy deposition in the material.

Some devices, like the VDCs, only read out TDC information, while others, like the shower counters, only read out ADC information.

All ADC and TDC cards were stored in read-out controller (ROC) boxes, with the boxes in the RHRS detector hut labeled ROC1 and ROC2, while the boxes in the LHRS detector hut were labeled ROC3 and ROC4.

In this experiment, due to the presence of the BigBite magnet and detector, as well as the neutron detector, necessary for one of other experiments, a third group of data acquisition systems were needed. These systems consisted of ROC5, ROC8, ROC9, and ROC10, all located in the BigBite weldment, situated on the Hall floor next to the RHRS.

In any experiment in which triggers are produced by various detectors, a system is needed to determine on which triggers to collect data. As mentioned earlier, the scintillators in both arms produced trigger signals, but it would be extremely inefficient to attempt to record data on every T1 or T3 signal, as it was only the T5 coincidence events that were experimentally relevant.

Prior to each run, prescale factors were determined to decide how often to record data based on the individual triggers. Using this system, a trigger event is only recorded after a certain number of events, based on the prescale factor. The prescale

factors are heavily dependent on the spectrometer configuration and would often change between different kinematic settings. As T5 coincidence events were indicative of the event type most important to the experiment, the T5 prescale was set to 1 and data was collected for every possible T5 event.

This process of determining when to collect data is performed by a device called the trigger supervisor (TS). A TS module exists in both HRS detector huts, but for this experiment, as well as the Deuteron Threshold and SRC experiments, the TS in the BigBite weldment was used instead. This meant cables had to be strung from the detectors down to the weldment for the trigger determination and then back up to the detector huts for the actual data recording.

The data recording process was performed by a software packaged developed at Jefferson Lab for its systems called the CEBAF On-line Data Acquisition (CODA) system. The program is run from a computer in the counting house, and typically one member of the shift crew on duty during data-taking is responsible for starting and stopping CODA runs, as well as adjusting prescales.

Raw data from CODA is then stored on the Jefferson Lab on-site computer systems, where researchers can access them for analysis, and eventually moved to their long-term storage tape drives for permanent storage.

2.6   The Proposal

The original proposal [1] for this experiment suggested splitting the runtime into fourteen different kinematic settings, split into three groups based on the momentum transfer values, as shown in Table 2.4.

Each of the groups would have multiple measurements at different angles. The first setting would be a parallel cross section measurement, in which the proton recoils in the same direction as the virtual photon, $\hat{q}$. Following that would be at least one pair of measurements taken at the same θ_{pq}^* values, but one at $\phi = 0°$ and one at $\phi = 180°$, allowing for comparisons of the "inside" and "outside" kinematic settings.

The first group would have a Q^2 setting of 0.04 $(\text{GeV}/c)^2$. The previous "N-Delta" experiment, performed at Mainz in 2003, was only able to reach a minimum of 0.060 $(\text{GeV}/c)^2$ [26] due to a physical limitation in the layout of Hall A1 at Mainz. The spectrometers in Hall A at Jefferson Lab can reach a minimum of 12.5°, which allows

Kin	Q^2 $(\text{GeV}/c)^2$	W (MeV)	θ^*_{pq} (deg)	θ_e (deg)	P'_e (MeV/c)	θ_p (deg)	P'_p (MeV/c)
1	0.040	1221	0	12.52	767.99	24.50	547.64
2	0.040	1221	30	12.52	767.99	12.52	528.12
3	0.040	1221	30	12.52	767.99	36.48	528.12
4	0.040	1260	0	12.96	716.42	21.08	614.44
5	0.090	1230	0	19.14	729.96	29.37	627.91
6	0.090	1230	40	19.14	729.96	14.99	589.08
7	0.090	1230	40	19.14	729.96	43.74	589.08
8	0.125	1232	0	22.94	708.69	30.86	672.56
9	0.125	1232	30	22.94	708.69	20.68	649.23
10	0.125	1232	30	22.94	708.69	41.03	649.23
11	0.125	1232	55	22.94	708.69	12.52	596.43
12	0.125	1232	55	22.94	708.69	49.19	596.43
13	0.125	1170	0	21.74	788.05	37.31	575.57
14	0.125	1200	0	22.29	750.16	34.06	622.63

Table 2.4: The proposed experimental settings, which assumed a beam energy of 1115 MeV and a 6 cm target. Data reproduced from the experiment proposal [1].

for a lower Q^2.

In addition to the parallel, inside, and outside kinematics, this group contained another parallel cross section measurement, but at a larger W value, in an effort to further explore the phase space at this Q^2 setting.

The second group would have a Q^2 value of 0.090 $(\text{GeV}/c)^2$, with the intention of obtaining the CMR between previously measured locations. There would be three measurements for this group, again one parallel cross section measurement and two measurements on either side of $\hat{q}$.

The third group would have a Q^2 value of 0.125 $(\text{GeV}/c)^2$, a location that had been previously measured in other experiments [1]. The purpose of these measurements would be to validate one or more of the previous measurements. This group would have a parallel cross section and two pairs of inside and outside measurements. There would also be two additional parallel cross section measurements at different W values to scan the phase space across the $\Delta(1232)$ resonance.

The proposed settings assumed a beam energy of 1115 MeV and a 6 cm liquid hydrogen target, from which rates and beamtimes were calculated. Like many experiments, though, the actual experiment deviated from the initial runplan.

Kin	Q^2 (GeV/c)^2	W (MeV)	θ^*_{pq} (deg)	θ_e (deg)	P'_e (MeV/c)	θ_p (deg)	P'_p (MeV/c)
1	0.045	1221	0	12.56	805.40	25.55	552.30
2	0.045	1221	33	12.56	805.50	12.53	528.80
3	0.045	1221	33	12.56	805.80	38.57	528.80
4	0.045	1260	0	12.98	754.70	22.08	618.40
5	0.090	1230	0	18.21	770.10	29.74	625.80
6	0.090	1230	45	18.21	769.80	13.61	577.80
7	0.090	1230	45	18.21	772.00	45.87	575.00
8	0.125	1232	0	21.80	749.10	31.30	670.00
9	0.125	1232	30	21.80	748.60	21.13	647.80
10	0.125	1232	30	21.80	751.00	41.48	644.80
11	0.125	1232	55	21.80	748.60	12.94	595.10
12	0.125	1232	55	21.80	751.20	49.67	591.30
13	0.125	1170	0	20.72	826.20	37.74	574.00
14	0.125	1200	0	21.21	789.40	34.49	620.60

Table 2.5: The updated experimental settings, using a beam energy of 1160 MeV and a combination of the 4 cm and 15 cm targets.

2.7 Settings

During preparations for the experiment, it was learned that the actual beam energy would be 1160 MeV and that the 6 cm "beer can" targets were longer in use, replaced with the 4 cm and 15 cm "cigar-shaped" targets. Modifications were made to the settings, including energy loss corrections, as shown in Table 2.5.

The increase in the beam energy altered the lowest possible Q^2 setting from 0.040 (GeV/c)^2 to 0.045 (GeV/c)^2. The change in the beam energy also meant that the lowest angle, 12.5°, now corresponded to a larger θ^*_{pq} angle for the lowest Q^2 setting, altering it from from 30° to 33°.

It was decided to run the first four kinematic settings with the 4 cm target, while the rest would use the 15 cm target. Further, if possible, all of the settings would use a current of 50 µA, though it was known that such a high current might produce too much deadtime[3] and would require test runs to find the highest acceptable current. The amount of time necessary to collected the desired statistics was also calculated, as well as the predicted event rates.

Since another detector system, called BigBite, would be in place on the right side

---
[3]For more information deadtime, see Section 4.2.3.

Kin	Q^2 (GeV/c)^2	W (MeV)	θ^*_{pq} (deg)	θ_e (deg)	P'_e (MeV/c)	θ_p (deg)	P'_p (MeV/c)
1	0.045	1221	0	12.5	805	25.5	552
2	0.045	1221	33	12.5	805	12.5	528
3	0.045	1221	33	12.5	805	38.5	528
4	0.045	1260	0	13.0	755	22.0	618
5	0.090	1230	0	18.0	770	30.0	626
6	0.090	1230	45	18.0	770	13.5	576
7	0.090	1230	45	18.0	770	46.0	576
8	0.125	1232	0	22.0	750	31.5	670
9	0.125	1232	30	22.0	750	21.0	646
10	0.125	1232	30	22.0	750	41.5	646
11	0.125	1232	50	22.0	750	14.5	606
12	0.125	1232	50	22.0	750	48.0	606
13	0.125	1170	0	20.5	826	37.5	574
14	0.125	1200	0	21.0	789	34.5	621

Table 2.6: The actual experimental settings. Currents used for each setting can be found in Table 2.7.

of the hall, it was decided that the right arm should detect electrons, since all of the electron angles are relatively low and the electron arm would not move as often as the proton arm.

The actual movement of the spectrometer arms was done using train-like wheels attached to the bottom of the devices. Two cameras were set up on each arm to record the position of the spectrometers relative to marks on the floor. For the front camera, these marks were every half-degree, with a caliper attached to the camera to allow for exact measurements of the spectrometer angle relative to the markings.

Prior to the experiment, it was suggested that it would be simpler to leave the calipers alone and keep the spectrometer movements to half-degrees. By setting the floor markings to $+29$ on the left arm's caliper and -34 on the right arm's caliper, it was assured that the spectrometers were at the desired angles without having to deal with parallax issues. Further, rounding the momentum settings to the nearest MeV and keeping them as consistent as possible between spectrometer configurations to minimize the time spent adjusting the magnets.

With these changes, and one last adjustment to the θ^*_{pq} values for Kinematics 11 and 12, the settings were finalized.

2.8 Timeline

As mentioned earlier, "N-Delta" was part of a family of experiments that ran in the spring of 2011.

The first experiment to run was E08-008 [44], nicknamed "Deuteron Threshold", which ran from February 22nd to February 28th. The experiment was designed to study the interaction between the proton and neutron within a deuteron and, as such, required knowledge about the polarization of the proton. The focal plane polarimeter (FPP) was installed in the LHRS for this purpose. Both "Deuteron Threshold" and "N-Delta" were relatively short experiments, only running for approximately a week each.

Following "N-Delta" was E07-006 [45], dubbed "SRC", a larger experiment designed to study short range correlations (SRC), a phenomenon in which pairs of nucleons form very strong bonds within the nucleus and behave violently when separated. Studying this phenomenon required information about the scattered electron, the recoil proton, and a third particle, either a proton or a neutron. By installing the BigBite magnet and its accompanying spectrometer, as well as a large neutron detector (HAND) set up behind the magnet, the researchers could study pp and pn pairings.

The last experiment was E08-014 [46], dubbed "$x > 2$", which also studied short range correlations, but in a regime where the Bjorken x (x_B) is larger than 2, indicating that nucleons were forming tight bonds in groups of three or more.

Researchers and graduate students associated with all four experiments worked together to prepare the equipment and participated in data collection.

Setup began in early January 2011 with the removal of equipment from the previous experiment and installation of equipment for the new experiments.

By mid-February, the equipment was ready for initial commissioning and the first test runs, which included pedestal runs used to set threshold limits on several of the detectors. The optical and spectrometer surveys, necessary for proper mispointing calibration, were performed during this time. This commissioning lasted until February 16th, when the calibrations started.

The calibration period included runs necessary to check spectrometer configurations using elastic runs and the first set of BPM calibration runs.

The calibration period was considered finished on February 22nd, and the Deuteron Threshold experiment officially began. The experiment ended with a series of "delta scans", in which the sieve slits were lowered and momentum settings were adjusted above and below the central momentum values for an elastic cross section, for the purposes of checking the spectrometers' optical matrices.

Following the end of the delta scans on February 28th, the N-Delta experiment began, starting with Kinematic 1. Almost immediately an error was detected, as the computer deadtime was near 90% at 50 µA, far higher than the 20% predicted. While this was being investigated, the current was dropped to 15 µA and data collection continued. With the lower current, the data collection took far longer than anticipated, 19 hours instead of the anticipated 4 hours.

Like Kinematic 1, Kinematics 2 and 3 were also stymied by the deadtime issue and the low current, with Kinematic 2 taking 18 hours instead of 5, and Kinematic 3 taking 17 instead of 8.

After the third kinematic setting, it was decided to return to the first kinematic's settings and take more data. Following that data collection, the deadtime issue was resolved, discovered to be a problem in the CRL code for ROC10.

One consequence of the high deadtime issue is that Kinematic 4, which planned to examine a higher W region with the lowest Q^2 setting, had to be completely eliminated. Further, only 85% of the desired statistics were collected for Kinematics 9 and 13.

Rather than move directly to Kinematic 5, it was decided to collect data for Kinematic 6 first, due to the small LHRS angle. Any spectrometer movement to an angle less than 14 degrees required the Hall to be opened so someone could visually inspect the movement to avoid potential collisions. As such, the run order of the kinematics was altered to allow such changes to take place during the day .

On March 5th, following Kinematic 6, the LHRS was moved to Kinematic 7 and then Kinematic 5, which finished up runs for the first two momentum transfer settings.

The first configuration of the new momentum transfer setting was Kinematic 11, again because the low angle of the LHRS made opening the hall necessary. While some test runs were performed with the 15 cm LH_2 target, it was decided to run Kinematic 11 using the 4 cm LH_2 target.

Kin	Start	Runs	Target	Current
1	28/02/11 15:12	2050 - 2085	4 cm	15 µA
2	01/03/11 10:53	2086 - 2207	4 cm	15 µA
3	02/03/11 20:31	2208 - 2280	4 cm	20 µA
1	03/03/11 23:14	2281 - 2298	4 cm	15 µA
6	04/03/11 07:02	2299 - 2360	4 cm	40 µA
7	05/03/11 00:59	2361 - 2388	4 cm	80 µA
5	05/03/11 11:25	2389 - 2408	4 cm	80 µA
11	05/03/11 16:26	2409 - 2435	4 cm	55 µA
12	06/03/11 02:53	2436 - 2461	4 cm	80 µA
8L	06/03/11 11:00	2462 - 2473	15 cm	40 µA
8S	06/03/11 14:02	2474 - 2486	4 cm	80 µA
9	06/03/11 18:22	2487 - 2521	15 cm	30 µA
10	07/03/11 02:02	2522 - 2546	15 cm	50 µA
13	07/03/11 07:57	2547 - 2561	15 cm	35 µA
14	07/03/11 12:02	2562 - 2573	15 cm	35 µA

Table 2.7: The experiment timeline, including the time of the first run, the runs included in the kinematic setting, the target used, and the approximate current.

Following that, on March 6th, the LHRS was moved to 48 degrees for Kinematic 12, which would be the most backward spectrometer setting of the experiment. Larger angles tended to produce less background noise in the data stream, making runs from this kinematic setting ideal for testing purposes during calibration and analysis, even at 80 µA.

With time still a problem, and the start of the SRC experiment imminent, it was decided to use the 15 cm target for the remaining kinematic settings. While the 15 cm target allows for more events in a shorter time, it also tends to produce more background events. Additionally, target boiling is more likely from a longer target, but the compromise had to be made. In order to ensure that our 4 cm and 15 cm results could be correlated, Kinematic 8 included runs using both targets.

Following Kinematic 12, the LHRS was moved to Kinematic 8's settings, first with the long target and then with the short target.

After Kinematic 8, Kinematics 9 and 10 were run using the longer target. With the longer target, each kinematic setting took far less time, with Kinematics 13 and 14 only taking 5 hours together. The experiment wrapped up in the afternoon on March 7th.

Chapter 3

Calibrations

An important part of any experiment is the calibration of the instruments used to collect the data. Without accurate calibrations, data from the detectors will not correctly reflect what happened, if the results make any sense at all.

Some calibrations were performed during the experiment to ensure that devices were working correctly. Some components of the experiment, such as the beam energy and spectrometer optics, had calibrations from previous experiments that were still applicable as the device measurements did not fluctuate appreciably.

The first calibration performed during the post-experiment offline analysis period was the beam current monitors (BCM), followed by a simple check for target boiling. The next attempted calibration involved the scintillators, but stalled due to an issue referred to as the "double-peak problem", which will be explained in more detail in Section 3.5. After several months attempting to solve that issue, the beam position monitor (BPM) calibration was performed, followed by a check on the vertical drift chambers (VDC). Work returned to the scintillator calibration and an attempt to extract a proper coincidence timing was performed. The last calibration was on the "mispointing", a measure of how misaligned the spectrometers were relative to the center of the hall for each spectrometer kinematic setting.

Two analyses were performed of this experiment, one with which this document is concerned and one performed by Adam Blomberg, a collaborating student at Temple University. His analysis differed in several ways, including attempts to limit the number of cut events and the use of particle identification with detectors not used in this analysis. His work will be mentioned several times in this document.

3.1 Beam Current Monitors

Runs for a BCM calibration were taken on March 3rd, 2011, during Kinematic 3 of the "N-Delta" experiment. There were four MCC[1] runs, 170 to 173, and three corresponding CODA runs, 2252 to 2254.

The first run, labeled MCC 170 and corresponding with CODA run 2252, was a calibration between the Faraday Cup and the 0L02 cavity. The current started at 80 µA and was stepped down through 50, 20, 10, 5, 2, 1, 0.5, and 0.2 µA, as shown in Figure 3.1.

Selecting data points[2] near the center of each plateau, the plot in Figure 3.2 between the current as measured by the Faraday Cup and the current as measured by the 0L02 cavity can be created, which produces the following relationship:

$$I(\text{FC}) = [0.999 \pm 0.012] \cdot I(0\text{L02})\text{µA}$$

The last run, labeled MCC 173 and corresponding with CODA run 2254, was a calibration between the BCM cavities and the 0L02 cavity. Again, the current started at 80 µA and was stepped down, producing Figure 3.3.

In a similar fashion to the previous plot[3], relationships between the 0L02 current and the scaler rates for the BCM measurements were created, displayed in Table 3.1.

3.2 Beam Position Monitors

The beam positioning monitor (BPM) system in Hall A consists of two sets of antenna detectors positioned 7.524 m (A) and 1.286 m (B) upstream of the target [28]. HARP scans are periodically run by the MCC to determine the exact positioning of the beam at those locations. That positioning is then supplied to the data stream through the Experimental Physics and Industrial Control System (EPICS) interface every 3-4 seconds through the variables IPM1H04A and IPM1H04B [47]. For both the A and B locations, there is an x and a y value, resulting in a total of four EPICS variables: Ax, Ay, Bx, and By.

---

[1]MCC stands for Machine Control Center, the command center where all accelerator systems are monitored and controlled during an experiment.

[2]Specifically, the points used were event numbers 100, 160, 220, 280, 340, 400, 460, 520, and 580.

[3]Using the points 46, 91, 136, 180, 284, 329, 374, 419, and 463.
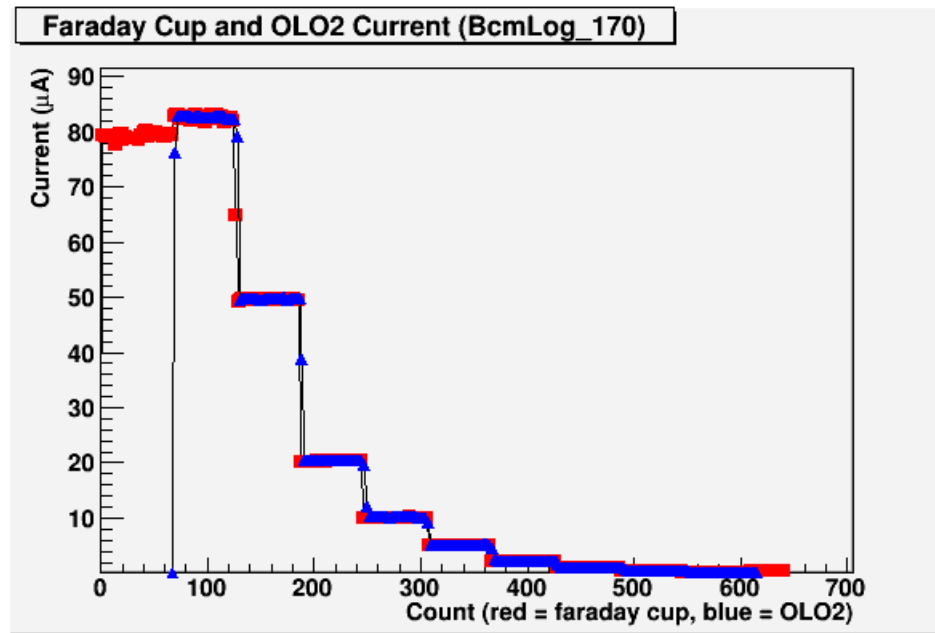
Figure 3.1: Plot of the Faraday Cup and 0L02 currents for MCC run 170. The Faraday Cup data is in red and the 0L02 data is in blue.
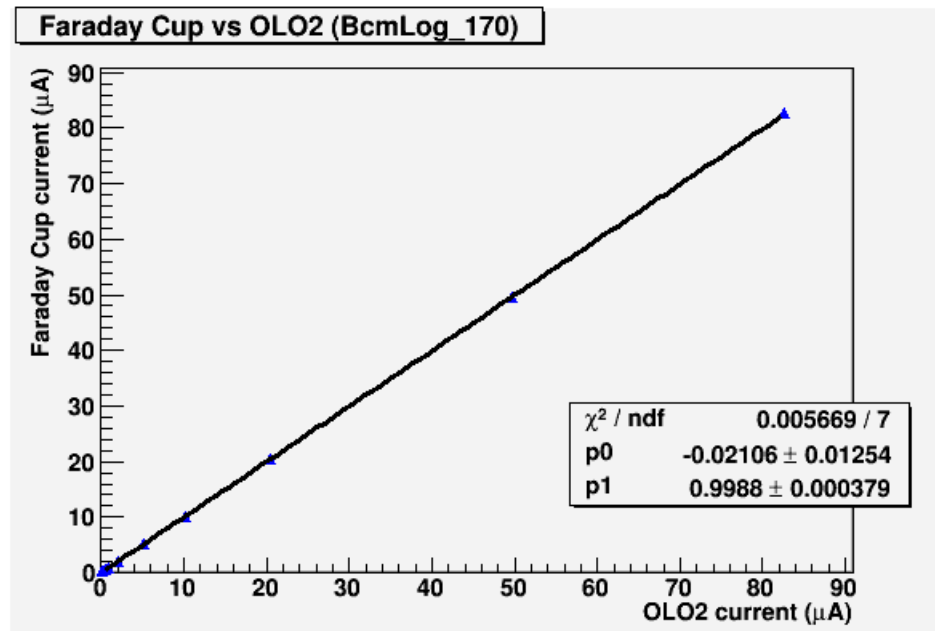
Figure 3.2: Plot of the Faraday Cup current as a function of 0L02 current for MCC run 170 using data from Figure 3.1.
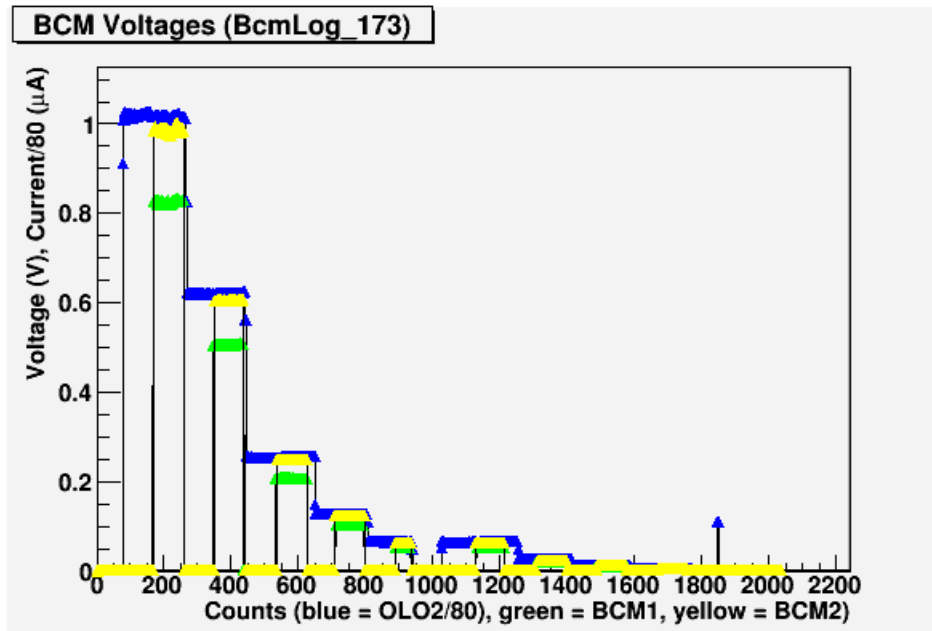
Figure 3.3: Plot of the 0L02 and BCM voltages for MCC run 173. The blue line represents the 0L02 data, the green line represents the BCM1 data, and the yellow line represents the BCM2 data.

Scaler	Coefficient (µA/Hz)
Left U1	$(4.81 \pm 0.06) \times 10^{-4}$
Left U3	$(1.55 \pm 0.02) \times 10^{-4}$
Left U10	$(0.52 \pm 0.03) \times 10^{-4}$
Left D1	$(8.03 \pm 0.10) \times 10^{-4}$
Left D3	$(1.30 \pm 0.02) \times 10^{-4}$
Left D10	$(0.41 \pm 0.02) \times 10^{-4}$
Right U1	$(9.66 \pm 0.12) \times 10^{-4}$
Right U3	$(3.14 \pm 0.04) \times 10^{-4}$
Right U10	$(1.03 \pm 0.01) \times 10^{-4}$
Right D1	$(8.05 \pm 0.10) \times 10^{-4}$
Right D3	$(2.60 \pm 0.03) \times 10^{-4}$
Right D10	$(0.86 \pm 0.01) \times 10^{-4}$

Table 3.1: Coefficients to convert from the BCM scaler rate to the 0L02 Current, from Run 2254, using the data from Figure 3.3.

Additionally, there are BPM antennae set up at the A and B locations to obtain event-by-event data, and like the EPICS variables, there are both x and y BPM values for each location, resulting in another four variables. The main goal of this calibration was to find a relationship between the BPM variables, obtained for each event, and the EPICS variables, assumed to be accurate.

To do this calibration, "bull's-eye" scans are needed, in which the beam is purposefully moved and the results measured. For the N-Delta experiment, runs 1579 to 1599 were taken for this purpose.

It should be noted that after the N-Delta experiment, another sets of scans were taken, corresponding to runs 4139 to 4149, for the SRC experiment that followed. The results from those scans differ little from those of the earlier runs, indicating that the beam positioning calibration was consistent throughout the N-Delta experiment.

Table 3.2 shows the relationship between the HARP scan numbers and CODA run numbers, as well as the approximate position of the beam for each run.

Due to the errors noticed in runs 1586, 1587, 1597, 1598, and 1599, these runs were not included in the analysis. However, that still left 16 runs which is more than enough for a proper calibration.

The first step in the BPM calibration is to determine the pedestal values of the BPM detectors. This is done with a BPM pedestal run, which in this case was run 1184, taken during commissioning. The results from the pedestal run are then entered into the analyzing software's input files and used when data runs are analyzed.

The second step in the BPM calibration is to plot the BPM and EPICS variables and look for any problems. Figure 3.4 shows the different variables annotated to indicate which run produced which point.

The top two plots correspond to the location of the BPM variables, while the bottom two plots correspond to the location of the EPICS variables, with the goal being to determine a relationship between the location of the points in the top plots with the "true" locations in the bottom plots.

Aside from some odd background noise in the lower-right corners of the BPM plots, which doesn't appear to affect the calibration, all of the points from the BPM plots seem to correspond to points in the EPICS plots, with the BPM variables appearing to be rotated clockwise from the EPICS variables.

HARP	A	B	CODA	Events	Notes
2531	$(-0.8, -0.4)$	$(+0.0, +1.0)$	1579	355159	
2532	$(-0.7, -0.5)$	$(+1.0, +1.0)$	1580	115234	
2533	$(-0.6, -0.6)$	$(+1.0, +0.0)$	1581	155610	
2534	$(-0.6, -0.8)$	$(+1.0, -1.0)$	1582	203110	
2535	$(-0.6, -1.0)$	$(+1.0, -2.0)$	1583	191526	
2536	$(-0.8, -1.0)$	$(+0.0, -2.0)$	1584	109162	
2537	$(-1.1, -1.0)$	$(-1.0, -1.6)$	1585	192655	
$-$	$-$	$(-2.0, -1.5)$	1586	13624	stopped early
2540	$(-1.3, -1.8)$	$(-2.0, -2.0)$	1587	175038	double peaks in EPICS variables
2541	$(-1.5, -1.8)$	$(-3.0, -2.0)$	1588	113599	
2542	$(-2.0, -1.8)$	$(-5.0, -2.0)$	1589	83786	
2543	$(-2.0, -1.6)$	$(-5.0, -1.0)$	1590	90600	
2544	$(-1.9, -1.4)$	$(-5.0, +0.0)$	1591	92806	
2545	$(-1.9, -1.1)$	$(-5.0, +1.0)$	1592	50447	
2546	$(-1.9, -1.0)$	$(-5.0, +1.6)$	1593	52352	
2547	$(-1.9, +0.2)$	$(-5.0, +3.0)$	1594	51811	
2549	$(-1.9, +1.4)$	$(-5.0, +4.0)$	1595	145387	
2550	$(-1.9, +1.5)$	$(-5.0, +5.0)$	1596	71348	
$-$	$-$	$-$	1597	$-$	junk
2551	$(-0.8, -0.8)$	$(+0.0, +0.0)$	1598	56012	incorrect values in EPICS variables
2552	$(-1.6, -0.4)$	$(-3.5, +2.0)$	1599	43526	incorrect values in EPICS variables

Table 3.2: Runs used in the BPM calibration, as well as the approximately position of the beam, in mm, and the number of events in each run.
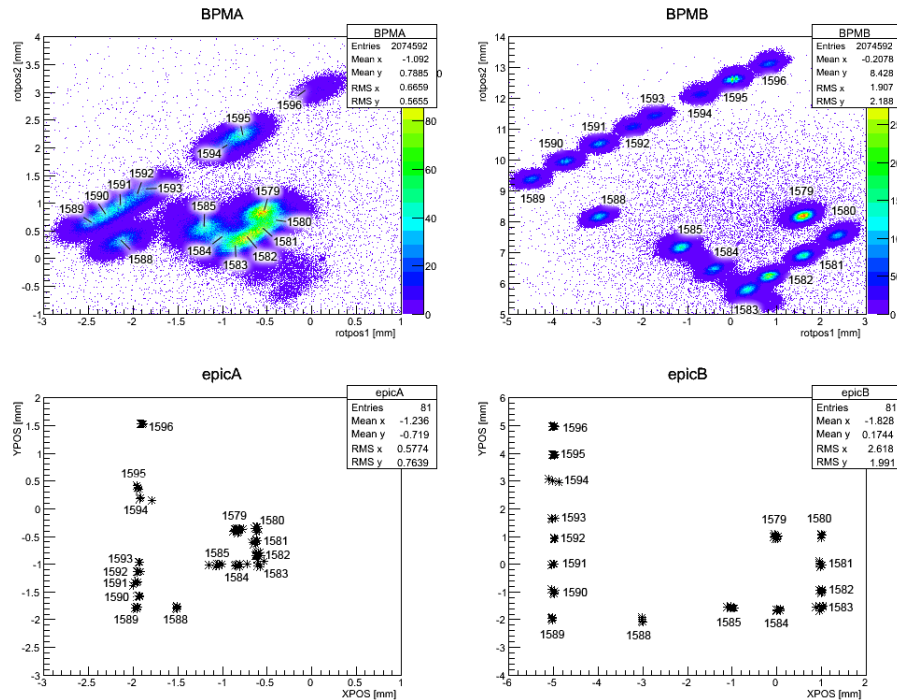
Figure 3.4: The annotated results from the BPM calibration, showing how the BPM values correspond to the EPICS values.

C(0,0)	C(0,1)	C(1,0)	C(1,1)	Offset(0)	Offset(1)
0.662394	-0.679424	0.662499	0.676307	0.126509	-0.589413
0.629603	-0.860538	0.684910	0.859816	5.897721	-6.984258

Table 3.3: BPM coefficients from runs 1579 to 1599.

The correlated points are processed into a matrix, which is then inverted and used to produce a set of beam position transformation coefficients used to transform the coordinates from the BPM frame to the lab frame, as seen in Table 3.3, where [38]

$$\begin{pmatrix} x \\ y \end{pmatrix}_{Lab} = \begin{pmatrix} C(0,0) & C(0,1) \\ C(1,0) & C(1,1) \end{pmatrix} \times \begin{pmatrix} x \\ y \end{pmatrix}_{BPM} + \begin{pmatrix} Offset(0) \\ Offset(1) \end{pmatrix}$$

Then, like the pedestals from before, these values are inserted into the analyzing software's input files.

The results from the second set of "bull's-eye" scans, taken during the SRC experiment, are given in Table 3.4.

C(0,0)	C(0,1)	C(1,0)	C(1,1)	Offset(0)	Offset(1)
0.668516	-0.684471	0.671702	0.683052	0.144645	-0.633772
0.655600	-0.798088	0.652480	0.802990	4.605999	-5.715147

Table 3.4: BPM coefficients from runs 4139 to 4149, after the experiment ended.

As can be seen in Table 3.4, these matrix elements change little over 2500 runs, so the results in Table 3.3 should be reliable for all the runs in the N-Delta experiment.

In addition to the main BPM matrix values, which should apply to all runs, values are calculated to take into account the effect of the raster on the beam. These raster constants can be calculated for individual runs or kinematic settings.

The raster constants come in three groups. The first group corresponds to BPMA, the second to BPMB, and the third to the target. Each group contains six values: the x offset, the y offset, the x amplitude, the y amplitude, the x slope, and the y slope.

For this analysis, raster constants were calculated for the BeO runs in each of the kinematics, whereupon it was discovered that the values did not change appreciably between the different kinematic settings. Rather than use different numbers for each kinematic, the averaged values from Table 3.5 were used for the entire experiment.

Value	BPMA	BPMB	Target
X Offset	-9.4413×10^{-3}	-1.2939×10^{-2}	-1.1621×10^{-2}
Y Offset	9.8341×10^{-3}	1.4837×10^{-2}	1.7268×10^{-2}
X Amplitude	2.7948×10^{-6}	3.3456×10^{-6}	2.7089×10^{-6}
Y Amplitude	-3.9704×10^{-6}	-5.2253×10^{-6}	-5.8416×10^{-6}
X Slope	0	0	0
Y Slope	0	0	0

Table 3.5: Averaged BPM raster constants.

3.3   Vertical Drift Chambers

As particles pass through the gas surrounding the sense wires of the VDCs, they ionize the gas and produce a shower of charged particles. These particles are either attracted to or repelled by the wires and this produces a voltage response in the wires that is detected as a signal which is discriminated and sent to the TDCs.

Figure 3.5 is an example of the combined signal from all the wires in the U1 layer. As is common in VDC histograms, as time advances, there is a steep rise toward a peak, which then drops to a plateau, which then eventually drops back to baseline. The peak is due to the sudden movement of charged particles close to the wires, while the plateau is due to the reaction of particles further from the wires.

The goal of this calibration was to determine the offset that will align the channels with the steepest slopes from each wire.

The first step is to look at the raw, uncalibrated time from the VDC TDCs for each wire. The TDCs from this experiment use a common stop, resulting in histograms where the the first events are at the highest channel.

Figure 3.6 shows the raw time channels for the U1 layer in the LHRS as a function of the wire number. Ideally, the right edge of this plot would form a vertical line.

An algorithm was written that processes each wire, producing a histogram and looking for the bin with the steepest slope and the bin with the largest number of counts, as seen in Figure 3.7, where the TDC channel has been subtracted from 1800 to make the plot easier to read.

The code identifies the bin with the highest count as the maximum peak and works its way toward the left edge of the histogram, measuring the difference in counts between each pair of adjacent bins, looking for the largest difference, which it
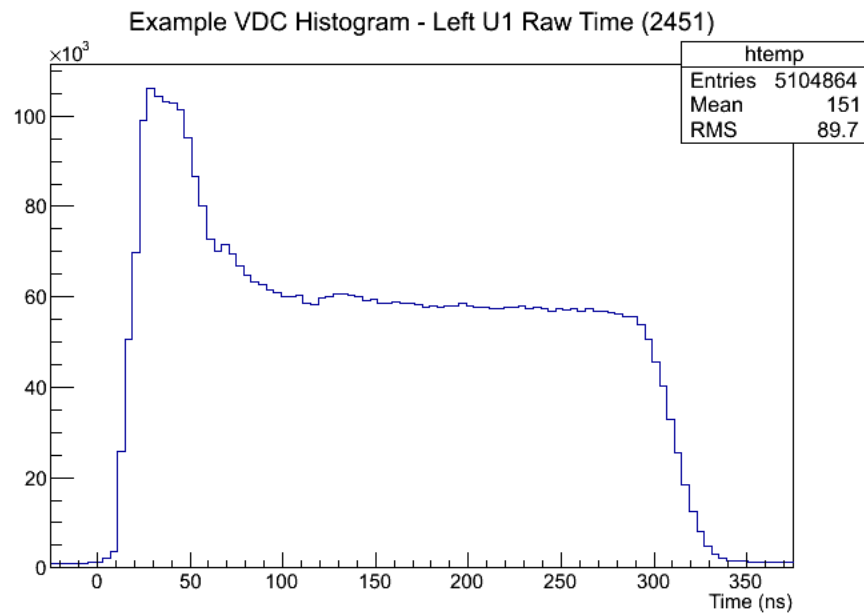
Figure 3.5: An example VDC histogram: the LHRS U1 raw time summed over all wires from Run 2451 in Kinematic 12.
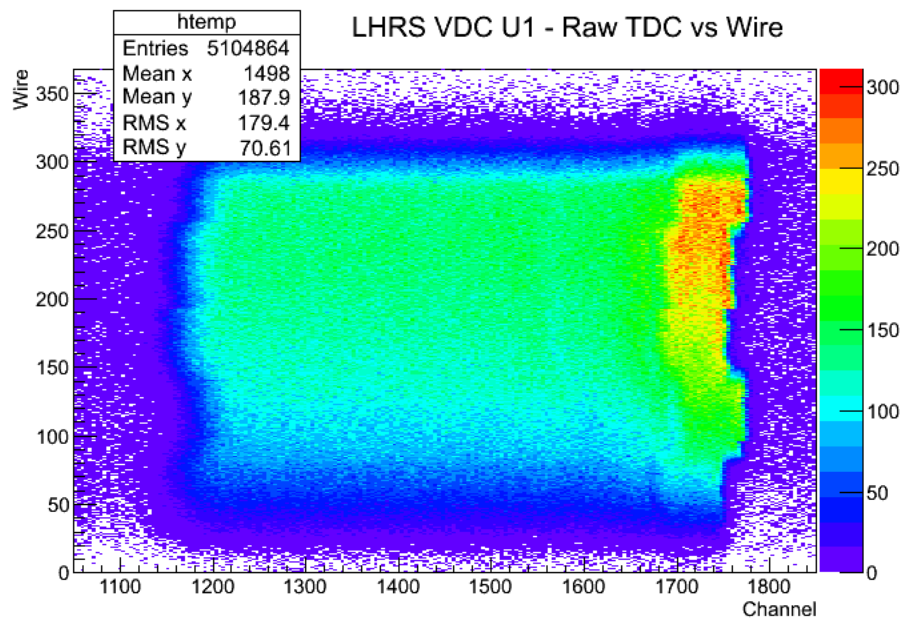
Figure 3.6: Example of VDC raw TDC spectrum before calibration: the LHRS U1 Raw TDC signal for all wires from Run 2451 in Kinematic 12. The TDC is common stop with a 0.5 ns resolution, so the highest channel is the earliest time.
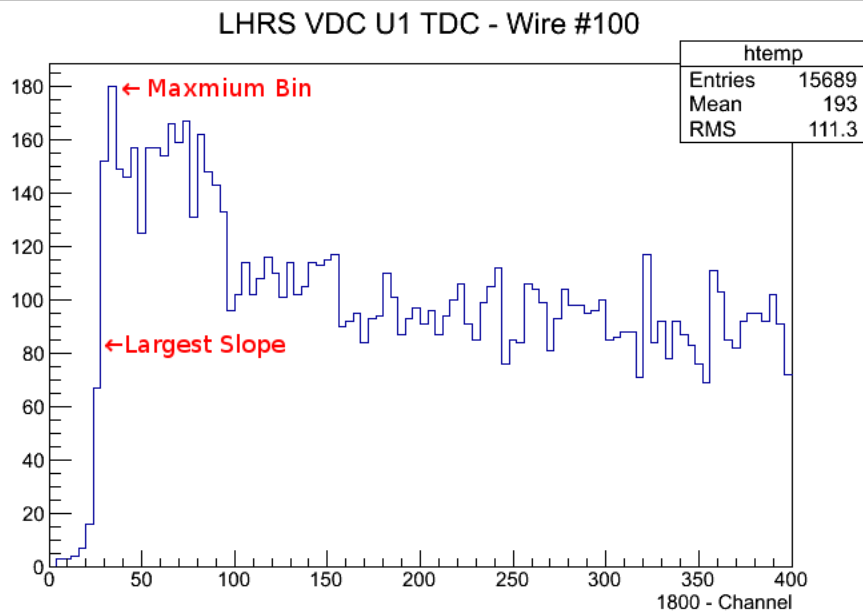
Figure 3.7: Annotated example of VDC signal LHRS U1 Wire #100 from Run 2451 in Kinematic 12. The TDC channel has been subtracted from 1800 to reverse the image horizontally.
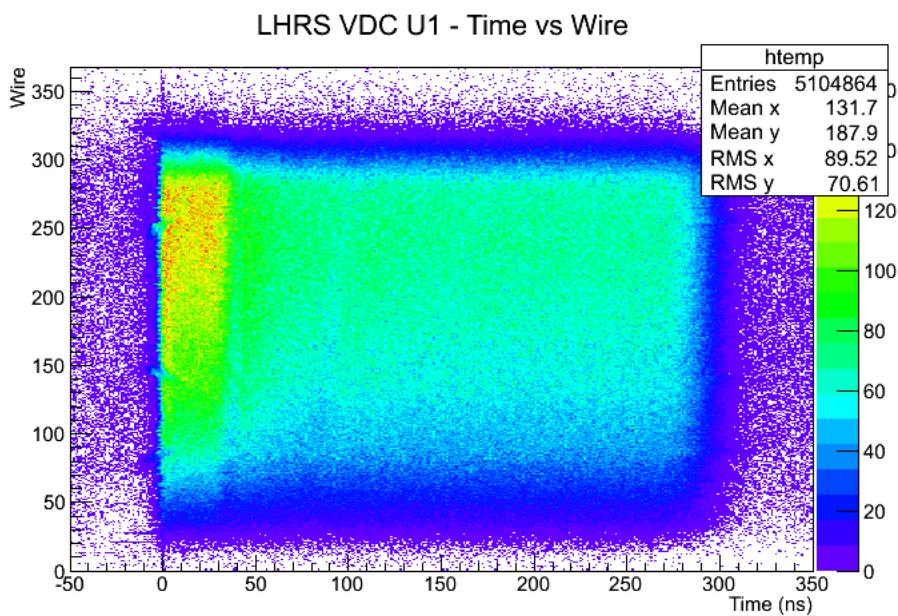
Figure 3.8: Example of VDC time spectrum after calibration: the LHRS U1 Raw Time for all wires from Run 2451 in Kinematic 12.

considers to be the maximum slope.

This process is repeated for each wire, with the resulting t0 recorded in one of the analyzing software's input files.

Figure 3.8 shows the VDC timing for each wire after replaying the run with the corrected t0 values. From there, a manual calibration can be done to adjust any problem areas.

3.4   Mispointing

Due to physical limitations in the mechanisms that move the spectrometers in Hall A, the axis of each spectrometer rarely points directly toward the exact center of the target chamber, and this "mispointing" needs to be taken into account when determining particle trajectories.

The mispointing can be determined in a number of different ways. The most straightforward of these is to simply have the Alignment Group perform target and optical surveys that determine the exact position of all the elements involved in the experiment. The survey reports then include the horizontal and vertical offsets of the spectrometers, which can be entered into one of the database files to correct the mispointing.

Unfortunately, this process is rather time-consuming, so it can only be used for experiments with few configuration changes. For experiments where many configuration changes are necessary, another option must be used, such as using special mispointing runs. These runs can be taken after each configuration change using one of the fixed solid targets, such as the carbon foils or the beryllium oxide target. The necessary mispointing offsets can then be calculated from the data taken during the run.

Normally the carbon foils would be used for this process, in which the seven carbon foils are used as a target, and the center foil is focused upon during analysis. Due to one of the other experiments, however, thirteen foils were used instead of the regular seven, which increased the difficulty in locating the center foil in the relevant histograms, so it was decided to use the single foil BeO target instead.

For each kinematic, then, a special optics run was taken using the BeO target.

Kinematic	Run	Left Arm Angle	Right Arm Angle	# Events
1a	2077	22.5°	12.5°	75965
1b	2281	22.5°	12.5°	77920
2	2152	12.5°	12.5°	64036
3	2210	38.5°	12.5°	188867
5	2402	30.0°	18.0°	61328
6	2359	13.5°	18.0°	18286
7	2371	46.0°	18.0°	59587
8	2479	31.5°	22.0°	51177
9	2506	21.0°	22.0°	13199
10	2532	41.5°	22.0°	44228
11	2423	14.5°	22.0°	17705
12	2448	48.0°	22.0°	46873
13	2549	37.5°	20.5°	37776
14	2562	34.5°	21.0°	53776

Table 3.6: List of BeO runs used for mispointing purposes, along with the angles and number of events in the run.

These runs, with additional information, are listed in Table 3.6. Note that the kinematics were not run in chronological order, so the run numbers in the table are not in numerical order.

Kinematic 1 has two entries in this list because data was collected during two different time periods with movement of the spectrometers in between, requiring that the mispointing for that kinematic be calculated twice.

3.4.1 Target and Optical Surveys

While it was not feasible to do a target and optical survey between each kinematic, there was one set of surveys performed prior to the experimental run.

The optical survey of the spectrometers recorded that the central ray of the RHRS was at 12.523° and offset from the target center by 2.83 mm downstream and −0.66 mm vertically, with up being positive. The central ray of the LHRS was at −16.489°, missing the target center by 2.31 mm upstream and 0.54 mm vertically, again with up being positive [48].

The target survey included offsets for each of the targets, but the BeO target specifically is listed as being located at −15.32 mm, with a +Z value being downstream. The BeO foil is also recorded as having a pitch of −0.014° and a yaw of
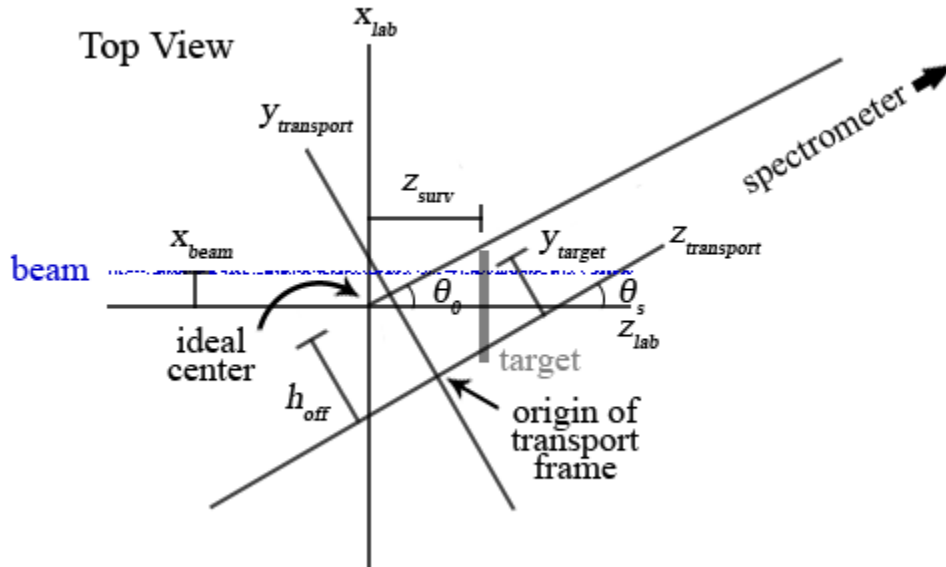
Figure 3.9: Geometry of the lab and transport frames, top view looking down. The beam runs horizontally through this image from the left side to the right.

0.256° [49].

In the individual spectrometer-based transport reference frames, which will be explained in the Section 3.4.2, the optical survey values could be recorded as:

$$\text{LHRS} : h_{surv} = 2.31 \text{ mm}, v_{surv} = -0.54 \text{ mm}$$

$$\text{RHRS} : h_{surv} = 2.83 \text{ mm}, v_{surv} = 0.66 \text{ mm}$$

In the survey reports, the horizontal offsets are not referred to as positive or negative, but in the transport frames as will be described later, "upstream" will effectively be positive for the LHRS, while "downstream" will be positive for the RHRS. Also, in both of these transport frames, vertically down is positive, as opposed to vertically up being positive as it is in the survey reports.

3.4.2 Geometry

Because the mispointing involves the frequent interaction between two different reference frames, the lab frame and the transport frame, it is useful to discuss the geometry of the systems involved, to better understand how the variables in Section 3.4.3 are connected.
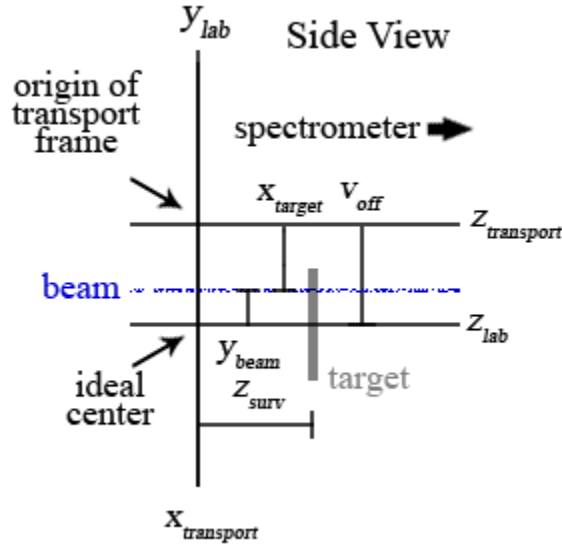
Figure 3.10: Geometry of the lab and transport frames, side view. The beam runs horizontally through this image from the left side to the right.

The lab frame consists of the z-axis pointing in the direction of the ideal beam, with its origin at the center of the target chamber, known as the ideal center. $+z$ points downstream and $-z$ points upstream. $+y$ points vertically up, with $-y$ pointing vertically down. The x-axis is the result of the cross product between the y and z axes; from above (with $+z$ pointing to the right as in Figure 3.9) $+x$ points up and $-x$ down. With this configuration, the x-z plane is parallel to the floor.

The transport frame is both rotated and translated from the lab frame. The z-axis of the transport frame lies along the spectrometer axis, with $+z$ pointing toward the spectrometer and $-z$ pointing away. Unlike the lab frame, however, in the transport frame the x-axis is the vertical axis, with $+x$ pointing down and $-x$ pointing up. The y-axis is defined as the cross product of the z and x axes; from above (with $+z$ pointing to the right), $+y$ points up and $-y$ down.

One important result of this configuration is that for the left arm, $+y_{transport}$ points upstream, while for the right arm, $+y_{transport}$ points downstream, which explains the situation with the signs on the h_{surv} values in the previous section.

Also, the y-z plane of the transport frame is parallel to the floor. This means that the $z_{transport}$ axis is not directly parallel to the spectrometer axis. The z-axis is instead the projection of the spectrometer axis on the transport frame's y-z plane. That is,

the z-axis of the transport frame is parallel to the floor, while the true spectrometer axis is not, as evidenced by its vertical offset.

One benefit of this particular arrangement is that, when viewed from above as in Figure 3.9, the vertical offsets have no effect, and the horizontal situation between the two frames can be handled as though it were two-dimensional.

With that geometry in mind, several variables can be defined.

3.4.3 Variable Definition

Lab Frame

- x_{surv}: x-component of a vector from the ideal center to the center of the target, assumed to be 0 for the BeO target

- y_{surv}: y-component of a vector from the ideal center to the center of the target, assumed to be 0 for the BeO target

- z_{surv}: z-component of a vector from the ideal center to the center of the target, presumably given by the target survey

- x_{beam}: x-component of a vector from the ideal center to the true beamline (at $z = 0$), given by the analyzer variable $rb.x$

- y_{beam}: y-component of a vector from the ideal center to the true beamline (at $z = 0$), given by the analyzer variable $rb.y$

- z_{beam}: non applicable

- x_{off}: x-component of a vector from the ideal center to the origin of the transport frame, ultimate goal of the mispointing calibration

- y_{off}: y-component of a vector from the ideal center to the origin of the transport frame, ultimate goal of the mispointing calibration

- z_{off}: z-component of a vector from the ideal center to the origin of the transport frame, ultimate goal of the mispointing calibration

- x_{react}: x-component of a vector from the ideal center to the interaction point in the target, given by the analyzer variables $rpl.x$ and $rpr.x$

- y_{react}: y-component of a vector from the ideal center to the interaction point in the target, given by the analyzer variables $rpl.y$ and $rpr.y$

- z_{react}: z-component of a vector from the ideal center to the interaction point in the target, given by the analyzer variables $rpl.z$ and $rpr.z$, analogous to z_{surv} after offsets are applied

Transport Frame

- x_{tgt}: x-component of a vector from the origin of the transport frame to the interaction point in the target, given by the analyzer variables $exL.x$ and $exR.x$

- y_{tgt}: y-component of a vector from the origin of the transport frame to the interaction point in the target, given by the analyzer variables $exL.y$ and $exR.y$

- z_{tgt}: not used

- h_{off}: y-component of a vector from the origin of the transport frame to the ideal center (at $z = 0$), penultimate goal of the mispointing calibration, analogous to h_{surv}

- v_{off}: x-component of a vector from the origin of the transport frame to the ideal center (at $z = 0$), penultimate goal of the mispointing calibration, analogous to v_{surv}

Other

- θ_s: angle between the lab frame and the transport frame, as seen from above

- θ_0: angle between the ideal beamline and a line connecting the ideal center with the vernier caliper, essentially the nominal angle of the spectrometer

- L: distance between the ideal center and the vernier calipers, assumed to be 9.9 m

3.4.4 Offset Calculations

As mentioned above, the ultimate goal here was to calculate the three lab frame offsets (x_{off}, y_{off}, and z_{off}), which themselves are calculated from the transport frame offsets (h_{off}, v_{off}).

In Figure 3.9, x_{beam}, z_{surv}, and y_{tgt} are all positive, based on their respective frames. If counter-clockwise rotation is positive, then θ_s and θ_0 are also positive.

Further, as h_{off} lies along the $y_{transport}$ axis, it should also be positive in the figure. Using trigonometric identities, it can be shown that h_{off} can be calculated as [38]

$$h_{off} = y_{tgt} + z_{surv} \sin \theta_s - x_{beam} \cos \theta_s \tag{3.1}$$

A problem with this equation is that it relies on θ_s, which is not yet known. As a first-order approximation, θ_0 can be used. Then, once a value for h_{off} has been found, it can be used to find a better approximation for θ_s, with the equation

$$\theta_s = \theta_0 + \sin^{-1} \frac{h_{off}}{L} \tag{3.2}$$

One method, then, for calculating the values for h_{off} and θ_s is to use an iterative process, continually making substitutions until the values converge.

Once h_{off} and θ_s are known, they can be used to find the two horizontal lab frame offsets.

$$x_{off} = -h_{off} \cos \theta_s \tag{3.3}$$

$$z_{off} = h_{off} \sin \theta_s \tag{3.4}$$

The signs in Equations 3.3 and 3.4 come from the direction of the lab frame vectors associated with h_{off}. That is, in Figure 3.9, if h_{off} is positive, then the origin of the transport frame is downstream of the ideal center, and h_{off} points upstream. But x_{off} and z_{off} point *from* the ideal center *to* the origin of the transport frame, so they point in the opposite direction. That makes x_{off} point in the negative direction and z_{off} point in the positive direction (downstream), as defined by the lab frame, hence the signs.

Like the horizontal offset, the vertical offset, v_{off} can be calculated from the variables in Section 3.4.3, though the derivation is much simpler.

$$v_{off} = y_{beam} + x_{tgt} \tag{3.5}$$

Since the horizontal planes of the two frames are parallel, the vertical offset is just a simple addition. As seen in Figure 3.10, if both variables are positive, y_{beam} points up from the x-z plane of the lab frame, x_{tgt} points down from the y-z plane of the transport frame, and v_{off} is just the sum of the two.

Further, y_{off} will be exactly equal to v_{off}, even though they point in opposite directions, as they are based on different reference frames, which allows them to both be positive in the directions they point.

3.4.5 Target Location

In order to properly calibrate the mispointing of the spectrometers using the BeO foil, it is necessary to first know the location of the foil relative to the ideal center of the target chamber. According to the target survey, the BeO target, as well as the rest of the solid targets, was 15.32 mm upstream of the ideal center [49].

One way to test this positioning is to use the θ_s, h_{off}, and v_{off} from the optical survey to calculate x_{off}, y_{off}, and z_{off} for a BeO run taken after the surveys but before the spectrometers were moved, such as with run 1201, a spot++ run[4].

A θ_s of 16.489°, an h_{off} of 2.31 mm, and a v_{off} of -0.54 mm gives an x_{off} of -2.215 mm, a y_{off} of -0.54 mm, and a z_{off} of 0.656 mm. When those were used, the reconstructed target appeared at a z_{react} of -15.38 ± 0.07 mm, as seen in Figure 3.11, indicating that the target survey and the optical survey are in agreement.

However, this does present a problem, as the target survey suggests that the center of the 4 cm LH_2 target cell is a mere 0.06 mm upstream of the ideal center [49], while the reconstructed position clearly shows it to be approximately 7 mm upstream, as seen in Figure 3.12.

Further analysis confirmed that all of the solid targets appear to be correctly centered at -15.32 mm, while the LH2 and LD2 targets are all approximately 7 mm upstream, not the fraction of a millimeter as written in the target surveys. No explanation for this discrepancy has been found.

---

[4]Spot++ runs are runs taken after a change in the beam, to make sure the beam is still on target and to check the beam raster, as seen in Figure 2.7.

BeO Target Z Position - Run 1201

htemp	
Entries	6874
Mean	-15.16
RMS	8.962
χ^2 / ndf	509.1 / 96
Constant	423 ± 8.7
Mean	-15.38 ± 0.07
Sigma	4.594 ± 0.067
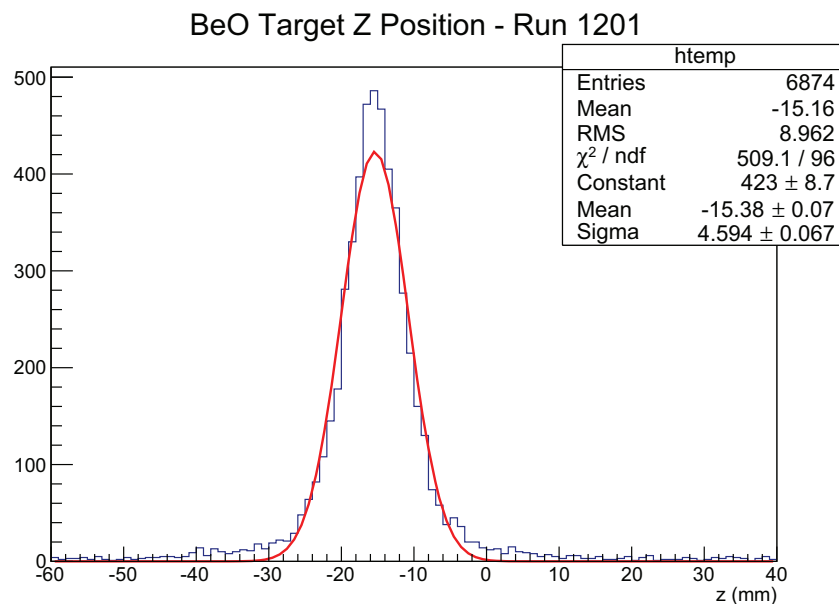
Figure 3.11: Example of a reconstructed BeO target z position, from Run 1201, a BeO run after the optical survey but before the spectrometers were moved.

4 cm LH2 Target Cell Position (z-direction)

h2	
Entries	146612
Mean	-0.705
RMS	1.97

blue: full target, red: coincidence peak only - z (cm)
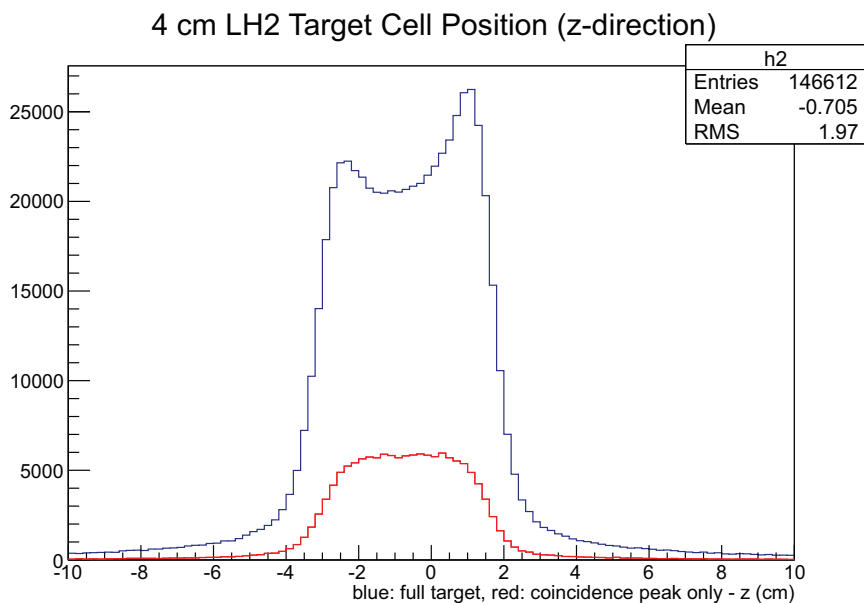
Figure 3.12: Example of a reconstructed 4 cm LH_2 target position. The larget peak represents the complete reconstructed target position with both the LH_2 from inside the cell and the aluminum from the cell walls. The smaller peak, which has had a coincidence timing cut applied, represents the reconstructed target position with the aluminum removed, revealing the LH_2 contribution.

Kin	Run	θ_0	θ_s	h_{off}	v_{off}	x_{off}	y_{off}	z_{off}
LHRS								
1a	2077	25.5	25.511	1.524	0.0394	-1.376	0.0394	0.656
1b	2281	25.5	25.511	2.616	0.0423	-2.351	0.0423	1.120
2	2152	12.5	12.366	4.870	0.0977	-4.756	0.0977	1.052
3	2210	38.5	38.461	-0.715	0.0462	0.557	0.0462	-0.445
5	2402	30.0	30.006	1.249	0.0551	-1.090	0.0551	0.619
6	2359	13.5	13.721	4.340	0.0896	-4.226	0.0896	1.019
7	2371	46.0	16.144	-3.224	0.0521	2.249	0.0521	-2.327
8	2479	31.5	31.616	1.288	0.0469	-1.086	0.0469	0.670
9	2506	21.0	21.019	2.465	0.0522	-2.307	0.0522	0.888
10	2532	41.5	41.743	-2.663	0.0453	1.993	0.0453	-1.766
11	2423	14.5	14.663	4.246	0.0902	-4.121	0.0902	1.059
12	2448	48.0	48.006	-3.506	0.0558	2.331	0.0558	-2.590
13	2549	37.5	37.476	0.0715	0.0528	-0.066	0.0528	0.048
14	2562	34.5	34.511	0.412	0.0642	-0.340	0.0642	0.228
RHRS								
1a	2077	-12.5	-12.365	9.473	0.1773	-9.255	0.177	-2.059
1b	2281	-12.5	-12.372	8.526	0.0898	-8.319	0.0898	-1.780
2	2152	-12.5	-12.357	6.5701	0.0094	-6.424	0.0094	-1.339
3	2210	-12.5	-12.361	8.7165	0.0828	-8.5109	0.0828	-1.855
5	2402	-18.0	-17.707	12.778	0.1143	-12.170	0.1143	-3.931
6	2359	-18.0	-17.793	12.691	0.0877	-12.058	0.0877	-3.910
7	2371	-18.0	-17.763	12.941	0.1327	-12.316	0.1327	-3.991
8	2479	-22.0	-21.918	12.177	0.0855	-11.308	0.0855	-4.528
9	2506	-22.0	-21.921	12.027	0.0873	-11.149	0.0873	-4.482
10	2532	-22.0	-21.939	12.345	0.0888	-11.450	0.0888	-4.591
11	2423	-22.0	-21.916	12.071	0.0779	-11.192	0.0779	-4.488
12	2448	-22.0	-21.915	12.379	0.1035	-11.479	0.1035	-4.594
13	2549	-20.5	-20.378	11.017	0.0885	-10.327	0.0885	-3.840
14	2562	-21.0	-21.003	11.441	0.0771	-10.681	0.0771	-4.081

Table 3.7: Offsets from the mispointing calibration for both arms for each kinematic setting.

Kin	Run	x_{beam}	x_{react}	y_{beam}	y_{react}	z_{surv}	z_{react}
LHRS							
1a	2077	-3.81227	-3.88533	2.60288	2.65963	-15.32	-15.2628
1b	2281	-3.84285	-3.90638	2.69468	2.74677	-15.32	-15.3246
2	2152	-3.84501	-3.90504	2.69833	2.75054	-15.32	-14.9581
3	2210	-3.83559	-3.91116	2.69392	2.74694	-15.32	-15.2817
5	2402	-3.83952	-3.90907	2.69194	2.74132	-15.32	-15.2898
6	2359	-3.84073	-3.90558	2.70194	2.73705	-15.32	-15.1097
7	2371	-3.84026	-3.90946	2.68627	2.7451	-15.32	-15.3198
8	2479	-3.78835	-3.87318	2.5235	2.57638	-15.32	-15.2903
9	2506	-3.85198	-3.92286	2.70403	2.74678	-15.32	-15.1355
10	2532	-3.84052	-3.9026	2.69362	2.74862	-15.32	-15.3004
11	2423	-3.84119	-3.89266	2.70055	2.74198	-15.32	-15.1546
12	2448	-3.84074	-3.91492	2.68825	2.73473	-15.32	-15.2891
13	2549	-3.85223	-3.91633	2.71412	2.74143	-15.32	-15.2759
14	2562	-3.84366	-3.90611	2.68648	2.74523	-15.32	-15.3183
RHRS							
1a	2077	-3.81227	-3.87644	2.60288	2.66585	-15.32	-15.106
1b	2281	-3.84285	-3.89764	2.69468	2.74406	-15.32	-15.1279
2	2152	-3.84501	-3.90343	2.69833	2.7552	-15.32	-15.1643
3	2210	-3.83559	-3.88961	2.69392	2.74698	-15.32	-15.167
5	2402	-3.83952	-3.89027	2.69194	2.74428	-15.32	-15.1914
6	2359	-3.84073	-3.89366	2.70194	2.76412	-15.32	-15.1623
7	2371	-3.84026	-3.89297	2.68627	2.73558	-15.32	-15.1849
8	2479	-3.78835	-3.85506	2.5235	2.57585	-15.32	-15.2002
9	2506	-3.85198	-3.90851	2.70403	2.74741	-15.32	-15.1469
10	2532	-3.84052	-3.91155	2.69362	2.7464	-15.32	-15.1691
11	2423	-3.84119	-3.90493	2.70055	2.75824	-15.32	-15.1878
12	2448	-3.84074	-3.89118	2.68825	2.73165	-15.32	-15.1674
13	2549	-3.85223	-3.90947	2.71412	2.76299	-15.32	-15.2622
14	2562	-3.84366	-3.90042	2.68648	2.73519	-15.32	-15.2547

Table 3.8: Comparisons between the actual and reconstructed beam and target positions after the mispointing calibration has been applied for both arms for each kinematic setting.

3.4.6   Offsets

Once the various offsets, listed in Table 3.7, have been calculated, they can be entered into the analyzing software's input files and the various runs can be replayed with the mispointing accounted for.

To check these results, the three *react* variables can be used, where they are compared to the *beam* and *surv* variables. If the calibration is correct, then z_{react} should be equivalent to z_{surv}, and x_{react} and y_{react} should correspond to the respective *beam* variables, as can be seen in Table 3.8.

3.5   Coincidence Timing

The most straightforward method of separating "good" pion electroproduction events from "bad" background events is to look at the relative timing of the events as recorded in both arms, more commonly referred to as the coincidence timing. During online analysis, the coincidence timing was calculated by subtracting the timing of the T3 trigger signal by the timing of the T1 trigger signal, as recorded in the BigBite weldment, an example of which can be seen in Figure 3.13.
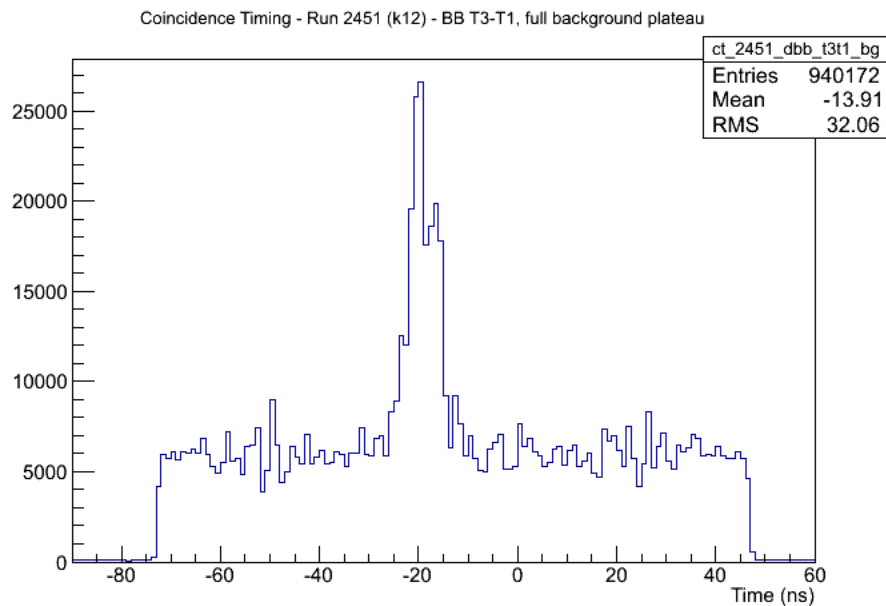
Figure 3.13: An example of coincidence timing from Run 2451 in Kinematic 12 using the BigBite copies of T3 and T1, including the full background plateau with the EDTM signal removed.
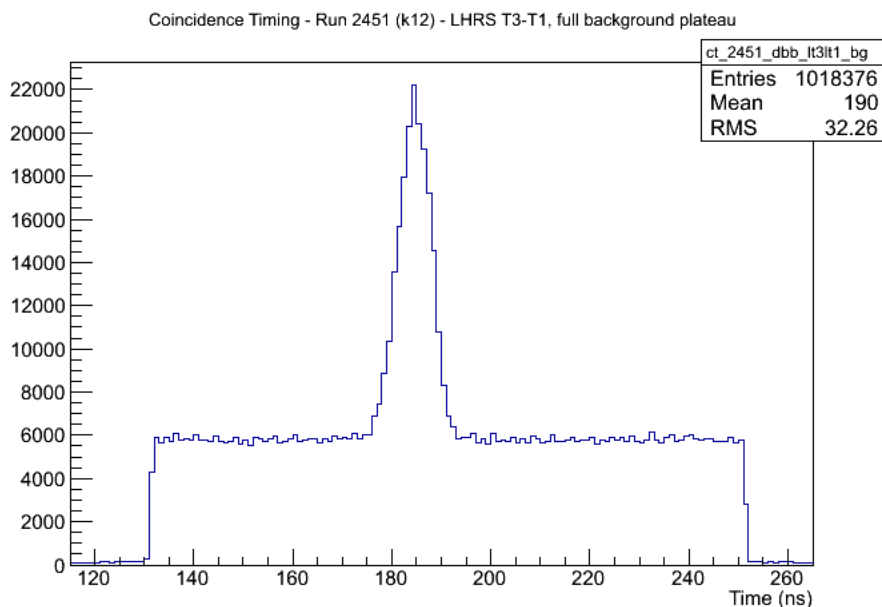
Figure 3.14: Example of coincidence timing from Run 2451 in Kinematic 12 using the LHRS copies of T3 and T1, including the full background plateau with the EDTM signal removed.

In that figure, a strong central peak can be seen towering over a background plateau. Events in the peak would appear to be those resulting from the wanted reaction, while the events in the background are random events that happened to arrive at the detectors within the pre-established coincidence timing window.

As such, a key action in this analysis is to separate the good events in the coincidence peak from the bad events in the background plateau.

The first step is to look at different signal sources for the timing. In addition to the BigBite weldment, the T3 and T1 signals, as well as several others, were also recorded in both arms individually. For example, Figure 3.14 shows the same coincidence timing as was shown in Figure 3.13 using the T3 and T1 copies as recorded in the LHRS. Due to a difference in wire lengths, the exact timing of the signals is different, though the overall structure is the same.

3.5.1 Double Peak Problem

When taking the difference between two timing signals, the two signals need to share a common reference time or the difference is meaningless. In many experiments, the

wire lengths connecting the PMTs to the electronics are carefully manipulated so that one set of signals always sets the timing for every other signal. Usually the PMTs on the right side of the S2m layer in each arm is chosen as that timing signal.

When this is done correctly, it allows for the simple subtraction of the S2m scintillator TDC signals in the LHRS with the S2m scintillator TDC signals in the RHRS. This should produce a coincidence timing signal much like Figure 3.14, except cleaner, since it obtains the signals directly from the scintillator layers.

Unfortuntately, in this experiment, the wire lengths were not manipulated correctly. In the LHRS, the wiring allowed the S1 layer to set the timing, while in the RHRS, the wire lengths for the S2m PMTs were exactly the same, which resulted in the timing switching back and forth between different sides of the S2m layer. In both cases, this resulted in a phenomenon referred to as the "double-peak problem".

Because the S1 and S2m layers have different bar configurations, particles passing through a particular bar in the S1 layer will not necessarily always pass through the same S2m bar, and vice versa. In Figure 3.15, which is a plot of the TDC timing versus the LHRS S2m bar, it can be seen that there are two distinct peaks for S2m bar 5. This occurred because one peak represents particles that passed through S1 bar 1 and the other represents particles that passed through S1 bar 2. Since the timing was based on the S1 bars, these signals ended up with different reference timings, and appear as multiple peaks. The same phenomenon can be seen for S2m bar 10.

The solution to this particular problem was to choose a common signal between the two arms and subtract that reference signal from the TDC signals before subtracting them from each other. When any signal is recorded in a particular arm, it shares the common timing with the rest of the signals in that arm. For example, the T1 trigger signal was recorded in both arms; in the LHRS, it would share the same common timing as the LHRS S2m TDC signals.

By subtracting the T1 signal, for example, from the S2m TDC signals, it sets the S2m TDC relative to that T1 signal, rather than whatever arbitrary common timing signal based on the wiring. If the same signal source is used for the LHRS and RHRS, then the S2m TDC signals are now both relative to the same signal. There would be a constant timing difference, due to the wire lengths in connecting the trigger signals to each arm, but as the only interest is in *relative* timing signals, this constant effect
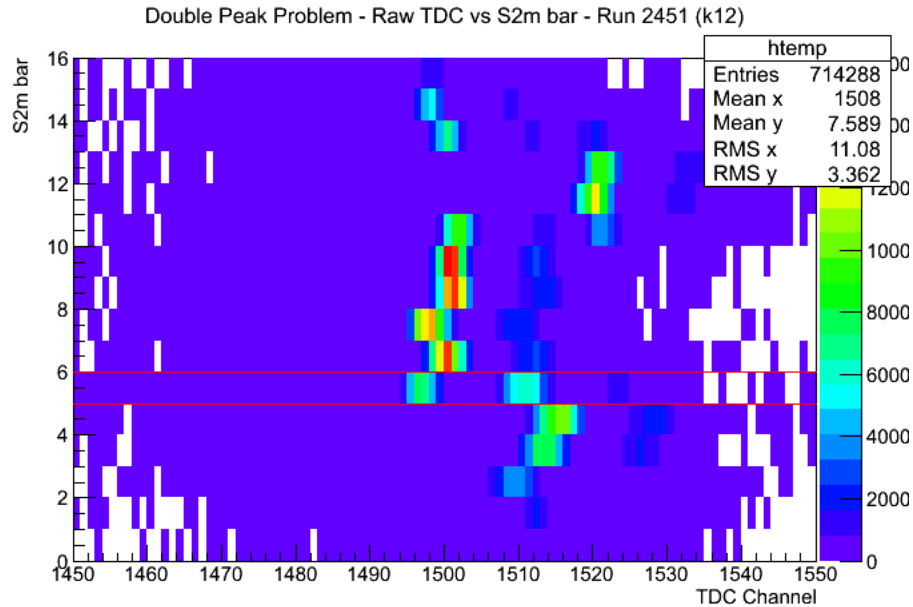
Figure 3.15: Example of the S2m TDC channel versus the LHRS S2m bars, with the double peak from bar 5 highlighted.

can be ignored.

Once the S2m TDC signals are relative to a common signal, they can be subtracted from each other to produce a coincidence timing as desired. This has the added benefit of removing the common signal from the equation, save for the constant timing mentioned above, so it will not affect the results.

With that procedure in place, the coincidence timing from the S2m TDCs looks similar to Figures 3.16 and 3.17, where the full-width half-maximum (FWHM) of the peak is approximately 8 ns.

3.5.2 Alignment

While the coincidence peak may seem quite narrow, plotting the coincidence timing with respect to the S2m bar, such as in Figure 3.18, shows that the peaks from individual bars are out of alignment.

With the understanding that the central, brighter region represents the coincidence peak and that the 1-D peaks presented so far are the projections of these plots on the x-axis, it can be imagined that for best results, those brighter sections should be *thin*, *aligned*, and completely *vertical*. Any deviation would cause our projected
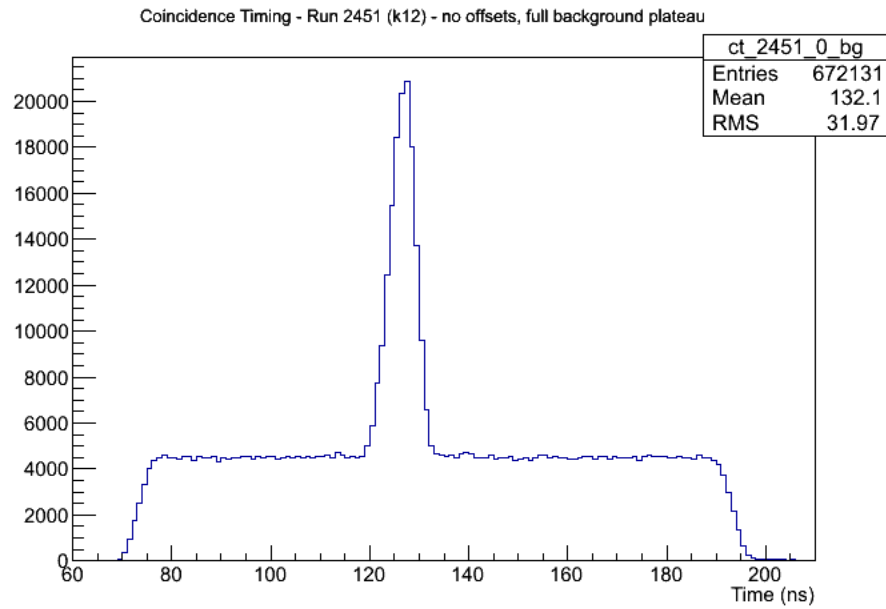
Figure 3.16: Example of coincidence timing from Run 2451 in Kinematic 12 using the S2m signals directly with no offsets, with the full background plateau.
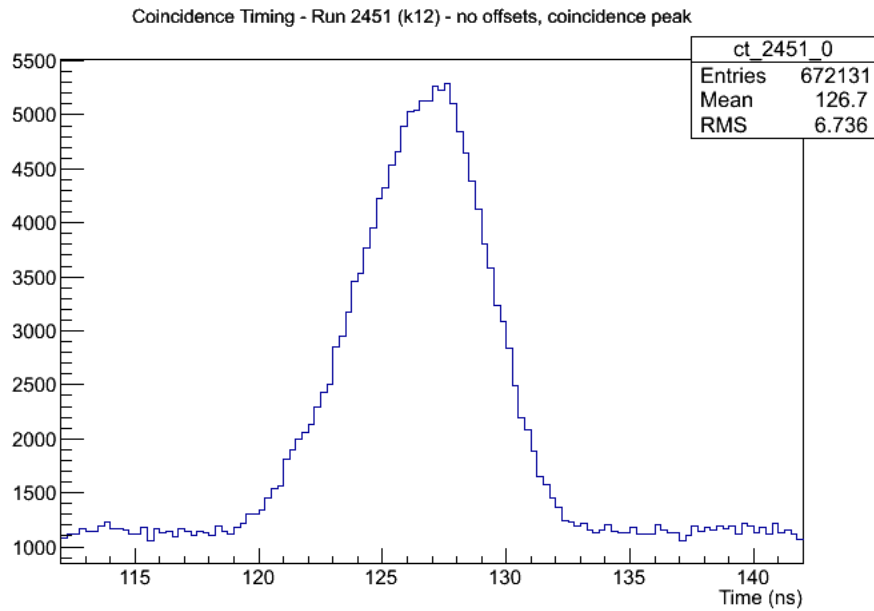
Figure 3.17: Example of coincidence timing from Run 2451 in Kinematic 12 using the S2m signals with no offsets, showing just the coincidence peak.
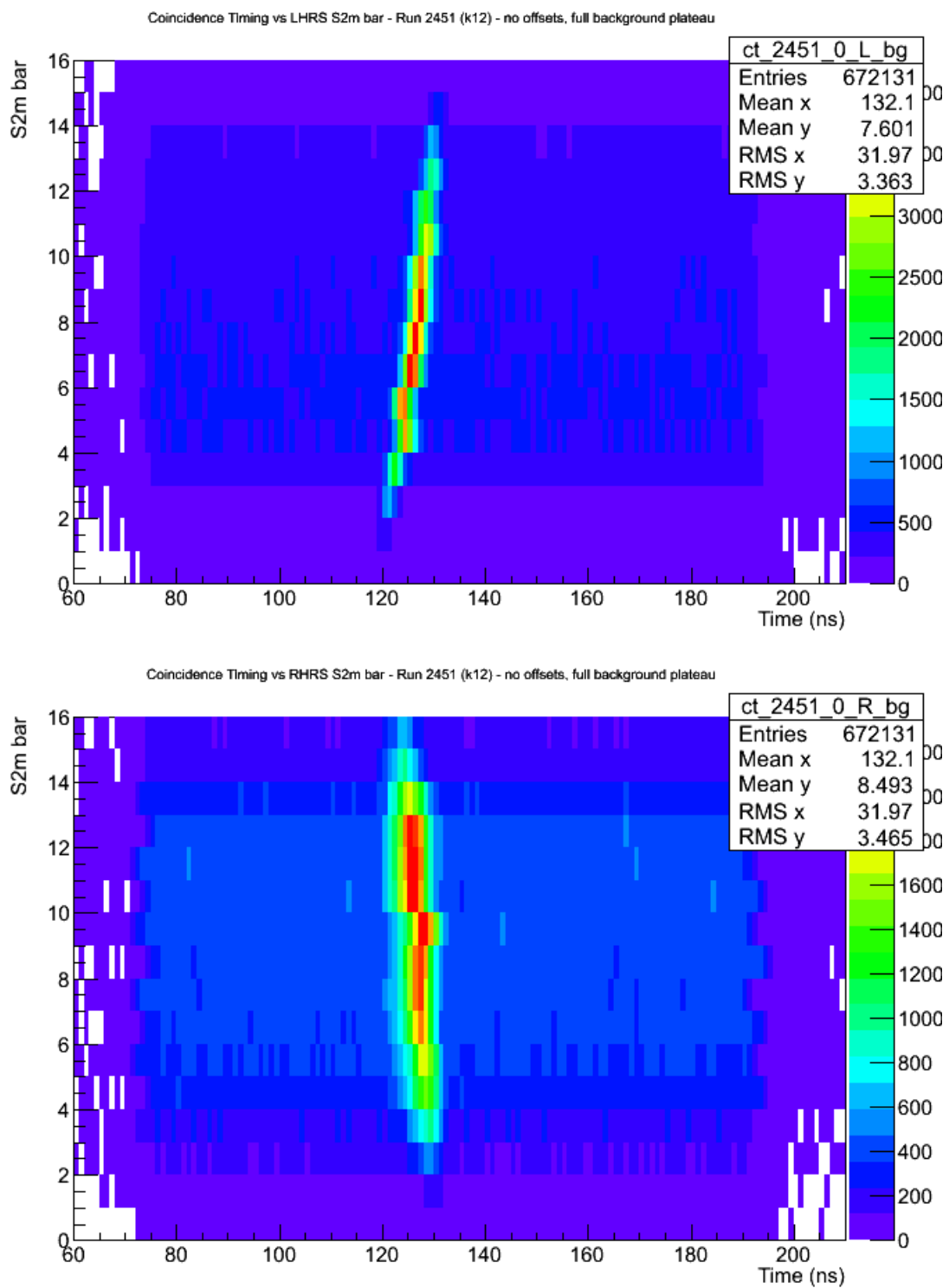
Figure 3.18: Example of the coincidence timing versus the LHRS and RHRS S2m bars from Run 2451 in Kinematic 12 with no offsets, with the full background plateau.
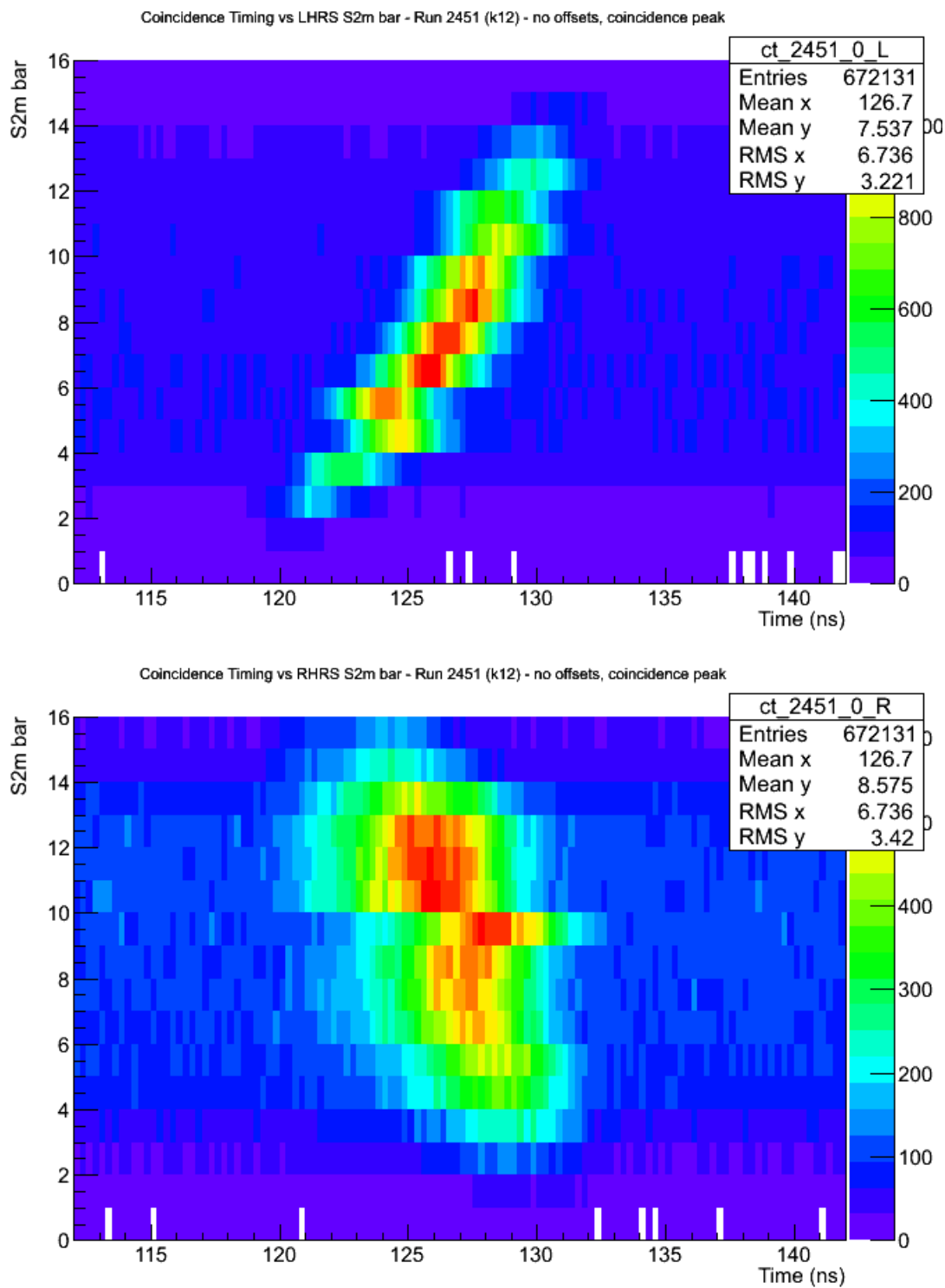
Figure 3.19: Example of the coincidence timing versus the LHRS and RHRS S2m bars from Run 2451 in Kinematic 12 with no offsets, showing just the coincidence peaks.
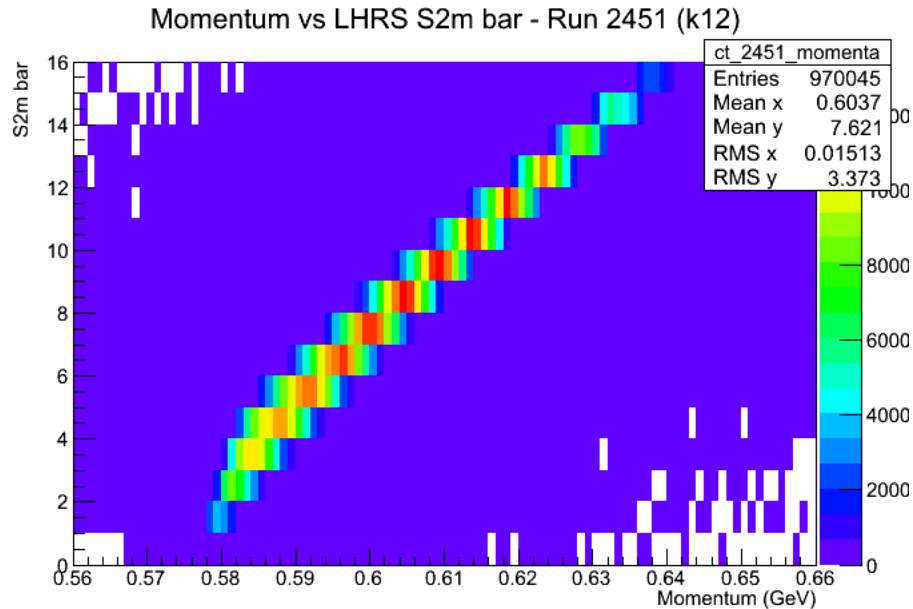
Figure 3.20: Example of the momentum versus the LHRS S2m bars from Run 2451 in Kinematic 12, showing how the momentum of a proton determines which S2m bar it hits. The higher-indexed bars are actually closer to the ground, so the higher momentum protons, which curve more in the magnetic field, hit those bars.

1-D peak to be wider than it needs to be.

Figure 3.19 is zoomed in on the coincidence peak itself to reveal how misaligned the individual peaks truly are.

There are generally three approaches to correct these alignment problems: pathlength corrections, calibration offsets, and time-walk corrections.

3.5.3 Pathlength Correction

The most likely cause of a tilt in the coincidence peaks relative to the LHRS S2m bars is that each bar corresponds to a different range of momenta. When the particles pass through the dipole magnet on the way to focal plane, the momentum of the particle determines how much its path will bend. The result is that particles with a lower momentum tend to hit the lower indexed bars (closer to the ceiling[5]) and those with a higher momentum tend to hit the higher indexed bars (closer to the floor), as demonstrated in Figure 3.20.

---

[5]While bar 15 is at the top of these plots, physically it's the lowest bar, making all plots showing the S2m bars on the vertical axis essentially upside-down.
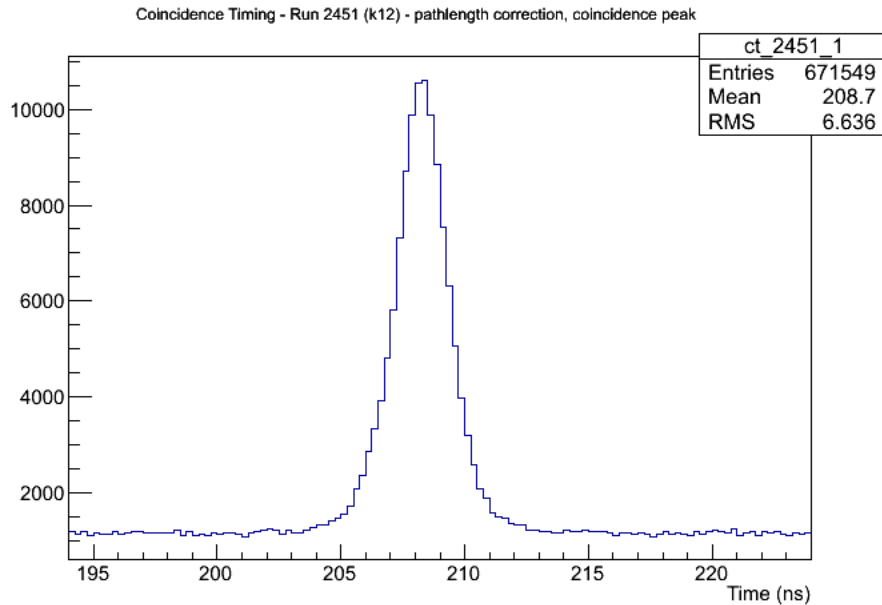
Figure 3.21: Example of the coincidence timing from Run 2451 in Kinematic 12, with pathlength corrections, showing just the coincidence peak.

Lower momentum particles will take longer to reach the S2m plane, so they will arrive later, relatively speaking, than the higher momentum particles. This can clearly be seen in the Figure 3.19, where the line of coincidence peaks is tilted clockwise. The higher momentum particles, which hit the higher indexed bars, arrive first, which give them a less negative coincidence time. The lower momentum particles, which hit the lower indexed bars, arrive last, and all of this gives the LHRS coincidence timing plot a clockwise tilt.

Because the electrons' speeds are relatively unaffected by the momentum range seen in this experiment, as they are all traveling at roughly the speed of light, the coincidence timing peaks relative to the RHRS do not have much of a tilt.

To correct for this difference in momenta, a pathlength correction can be introduced, which adjusts the timing of each bar according to the momentum of the particle. Specifically, a time offset based on the pathlength of the particle and its speed is introduced.

The distance between the target and the focal plane, which is defined to be the first VDC layer, is approximately 23.43 m and is given by the analyzer variable "X.tr.pathl", where "X" is either "L" or "R" depending on the spectrometer [43].
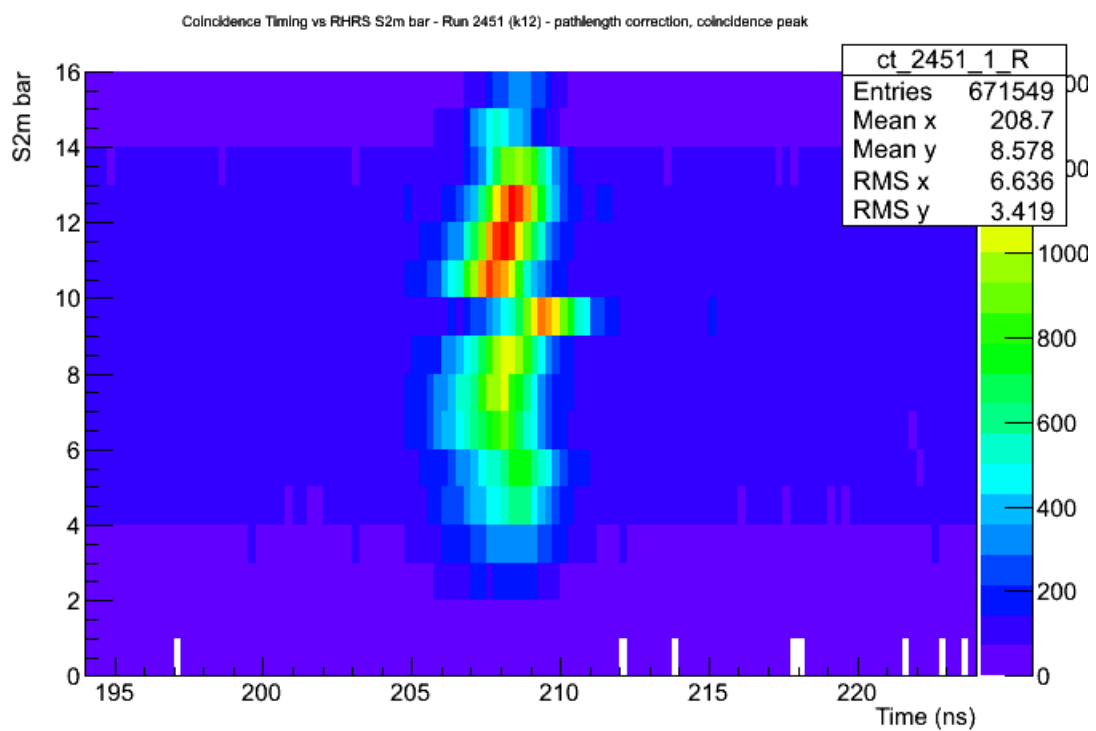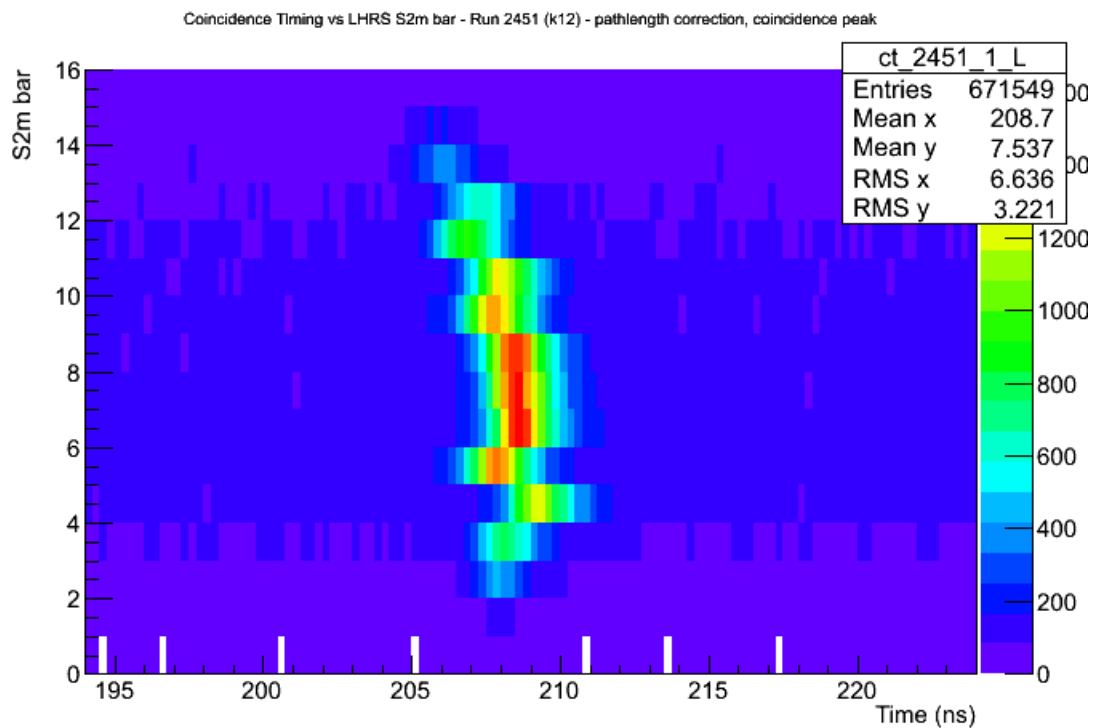
Figure 3.22: Example of the coincidence timing versus the LHRS and RHRS S2m bars from Run 2451 in Kinematic 12, with pathlength corrections, showing just the coincidence peaks.

Likewise, the distance between the focal plane and the S2m layer in both arms is approximately 3.14 m and given by the analyzer variable "X.s2.trpath". Together, these two variables can be added together to obtain a calculated distance between the target and the S2m layer.

As for the speed of the particle, this can be calculated from the particle's momentum and its energy, which is itself calculated from the momentum and the mass of the desired particle. This speed, as a fraction of the speed of light, is then converted into meters per second by multiplying by the speed of light. After converting this speed into meters per *nanosecond* to fit with our timing values, the quotient of the pathlength and speed is added to the coincidence timing. The resulting coincidence peak, with a FWHM of approximately 5 ns, is shown in Figure 3.21, which can be directly compared with Figure 3.17.

Looking at the relationship between the peaks and the S2m bars, in Figure 3.22, the difference can also be seen. The tilt appears to be gone, as expected, but the peaks are still misaligned. To correct the misalignment, manual calibration offsets need to be applied.

3.5.4 Calibration Offsets

Though there are different methods for calculating calibration offsets, and many were tried, the most effective practical method was to simply look at the coincidence timing bar by bar and adjust the offsets to center the peak at an arbitrary value, in this case, 210 ns.

Average offsets from each kinematic were calculated by selecting two[6] runs from different parts of the kinematic runtime, calculating their offsets, and averaging the resulting offsets together. Table 3.9 shows the average offsets for each kinematic.

These offsets are then applied to the coincidence timing, with the effects on the coincidence peak for run 2451 shown in Figure 4.1, where the FWHM has now dropped to approximately 1.7 ns.

The wavy pattern at the top of the background plateau is caused by the 2 ns timing structure of the beam. The fact that this signal can be resolved is a sign of a good coincidence timing calibration.

---

[6]Only one run was used for Kinematics 13 and 14, since they were both relatively short.

	Kinematic 1		Kinematic 2		Kinematic 3	
Bar	LHRS	RHRS	LHRS	RHRS	LHRS	RHRS
0	1.59	1.84	1.55	1.47	1.84	0.96
1	0.96	−1.47	0.71	−1.21	0.61	−1.29
2	1.00	−0.42	0.63	−0.36	0.59	−0.44
3	0.74	−0.53	0.37	−0.58	0.36	−0.55
4	−0.34	−0.45	−0.75	−0.41	−0.76	−0.47
5	1.02	−0.5	0.61	−0.51	0.59	−0.52
6	0.25	0.18	−0.16	0.15	−0.15	0.16
7	0.38	0.27	−0.02	0.25	−0.03	0.26
8	0.47	0.07	0.05	0.08	0.04	0.06
9	1.19	−1.19	0.77	−1.17	0.78	−1.16
10	1.00	0.63	0.6	0.63	0.62	0.63
11	2.27	0.34	1.81	0.33	1.83	0.35
12	1.88	0.06	1.46	0.03	1.46	0.03
13	3.12	−0.09	2.78	−0.09	2.73	−0.10
14	3.32	0.51	2.96	0.62	2.94	0.51
15	4.07	−0.07	3.68	−0.07	3.60	−0.20

	Kinematic 5		Kinematic 6		Kinematic 7	
Bar	LHRS	RHRS	LHRS	RHRS	LHRS	RHRS
0	2.70	0.12	2.14	0.97	2.23	0.55
1	2.07	−1.18	1.37	−1.54	1.40	−1.29
2	2.16	−0.51	1.39	−0.43	1.45	−0.47
3	1.92	−0.55	1.16	−0.57	1.19	−0.55
4	0.84	−0.45	0.13	−0.45	0.10	−0.46
5	2.21	−0.53	1.43	−0.48	1.46	−0.52
6	1.47	0.17	0.70	0.15	0.71	0.17
7	1.34	0.27	0.58	0.24	0.81	0.28
8	1.69	0.05	0.91	0.04	0.93	0.06
9	2.41	−1.19	1.62	−1.18	1.67	−1.18
10	2.23	0.62	1.44	0.65	1.46	0.63
11	3.49	0.34	2.73	0.36	2.73	0.36
12	3.09	0.05	2.31	0.05	2.34	0.06
13	4.33	−0.08	3.61	−0.08	3.62	−0.09
14	4.55	0.51	3.72	0.59	3.80	0.57
15	5.12	−0.04	4.46	−0.12	4.48	−0.03

Bar	Kinematic 8		Kinematic 9		Kinematic 10	
	LHRS	RHRS	LHRS	RHRS	LHRS	RHRS
0	3.50	−0.23	3.49	0.05	3.44	0.15
1	2.76	−1.42	2.33	−1.24	2.48	−1.24
2	2.75	−0.48	2.41	−0.49	2.45	−0.45
3	2.55	−0.53	2.26	−0.55	2.27	−0.51
4	1.43	−0.46	1.11	−0.45	1.16	−0.43
5	2.81	−0.50	2.50	−0.50	2.52	−0.51
6	2.09	0.19	1.78	0.19	1.78	0.19
7	1.94	0.28	1.48	0.27	1.51	0.28
8	2.25	0.07	1.95	0.09	1.98	0.06
9	3.00	−1.17	2.68	−1.18	2.73	−1.17
10	2.80	0.62	2.48	0.62	2.51	0.63
11	4.07	0.35	3.76	0.34	3.81	0.36
12	3.70	0.03	3.38	0.06	3.39	0.06
13	4.87	−0.08	4.60	−0.07	4.62	−0.09
14	5.07	0.54	4.70	0.61	4.82	0.57
15	5.67	0.04	5.41	−0.06	5.35	−0.03

Bar	Kinematic 11		Kinematic 12		Kinematic 13		Kinematic 14	
	LHRS	RHRS	LHRS	RHRS	LHRS	RHRS	LHRS	RHRS
0	2.64	1.55	2.64	0.60	2.64	0.74	2.64	−1.04
1	1.85	−1.31	1.89	−0.73	1.43	−1.23	2.10	−1.28
2	1.89	−0.48	1.89	−0.43	1.36	−0.42	2.07	−0.48
3	1.65	−0.50	1.68	−0.50	1.18	−0.51	1.90	−0.53
4	0.55	−0.42	0.58	−0.43	0.07	−0.43	0.79	−0.43
5	1.91	−0.50	1.95	−0.49	1.45	−0.49	2.16	−0.49
6	1.19	0.19	1.20	0.19	0.69	0.18	1.43	0.21
7	0.92	0.29	1.27	0.29	0.40	0.29	1.20	0.31
8	1.38	0.09	1.40	0.08	0.88	0.09	1.60	0.08
9	2.12	−1.17	2.14	−1.16	1.63	−1.17	2.33	−1.16
10	1.88	0.64	1.95	0.65	1.40	0.62	2.14	0.62
11	3.18	0.36	3.21	0.36	2.68	0.37	3.39	0.35
12	2.81	0.09	2.85	0.06	2.31	0.07	2.99	0.03
13	4.03	−0.10	4.09	−0.06	3.54	0.05	4.26	−0.10
14	4.27	0.64	4.23	0.58	3.69	0.53	4.43	0.58
15	4.83	−0.08	4.87	0.01	4.43	−0.09	5.26	−0.12

Table 3.9: The coincidence timing calibration offsets, in ns, for the 16 S2m bars for both arms for each kinematic setting.
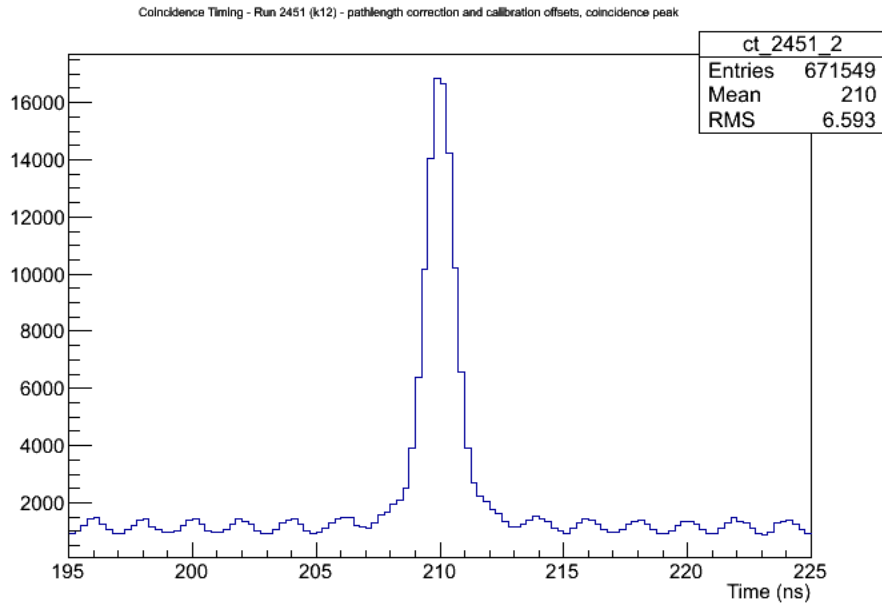
Figure 3.23: Example of the coincidence timing from Run 2451 in Kinematic 12, with pathlength corrections and calibration offsets, showing just the coincidence peak, with the RF signal frequency visible in the background.

The alignment of the 2-D plots can be seen in Figure 3.24.

3.5.5 Time-walk Correction

The last of the coincidence timing corrections is called time-walk. Time-walk is the effect in which larger amplitude signals produce earlier TDC signals than smaller signals. This is due to the fact that discriminators are based on thresholds, and larger amplitude signals reach that threshold before smaller amplitude signals, so larger amplitude signals appear to arrive earlier.

To calculate the effect due to time-walk, the ADC signals are examined with respect to the TDC signals and a relationship is determined between them to adjust the timing.

As the titles of the plots in Figure 3.25 indicate, they are plots of the ADC channel as a function of the TDC channel. In both plots, the left PMT of bar 7 is being examined; the top plot is for the LHRS and the bottom plot is for the RHRS. The cut-off at the bottom of each plot corresponds to the pedestal suppression region; below that ADC channel, no data was recorded.
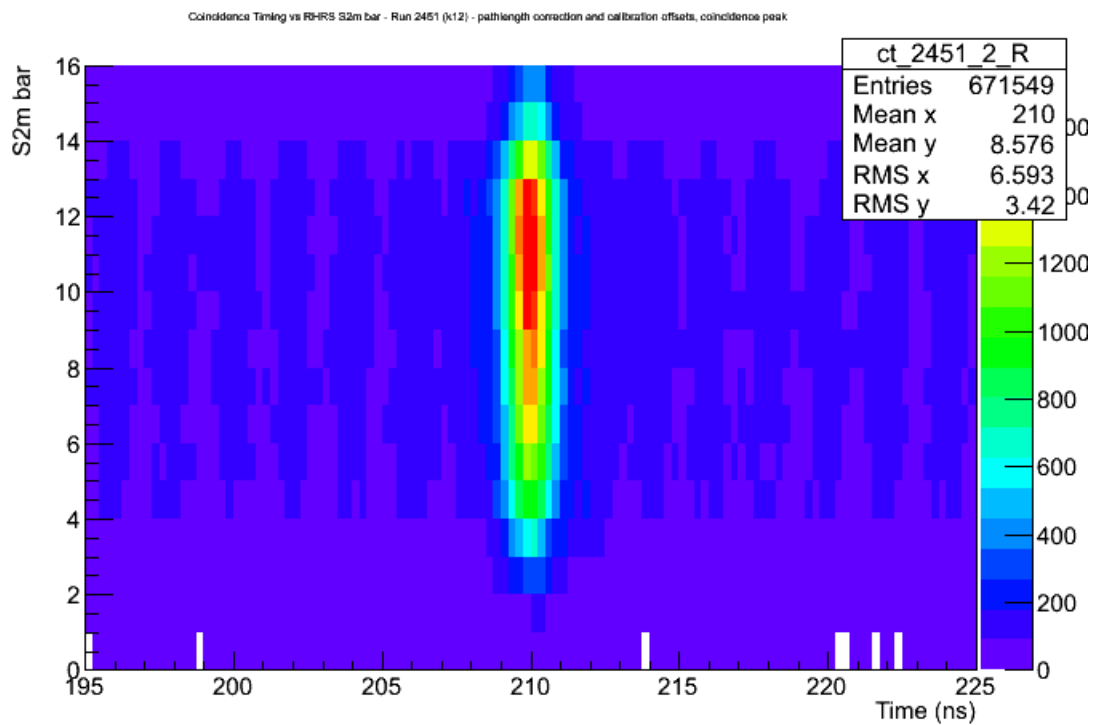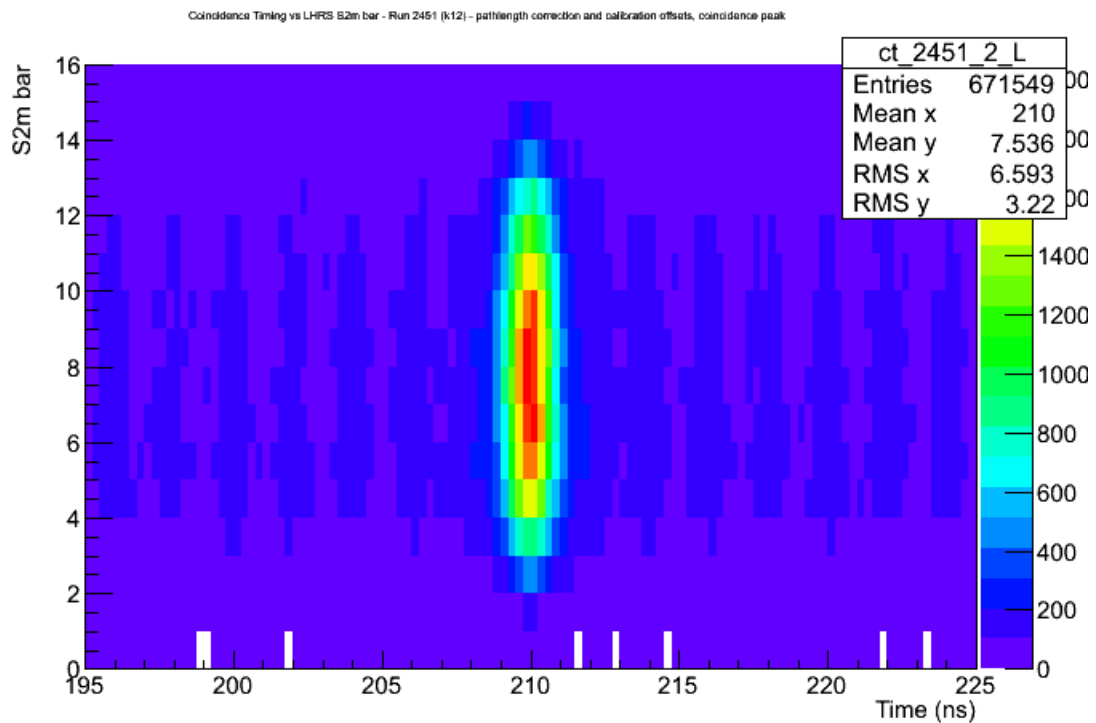
Figure 3.24: Example of the coincidence timing versus LHRS and RHRS S2m bars from Run 2451 in Kinematic 12, with pathlength corrections and calibration offsets, showing just the coincidence peak.
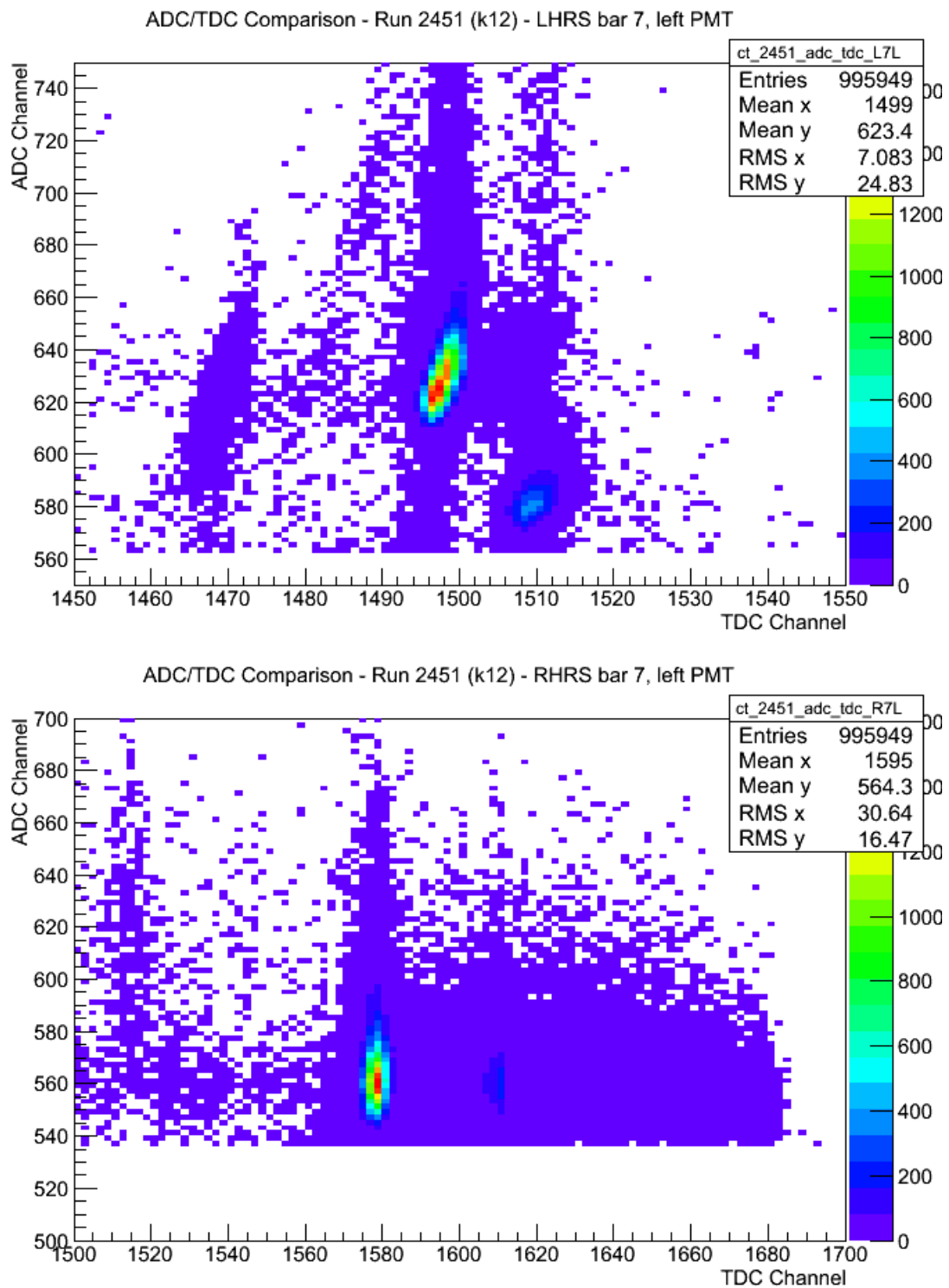
Figure 3.25: Examples of ADC/TDC comparisons to show timewalk effects, from Run 2451 in Kinematic 12, using data from the left PMT from bar 7 in both the LHRS and RHRS.

Interestingly, these plots could be useful for particle identification. In the top plot, there is a clear separation between the protons and pions, with the pions arriving earlier, at channel 1510[7], and with less energy. In the bottom plot, something similar is seen, although the equivalent energy deposition would indicate that these are also electrons, merely arriving earlier than the rest, most likely related to double-peak issues in that arm.

More importantly, there is a clear tilt in the proton signal, indicating that there is some relationship between the the ADCs and the TDCs. That is, a higher ADC channel corresponds to a higher TDC channel, suggesting that the higher energy events are arriving at an earlier time. While this sounds similar to the pathlength correction situation, this effect is smaller and applies to individual PMTs.

As for the electrons in the right arm, we see that this effect is almost non-existent.

Further complicating the issue of time-walk is the absence of ADC information for the right PMTs in the LHRS. Presumably the pedestal suppression was done incorrectly and all ADC information for those PMTs has been lost.

With no information for half of the left arm and no correction necessary for the right arm, calculating a time-walk correction doesn't seem possible or, given the RF structure seen in Figure 4.1, necessary.

---

[7]As the TDCs used were common stop, events at a higher channel occur earlier.

Chapter 4

Analysis

Once the calibrations have been completed, the next step is to analyze the data, which involves separating "good" events from "bad" events, as described earlier, and determining what percentage of good events may have been missed and need to be added back into the data yields.

Another integral part of the analysis process is the examination of simulated data, for comparison with the experimental data as well as applying correction factors to extract the wanted cross sections in the end.

4.1 Cut Determination

There are five main areas where the data can be cut to separate events: acceptance, tracking, scintillator hits, coincidence timing, and particle identification.

4.1.1 Acceptance Cuts

The spectrometers have a physical acceptance through which events can pass. As recorded in Table 2.3, the horizontal angular acceptance is ± 28 mr, the vertical angular acceptance is ± 60 mr, and the momentum acceptance is $\delta p/p = \pm 4.5\%$. This would seem to indicate that there should be no events with angle or momentum values larger than these acceptances, but the tracking software often identifies particles as having traveled in from outside the acceptance, indicating that these are not real events.

As such, it is a simple matter to apply an acceptance cut based on these focal plane variables. Indeed, it can sometimes be advantageous to artificially limit the acceptance further to remove any effects due to the edges of the spectrometer collimator.

As an example of the effect of these acceptance cuts, run 2451 from Kinematic 12 has a total of 1,002,554 recorded events before any processing. Of these, 97,997

Kinematic	Total Events	Events After Cut	Percentage of Events Cut
1	29,690,798	17,957,727	39.52%
2	42,346,040	24,413,247	42.35%
3	50,582,164	30,225,994	40.24%
5	23,071,173	14,693,348	36.31%
6	50,365,624	30,163,372	40.11%
7	43,527,476	26,958,813	38.06%
8S	12,237,124	7,429,076	39.29%
8L	13,913,723	8,540,856	38.62%
9	65,817,512	41,057,453	37.62%
10	45,404,262	28,115,537	38.08%
11	32,716,532	19,686,056	39.83%
12	26,161,904	8,727,027	42.44%
13	22,799,175	13,934,713	38.88%
14	18,972,173	11,834,151	37.62%

Table 4.1: Results of the acceptance cuts for each kinematic including the total number of events before the cuts were applied, the number of events left after the cut, and the percentage of the total events that were cut.

(113,123) exceed the vertical angular acceptance of the LHRS (RHRS) , while 102,123 (134,841) events exceed the LHRS (RHRS) horizontal angular acceptance. Further, 45,416 (102,052) events exceed the momentum acceptance of the LHRS (RHRS).

As an event that exceeds one acceptance often exceeds another, many of these events are the same. Together, a total of 417,263 events are considered outside the spectrometers' acceptances, so by applying these cuts, 41.6% of the events are immediately removed from the data.

Table 4.1 shows the number and percentage of events in each kinematic that were cut due to the acceptance cut values listed above.

4.1.2   Tracking Cuts

When a particle passes through the VDC layers, it leaves behind voltage spikes in the sensory wires. The analyzing software attempts to use the change in these wire voltages to determine a trajectory for the particle. In many cases, the trajectory is clear and the analyzer produces only a single track. In some cases, something may happen during the process that produces multiple tracks, and the analyzer is unable

to determine which path belongs to the wanted particle. Through a chi-squared analysis, the analyzer will attempt to identify the correct trajectory and label it the "golden" track [43].

For example, in run 2451 from Kinematic 12, there were 585,291 events that survived the acceptance cuts. Of those, 561,835 events (96%) had a single track in the left arm and 519,430 events (89%) had a single track in the right arm. Together, 498,662 events (85%) recorded single tracks in both arms. For those events, there is no confusion over which tracks might belong to the wanted particle and which might belong to background particles or other processes.

There are three approaches on how to handle the situation from this point. One approach is to assume that the analyzer software is correct and use the golden tracks, though without knowing the exact method used to calculate the golden tracks, this can reduce confidence in the results.

Another approach is to examine each track, following it to the scintillator layers, and determine from there which track is most likely to be the correct track. This approach can become increasingly difficult if the rate of background events is high.

A third, less complicated approach was used for this analysis, in which any events with more than a single track in each arm are cut, and the results are later scaled to account for the difference. For example, for run 2451, eliminating non-single track events would cut out approximately 15% of the events that survive the acceptance cuts. By then increasing the final results by 15%, which assumes that the behavior of the cut events is similar to that of the remaining 85%, those cut events are essentially re-incorporated into the data. This does nothing to improve the statistical uncertainty, but this process eliminates any issues that may be encountered while attempting to filter events based on tracks.

Table 4.2 lists the kinematic settings, the number of events with tracks, the number of single-track events, and the percentage of events cut.

4.1.3   Scintillator Hit Cuts

When a particle hits the scintillator bars, it sets off a chain reaction that can ultimately lead to the recording of an event. In addition to recognizing that an event took place, the electronics are also capable of reporting in which bar the hit was recorded.

Kinematic	Events with Tracks	Events with Single Tracks	Percentage of Events Cut
1	17,957,727	14,904,718	17.00%
2	24,413,247	20,147,799	17.47%
3	30,225,994	22.734,794	24.78%
5	14,693,348	10,687,078	27.27%
6	30,163,372	24,677,292	18.19%
7	26,958,813	20,294,631	24.72%
8S	7,429,076	6,143,702	17.30%
8L	8,540,856	6,403,488	25.03%
9	41,057,453	30,477,903	25.77%
10	28,115,537	20,364,431	27.57%
11	19,686,056	16,437,952	16.50%
12	8,727,027	7,456,271	14.56%
13	13,934,713	10,408,821	25.30%
14	11,834,151	8,713,145	26.37%

Table 4.2: Results of the tracking cuts for each kinematic including the total number of events before the cuts were applied, the number of events left after the cut, and the percentage of the total events that were cut.

This allows for a crude check on the trajectory of the particle from the VDC layers.

Like the VDCs, the scintillators can also detect multiple particles during a single event. Sometimes a single bar will record multiple hits, as well as multiple bars recording hits from a single event.

Adding to the confusion, the TDC for each bar typically only records the timing of the last hit, so if a background particle hit the detectors after the desired particle, additional processing is required to determine which hit is the correct one.

Like the tracking, one solution is to follow each particle trajectory from the VDC layer to the scintillator layer to determine which bar should have been hit, and look further into the timing of the event to match up the correct track with the correct hit. For example, if the PMT on one end of a scintillator bar recorded two hits but the other only recorded one, it should be possible to match the correct pair of signals based on the length of time required for light to traverse the bar. This can become even more complicated if there are multiple possible tracks from the VDC layers, leading to a cascade of potential track-hit combinations.

One solution is to cut out any events in which more than one hit was recorded in the scintillator bars, much like single tracks from the VDC layers. For example, of

Kinematic	Events with Single Tracks	Events with Single Hits	Percentage of Events Cut
1	14,904,718	13,799,527	7.42%
2	20,147,799	18,629,269	7.53%
3	22,734,794	20,801,287	8.50%
5	10,687,078	9,726,330	8.97%
6	24,677,292	22,720,474	7.89%
7	20,294,631	18,497,750	8.82%
8S	6,143,702	5,644,512	8.10%
8L	6,403,488	5,853,166	8.58%
9	30,477,903	27,872,624	8.53%
10	20,364,431	18,515,790	9.06%
11	16,437,952	15,156,898	7.77%
12	7,456,271	6,864,415	7.89%
13	10,408,821	9,586,589	7.88%
14	8,713,145	8,003,937	8.12%

Table 4.3: Results of the scintillator hit cuts for each kinematic including the total number of events before the cuts were applied, the number of events left after the cut, and the percentage of the total events that were cut.

the 498,662 single-track events from run 2451 in kinematic 12, 490,821 events (98%) recorded single hits in the LHRS S2m layer and 465,575 events (93%) recorded single hits in the RHRS S2m layer. Together, 458,500 single-track events (92%) recorded single hits in the S2m layers.

This would result in about 8% of the single-track events that hit the S2m layer being removed from the data set, and the remaining events being scaled back up by that 8%.

A parallel analysis worked on a method using the multiple tracks and multiple scintillator hits to determine the most correct tracks in an attempt to keep as many events as possible in an effort to improve statistical uncertainty.

Table 4.3 lists the kinematics, the number of single-track events, the number of single-hit events, and the percentage of events cut.

4.1.4 Coincidence Timing Cuts

In Section 3.5, the calculation of the coincidence timing was discussed. Using the timing, a separation between true coincidence events and background events can be

made.

Looking at an example coincidence timing plot, Figure 4.2, it can be seen that the true coincidence events appear to form a Gaussian peak at the arbitrarily chosen 210 ns central coincidence timing. Overlaid on that peak is the background, the top of which appears to be a sine wave with a period of 2 ns, due to the RF nature of the beam.

To separate the true coincidence events from the background, a timing cut would be applied to either side of the coincidence peak wide enough to include the tails of the gaussian. Such a cut also includes the underlying background present in that region.

One approach to dealing with the background is to attempt to fit an equation to the structure of the background plateau and use that equation to determine the number of background events in each bin in the coincidence peak. Another approach is to measure the background plateau at regions far from the coincidence peak, and use the number of events in those regions to subtract a proportional number of background events from the events included in the cut on the peak, as seen in Figure 4.2.

For example, with run 2451 from Kinematic 12, after the previous cuts have been applied, there are 458,500 events left. Applying a ±5 ns cut around the coincidence peak leaves 107,935 (24%) events behind, some of which are background events. Applying a ±10 ns cut centered at 185 ns reveals that the background in that region contains 60,800 events. A ±10 ns cut centered at 235 ns reveals 60,852 events there. Averaging and scaling these sections together indicates that there should be approximately 30,413 background events under the coincidence peak, leaving 77,522 coincidence events.

Table 4.4 lists the number of events in the ±5 ns coincidence peak, the calculated number of background events in that peak, and the number of "true" coincidence events remaining.

4.1.5 Particle Identification

Another place where cuts can be introduced is particle identification. Using the Cherenkov detector or the shower counters, particles can be identified by their timing or energy deposition.
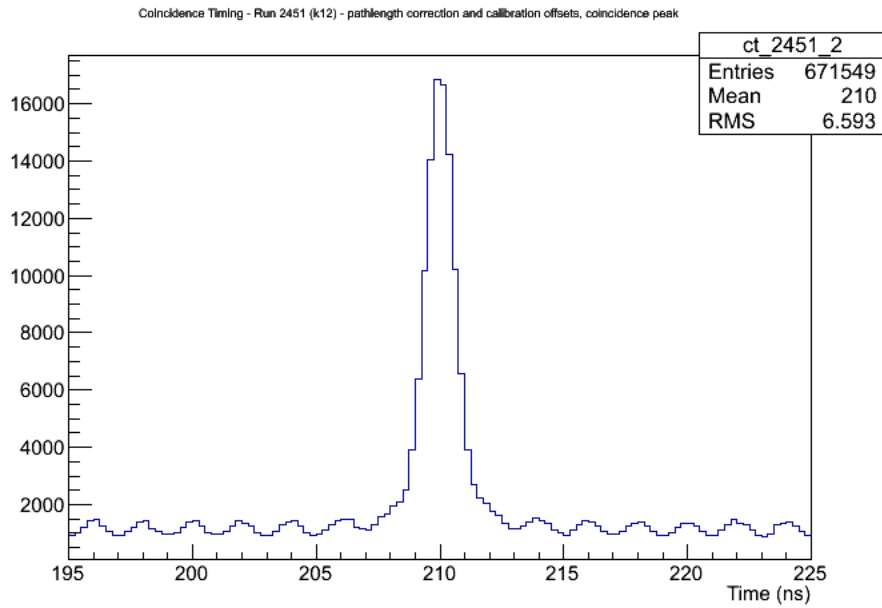
Figure 4.1: Example of the coincidence timing peak for Run 2451, Kinematic 12, with pathlength corrections and calibration offsets applied.
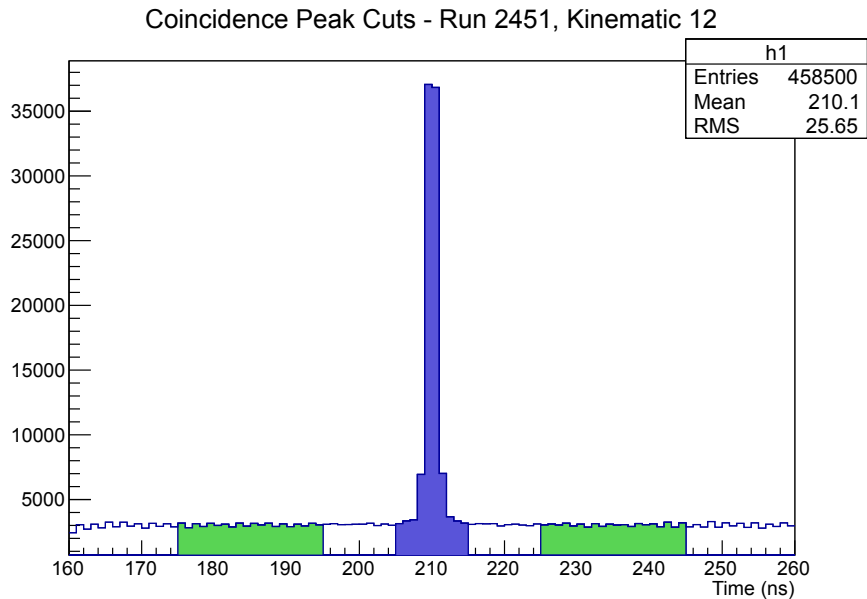
Figure 4.2: Example of the coincidence timing peak and background for Run 2451, Kinematic 12. The shaded region around the peak represents the ± 5 ns cut around 210 ns, while the two shaded regions in the background represent the ± 10 ns cuts centered around 185 ns and 235 ns.

Kinematic	Total Events	Events in Peak	Scaled Background Events in Peak	Net Coincidence Events
1	19,908768	2,245,984	1,229,622	1,016,362
2	26,857,603	3,234,386	2,225,075	1,009,311
3	30,133,846	5,089,625	2,309,742	2,779,883
5	14,234,096	1,516,224	1,076,076	440,148
6	33,193,116	3,349,576	2,592,043	757,533
7	27,201,054	4,261,435	1,926,985	2,334,450
8s	8,209,171	1,057,631	621,372	436,259
8l	8,826,414	958,082	675,957	282,125
9	41,549,890	3,909,221	3,262,593	646,628
10	27,916,751	3,623,162	2,053,403	1,569,759
11	22,062,781	2,259,001	1,733,937	525,064
12	9,906,008	2,237,274	660,658	1,576,616
13	14,464,174	1,612,404	1,098,676	513,728
14	11,948,642	1,349,474	905,733	443,741

Table 4.4: Results of the coincidence timing cuts for each kinematic including the total number of events before the cuts were applied, the number of events left in the coincidence peak after the cut, the scaled number of background events left in the peak, and the total number of events remaining after thebackground subtraction.

While the parallel analysis did extensive research into this, it was found that due to the larger tracking and scintillator hit cuts applied in this analysis, any cuts due to particle identification were already included and therefore unnecessary.

4.2   Correction Factors

Due to either cuts or flaws in the detector system, some data is lost, which will affect the final yield and cross section values. To take these losses into account, correction factors need to be applied to the yields obtained following the cuts from the previous sections to boost the yields back up to their "real" values.

Though these correction factors affect the yields, they do not affect the statistical error. Because data is lost, the statistical error is larger than it would be otherwise. By using smaller but more complicated cuts, the parallel analysis included more events, which resulted in a smaller statistical error.

Kinematic	Correction Factor
1	1.229
2	1.238
3	1.357
5	1.400
6	1.246
7	1.351
8S	1.232
8L	1.357
9	1.376
10	1.404
11	1.222
12	1.191
13	1.372
14	1.386

Table 4.5: Average tracking efficiency correction factors for the kinematic settings. The actual correction factors are calculated on a run-by-run basis.

4.2.1 Tracking Efficiency

As mentioned earlier, the analyzer attempts to calculate tracks from the particles passing through the VDCs. In this analysis, any event with multiple tracks was cut, but not every event with a multiple track was necessarily a bad event. In fact, it is assumed that the percentage of good multiple-track events is identical to the percentage of good single-track events.

For this reason, the percentage of events to be scaled back into the data is the same as the percentage of events cut. The simplest way to calculate this is to look at the number of events with single tracks and divide by the number of events with at least one track.

For example, run 2451 in Kinematic 12 had 860,891 events with at least one track and 720,169 events with only single tracks. This indicates that approximately 16.35%, with a relative error of 0.22%, of the events were removed solely due to the single-track cut and need to be scaled back in. The correction factor would then be approximately 1.195.

This was done on a run-by-run basis, and Table 4.5 shows the average correction factor for each kinematic setting.

Kinematic	Correction Factor
1	1.082
2	1.083
3	1.095
5	1.101
6	1.087
7	1.099
8S	1.090
8L	1.096
9	1.096
10	1.102
11	1.086
12	1.088
13	1.088
14	1.091

Table 4.6: Average scintillator hit efficiency correction factors for the kinematic settings. The actual correction factors are calculate on a run-by-run basis.

4.2.2 Hit Efficiency

Like the tracking efficiency, it is assumed that not every event that had multiple hits in the S2m layers was necessarily a bad event. For this reason, the yields are scaled back up according to the percentage of events cut.

For example, run 2451 in Kinematic 12 had 719,597 single-track events that struck the S2m planes. Of those, 660,691 events had only single hits in the S2m bars, indicating that approximately 8.19%, with a relative error of 0.24%, of the events were cut by this process, producing a correction factor of 1.089.

This cut was also performed on a run-by-run basis, with the kinematic averages in Table 4.6.

4.2.3 Computer Livetime

When an event is detected by the trigger supervisor, a signal is sent to all of the detectors to halt operations while the data is being recorded. If any events arrive during this "deadtime", they may be missed. To take these possible events into account, the computer livetime is calculated and these events are scaled back into the yields.

Kinematic	Correction Factor
1	1.227
2	1.223
3	1.269
5	1.117
6	1.048
7	1.055
8S	1.038
8L	1.109
9	1.117
10	1.120
11	1.037
12	1.030
13	1.102
14	1.121

Table 4.7: Average computer livetime correction factors for the kinematic settings. The actual correction factors are calculate on a run-by-run basis.

To calculate the computer livetime or deadtime, the process is to examine the number of coincidence events recorded into the data stream and compare that to the number of coincidence triggers recorded by the scalers, which are not affected by the trigger supervisor or computer deadtime.

For example, for run 2451 in Kinematic 12, there were approximately 868,097 T5 trigger events recorded by the data acquisition system. The scalers in the LHRS recorded 894,676 T5 triggers, which indicates that 2.97%, with a relative error of 0.21%, of the T5 triggers that formed were lost due to deadtime. As such, the computer deadtime would be recorded as approximately 3% with a computer livetime of 97%, which would produce a correction factor of 1.031.

The computer livetime was calculated on a run-by-run basis, with the values in Table 4.7 being averaged over the kinematic settings.

4.2.4   Electronic Livetime

Like the computer deadtime, there is a deadtime associated with the electronics. Unlike the computer deadtime, there are no signals sent out to halt any processes, but there are timing windows in which the electronics wait for other signals. If events
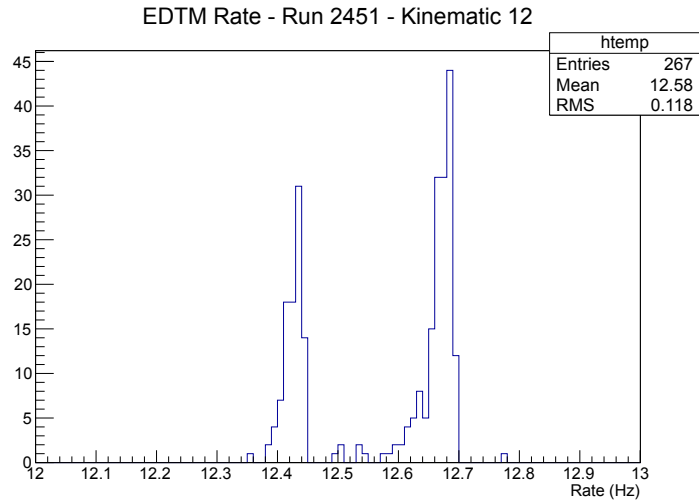
Figure 4.3: Example of the EDTM Rate from Run 2451 in Kinematic 12, where the right peak is presumably the EDTM signal with no losses and the left peak is the signal with one loss.

were to occur during these windows, they may be lost or accidentally processed into other events. This resulting loss of data is referred to as the electronic deadtime.

Generally the electronic deadtime is considered small enough to safely ignore, but for this experiment, an attempt was made to measure it nonetheless. This was done using a system called the Electronic Dead-Time Module (EDTM), which produced a regular pulse into the electronics, treated as any other event. By looking for places where this signal is absent, a measure of electronic deadtime can be estimated.

The first step in this process is to examine the structure of the EDTM signal, as recorded in the scalers. As can be seen in Figure 4.3, the rate of the EDTM pulses appears to be in two distinct peaks, with approximately 36% of the events in the left peak at 12.4Hz and the remaining 64% of the events in the right peak at 12.65 Hz.

As this rate is calculated by taking the number of EDTM pulses during some time period and dividing by the number of clock counts during the same time period, it can be presumed that the difference between the two peaks is that the left peak is simply missing one or two EDTM pulses relative to the right peak. Assuming that the electronic deadtime is sufficiently low, it could be presumed that the right peak is the peak formed when no EDTM pulses are lost and the left peak is formed when exactly one EDTM pulse has been lost.

One way to then calculate the electronic deadtime is to assume that the rate of

Kinematic	Correction Factor
1	1.010
2	1.010
3	1.009
5	1.009
6	1.009
7	1.009
8S	1.010
8L	1.010
9	1.010
10	1.010
11	1.010
12	1.010
13	1.010
14	1.010

Table 4.8: Average electronic livetime correction factors for the kinematic settings. The actual correction factors are calculate on a run-by-run basis.

the right peak is the actual rate at which the EDTM pulses were being produced, calculate how many EDTM pulses should have accumulated over the course of a run, and compare this with the number of EDTM pulses recorded in the scalers.

With this method, a fit can be applied to the second peak which indicates an EDTM rate of approximately 12.682 ± 0.007 Hz.

In run 2451 from Kinematic 12, there were 110,749,433 clock counts produced by the 103.7 kHz pulser, which translates into a total time of 1068 seconds. With an EDTM rate of 12.68 Hz, this indicates that approximately 13,542 EDTM pulses should have been produced. According to the scalers, 13,416 counts were recorded, for an electronic deadtime of 0.93%, with a relative error of 1.3%, and a livetime of 99.07%, which confirms the assumption that the electronic deadtime is quite low.

This would produce a correction factor of 1.009.

Like the computer livetime, the electronic livetime was calculated on a run-by-run basis, with the averaged kinematic results shown in Table 4.8.

Kinematic	LHRS Factor	RHRS Factor
1	1.001	1.011
2	1.001	1.011
3	1.001	1.013
5	1.003	1.014
6	1.002	1.011
7	1.003	1.014
8S	1.003	1.012
8L	1.003	1.013
9	1.003	1.012
10	1.003	1.015
11	1.003	1.011
12	1.002	1.012
13	1.003	1.016
14	1.003	1.014

Table 4.9: Average trigger efficiency correction factors for the kinematic settings. The actual correction factors are calculate on a run-by-run basis.

4.2.5   Trigger Efficiency

Not every particle that passes through the scintillator layers necessarily produces a noticeable signal in the PMTs. For this reason, it is necessary to know how many events might have been missed in either of the two sets of scintillators.

To determine this quantity, a third detector is used in conjunction with the S1 and S2m layers, usually the Cherenkov detector or the S0 layer. For this experiment, S0 was used, though the S0 layer in the left arm needed to be replaced due to the presence of the FPP. Both S0 layers consisted of a single vertically-oriented scintillator bar.

Due to the electronic logic of the T1 and T3 triggers, those triggers are only produced when both S1 and S2m layers detect a particle. If one of the layers fails to detect a particle, T1 and T3 will not be produced. As any particles passing through both S1 and S2m should also pass through S0, the efficiency trigger is built to look for a particle that is detected by S0 and either S1 or S2m, but not both.

That is, the efficiency triggers, T2 in the RHRS and T4 in the LHRS, are only produced when only *one* of S1 or S2m detects a particle, in conjunction with S0 detecting a particle. To calculate the trigger efficiency, the number of T1 (T3) triggers

is compared to the sum of the T1 (T3) and T2 (T4) triggers.

For example, in run 2451 in Kinematic 12, the scalers counted 138,669,703 T1 triggers and 1,653,126 T2 triggers. This suggests that 1,653,126 possible particles were not properly detected by the S1 and S2m layers in the RHRS, producing a right arm trigger efficiency of 98.82%. Likewise, in the LHRS, 47,883,038 T3 triggers and 112,463 T4 triggers were counted, producing a left arm trigger efficiency of 99.77%.

The correction factor for the RHRS trigger would then be 1.012 and the correction factor for the LHRS trigger would be 1.002.

The trigger efficiencies were calculated on a run-by-run basis and the averaged values for each kinematic are listed in Table 4.9.

4.2.6 Proton Absorption

Sometimes after being created in the target, the recoil proton is absorbed by the intervening material before it can reach the detectors. To account for these lost protons, a proton absorption correction factor is applied, using the equation [10]:

$$\epsilon_{abs} = 1 + \left(\frac{\rho_{LH_2} \cdot t_{LH_2} + \rho_{Al} \cdot t_{wall}}{\sin\theta_p} + \rho_{Al} \cdot t_{exit} + \rho_{air} \cdot t_{air} + \rho_{kapton} \cdot t_{spec}\right) N_0 \sigma(p_p) \quad (4.1)$$

where

- ρ_{LH_2} is the density of the liquid hydrogen, 0.0723 g/cm^3

- t_{LH_2} is the average distance the proton must travel to exit the target cell, 2.033 cm

- ρ_{Al} is the density of the aluminum in the target cell and target chamber walls, 2.81 g/cm^3

- t_{wall} is the thickness of the target cell walls, 0.014 cm

- t_{exit} is the thickness of the exit window, 0.041 cm

- ρ_{air} is the density of air, present between the target chamber and the spectrometer entrance window, 0.00129 g/cm^3

- t_{air} is the distance through the air that the proton must travel, 65.1 cm

Line Number	Momentum (GeV)	XS (mb)	Stat Error	Sys Error	Source
10	0.44	27.7	$^{+1.3}_{-1.3}$	$^{+0}_{-0}$	BARASHENKOV 61
11	0.49	24.8	$^{+0.8}_{-0.8}$	$^{+0}_{-0}$	BARASHENKOV 61
12	0.54	25.2	$^{+1.2}_{-1.2}$	$^{+0}_{-0}$	BARASHENKOV 61
13	0.57	26.1	$^{+1}_{-1}$	$^{+0}_{-0}$	BARASHENKOV 61
14	0.59	23.2	$^{+1.9}_{-1.9}$	$^{+0}_{-0}$	BARASHENKOV 61
15	0.607	24.4	$^{+0.244}_{-0.244}$	$^{+0}_{-0}$	SCHWALLER 71
16	0.65847	25.8	$^{+2}_{-2}$	$^{+0}_{-0}$	CARVALHO 54
17	0.69	22.4	$^{+0.9}_{-0.9}$	$^{+0}_{-0}$	BARASHENKOV 61
18	0.72	22.4	$^{+1.8}_{-1.8}$	$^{+0}_{-0}$	BARASHENKOV 61
19	0.75	22.6	$^{+1.3}_{-1.3}$	$^{+0}_{-0}$	BARASHENKOV 61
20	0.757	23.7	$^{+0.213}_{-0.213}$	$^{+0}_{-0}$	SCHWALLER 71

Table 4.10: Relevent selection of total pp cross sections from Ref [50], including the line number, the momentum of the measurement, the cross section, the statistical and systematic errors for each measurement, and the source of the data point.

Kinematic	P_p (MeV/c)	θ_p (deg)	σ_p (mb)	Correction Factor
1	553.69	25.30	25.6	1.010
2	530.02	12.53	25.1	1.017
3	530.02	38.57	25.1	1.008
5	627.91	29.74	24.9	1.009
6	579.01	13.61	25.2	1.016
7	579.01	45.87	25.2	1.008
8	672.56	31.30	24.6	1.009
9	649.23	21.13	25.5	1.012
10	649.23	41.48	25.5	1.008
11	609.04	14.54	24.3	1.014
12	609.04	48.07	24.3	1.007
13	575.56	37.74	25.5	1.008
14	622.63	35.46	24.8	1.008

Table 4.11: The proton absorption correction factors for each kinematic setting. These factors were calculated using a single calculated proton momentum and angle at the target for each kinematic, which was then used to calculate a pp cross section and a correction factor.

- ρ_{kapton} is the density of the Kapton spectrometer entrance window, 1.42 g/cm^3

- t_{spect} is the thickness of the spectrometer entrance window, 0.036 cm

- N_0 is Avogadro's number, 6.022×10^{23}

- $\sigma(p_p)$ is the total cross section of the pp reaction, a reasonable argument as to the cross section of proton absorption by any of the materials it encounters

Using the proton momentum, the total pp cross section can be interpolated from a table found on the Particle Data Group website [50], a selection of which is included in Table 4.10.

For example, the runs in Kinematic 12 have a proton momentum at the target of approximately 609 MeV/c. That places it between points 15 and 16, which have cross sections of 24.4 and 25.8 mb, respectively. A cubic interpolation would estimate that the cross section for Kinematic 12 would be approximately 24.48 mb, while a linear interpolation would estimate a cross section of approximately 24.46 mb. Putting those together with rest of the variables above produces a correction factor of approximately 1.0072.

As for the error, due to the nature of the interpolation, it may not be possible to get an exact value, but the 25.8 mb cross section has a nearly 8% error associated with it, so one might expect the overall error to be along those lines, likely something closer to 10% or even 15% given the assumption in using the pp cross section.

Unlike the rest of the correction factors, a single value was used for the entire kinematic, based on the theoretical momentum and angle of the proton at the target immediately after the reaction. Table 4.11 gives the correction factors for the kinematic settings.

4.2.7 Density Correction

The last correction to be applied is the density correction. As the beam passes through the liquid hydrogen target, it can warm the material, decreasing its density. This decrease in density is referred to as "boiling", though no actual phase change takes place.

Early in the calibration process, a simple boiling test was performed using a set of detectors located in the Hall's "beam dump", where the beam ends up after passing through the target chamber. Installed during a previous experiment, called HAPPEX [51], these luminosity detectors were specifically installed to measure the luminosity over the course of that experiment. Though they were not calibrated during this experiment, they were still functional and data was recorded in the RHRS scalers.

Of the eight detectors, it was found that one was no longer functional, but the other seven still worked. Using a set of runs in Kinematic 12 specifically designed to test for boiling, the rates as detected by these scintillators could be compared with the current. The runs[1], the currents, and the rates for the fifth luminosity bar are listed in Table 4.12 and plotted in Figure 4.4.

The linear behavior of the results suggested that no boiling was taking place for the 4 cm LH_2 target, and examination of several 15 cm runs suggested something similar. Later analysis revealed this was not the case, and further work needed to be done.

Density changes in the liquid targets are always of concern, and several studies have been done to examine the phenomenon. A study in 2005 performed by P. E. Ulmer [52] concluded that the density of the 4 cm target was a function of the current and the position within the target cell, but only after a current threshold of 40 µA. Prior to the threshold, the density remained constant, presumably due to "overcooling", a process in which the pressure in the target cell keeps the target material flowing fast enough that any heat due to the beam is quickly removed.

No information about the 15 cm target was presented in the Ulmer study, but generally the belief is that longer targets are more affected by boiling, as the beam spends longer interacting with the target and the longer cell makes circulation more difficult.

The parallel analysis examined this issue by looking at cross section behavior as a function of current. That analysis determined that no density correction was necessary for less than 40 µA for the 4 cm target, but thereafter a linear correction was necessary, with a correction of approximately 4% needed on currents of 80 µA.

Upon reanalysis of the boiling runs, it was found that some density change does

---

[1]Run 2443, run at 50 µA, was not included in this list due to a beam trip.

Run	Mean Current (µA)	Average Rate (kHz)
2439	10.25	316.89
2440	20.47	428.16
2441	30.83	541.45
2442	41.00	652.97
2444	51.24	764.88
2445	61.42	876.78
2446	71.22	988.46
2447	80.97	1104.50

Table 4.12: Rate of HAPPEX luminosity bar 5 as a function of current for the boiling test runs.
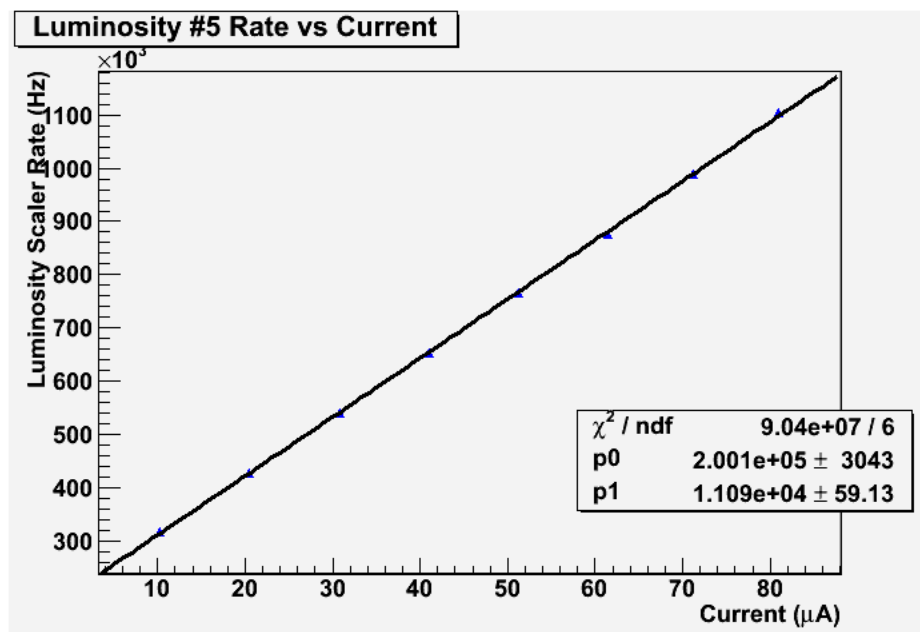
Figure 4.4: Rate of HAPPEX luminosity bar 5 as a function of current for the boiling test runs.

take place, but the effect can be difficult to detect, as the linear terms in a rate equation can easily overpower any non-linear terms.

The procedure to determine a density correction begins with the assumption that the rate of a detector, such as the T1 trigger rate in the RHRS, is dependent on the current, with an equation such as

$$R = cI + R_0 \tag{4.2}$$

where R is the trigger rate of the scintillator as read by the scalers; c is a value presumably based on the density and thickness of the material interacting with the beam and possibly the spectrometer setting, and not necessarily constant; I is the current of the beam, also as read by the scalers; and R_0 is the rate read by the detector when the current is zero.

Run 2307 from Kinematic 6 was a "cosmics" run, where no beam was present and the only source of events is background radiation. Using this run, it was determined that the zero-current rate of the T1 trigger is $R_0 = 14.6 \pm 1.1$ Hz.

If a run using the dummy aluminum targets is examined, this c term should be constant, and presumably composed of a term related to the aluminum and a term related to the spectrometer setting. Equation 4.2 can become

$$R = c_{Al}X_{Al}I + R_0 \tag{4.3}$$

where $X_{Al} = \rho_{Al}t_{Al}$ is the "thickness" of the aluminum in g/cm^2. The aluminum alloy used in the dummy targets and cryotarget cells [40] has a density of $\rho_{Al} = 2.810 \pm 0.001$ g/cm^3 [41].

For the 4 cm dummy target, the upstream foil had a thickness of 0.1140 ± 0.0002 g/cm^2 while the downstream foil had a thickness of 0.1160 ± 0.0002 g/cm^2. The 15 cm dummy target's upstream and downstream foils had thicknesses of 0.2700 ± 0.0003 g/cm^2 and 0.2750 ± 0.0003 g/cm^2 [40], respectively. The T1 trigger rate showed no dependence on the z-position of the target, so the thicknesses can be combined into one effective thickness, with the 4 cm dummy target having a combined thickness of 0.230 g/cm^2 and the 15 cm target a thickness of 0.545 g/cm^2.

Plotting the T1 rate as a function of the current can then be used to extract the c_{Al} term, which presumably stays constant for other runs using the same spectrometer
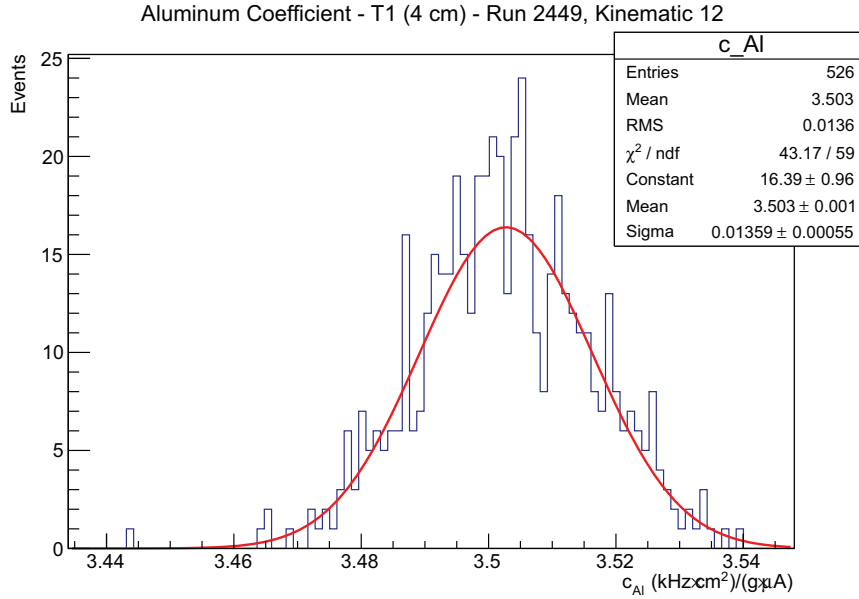
Figure 4.5: c_{Al} measurement, from run 2449, the dummy target run in Kinematic 12.

configuration. T1 is measured from the RHRS, which didn't move for Kinematics 8 through 12, allowing any runs from those settings to be used for this purpose.

To more easily measure c_{Al}, Equation 4.3 can be rearranged to

$$\frac{R - R_0}{X_{Al}I} = c_{Al} \tag{4.4}$$

Using run 2449, the 4 cm aluminum dummy run from Kinematic 12, and plotting Equation 4.4, it can determined that $c_{Al} = 3.50 \pm 0.01$ (g·kHz)/(μA·cm^2), as seen in Figure 4.5.

With a liquid hydrogen target, like the 4 cm target used in the boiling test runs, Equation 4.2 would look something like

$$R = (c_{LH_2}\rho_{LH_2}l_{LH_2} + c_{Al}X_{Al})I + R_0 \tag{4.5}$$

where ρ_{LH_2} is the density of the liquid hydrogen and not necessarily a constant; l_{LH_2} is the length of the hydrogen target, believed to be 3.860 ± 0.004 cm; and X_{Al} is now the thickness of the aluminum in the target cell.

The entrance windows for the 4 cm and 15 cm LH$_2$ targets are 0.145 ± 0.004 mm and 0.081 ± 0.004 mm thick, respectively. The end caps are 0.149 ± 0.008 mm and 0.207 ± 0.055 mm, also respectively [40]. Together with the density of the aluminum,
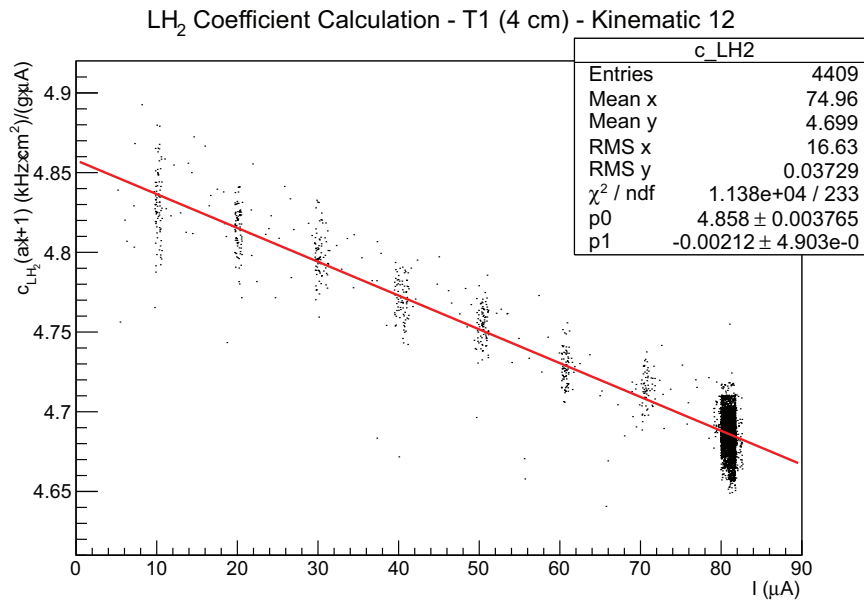
Figure 4.6: c_{LH_2} measurement for the 4 cm target, using all of the runs from Kinematic 12.

this produces a thickness of 0.083 ± 0.003 g/cm^2 for the 4 cm target and 0.081 ± 0.016 g/cm^2 for the 15 cm target.

If the density of the hydrogen is not constant, it must have some dependence on the current. This relationship may be linear or non-linear; further analysis indicated a linear relationship, though this does not agree with the results of the Ulmer study or the method used by the parallel analysis.

Moving the zero-current rate, R_0, to the left-hand side of Equation 4.5, dividing that side by the current, I, and moving the aluminum terms, $c_{Al}X_{Al}$, to the left side, the equation becomes

$$\frac{R - R_0}{I} - c_{Al}X_{Al} = c_{LH_2}\rho_{LH_2}l_{LH_2} \tag{4.6}$$

A plot of Equation 4.6 for the 4 cm LH$_2$ target looks something like the plot in Figure 4.6, where a linear trend can be clearly seen. It was found that care must be taken with the aluminum term, for slight changes in its value can cause the lower current points in the figure to shift vertically, seeming to remove the linear nature of the plot and replace it with something quadratic or cubic, even to the extent that the density can appear to be *increasing* with current.

Assuming linearity with the current, the density can become

$$\rho_{LH_2} = \rho_0(aI + 1) \tag{4.7}$$

where a is a constant density coefficient and ρ_0 is the density of the liquid hydrogen target with no beam. Many sources [28, 47, 38] cite this density as 0.0723 g/cm^3, but given the near constant temperature of 19 K and pressure of 210 kPa during the experiment [39], this value is likely closer to 0.0725 ± 0.0001 g/cm^3 [53].

With this new density term, Equation 4.5 expands into

$$R = c_{LH_2}\rho_0 l_{LH_2} aI^2 + (c_{LH_2}\rho_0 l_{LH_2} + c_{Al}X_{Al})I + R_0 \tag{4.8}$$

and Equation 4.6 becomes

$$\frac{R - R_0}{I} - c_{Al}X_{Al} = c_{LH_2}\rho_0 l_{LH_2} aI + c_{LH_2}\rho_0 l_{LH_2} \tag{4.9}$$

which can further processed into

$$\frac{\frac{R-R_0}{I} - c_{Al}X_{Al}}{\rho_0 l_{LH_2}} = c_{LH_2} aI + c_{LH_2} \tag{4.10}$$

Plotting Equation 4.10, seen in Figure 4.6, allows a calculation of the intercept term, which gives a value for c_{LH_2} of 4.858 ± 0.004 (g·kHz)/(µA·cm^2).

While the a term can be obtained from the slope of this linear fit, another approach is to use the newly-found c_{LH_2} and rearrange Equation 4.10, moving everything except the a term to the left-hand side.

$$\frac{\frac{R-R_0}{I} - c_{Al}X_{Al} - c_{LH_2}\rho_0 l_{LH_2}}{c_{LH_2}\rho_0 l_{LH_2} I} = a \tag{4.11}$$

Plotting Equation 4.11 produces a single peak, as seen in Figure 4.7, from which a value of $a = (-4.4 \pm 0.4) \times 10^{-4}$ (g/cm^3/µA) is obtained.

This constant should be independent of spectrometer configuration or kinematic setting. It is dependent on the length of the target, but from this value a current-based density correction can be applied to all 4 cm LH$_2$ runs.

As for the 15 cm LH$_2$ target, a series of runs taken from Kinematics 8 through 11 were put through the same procedure. Using a 15 cm dummy run, a value of $c_{Al} = 3.068 \pm 0.009$ (g·kHz)/(µA·cm^2) was obtained, plotted in Figure 4.8. That value was

Density Correction Coefficient - T1 (4 cm) - Kinematic 12

a	
Entries	4409
Mean	-0.0004388
RMS	9.928e-05
χ^2 / ndf	151.1 / 31
Constant	2690 ± 51.8
Mean	-0.0004359 ± 0.0000006
Sigma	$3.601\text{e-}05 \pm 4.178\text{e-}07$
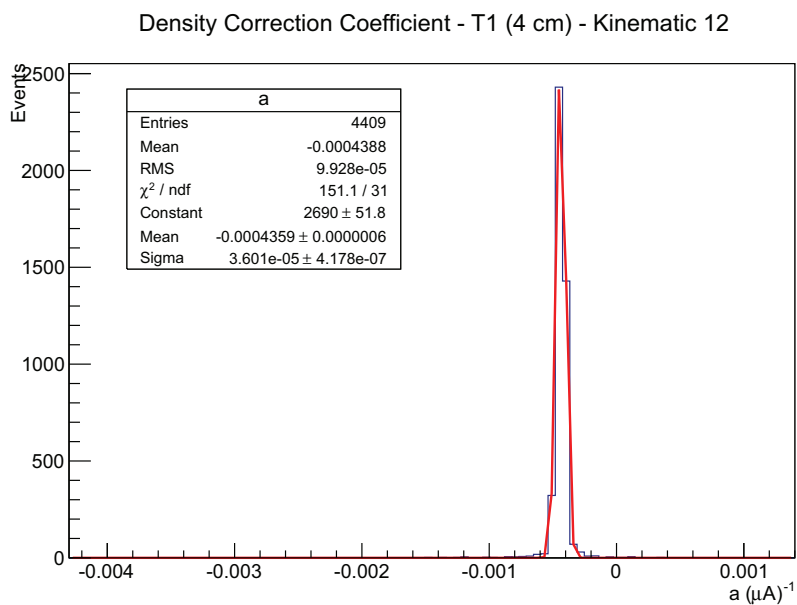
Figure 4.7: Density coefficient measurement for the 4 cm target, using all of the runs from Kinematic 12.

Aluminum Coefficient - T1 (15 cm) - Kinematics 8-10

c_Al	
Entries	1045
Mean	3.068
RMS	0.009555
χ^2 / ndf	68.38 / 73
Constant	29.42 ± 1.19
Mean	3.068 ± 0.000
Sigma	0.009333 ± 0.000241
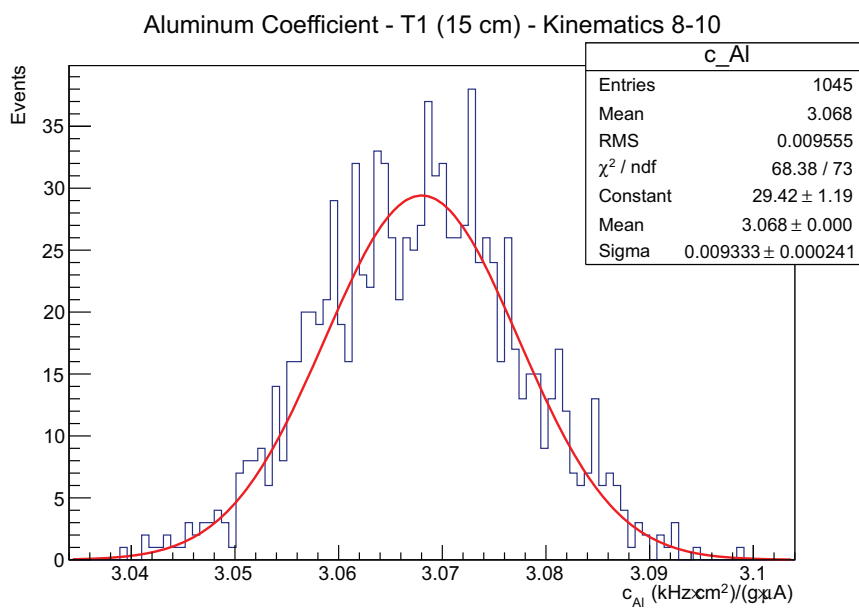
Figure 4.8: Aluminum coefficient measurement for the 15 cm target, using the Runs 2473, 2505, and 2533, the dummy runs from Kinematics 8, 9, and 10, respectively.
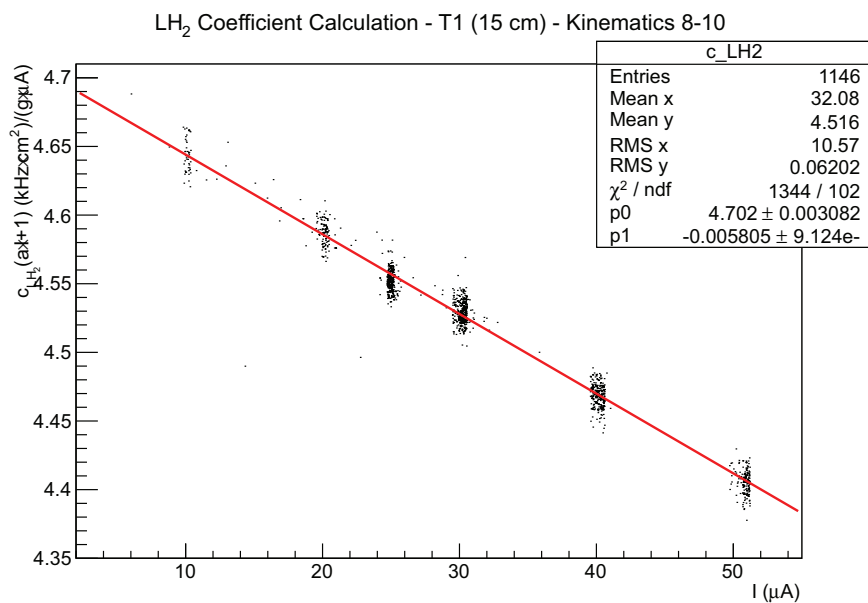
Figure 4.9: LH_2 coefficient measurement for the 15 cm target, using selected runs from Kinematics 8 through 10.
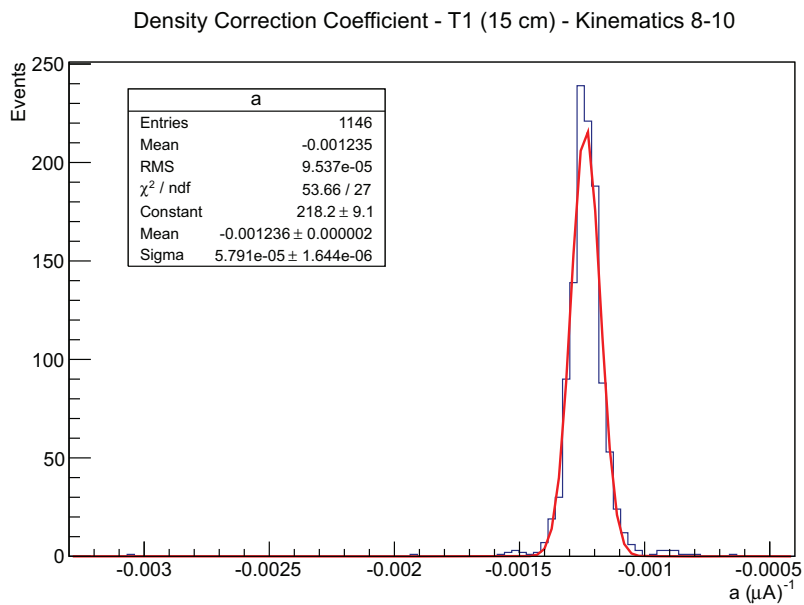
Figure 4.10: Density coefficient measurement for the 15 cm target, using selected runs from Kinematics 8 through 10.

Kinematic	Current (µA)	Target	Correction Factor	Density (g/cm^3)
1	15	4 cm	0.65%	0.0720
2	15	4 cm	0.65%	0.0720
3	20	4 cm	0.87%	0.0719
5	80	4 cm	3.49%	0.0700
6	40	4 cm	1.74%	0.0712
7	80	4 cm	3.49%	0.0700
8S	80	4 cm	3.49%	0.0700
8L	40	15 cm	4.79%	0.0690
9	30	15 cm	3.60%	0.0699
10	50	15 cm	5.99%	0.0682
11	55	4 cm	2.40%	0.0708
12	80	4 cm	3.49%	0.0700
13	35	15 cm	4.19%	0.0695
14	35	15 cm	4.19%	0.0695

Table 4.13: Density correction factors based on an example current for each kinematic setting, including the deviation from standard density and the value of the corrected density. The actual correction was based on the actual current and applied to each scaler-block as part of the luminosity.

used to produce the plot in Figure 4.9, which resulted in a value of $c_{LH_2} = 4.702 \pm 0.003$ (g·kHz)/(µA·cm^2), and that was used to produce the plot seen in Figure 4.10, with $a = (-1.24 \pm 0.06) \times 10^{-3}$ (g/cm^3/µA).

Table 4.13 lists the density correction factors that would be applied for each kinematic setting based on their nominal currents. The actual correction was applied directly to the density during the yield extraction process as part of the luminosity.

4.3 Simulations

Simulations for this experiment were carried out using the Monte-Carlo for Electro-Nuclear Coincidence Experiments (MCEEP) program, written by P. E. Ulmer [54]. The Fortran program was designed to simulate coincidence experiments using different theoretical models over an experimental acceptance. This program was primarily used for simulating the spectrometers and calculating the phase space for each of the experiment's kinematic settings.

Although the program has the capability of simulating many different reactions,

for this analysis it was primarily used for bound-state reactions using externally-supplied multipoles.

The simulation's output was stored in Ntuple files that could be converted into ROOT files and manipulated in a manner similar to that of the experimental data, ensuring that any relevant cuts applied to the experimental data could also be applied to the simulated data.

The simulation's input information, such as angles and momentum values, were stored in text-based input files. These input files inform the MCEEP program of the specifics of the reaction, including the masses and charges of the particles involved; the specifics of the spectrometer configuration, including momentum and angle settings of both spectrometers as well as target information; and the level of simulation detail to include, such as types of energy loss to incorporate and what level of "blurring" to include as the particle virtually navigates the spectrometer magnets.

The statistical error on the simulations is determined by a value in the input file called "tries". For each "try", the program randomly selects a position and momentum within the predefined spectrometer acceptance windows. The program then determines if that particle trajectory will result in an event or not. For this reason, only a small percentage of the tries "thrown" at the simulation will necessarily result in an event. As the acceptance listed in the input file increases, the percentage of events in the output file decreases.

Since the program only simulates events already in the acceptance, any events which would enter the acceptance after radiative corrections were applied would be missed. To account for this, the acceptance values in the input file were deliberately set larger than the physical acceptances of the spectrometers, allowing for the creation of events that might enter the acceptance after radiative effects have been calculated. Any events that remain outside of the normal acceptance can be later removed through acceptance cuts. The ultimate size of the programmed acceptance was determined by increasing the acceptance until resulting yield integrals stabilized.

Once an event has been accepted, the program then calculates any energy losses between the simulated target and the simulated detectors, if applicable, and calculates the cross section for that event. The unaltered program uses an internal cross section model based on the routines of R. W. Lourie [54], with modifications by G. A. Warren,

all based on the theoretical work of R. C. E. Devenish and D. H. Lyth [55]. As this analysis worked with other models, such as MAID and DMT, the code was modified to read in multipole values from those models and calculate cross sections from there, using the equations presented in Section 1.4.

For the MAID multipoles, values were obtained directly from the MAID2007 website [30], maintained by the University of Mainz. The DMT multipoles were obtained from the same website, using the DMT2001 model. The SAID multipoles were obtained from the CNS website [32], maintained by George Washington University, and converted to match the format of the MAID and DMT multipoles. The Sato-Lee multipoles were obtained directly from their research group, through Cole Smith.

Using W and Q^2 values for a particular event, the multipoles are interpolated from the file using a bicubic interpolation algorithm [56], from which CGLN amplitudes are constructed, as detailed in Section 1.4. Reponse functions are constructed from the CGLN amplitudes, and the model cross section is calculated from there. Aside from the multipole-to-cross section calculations and some minor menu modifications, the rest of the MCEEP program was left unaltered.

Once the cross section for a particular event has been calculated, that cross section is multiplied by the phase space to obtain a yield. The yield and phase space, along with other polarization variables, can then be written to Ntuple files or histograms, depending on entries in the input file. In the case of Ntuples, the yield or phase space results are stored in a weighting factor. Using these weighting factors, histograms of the yield, phase space, and average cross section can be constructed.

The cross sections produced by MCEEP are five-fold cross sections in the lab frame using the proton solid angle, in units of $fm^2/MeV/sr^2$. As cross sections in the literature are often two-fold cross sections in the center-of-mass frame using the pion solid angle, in units of µb/sr, the MCEEP cross sections needed to be converted. A simple way to do this is to multiply the phase space weighting factor in the Ntuple file by the Jacobian, the virtual photon flux, and a 10^4 factor to convert from fm^2 to µb. This produced a modified phase space that produces a two-fold average cross section when used in conjunction with the yields.

Another important part of the input file is the luminosity and beamtime values,

which are typically used to scale the simulated results to match experimental conditions. These factors do not affect the statistical nature of the results. For this analysis, rather than scaling the simulations to match the experimental results, the simulations and experimental results were all scaled to a standard of 1 $\mu A \cdot g/cm^2$ and a beamtime of 1 hour, which allowed for comparison of results for entire kinematics as well as individual runs without further manipulation

During the program's start-up procedure, the user is given three options concerning radiative corrections to apply to the simulated data. The user's first option is to include no radiative effects, the second option is to include normal radiative effects, and the third is to include radiative effects with multi-photon corrections. For this analysis, the first and third options were used, with the intention of using the non-radiatively-corrected data to construct average cross sections, while the third option allowed for direct comparison with the experimental data. For each kinematic setting, then, one simulation was performed which had no radiative corrections applied, and one was performed with full radiative corrections applied, with a 1 MeV upper limit on the photon energy.

The two sets of files could then be compared to determine a radiative correction factor, which was used to remove the naturally-occurring radiative effects from the experimental results and produce a non-radiatively-corrected experimental yield. This yield could then be treated like the non-radiatively-corrected simulated yields and divided by the phase space to obtain an average cross section, as discussed in Section 4.5.

4.4 Data Yield Calculation

The first step in the process to convert raw data into experimental yields is to "replay" the raw CODA data files into analyzed ROOT files. This is done with the Hall A analyzing software, known as "Podd" or, simply, the "analyzer" [43]. Used extensively by all Hall A researchers, both during experiments and after, the program is essentially a group of special ROOT libraries which runs inside the ROOT program, which is itself a group of libraries running inside a C-interpreter. Nonetheless, the analyzer program processes raw CODA data using values obtained from calibration processes, such as those discussed in Chapter 3, which are stored in database files the analyzer

can access.

In a specific macro called "replay", which runs in the analyzer, users can define which detectors were used in the experiment and which, if any, analysis libraries should be used to process the data during this runtime. For example, if the LHRS spectrometer was used during an experiment, an instance of a spectrometer class object is created, which then loads in all of the information about the spectrometers for the analyzer to use.

Typically, the event-by-event data is then stored in a "T" tree inside the output ROOT file. Scalers are also stored in that tree, though since they are not updated with every event, they are also stored in separate trees, one for each spectrometer arm.

It is these replayed runs that are analyzed during the calibration and analysis processes, often with the data being replayed multiple times as calibrations are performed and the database files are updated.

To obtain kinematic information about the data, one option is to use libraries in the replay code, specifically "Primary Kinematics" and "Secondary Kinematics". The Primary Kinematics library calculates information about the electron, including W and Q^2, while the Secondary Kinematics library calculates information about the proton and pion, including θ_{pq}^* and ϕ_{pq}^*. However, as the specific algorithms used by these libraries were not fully known, the research group behind this experiment decided original code would be preferable.

The program specifically written to process the experimental data for this analysis had several components and functions, such as a function written to calculate energy loss of the particles using the Bethe-Bloch equation. Aspects of the calibration process not inserted directly into database files were incorporated into this program, such as the calibration of the coincidence timing, as the presence of the double-peak problem made the usual methods unavailable.

The program also handled calculation of the correction factors discussed in Section 4.2. The first factor calculated was the total beamtime, necessary for scaling the end results to the standard of one hour. To do this, each run file to be included in the analysis of the kinematic setting was opened and the number of clock-counts as recorded by the scalers was summed to determine the total beamtime of the entire

kinematic.

Following that, each file was opened individually and the correction factors determined on a run-by-run basis, such as the computer livetime and trigger efficiencies, were calculated.

The current was also calculated using the scalers. As the scalers updated every four seconds, each group of events with the same scaler values were referred to as a "scaler-block", with all of the events in the same scaler block sharing an average current. Using this current and the corrected density and target length, the luminosity for this scaler-block was calculated. Like the beamtime, the luminosity was used to scale the resulting yields to match the simulated data.

The next step was to process each event, calculating the event's kinematic variables. This was done by first acquiring the event's momentum and angle values from the replayed file. The momentum values were then adjusted to account for energy loss between the target and the spectrometers, returning the momenta to their values as they would have been during the reaction in the target.

For the beam electron, this energy loss consisted of an interaction with the 14 µm thick aluminum target cell window and any liquid hydrogen it encountered before reaching the interaction point. For the scattered electron and recoil proton, each interacted with the liquid hydrogen on the way to the cell wall, the aluminum in the cell wall, the 0.4064 mm thick aluminum exit window, 65.1 cm of air, and the 0.3556 mm thick Kapton spectrometer window. The angle of the particles determined how much liquid hydrogen and aluminum the particles passed through as they exited the target cell.

The values present in the energy loss calculations are very similar to those in the proton absorption correction factor in Section 4.2.6.

With the particles' angles and corrected momenta, the kinematic variables are then calculated using Lorentz four-vectors.

The end result was a single ROOT file which contained experimental yields for the entire kinematic setting and could be compared directly with the radiatively-corrected simulated yields. These yield values can be found in Section 5.1.

4.5   Cross Section Calculation

Like the experimental yield extraction, calculating the cross sections from the exper-
imental data required programs written exclusively for that purpose. Also like the
yield extraction code, functions were written to handle specialized processes, such as
a function to calculate Legendre polynomials, needed for the CGLN amplitudes, and
for the bicubic interpolation of the multipoles obtained from the various models.

The basic procedure to convert an experimental yield to a central experimental
cross section starts with plotting the experimental yield, the phase space, and the
radiatively-corrected and non-radiatively-corrected simulated yields. By comparing
the two varieties of simulated yields, a radiative correction factor can be calculated
for each model. An average radiative correction factor can then be produced, which
can be applied to the naturally radiatively-corrected experimental yield to produce a
non-radiatively-corrected experimental yield.

$$Y_{exp}^{nrc} = Y_{exp}^{rc} \times \frac{Y_{sim}^{nrc}}{Y_{sim}^{rc}} \tag{4.12}$$

Next, the non-radiatively-corrected yields, both simulated and experimental, can
be divided by the phase space to produce an average cross section.

$$XS^{avg} = \frac{Y^{nrc}}{PS} \tag{4.13}$$

As mentioned in Section 4.3, the cross sections normally produced by MCEEP
are five-fold cross sections in the lab frame using the proton solid angle, in units
of $fm^2/MeV/sr^2$. The cross sections here use a modified version of the phase space
which produces two-fold cross sections in the center-of-mass frame using the pion
solid angle, in units of µb/sr.

Using the simulated cross section plots and the model cross sections, which can
be calculated using the model multipoles and the mean kinematic variable values,
collapse factors can be calculated for each model. Like the radiative correction factors,
an average collapse factor can be produced and applied to the average experimental
cross section to produce a central experimental cross section value.

$$XS_{exp}^{cen} = XS_{exp}^{avg} \times \frac{XS_{sim}^{point}}{XS_{sim}^{avg}} \tag{4.14}$$

Kinematic	W (GeV)	Q^2 (GeV/c)^2	θ^*_{pq} (deg)	ϕ^*_{pq} (deg)
1	1.22629	0.0450603	0	—
2	1.22629	0.0450603	34.9197	359.814
3	1.22629	0.0450603	34.9197	179.997
5	1.23544	0.0881398	0	—
6	1.23544	0.0881398	46.6699	359.846
7	1.23544	0.0881398	46.6699	180.024
8	1.23434	0.126781	0	—
9	1.23434	0.126781	31.2557	359.916
10	1.23434	0.126781	31.2557	179.803
11	1.23434	0.126781	51.0383	359.856
12	1.23434	0.126781	51.0383	180.236
13	1.18069	0.120481	0	—
14	1.20972	0.119839	0	—

Table 4.14: Mean kinematic variables used for the cut fraction analysis, based on the mean values obtained from the MCEEP phase space histograms.

As the cross section is a function of the four kinematic variables W, Q^2, θ^*_{pq}, and ϕ^*_{pq}, it exists in a four-dimensional phase space, in which each kinematic variable is typically broken up into bins, with the above process occurring bin by bin. As such, bin size is crucial. The bin width should be small enough to ensure that the collapse between average and central cross section values is well behaved, but large enough to include enough events to keep the statistical error low.

For this analysis only a single bin was used, centered on the average values for each kinematic variable. This means that the size of the bin is determined by cuts made on each of the kinematic variables. To determine the best place to make these cuts, several possible cut widths were examined, with central cross sections being calculated for each value and then compared.

First, the MCEEP-calculated phase space was plotted as a function of each kinematic variable, with the W plot having 200 bins between 1.1 and 1.3 GeV, the Q^2 plot having 180 bins between 0.0 and 0.18 (GeV/c)^2, the θ plot having 90 bins between 0 and 90 degrees, and the ϕ plot having 360 bins between 0 and 360 degrees or 180 and 540 degrees, depending on the mean value of ϕ. Table 4.14 lists the mean kinematic values that were used for each kinematic.

For each of these plots, the bin containing the mean value was located, and an average peak count was calculated using the mean bin and its four nearest neighbors.
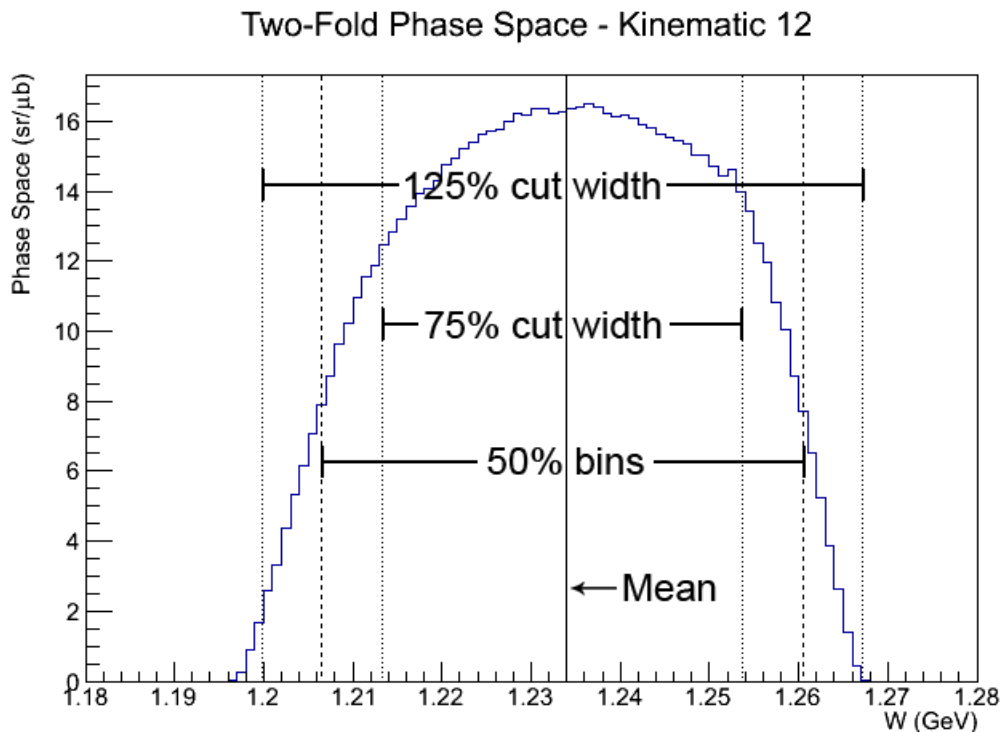
Figure 4.11: Annotated plot of the two-fold phase space as a function of W for Kinematic 12, illustrating how the 50% bins and cut widths are calculated.

Moving left and right away from the mean, the bins where the count drops to 50% of the peak count were located and labeled the "50% bins".

For example, in the W plot for Kinematic 12, seen annotated in Figure 4.11, which had 100 bins from 1.18 to 1.28 GeV, the mean value was 1.2339 GeV, indicated by the solid black line. The bin that contained that value was 134, which had a phase space value of 16.43 sr/µb. Its nearest neighbors would be bins 132, 133, 135, and 136, which had bin values of 16.55, 16.07, 16.21, and 16.59 sr/µb, respectively. These five bins would produce an averaged peak count of 16.37 sr/µb. The goal, then, would be to locate the bins on both sides of the mean bin where the value first drops to less than 8.19 sr/µb. For this plot, the bin on the left side turned out to be 107, with a value of 7.83 sr/µb, and the bin on the right side was 161, with a value of 7.64 sr/µb.

The 50% bins then acted as starting points for the bin width survey. Cutting on them would be considered a cut fraction of 1.0. As seen in Figure 4.11, using a cut width of less than 1.0 would cut out more event and a cut width larger than 1.0 would cut out less events. For each of the kinematics, a variety of cut fractions was

Experimental Cross Section vs Cut Fraction - Kinematic 12
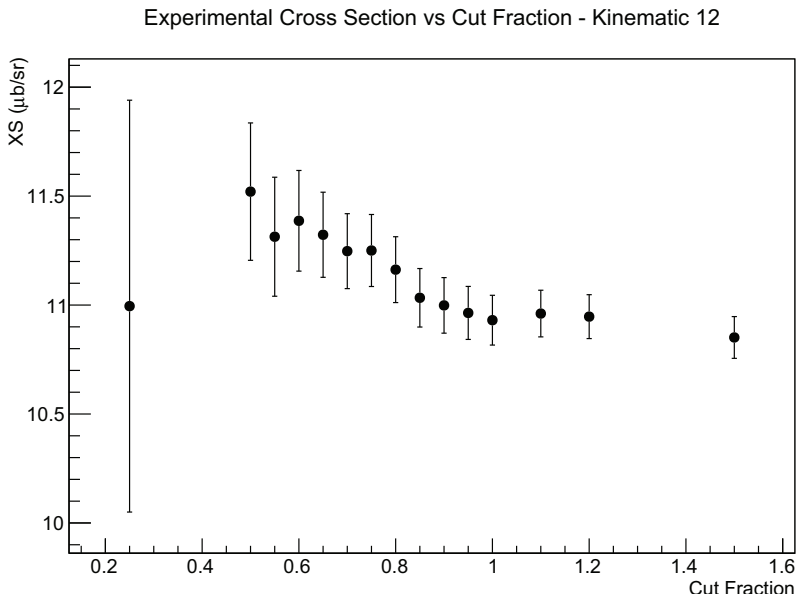
Figure 4.12: Kinematic 12 cross section as a function of cut fraction. The values used to create this plot can be found in Table 4.15.

examined, ranging from 0.25 to 1.5. The values for Kinematic 12, as an example, are listed in Table 4.15 and seen in Figure 4.12.

The resulting cross sections can then be examined for stability and statistical error. For this analysis, it was decided to use the 0.75 cut fraction on all kinematics. The actual kinematic cuts for each variable and each setting are shown in Table 4.16.

There are some oddities to mention concerning θ and ϕ for the parallel kinematics. First, a plot of ϕ for a parallel cross section does not produce a discernible central peak; instead, the values range from 0° to 360°, hence the lack of cut values for that variable.

If the reaction vertex were two-dimensional and ϕ was either 0° or 180° only, it could be simpler to think of θ as being positive or negative, depending on the orientation relative to the direction of the virtual photon, $\hat{q}$. For the parallel kinematics, where about half of events fall on one side of $\hat{q}$ and half fall on the other, one might expect a θ peak centered at 0. Instead, because this is a three-dimensional reaction vertex and θ is always positive, the actual θ plot show only positive values, centered at a non-zero peak. To account for this, the mean value for θ is forced to 0° for the parallel kinematics; the 50% widths are still calculated in the same way, but only the

Cut Fraction	W (GeV)	Q^2 (GeV/c)^2	θ (deg)
0.25	1.229 - 1.239	0.122 - 0.131	49.4 - 52.7
0.50	1.225 - 1.244	0.118 - 0.136	47.8 - 54.3
0.55	1.224 - 1.245	0.117 - 0.137	47.5 - 54.6
0.60	1.223 - 1.246	0.116 - 0.138	47.1 - 54.9
0.65	1.222 - 1.247	0.115 - 0.138	46.8 - 55.3
0.70	1.221 - 1.248	0.114 - 0.139	46.5 - 55.6
0.75	1.220 - 1.249	0.113 - 0.140	46.2 - 55.9
0.80	1.219 - 1.250	0.112 - 0.141	45.8 - 56.2
0.85	1.218 - 1.251	0.111 - 0.142	45.5 - 56.6
0.90	1.217 - 1.252	0.111 - 0.143	45.2 - 56.9
0.95	1.216 - 1.253	0.110 - 0.144	44.9 - 57.2
1.00	1.215 - 1.254	0.109 - 0.145	44.5 - 57.5
1.10	1.213 - 1.256	0.107 - 0.147	43.9 - 58.2
1.20	1.211 - 1.258	0.105 - 0.148	43.2 - 58.8
1.50	1.205 - 1.264	0.100 - 0.154	41.3 - 60.8

Cut Fraction	ϕ (deg)	Exp. XS (µb/sr)
0.25	174.7 - 185.7	16.57 ± 0.60
0.50	169.2 - 191.2	16.08 ± 0.11
0.55	168.1 - 192.3	15.94 ± 0.09
0.60	167.0 - 193.4	15.90 ± 0.09
0.65	165.9 - 194.5	15.86 ± 0.11
0.70	164.8 - 195.6	15.85 ± 0.15
0.75	163.7 - 196.7	15.62 ± 0.12
0.80	162.6 - 197.8	15.48 ± 0.11
0.85	161.5 - 198.9	15.32 ± 0.10
0.90	160.4 - 200.0	15.22 ± 0.08
0.95	159.3 - 201.1	15.14 ± 0.08
1.00	158.2 - 202.2	15.10 ± 0.07
1.10	156.0 - 204.4	15.07 ± 0.06
1.20	153.8 - 206.6	15.06 ± 0.06
1.50	147.2 - 213.2	14.83 ± 0.05

Table 4.15: Example cut fraction data for Kinematic 12, showing the ranges of the kinematic variables that represent the cut fractions and the resulting cross sections, which are plotted in Figure 4.12. The central kinematic values for Kinematic 12 can be found in table 5.4.

Kinematic	W (GeV)	Q^2 (GeV/c)^2	θ (deg)	ϕ (deg)
1	1.216 - 1.237	0.0364 - 0.0537	-13.50 - 13.50	0 - 360
2	1.216 - 1.237	0.0364 - 0.0537	28.54 - 41.29	347.06 - 372.56
3	1.216 - 1.237	0.0364 - 0.0537	28.54 - 41.29	150.75 - 209.25
5	1.222 - 1.249	0.0765 - 0.0998	-12.75 - 12.75	0 - 360
6	1.222 - 1.249	0.0765 - 0.0998	41.04 - 52.29	350.47 - 369.22
7	1.222 - 1.249	0.0765 - 0.0998	41.04 - 52.29	160.90 - 199.15
8	1.220 - 1.249	0.1133 - 0.1403	-12.00 - 12.00	0 - 360
9	1.220 - 1.249	0.1133 - 0.1403	26.01 - 36.51	344.54 - 375.29
10	1.220 - 1.249	0.1133 - 0.1403	26.01 - 36.51	155.80 - 203.80
11	1.220 - 1.249	0.1133 - 0.1403	46.16 - 55.91	351.23 - 368.48
12	1.220 - 1.249	0.1133 - 0.1403	46.16 - 55.91	163.74 - 196.74
13	1.166 - 1.949	0.1066 - 0.1343	-15.75 - 15.75	0 - 360
14	1.195 - 1.225	0.1060 - 0.1337	-13.50 - 13.50	0 - 360

Table 4.16: Kinematic variable cuts for each kinematic setting. The central values for each of these kinematic variables can be found in Table 5.4.

larger value is used in the calculation of the cut widths.

Once the cut fraction has been determined, final cross section values for each kinematic setting can be calculated. These values can be found in Section 5.2.

4.6 Multipole Extraction

The program used to extract the multipoles was based on a model-independent multipole extraction method devised by E. Stiliaris and C. N. Papanicolas [37]. The method involves randomly assigning multipole values within limits, then calculating observables from those multipoles and comparing the resulting values with those derived from the experimental data. For this experiment, the observables to compare were the central experimental cross sections for each Q^2 kinematic group.

Using the W and Q^2 values from each group of kinematic settings, the charge channel MAID multipoles up to $l = 5$ were interpolated, and variables used in the cross section calculation but not dependent on θ or ϕ were calculated prior to entering a loop of 100 million iterations. Once in the loop, the multipoles were randomized within a window surrounding the MAID multipole values. This window was varied to examine its effect on the results, with a final width of $\pm 80\%$ being used.

An internal loop was then run, which iterated through the different kinematic settings within the same Q^2 group, each with different θ and ϕ values. The $Q^2 =$

0.045 (GeV/c)^2 group contained three settings, Kinematics 1, 2, and 3; the $Q^2 = 0.088$ (GeV/c)^2 group contained three settings, Kinematics 5, 6, and 7; and the $Q^2 = 0.127$ (GeV/c)^2 group contained five settings, Kinematics 8, 9, 10, 11, and 12.

The randomized multipoles, θ, and ϕ were then used to construct the the CGLN amplitudes, response functions, and ultimately a two-fold cross section for that kinematic setting, as described in Section 1.4. The calculated cross section was then compared to the experimentally-derived cross section for that kinematic setting, with a χ^2 value being determined from:

$$\chi^2 = \sum_k \left(\frac{XS_k^{calculated} - XS_k^{experimental}}{\epsilon_k} \right)^2 \tag{4.15}$$

where ϵ is the error on the experimentally-derived cross section and k is the index of the individual kinematic setting. This χ^2 value is then applied as a weight to each iteration of the main loop as a measure of how well the individual multipole values approximated the experimental reality.

As a test of this multipole extraction method, the MAID cross sections for the kinematic settings in the third group, $Q^2 = 0.127$ (GeV/c)^2, were substituted for the experimental cross sections and the program was run. With the MAID cross sections as the goal and the MAID multipoles as the starting points, the results should match the MAID multipoles without any difficulty.

As can be seen in Figure 4.13, when no cut on the χ^2 weighting factor is applied, the results form an even plateau, indicating that each possible value for M_{1+} within the randomized window was given equal treatment.

Successively larger cuts on χ^2 then start to produce a shape out of the plateau, as seen in Figure 4.13. Tighter χ^2 cuts produce thinner peaks at the expense of fewer events remaining in the peak. Ultimately it was decided to use a χ^2 cut that leaves 10,000 events for optimal confidence. For this kinematic group, that cut was $\chi^2 < 215$, which produced the multipoles shown in Figure 4.14 and listed in Table 4.17.

As can be seen, all of the extracted results are within a standard deviation of the actual MAID multipole values.

The multipoles values obtained from the experimental cross sections are recorded in Section 5.3.
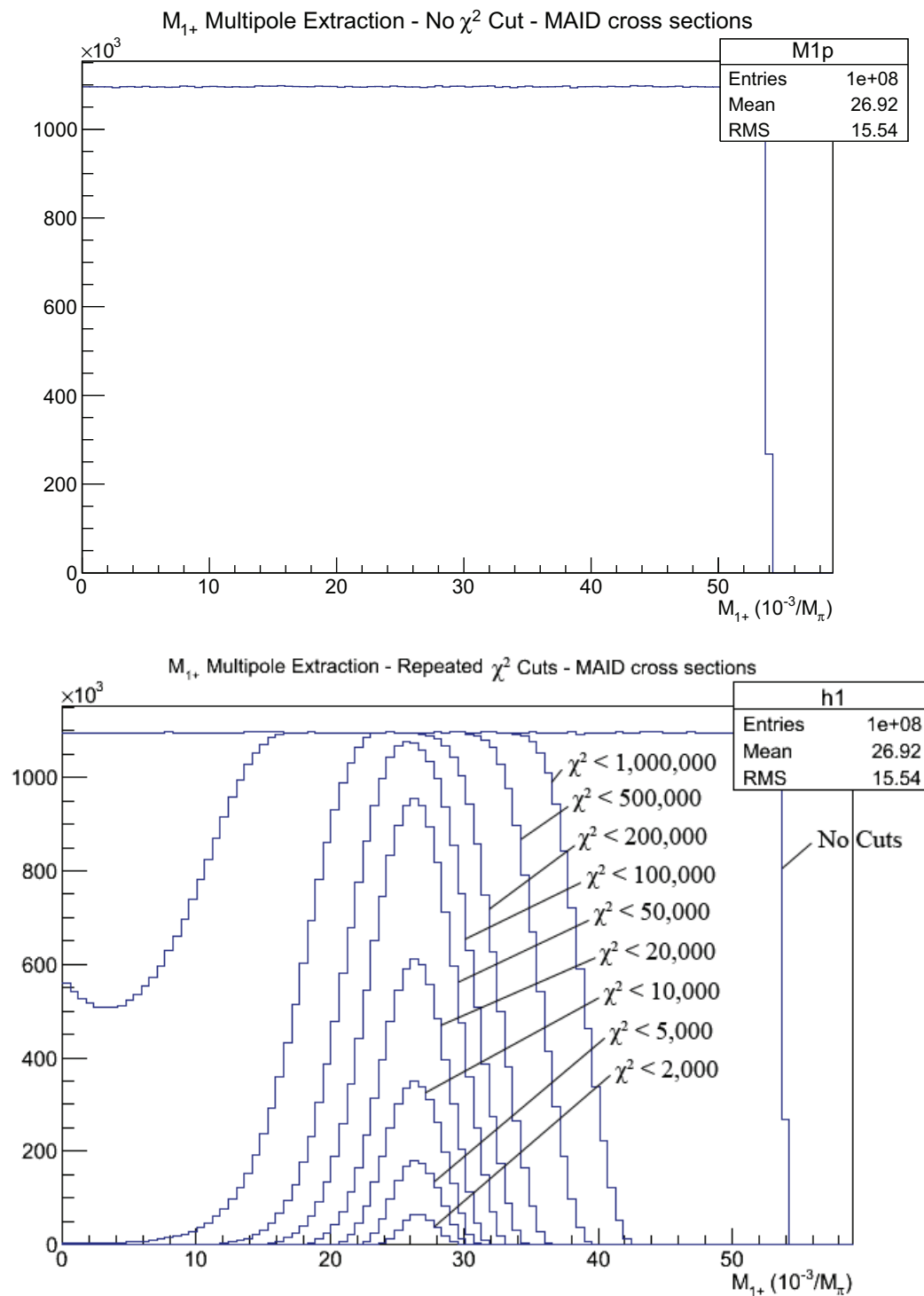
Figure 4.13: Example M_{1+} multipoles with MAID cross sections, showing how cuts on χ^2 affect the results. In the first diagram, with no cuts on χ^2, the plot is simply a flat plateau. The second plot shows how different χ^2 cuts produce peaks.
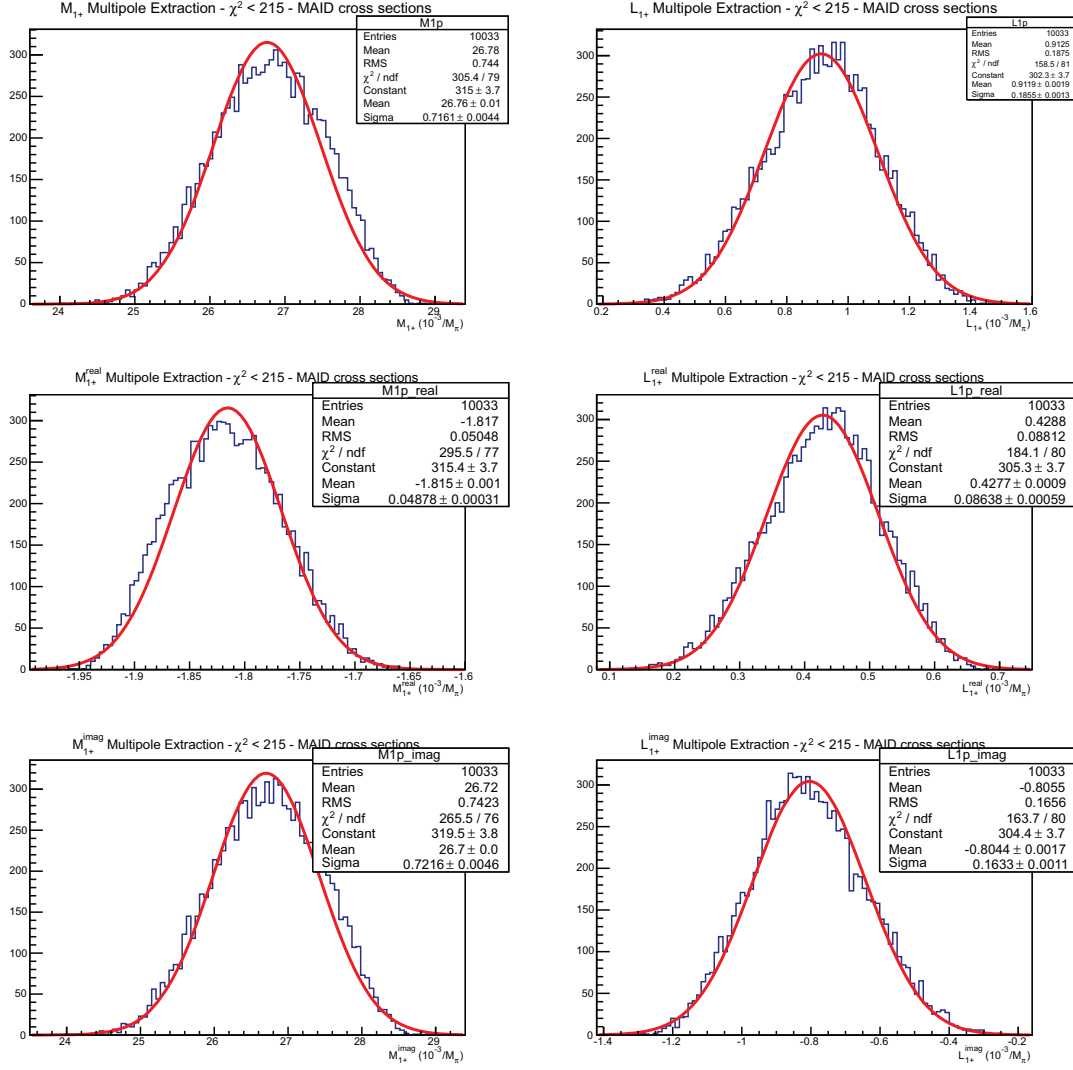
Figure 4.14: Extracted MAID multipoles using the MAID cross sections as the "goal" as a test of the multipole extraction method.

Multipole	Actual	Extracted
M_{1+}	26.917	26.8 ± 0.7
M_{1+}^{real}	-1.826	-1.82 ± 0.05
M_{1+}^{imag}	26.855	26.7 ± 0.7
L_{1+}	0.872	0.9 ± 0.2
L_{1+}^{real}	0.410	0.43 ± 0.09
L_{1+}^{imag}	-0.770	-0.8 ± 0.2

Table 4.17: Results of the multipole extraction method using the MAID cross sections as the "goal" as a test of the multipole extraction method. The "Actual" column contains the actual model multipole values and the "Extracted" column contains the extracted multipoles using this method. Multipole values are in units of $(10^{-3}/M_\pi)$.

4.7 Systematic Uncertainties

In addition to the statistical uncertainties, there are also systematic uncertainties always present in the data collection and analysis process. Some of these uncertainties have already been discussed, such as the errors associated with the correction factors from Section 4.2, while others are based on limitations in the hardware itself.

Some of the systematic uncertainties are based on the resolution of the detection instruments, such as the 1×10^{-4} momentum resolution or the 0.6 mr horizontal and 2.0 mr vertical angular resolution of the focal plane. Table 4.18 lists the different error sources and the approximate error values used to evaluate the systematic uncertainty.

The relative error on the proton absorption is difficult to quantify, but should be no more than 15%. The relative error on the livetimes and the efficiencies were based on the statistical uncertainties in the values used to calculate those factors. The relative error on the current comes from the uncertainty of the conversion between the BCM readings and the 0L02 measurement, from Section 3.1.

The relative error on the density comes from the uncertainty in the density correction factor, from Section 4.2.7. The relative error on the beam energy comes from a 2 MeV spread [38], while the relative errors on the beam position, spectrometer angle, and target location are all from values measured during the mispointing calibration, discussed in Section 3.4.

There are several methods for calculating systematic error. One method is to make modifications to a MCEEP input file using some of the values in Table 4.18 and repeatedly run simulations, seeing how those modifications affect the final cross sections. An approach similar to this was used in the parallel analysis.

This analysis used a somewhat simpler method, known as "means and extremes", where each of the values in Table 4.18 was adjusted within its systematic uncertainty limits to produce the largest possible yield for a run or kinematic. That "extreme" yield was then compared to the "mean" yield produced using the central values. The difference between the "mean" and "extreme" yields was the systematic uncertainty for that run or kinematic.

For example, using the central values from Table 4.18, Run 2451 from Kinematic 12 has an integrated yield of 16,386 events. The target length has a central value of 3.860 ± 0.004 cm. Given its uncertainty, the largest possible target length would be

Source	Central Value	Relative Error	Relative Effect
Proton Absorption	0.72%	~15%	0.11%
Computer Livetime	2.97%	0.21%	0.01%
Electronic Livetime	0.93%	1.3%	0.01%
Tracking Efficiency	16.35%	0.22%	0.04%
Hit Efficiency	8.19%	0.24%	0.02%
RHRS Trigger Efficiency	1.18%	0.02%	0.00%
LHRS Trigger Efficiency	0.23%	0.03%	0.00%
Current	1.55×10^{-4} (µA/Hz)	1%	0.96%
Target Length	3.86 cm	0.1%	0.10%
Density	-4.36×10^{-4} (g/cm^3/µA)	8.24%	0.30%
Beamtime	1068 s	0.37%	0.37%
Electron Vertical Focal Plane Angle	± 60 mr	1.07%	0.40%
Proton Vertical Focal Plane Angle	± 60 mr	1.07%	0.54%
Electron Horizontal Focal Plane Angle	± 28 mr	1.67%	0.78%
Proton Horizontal Focal Plane Angle	± 28 mr	1.67%	0.68%
Electron Fractional Momentum	$\pm 4.5\%$	0.1%	0.03%
Proton Fractional Momentum	$\pm 4.5\%$	0.1%	0.01%
Beam Energy	1.160 GeV	0.17%	0.00%
Beam Position (x)	-3.84 mm	3.68%	0.02%
Beam Position (y)	2.69 mm	5.29%	0.00%
Target Location	-15.32 mm	2.35%	0.04%
Central Electron Spectrometer Angle	22.0°	1.64%	0.03%
Central Proton Spectrometer Angle	48.0°	1.64%	0.00%

Table 4.18: Example systematic error contributions from Run 2451 in Kinematic 12. The central value indicates the recorded value for each source, along with the relative systematic error associated with that value. Each value was adjusted to its maximum and minimum values to determine the relative effect on the integrated yield for Run 2451, listed in the last column.

Kinematic	Mean Yield	Extreme Yield	Systematic Error
1	27,750	28,918	4.21%
2	19,539	20,394	4.38%
3	39,010	40,648	4.20%
5	13,249	13,855	4.57%
6	8,191	8,552	4.41%
7	21,494	22,472	4.55%
8S	9,300	9,713	4.44%
8L	6,139	6,421	4.59%
9	4,516	4,720	4.52%
10	9,916	10,341	4.29%
11	5,399	5,638	4.43%
12	16,529	17,252	4.37%
13	7,871	8,195	4.11%
14	9,580	9,971	4.08%

Table 4.19: Example systematic errors for each kinematic setting. The mean yield is the yield calculated using the mean values for each of the sources in Table 4.18, and the extreme yield is the yield calculated using the adjusted values that were found to produce the largest possible yield. The systematic error is the relative difference between them.

3.864 cm. Using that value, the run produces a yield of 16,369 events, a decrease of approximately 0.1%. This indicates that a larger target length produces a smaller yield, so to produce a larger yield, the target length must be adjusted downward.

In this manner, each of the values in Table 4.18 was individually adjusted to its minimum and maximum values to determine which limit produced the larger yield. The relative change in the yield compared to the mean yield for each value is listed in the column labeled "Relative Effect". From this, it can be seen that adjustments to several values, such as the beam energy and the horizontal beam position, had little effect on the overall yield. It can also be seen that the largest contribution to the systematic uncertainty is from the current, with an error of almost 1%.

These adjustments were then combined to determine the overall "extreme" yields for each kinematic, listed in Table 4.19, along with the "mean" yields and the overall systematic errors.

Chapter 5

Results

The results for this experiment come in four different varieties, each of which lends itself to comparison with theoretical results.

First, there are the yields obtained directly from the data. These yields are independent of any model interference, but can be compared directly to the radiatively-corrected simulated yields.

Second, there are the cross sections extracted with help from the models in the form of radiative correction factors and collapse factors. These collapsed, central experimental cross sections should be directly comparable to the model results, independent of any Monte-Carlo simulations.

Third, there are the extracted multipole values for the three W-Q^2 kinematic groups. From the experimental side, these values suffer the same model dependency, however little, as the experimental cross sections, though this is somewhat alleviated through the model-independent multipole extraction method. These results should be directly comparable to the multipoles extracted from the models themselves.

Fourth, there are the three CMR values that were the goal of this experiment. Constructed from the multipole values, these can be compared to model predictions and narrow any comparison between experiment and theory to just three values.

5.1   Yield Results

The integrated experimental yield results for the fourteen kinematics are listed in Table 5.1, along with their errors and the corresponding radiatively-corrected simulated yield results. These results have all of the cuts and correction factors from Sections 4.1 and 4.2 applied, as well as the kinematic variable cuts discussed in Section 4.5.

Table 5.2 lists the radiative correction factors for each of the four models used, as well as the average correction factor that was applied to the experimental yields. Ideally the correction factors should fluctuate little between models, suggesting that

Kin	MAID	DMT	Sato-Lee	SAID	Experimental
1	12443 ± 14	11475 ± 13	11664 ± 13	13857 ± 15	12149 ± 42
2	3757 ± 7	3336 ± 6	3831 ± 7	3949 ± 7	3788 ± 23
3	14566 ± 17	14602 ± 17	14016 ± 16	16210 ± 18	13305 ± 34
5	6129 ± 6	5837 ± 5	5710 ± 5	6971 ± 7	5316 ± 48
6	1581 ± 3	1432 ± 2	1696 ± 3	1703 ± 3	1422 ± 16
7	7869 ± 8	8348 ± 8	7696 ± 8	8601 ± 9	6618 ± 33
8S	4245 ± 4	3965 ± 4	3892 ± 3	4741 ± 4	3640 ± 18
8L	3734 ± 4	3490 ± 3	3424 ± 3	4172 ± 4	2616 ± 40
9	1065 ± 2	929 ± 2	1065 ± 2	1056 ± 2	808 ± 9
10	4234 ± 4	4324 ± 5	4004 ± 4	4634 ± 5	3203 ± 20
11	1118 ± 2	1021 ± 2	1200 ± 2	1199 ± 2	1042 ± 14
12	5581 ± 5	5860 ± 6	5453 ± 5	5942 ± 6	4657 ± 36
13	4776 ± 5	3781 ± 4	4173 ± 5	4719 ± 5	3315 ± 21
14	6057 ± 6	5067 ± 5	5238 ± 5	6237 ± 6	4247 ± 62

Table 5.1: Radiatively-corrected yield integrals, with all cuts and correction factors applied.

Kin	MAID	DMT	Sato-Lee	SAID	Average	Uncertainty
1	1.051	1.055	1.054	1.054	1.053	± 0.002
2	1.059	1.061	1.062	1.062	1.061	± 0.003
3	1.047	1.052	1.051	1.050	1.050	± 0.002
5	1.053	1.060	1.055	1.057	1.056	± 0.002
6	1.061	1.063	1.063	1.064	1.063	± 0.003
7	1.040	1.048	1.043	1.044	1.044	± 0.002
8S	1.049	1.056	1.051	1.053	1.053	± 0.001
8L	1.063	1.070	1.065	1.067	1.066	± 0.002
9	1.087	1.089	1.087	1.089	1.088	± 0.003
10	1.034	1.044	1.038	1.039	1.039	± 0.002
11	1.076	1.077	1.077	1.078	1.077	± 0.003
12	1.016	1.027	1.020	1.022	1.021	± 0.002
13	1.094	1.094	1.091	1.094	1.093	± 0.002
14	1.075	1.079	1.077	1.078	1.077	± 0.002

Table 5.2: Radiative correction factors based on the ratio between the non-radiatively-corrected simulated yields and the radiatively-corrected simulated yields. All of the factors for each kinematic share similar uncertainties.

Kin	MAID	DMT	Sato-Lee	SAID	Experimental
1	13071 ± 17	12109 ± 16	12290 ± 16	14606 ± 19	12798 ± 45
2	3978 ± 9	3541 ± 8	4066 ± 9	4194 ± 9	4018 ± 25
3	15244 ± 21	15366 ± 21	14725 ± 20	17022 ± 23	13969 ± 38
5	6456 ± 7	6184 ± 7	6025 ± 7	7369 ± 8	5615 ± 51
6	1678 ± 4	1522 ± 3	1803 ± 4	1812 ± 4	1511 ± 17
7	8186 ± 10	8748 ± 11	8023 ± 10	8981 ± 11	6908 ± 35
8S	4454 ± 5	4188 ± 5	4090 ± 4	4994 ± 5	3831 ± 19
8L	3970 ± 5	3733 ± 4	3645 ± 4	4451 ± 5	2789 ± 43
9	1157 ± 2	1012 ± 2	1158 ± 2	1258 ± 2	879 ± 10
10	4380 ± 6	4515 ± 6	4155 ± 5	4815 ± 6	3327 ± 21
11	1203 ± 2	1100 ± 2	1292 ± 3	1293 ± 3	1122 ± 15
12	5671 ± 7	6019 ± 7	5561 ± 7	6070 ± 7	4911 ± 37
13	5223 ± 7	4137 ± 6	4552 ± 6	5161 ± 7	3623 ± 23
14	6512 ± 8	5469 ± 7	5641 ± 7	6722 ± 8	4575 ± 67

Table 5.3: Non-radiatively-corrected yields, with all cuts and correction factors applied.

the radiative effects are model-independent.

Table 5.3 lists the integrated non-radiatively-corrected yields and errors for the experimental and simulated data for all fourteen kinematic settings.

5.2 Cross Section Results

The mean kinematic values used for each kinematic setting and the MCEEP-calculated, two-fold modified phase space values used to convert the non-radiatively-corrected yields into two-fold average cross sections are listed in Table 5.4.

The average experimental cross sections for the fourteen kinematic settings are listed in Table 5.5, along with their errors and the corresponding average simulated cross sections.

Table 5.6 lists the collapse factors calculated using the average simulated cross sections and the point model cross sections for the four models used in this experiment. The average of the four factors used to convert from the average experimental cross section to the central experimental cross section is also listed. Like the radiative correction factor, a small fluctuation in the collapse factor across the different models would indicate a model-independence of the collapse factor.

The central experimental cross sections for the fourteen kinematics are listed in

Kinematic	W (GeV)	Q^2 (GeV/c)^2	θ^*_{pq} (deg)	ϕ^*_{pq} (deg)	Phase Space
1	1.22629	0.0450603	0	—	831.2 ± 1.1
2	1.22629	0.0450603	34.9197	359.814	283.3 ± 0.6
3	1.22629	0.0450603	34.9197	179.997	729.0 ± 1.0
5	1.23544	0.0881398	0	—	450.7 ± 0.5
6	1.23544	0.0881398	46.6699	359.846	126.6 ± 0.3
7	1.23544	0.0881398	46.6699	180.024	374.0 ± 0.5
8S	1.23434	0.126781	0	—	300.4 ± 0.3
8L	1.23434	0.126781	0	—	266.2 ± 0.3
9	1.23434	0.126781	31.2557	359.916	92.3 ± 0.2
10	1.23434	0.126781	31.2557	179.803	214.7 ± 0.3
11	1.23434	0.126781	51.0383	359.856	85.8 ± 0.2
12	1.23434	0.126781	51.0383	180.236	238.7 ± 0.3
13	1.18069	0.120481	0	—	290.7 ± 0.4
14	1.20972	0.119839	0	—	299.0 ± 0.4

Table 5.4: The mean kinematic variables and phase space values for each kinematic setting.

Kin	MAID	DMT	Sato-Lee	SAID	Exp
1	15.73 ± 0.03	14.57 ± 0.03	14.79 ± 0.03	17.57 ± 0.03	15.40 ± 0.06
2	14.04 ± 0.04	12.50 ± 0.04	14.35 ± 0.04	14.80 ± 0.05	14.19 ± 0.09
3	20.91 ± 0.04	21.08 ± 0.04	20.20 ± 0.04	23.35 ± 0.05	19.16 ± 0.06
5	14.33 ± 0.02	13.72 ± 0.02	13.37 ± 0.02	16.35 ± 0.03	12.46 ± 0.11
6	13.26 ± 0.04	12.02 ± 0.04	14.25 ± 0.04	14.32 ± 0.04	11.94 ± 0.14
7	21.89 ± 0.04	23.39 ± 0.04	21.45 ± 0.04	24.02 ± 0.04	18.47 ± 0.10
8S	14.83 ± 0.02	13.94 ± 0.02	13.62 ± 0.02	16.63 ± 0.03	12.76 ± 0.06
8L	14.91 ± 0.02	14.02 ± 0.02	13.69 ± 0.02	16.72 ± 0.03	10.48 ± 0.16
9	12.55 ± 0.03	10.97 ± 0.03	12.55 ± 0.03	13.64 ± 0.04	9.53 ± 0.11
10	20.40 ± 0.04	21.03 ± 0.04	19.36 ± 0.03	22.43 ± 0.04	15.50 ± 0.10
11	14.02 ± 0.04	12.82 ± 0.04	15.06 ± 0.04	15.07 ± 0.04	13.08 ± 0.18
12	23.76 ± 0.04	25.22 ± 0.04	23.30 ± 0.04	25.44 ± 0.04	19.93 ± 0.16
13	17.97 ± 0.03	14.23 ± 0.03	15.66 ± 0.03	17.76 ± 0.03	12.47 ± 0.08
14	21.78 ± 0.04	18.29 ± 0.03	18.87 ± 0.03	22.48 ± 0.04	15.30 ± 0.22

Table 5.5: Average cross sections, in µb/sr, calculated by dividing the non-radiatively-corrected yields by the two-fold phase space.

Kin	MAID	DMT	Sato-Lee	SAID	Average	Uncertainty
1	0.739	0.735	0.739	0.744	0.739	±0.001
2	0.746	0.753	0.764	0.757	0.755	±0.002
3	0.750	0.754	0.751	0.757	0.753	±0.001
5	0.732	0.731	0.734	0.739	0.734	±0.001
6	0.721	0.736	0.740	0.740	0.734	±0.002
7	0.768	0.776	0.773	0.774	0.773	±0.001
8S	0.747	0.751	0.750	0.756	0.751	±0.001
8L	0.743	0.747	0.746	0.752	0.747	±0.001
9	0.750	0.753	0.759	0.758	0.755	±0.002
10	0.766	0.776	0.772	0.772	0.772	±0.001
11	0.754	0.762	0.767	0.767	0.762	±0.002
12	0.779	0.788	0.786	0.783	0.784	±0.001
13	0.698	0.684	0.685	0.697	0.691	±0.001
14	0.738	0.730	0.732	0.741	0.735	±0.001

Table 5.6: Cross section collapse factors, calculated from the ratio of the point model cross sections and the average cross sections. All factors for each kinematic setting share similar uncertainties.

Table 5.7, along with their errors. As these experimental cross sections are derived from the experimental yields in the previous section, they include all cuts and corrections included there. Additionally, these cross sections have also had the kinematic variable cuts discussed in Section 4.5 applied during their calculation.

As there are some unknown quantities involved in use of the 15 cm target, it was felt that it would be useful to collect data at the same spectrometer configuration using both targets, which could then be compared afterwards. This resulted in runs for Kinematic 8 being taken with both the short target and the long, designated as "8S" and "8L", respectively. This would suggest that the difference between the cross sections for 8L and 8S would be due to the use of the 15 cm targets, and the cross sections for the 15 cm targets could be scaled so that 8S and 8L match. These values are listed in the third column of Table 5.7.

Additionally, it was felt that the cross sections from this experiment needed to be scaled to some known value in order to set the absolute normalization scale for all measurements. It was hoped that could be done using elastic cross sections, as is the standard, but complications arose in achieving reliable cross sections from the particular elastic scattering runs associated with this run period, and another standard needed to be chosen. The parallel analysis chose previous pion electroproduction

Kinematic	Unscaled	15 cm Scaled	Normalized
1	11.38 ± 0.04	11.38 ± 0.04	13.17 ± 0.05
2	11.20 ± 0.07	11.20 ± 0.07	12.39 ± 0.08
3	17.66 ± 0.05	17.66 ± 0.05	16.69 ± 0.05
5	9.15 ± 0.08	9.15 ± 0.08	10.58 ± 0.10
6	8.77 ± 0.10	8.77 ± 0.10	10.14 ± 0.12
7	14.27 ± 0.07	14.27 ± 0.07	16.51 ± 0.09
8S	9.58 ± 0.05	9.58 ± 0.05	11.08 ± 0.06
8L	7.82 ± 0.12	9.58 ± 0.35	11.08 ± 0.63
9	7.19 ± 0.08	8.80 ± 0.28	10.18 ± 0.54
10	11.96 ± 0.08	14.64 ± 0.40	16.94 ± 0.81
11	9.97 ± 0.13	9.97 ± 0.13	11.53 ± 0.16
12	15.62 ± 0.12	15.628 ± 0.12	18.07 ± 0.14
13	8.61 ± 0.06	10.55 ± 0.29	12.20 ± 0.58
14	11.25 ± 0.17	13.77 ± 0.49	15.93 ± 0.89

Table 5.7: Scaled central experimental cross sections in µb/sr. The "Unscaled" column contains the direct results of the average experimental cross section divided by the MCEEP-calculated, two-fold modified phase space. The middle column contains values such that the kinematics using the 15 cm targets are scaled such that the two Kinematic 8 cross sections match. The "Normalized" column has the results scaled such that the Kinematic 8 cross sections match the MAID cross section for the kinematic variable values.

data, while this analysis chose to use the MAID cross section value for the Kinematic 8 settings, as it was felt that of all the kinematic settings, the $W \approx 1.232$ GeV, $Q^2 \approx 0.125$ $(\mathrm{GeV}/c)^2$ setting has been previously measured and would have the greatest chance of being correctly predicted by the most recent version of MAID.

For example, the unscaled Kinematic 8 cross section was calculated as 9.58 (7.82) µb/sr for the 4 cm (15 cm) target. The MAID2007 cross section using the same mean kinematic variable values is 11.08 µb/sr. All of the kinematics using the 4 cm target would be scaled by a factor of $^{11.08}/_{9.58} = 1.157$, and all of the kinematics using the 15 cm target would be scaled by a factor of $^{11.08}/_{7.82} = 1.417$.

The last column of Table 5.7 lists these "MAID scaled" or "normalized" cross sections and their errors, along with the unscaled values and, as previously mentioned, the "15 cm scaled" cross sections.

Table 5.8 lists the normalized experimental cross sections and the model cross sections at the same mean kinematic variable values for comparison.

Kinematic	MAID	DMT	Sato-Lee	SAID	Experimental
1	11.61	10.71	10.93	13.08	13.17 ± 0.05
2	10.48	9.41	10.96	11.20	12.39 ± 0.08
3	15.69	15.89	15.17	17.66	16.69 ± 0.05
5	10.49	10.03	9.81	12.09	10.58 ± 0.10
6	9.56	8.85	10.55	10.59	10.14 ± 0.12
7	16.81	18.15	16.58	18.58	16.51 ± 0.09
8S	11.08	10.47	10.21	12.58	11.08 ± 0.06
8L	11.08	10.47	10.21	12.58	11.08 ± 0.63
9	9.40	8.26	9.52	10.34	10.18 ± 0.54
10	15.62	16.33	14.95	17.32	16.94 ± 0.81
11	10.57	9.77	11.55	11.56	11.53 ± 0.16
12	18.51	19.86	18.31	19.92	18.07 ± 0.14
13	12.54	9.73	10.73	12.38	12.20 ± 0.58
14	16.07	13.35	13.81	16.67	15.93 ± 0.89

Table 5.8: Central cross sections in µb/sr. The model cross sections are calculated from the model multipoles using the mean kinematic variable values for each kinematic setting. The experimental cross sections are calculated from the average experimental cross section and the average collapse factor, and then normalized to the MAID results for Kinematic 8.

Figure 5.1 plots the normalized parallel cross sections for Kinematics 1, 5, and 8 with the cross section results for the four models. The model cross sections in the regions surrounding the data point use the same W and Q^2 values as the data point.

As can be seen, the normalized cross section for Kinematic 1 is very close to the SAID prediction for that region, while the cross sections for Kinematics 5 and 8 closely match the MAID results, which shouldn't be surprising for Kinematic 8, as that was the normalization point.

Figure 5.2 shows the normalized cross sections for the parallel kinematics as functions of W. In the top plot, the normalized cross section for Kinematic 1 matches the SAID results fairly well, much like Figure 5.1.

In the middle plot, the scaled cross section for Kinematic 5 matches MAID fairly well. The three points in the bottom plot represent the cross sections for Kinematics 8, 13, and 14. This is the only plot to reference the last two kinematic settings. As can be see, they match the MAID results fairly well, though it should be noted that the Q^2 values for the last two kinematics are not precisely the 0.127 $(\text{GeV}/c)^2$ used by the models in the plot.
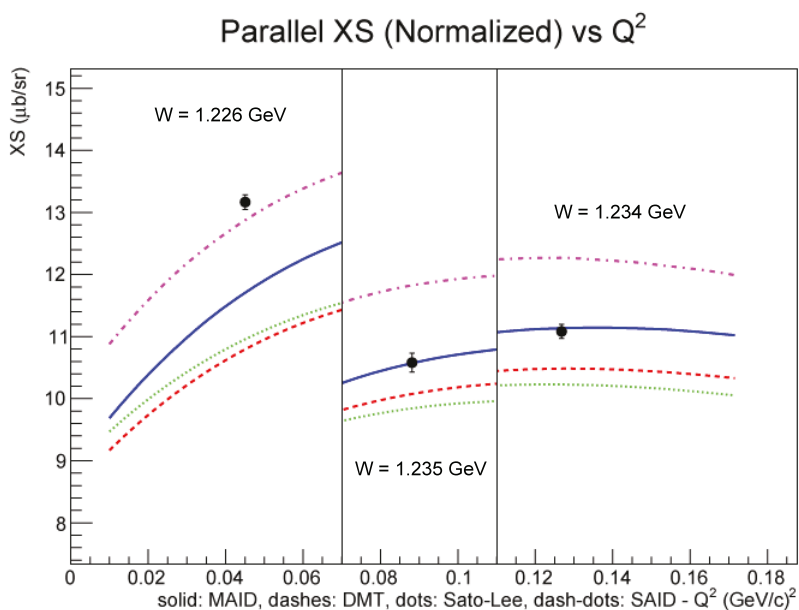
Figure 5.1: Normalized parallel cross sections as a function of Q^2. The solid blue line represents the MAID cross sections, the red dashed line represents DMT, the green dotted line represents the Sato-Lee model, and the magenta dash-dotted line represents SAID. The plot is divided into three regions based on the W and Q^2 values for the data point contained in that region. The model cross sections all use $\theta^*_{pq} = 0°$, and $\phi^*_{pq} = 0°$.
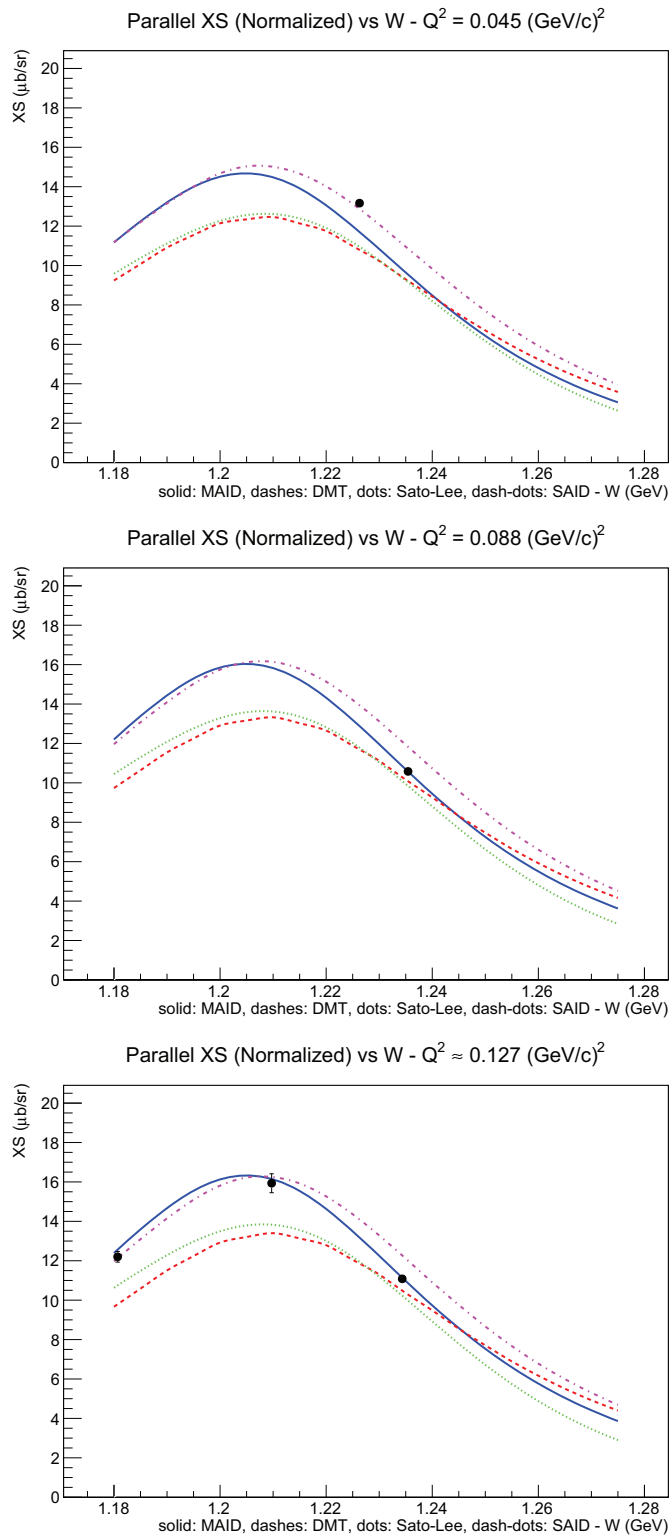
Figure 5.2: Scaled parallel cross sections as functions of W. The solid blue line represents the MAID cross sections, the red dashed line represents DMT, the green dotted line represents the Sato-Lee model, and the magenta dash-dotted line represents SAID. The Q^2 values for each plot is based on the mean value listed in the title of each, with the caveat that the Q^2 values for Kinematics 13 and 14 are slightly different. The θ and ϕ values are set to $0°$.

Figure 5.3 shows the normalized cross sections as functions of θ^*_{pq} for the parallel and "inside" kinematics, where $\phi^*_{pq} = 0°$. The top plot represents the lowest Q^2 setting, showing the results for Kinematics 1 and 2. As can be seen, Kinematic 1 again matches the SAID results, as was seen in Figures 5.1 and 5.2, but the cross section for Kinematic 2 does not match any of the models.

The middle plot shows the normalized cross sections for Kinematics 5 and 6, which both seem to match the MAID results fairly well. The bottom plot shows the results for Kinematics 8, 9, and 11. The Kinematic 8 results match the MAID plot, as expected since that was the normalization point, but the results for Kinematics 9 and 11 seem to match SAID better.

Figure 5.4 shows the normalized cross sections as functions of θ^*_{pq} for the parallel and "outside" kinematics, where $\phi^*_{pq} = 180°$. The top plot represents the lowest Q^2 settings, with Kinematics 1 and 3. As before the cross section for Kinematic 1 matches up with the SAID results, while the Kinematic 3 results appear to reside between the SAID results and the rest of the models.

The middle plot shows the results from Kinematics 5 and 7, with they both appear to match up with the MAID results. The bottom plot shows results from Kinematics 8, 10, and 12. Kinematics 8 and 12 appear to match up with MAID, while the Kinematic 10 results appear to favor the SAID cross sections.
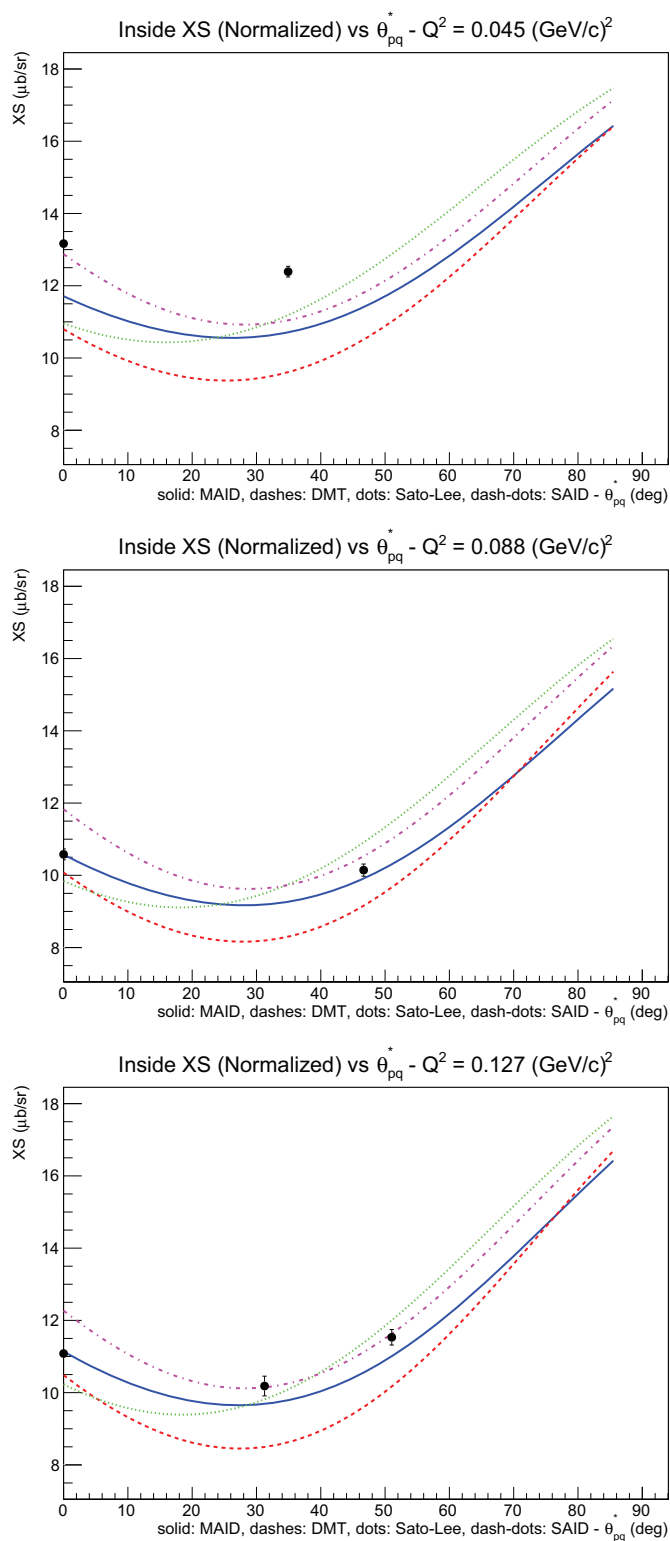
Figure 5.3: Scaled inside cross sections as functions of θ. The solid blue line represents the MAID cross sections, the red dashed line represents DMT, the green dotted line represents the Sato-Lee model, and the magenta dash-dotted line represents SAID.
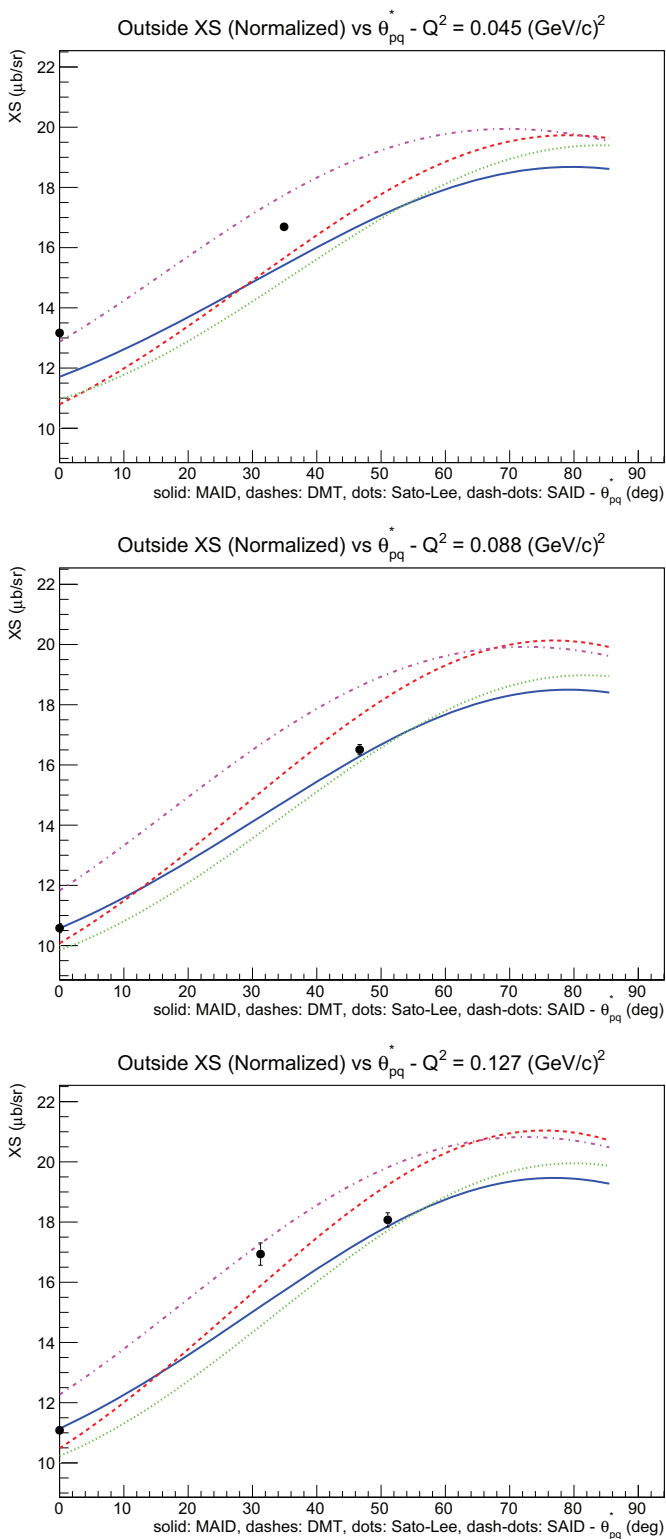
Figure 5.4: Scaled outside cross sections as functions of θ. The solid blue line represents the MAID cross sections, the red dashed line represents DMT, the green dotted line represents the Sato-Lee model, and the magenta dash-dotted line represents SAID.
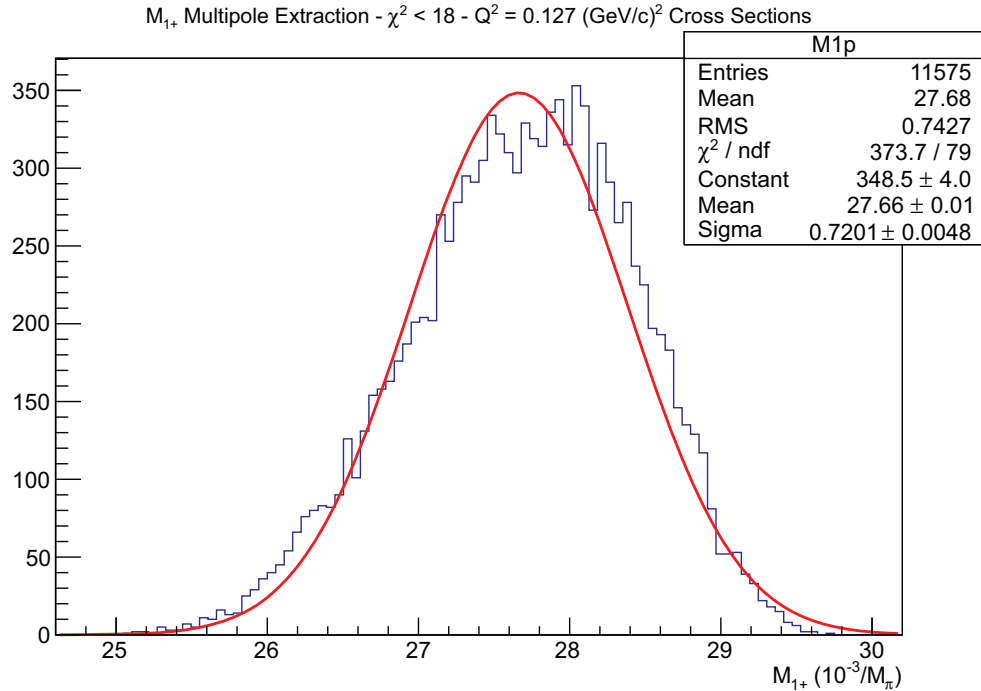
Figure 5.5: Example M_{1+} multipole fit for the $Q^2 = 0.127$ $(\mathrm{GeV}/c)^2$ group, with a χ^2 cut of 18, which left 11,575 events.

5.3   Multipole Results

Using the cross sections from the previous section, multipole values were obtained using the model-independent extraction method discussed in Section 4.6. 100 million iterations were used, with χ^2 cuts removing all but approximately 10,000 results. Multipoles from both the scaled and unscaled cross sections were examined, but only the results from the normalized cross sections are presented here.

Table 5.9 lists the results for the M_{1+} charge channel multipole, broken down into the different kinematic groups. These values are the result of a Gaussian fit on the cut data, an example of which is seen in Figure 5.5, with the error being the standard deviation of the fit. The real and imaginary parts are included as well as the absolute value. The results from the four models are also included for comparison.

These results are visualized in Figure 5.6, where the model multipoles in the region surrounding each of the points shares that point's W and Q^2 values. It would appear that the value for the largest Q^2 may contain all four model predictions within its uncertainty, though the MAID multipole is very close to the edge and its central value

	M_{1+}	M_{1+}^{real}	M_{1+}^{imag}	Uncertainty
$W = 1.226$ GeV, $Q^2 = 0.045$ $(\text{GeV}/c)^2$				
MAID	27.712	1.650	27.663	—
DMT	27.720	1.914	27.654	—
Sato-Lee	28.157	1.283	28.128	—
SAID	28.716	1.897	28.653	—
Experimental	28.885	1.720	28.820	3.2%
$W = 1.235$ GeV, $Q^2 = 0.088$ $(\text{GeV}/c)^2$				
MAID	26.691	-2.495	26.575	—
DMT	26.913	-2.266	26.817	—
Sato-Lee	27.120	-3.433	26.902	—
SAID	28.046	-2.527	27.932	—
Experimental	26.814	-2.506	26.694	3.0%
$W = 1.234$ GeV, $Q^2 = 0.127$ $(\text{GeV}/c)^2$				
MAID	26.917	-1.826	26.855	—
DMT	27.051	-1.629	27.002	—
Sato-Lee	27.342	-2.752	27.203	—
SAID	28.224	-1.878	28.161	—
Experimental	27.665	-1.877	27.596	2.6%

Table 5.9: Results for the M_{1+} multipole in $(10^{-3}/M_\pi)$, based on the normalized cross sections, with the relative standard error. The model multipoles are included for comparison.
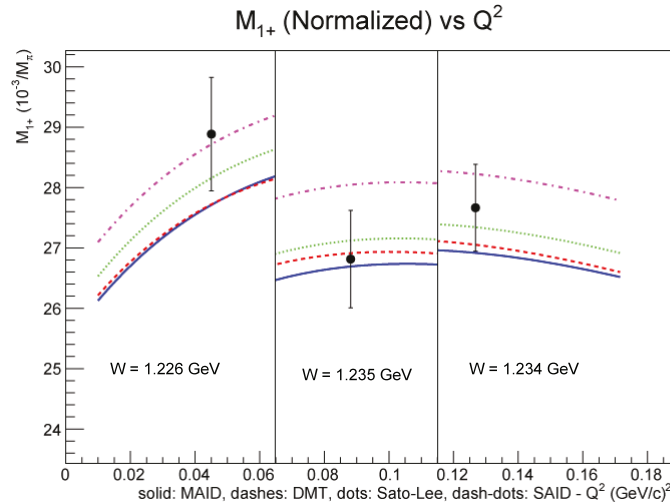
Figure 5.6: M_{1+} multipole results for the normalized cross sections. The solid blue line represents the MAID cross sections, the red dashed line represents DMT, the green dotted line represents the Sato-Lee model, and the magenta dash-dotted line represents SAID. A W value of 1.232 GeV was used for the model calculations, though the W values of the experimental results are those listed in Table 5.9.
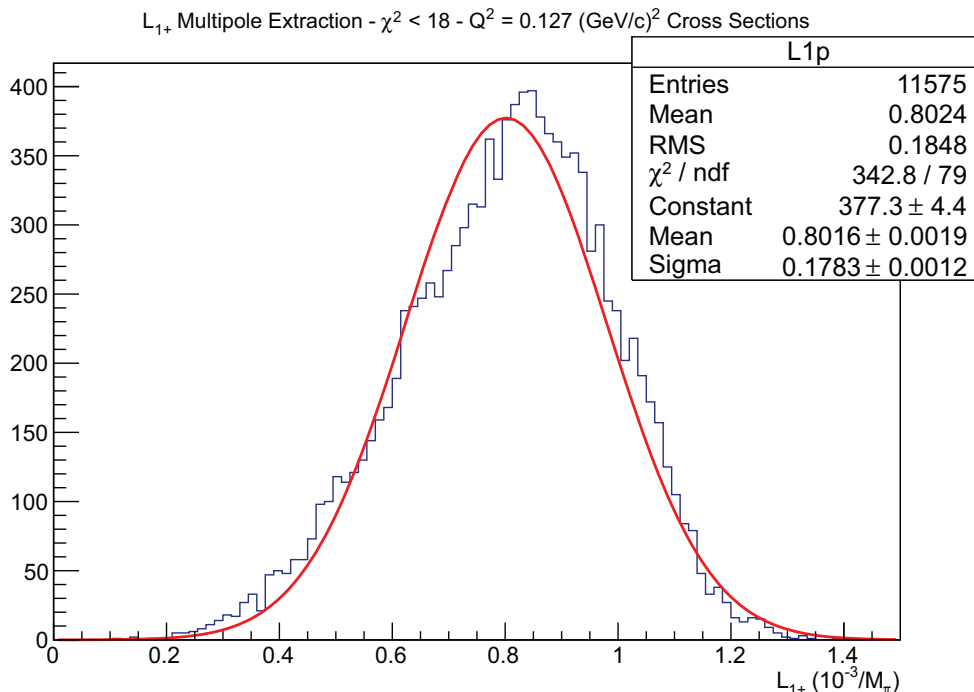
Figure 5.7: Example L_{1+} multipole fit for the $Q^2 = 0.127$ $(\text{GeV}/c)^2$ group, with a χ^2 cut of 18, which left 11,575 events.

is closest to the Sato-Lee multipole value.

The uncertainty for the middle Q^2 setting includes all but the SAID multipoles, with its central value between the DMT and MAID predictions. Like in the previous section, the lowest Q^2 value appears be very close to the SAID multipoles, though the Sato-Lee predictions are within the uncertainty.

Like the M_{1+} multipole, Table 5.10 lists the results for the L_{1+} charge channel multipole, with an example of the Gaussian fit in Figure 5.7. The non-dominance of the multipole resulted in much wider Gaussian peak and a larger error.

Figure 5.8 shows the L_{1+} multipoles as a function Q^2, once again the model multipoles surrounding the experimental data points sharing the same W and Q^2 values. The lowest Q^2 point is closest to the Sato-Lee multipole value, though the SAID value is within its uncertainty. The central Q^2 point is between the SAID and Sato-Lee values, though it contains both DMT and MAID within its uncertainty. Lastly, the highest Q^2 value is very close to the SAID prediction, with the other three models within its error.

	L_{1+}	L_{1+}^{real}	L_{1+}^{imag}	Uncertainty
$W = 1.226$ GeV, $Q^2 = 0.045$ $(\text{GeV}/c)^2$				
MAID	1.277	0.615	-1.112	—
DMT	1.363	0.608	-1.220	—
Sato-Lee	0.936	0.543	-0.762	—
SAID	1.228	0.589	-1.078	—
Experimental	0.739	0.347	-0.652	26%
$W = 1.235$ GeV, $Q^2 = 0.088$ $(\text{GeV}/c)^2$				
MAID	1.022	0.573	-0.846	—
DMT	1.151	0.592	-0.987	—
Sato-Lee	0.784	0.498	-0.605	—
SAID	0.950	0.568	-0.761	—
Experimental	0.869	0.488	-0.723	33%
$W = 1.234$ GeV, $Q^2 = 0.127$ $(\text{GeV}/c)^2$				
MAID	0.872	0.410	-0.770	—
DMT	0.981	0.429	-0.883	—
Sato-Lee	0.679	0.368	-0.571	—
SAID	0.783	0.418	-0.662	—
Experimental	0.802	0.377	-0.708	22%

Table 5.10: Results for the L_{1+} multipole in $(10^{-3}/M_\pi)$, based on the normalized cross sections, with the relative standard error. The model multipoles are included for comparison.
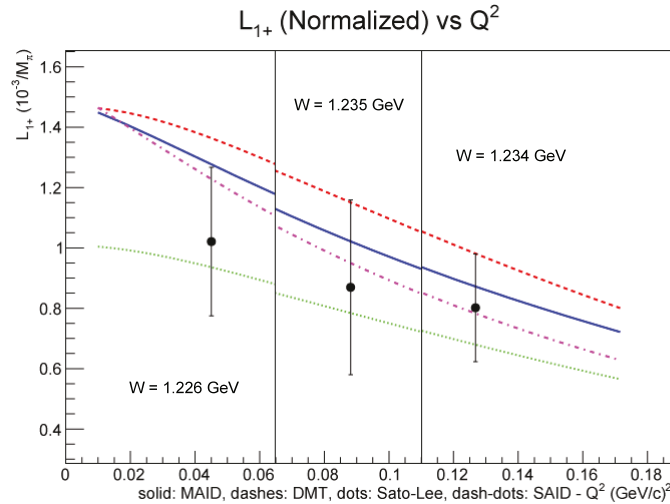
Figure 5.8: L_{1+} multipole results based on the normalized cross sections. The solid blue line represents the MAID cross sections, the red dashed line represents DMT, the green dotted line represents the Sato-Lee model, and the magenta dash-dotted line represents SAID. A W value of 1.232 GeV was used for the model calculations, though the W values of the experimental results are those listed in Table 5.10.

Attempts to extract the E_{1+} multipole were made, but the results were wildly inconsistent. While there did appear to be some sensitivity, there weren't enough observables to produce significant results. Other multipoles, such as L_{0+} and E_{0+} did not show any sensitivity.

5.4   Coulomb-to-Magnetic Ratio

The ultimate goal of this experiment was to produce the CMR values in Table 5.11, which are visualized in the plots in Figure 5.10. Produced using the M_{1+} and L_{1+}/S_{1+} multipoles from the previous section, these results could also be fit to a Gaussian curve with the standard deviation as error, as seen in Figure 5.9.
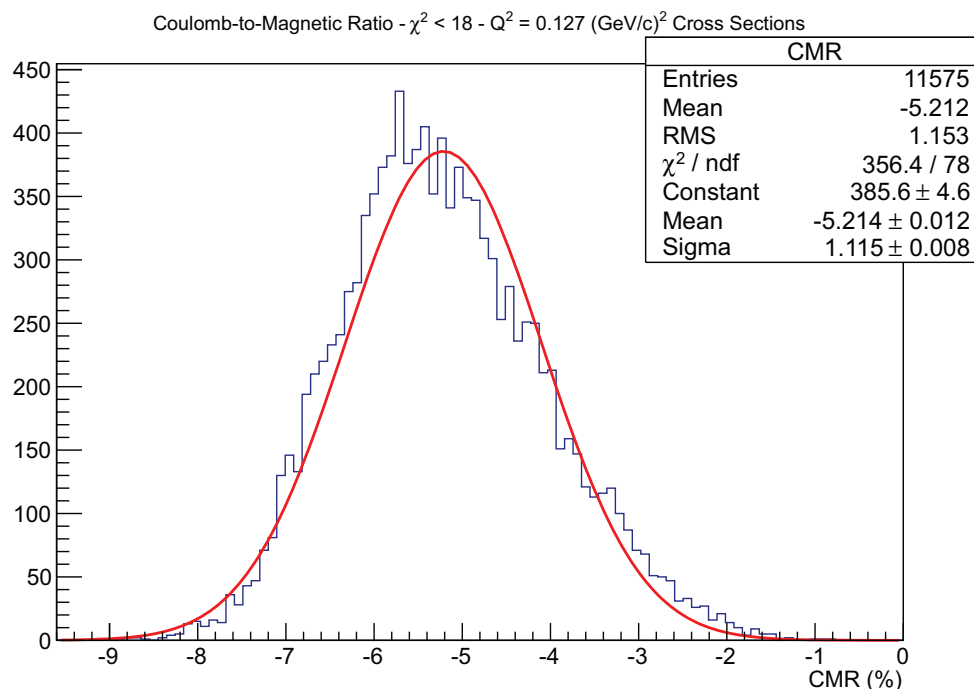
Figure 5.9: Example CMR fit for the $Q^2 = 0.127$ $(GeV/c)^2$ group, with a χ^2 cut of 18, which left 11,575 events.

Much like the L_{1+} multipoles, the error bars on these CMR values are fairly large, often encompassing multiple models, though none of the experimental uncertainties included the DMT values. The lowest Q^2 setting is closes to the Sato-Lee results, while the other two are closest to the SAID results, which appear to be relatively flat as a function of Q^2.

W (GeV)	1.226	1.235	1.234
Q^2 (GeV/c)^2	0.045	0.088	0.127
MAID (%)	-5.24	-5.55	-5.84
DMT (%)	-5.70	-6.34	-6.62
Sato-Lee (%)	-3.52	-4.04	-4.37
SAID (%)	-4.86	-4.77	-4.81
Experimental (%)	-4.02 ± 0.94	-4.66 ± 1.48	-5.21 ± 1.12

Table 5.11: CMR results using the M_{1+} and S_{1+} multipoles, based on the normalized cross sections, with the relative standard error. The central kinematic variable values and the model CMR values are included for comparison.
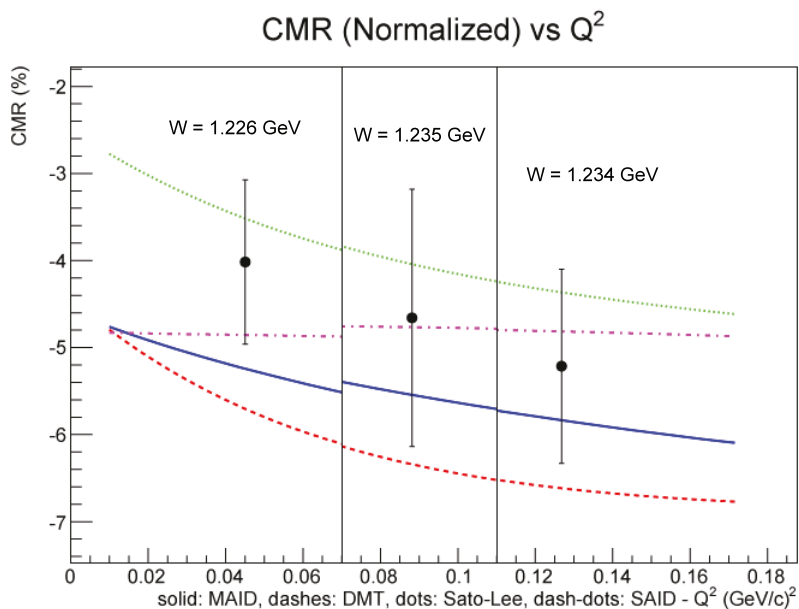
Figure 5.10: CMR results based on the normalized cross section values. The solid blue line represents the MAID cross sections, the red dashed line represents DMT, the green dotted line represents the Sato-Lee model, and the magenta dash-dotted line represents SAID. A W value of 1.232 GeV was used for the model calculations, though the W values of the experimental results are those listed in Table 5.11.
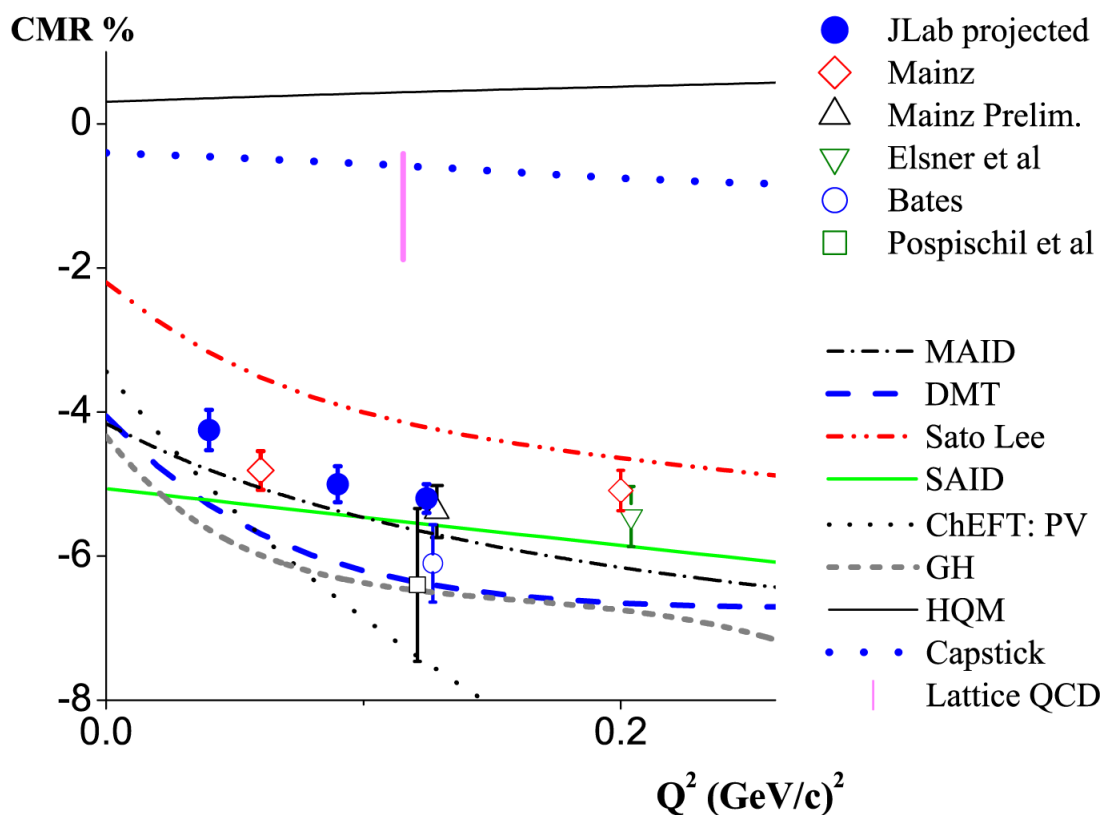
Figure 5.11: Original CMR plot from the experimental proposal, including the projected data points for this experiment [1].

5.5 Conclusions

The ultimate goal of this experiment was to produce three new CMR data points, which could be used to constrain and guide theoretical models. In the experimental proposal, Figure 5.11 was displayed, comparing the projected results from this experiment with data from other experiments and models.

Using this plot as an example, the CMR values from this analysis can be plotted along with the projected values and previous data points, producing Figure 5.12.

Comparing the projected points with the experimental results, it can be seen that the experimental results appear to be in approximately the projected locations. With regard to the Q^2 positioning, the first point is at a larger Q^2 than projected due to the higher beam energy. The second point is at a slightly lower Q^2 and the third
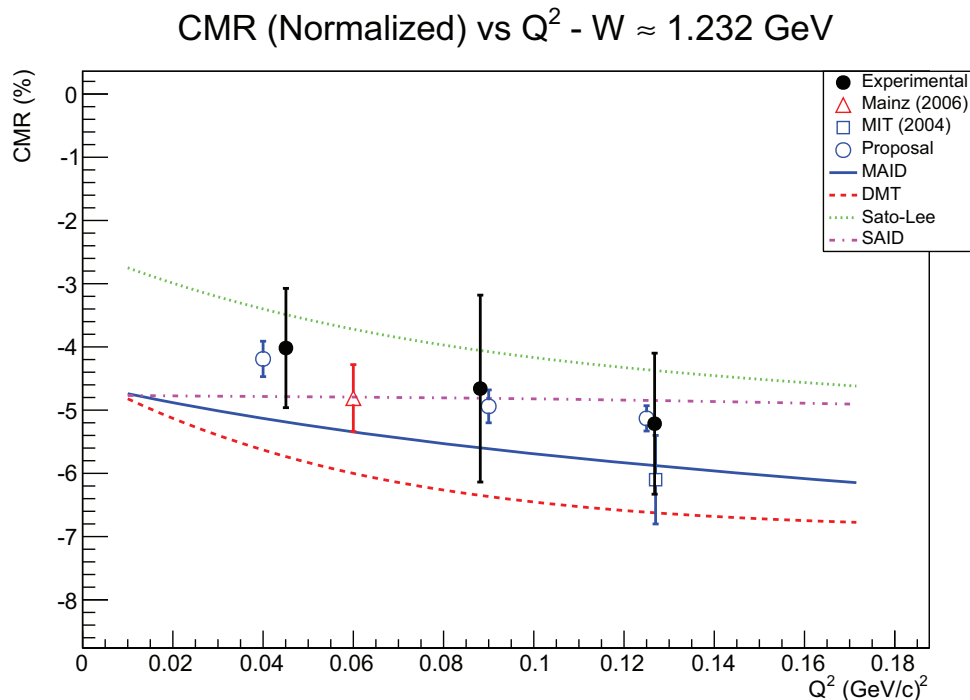
Figure 5.12: A comparison CMR plot showing the new data, in black, with the projected points from the proposal, with hollow blue circles, as well as the model predictions and the relevant data points from the Mainz and MIT experiments.

point is at a slightly larger Q^2, but this appears to be the result of limitations in the experiment.

Regarding the CMR values, the central locations of the first two points are at a slightly lower CMR than expected, while the third point is slightly higher, but the projected points all fall within the rather large error bars of the experimental data, which is something of a problem. With such large error bars, it is difficult to make any real determinations about the success or failure of any of the theoretical models, except to say that the DMT model fails for all three points.

Another question concerns the difference between the uncertainties on the projected values and those of the experimental results. That is, why are the uncertainties on the proposal's projections so much smaller than those of the results of this analysis? Is it a fault of the multipole extraction method chosen? Would using the model-dependent extraction or the truncated multipole expansion methods have resulted in smaller error bars? If not, how were the uncertainties in the proposal calculated?

While this topic cannot be further researched in this analysis, the parallel analysis at Temple University will continue to explore these questions in preparation for the published paper concerning the experiment.

Regarding the predicting ability of the models for all of the experimental results, the MAID model did quite well at predicting the parallel cross section, Figure 5.1, of the $Q^2 = 0.88$ $(\text{GeV}/c)^2$ settings, and some moderate success with the $Q^2 = 0.127$ $(\text{GeV}/c)^2$ settings, though since Kinematic 8 was normalized to the MAID cross section, that should be expected. But MAID tended to fail when comparing multipoles and the CMR, especially at the lowest Q^2 setting, which is surprising given that the multipole extraction method started with the MAID multipoles. As a test, the multipoles were extracted using the different models as starting points, and the results were not significantly different.

The DMT model fared well when compared to the experimental yields, but tended to fail at everything else, including being the only model of the four to not fall within the uncertainties of the extracted CMR values.

The Sato-Lee model also produced yields similar to the experimental results, and while the model did not do well at predicting the cross section values, it did fall within the uncertainties of the multipoles and CMR, often on the opposite side of the mean values from the other models.

Lastly, the SAID results were interesting, as while its yields were generally the largest of the models, far beyond what the experimental yields were, it did surprisingly well at matching the lowest Q^2 cross sections, as well as the M_{1+} multipole value. It also matched the L_{1+} multipoles fairly well, especially for the highest Q^2 setting. And while its CMR value looks relatively flat and did not well match the relationship between the three CMR values, its results did fall within the uncertainty of each of the experimental data points.

But none of the models did well at predicting the behavior at all three of the Q^2 settings, for cross sections, multipoles, or the CMR, which indicates that none of the models are correctly predicting the behavior of these variables, especially at low Q^2.

As the normalization of the cross sections does not affect the behavior of the cross sections relative to each other, even if a different normalization point was chosen, the relationship between the parallel cross sections in Figure 5.1 will remain the same,

and none of the models in that figure correctly match the relationship between those three points.

Likewise, looking at Figure 5.6, it can be seen that none of the four models correctly match the relationship of those points, indicating that none of the models have correctly mapped the M_{1+} multipole in the low momentum transfer region.

Clearly more work needs to be done in this region to better understand the Q^2 evolution of these values and how the pion cloud factors into the proton deformation.

Appendix A

Run List

This is the runlist for the N-Delta experiment. Though production for the experiment didn't start until February 28th, this timeline starts on the 26th and covers many of the delta scan runs that were taken at the time.

Each entry indicates the start date and time of the entry/run. Each run entry contains information about the kinematic, the target, the current, and the approximate number of events in the run. Each change in the target or configuration indicates which runs it occurs between. To the right of each entry is a comment about that entry.

A series of question marks in place of the number of events in a run indicate that the exact number of events for a particular run are unknown, usually due to an error in the run, making the data for that run unusable. Likewise, an asterisk next to an event's start time indicates that the exact start time for the event is unknown, and the time listed is merely approximate.

Date	Time	Run	Kin	Target	Current	Events	Comments
Saturday, February 26th, 2011							
02/26/11	00:14	1872	K	Empty	0 uA	54k	deadtime testing
02/26/11	00:15	Alarm on FPP HV, turned off FPP					
02/26/11	00:21	1873	K	Empty	0 uA	93k	deadtime testing
02/26/11	00:32*	1874	K	Empty	0 uA	???	junk
02/26/11	00:43*	1875	K	Empty	0 uA	???	junk
02/26/11	00:46	1876	K	Empty	0 uA	65k	deadtime testing
02/26/11	01:30	MCC said beam was ready, asked for beam permit					
02/26/11	01:58	MCC asked to send tune beam					
02/26/11	02:08	1877	K	Empty	0 uA	5.5k	optics
02/26/11	02:08	Turned off E/dE/HAND HV due to alarms					
02/26/11	02:08	T6 now LHRS+BB Coincidence (late entry)					
							Continued on next page

Date	Time	Run	Kin	Target	Current	Events	Comments
02/26/11	02:35	MCC asked to send CW beam, with no Compton					
02/26/11	02:40	5 uA beam supplied to Hall					
02/26/11	02:45	Beam back, starting sieve optics runs					
02/26/11	03:05	Low rate, asked for 10 uA					
02/26/11	03:07	Target moved from Empty to 4cm LH2 (1877/1878)					
02/26/11	03:08	1878	K	4cm LH2	10 uA	1.9k	optics
02/26/11	03:30	1879	K	4cm LH2	10 uA	280k	optics
02/26/11	03:45	Failed to do beam checks after beam recovery					
02/26/11	03:50	1880	K	4cm LH2	2 uA	8.7k	optics
02/26/11	03:50	Asked MCC for harp scan and visual check on beam dump					
02/26/11	04:00	MCC couldn't see beam at dump, probably due to bad viewer					
02/26/11	04:10	Visual check on BeO					
02/26/11	04:20	Raster off, changed beam position to 4A(-1.5,0), 4B(-3.5,2)					
02/26/11	04:30	Beam centered, checked rates					
02/26/11	04:32	1881	K	4cm LH2	5 uA	100k	optics
02/26/11	04:45	Raster returned to 2x2 (6x4 MCC)					
02/26/11	04:52	1882	K	4cm LH2	5 uA	310k	optics
02/26/11	05:00	Target moved from 4cm LH2 to 4cm LD2 (1882/1883)					
02/26/11	05:06	1883	K	4cm LD2	5 uA	260k	optics
02/26/11	05:15	Target moved from 4cm LD2 to Optics (1883/1884)					
02/26/11	05:20	1884	K	Optics	5 uA	290k	optics
02/26/11	05:39	Spectrometers changed from Kinematic K to Kinematic J (1884/1885)					
02/26/11	05:40	Target moved from Optics to 4cm LH2 (1884/1885)					
02/26/11	05:45	1885	J	4cm LH2	5 uA	56k	optics
02/26/11	05:46	1886	J	4cm LH2	2.5 uA	280k	optics
02/26/11	05:55	Target moved from 4cm LH2 to 4cm LD2 (1886/1887)					
02/26/11	05:58	1887	J	4cm LD2	2.5 uA	390k	optics
02/26/11	06:10	Target moved from 4cm LD2 to Optics (1887/1888)					
02/26/11	06:14	1888	J	Optics	2.5 uA	280k	optics
02/26/11	06:15	Energy lock switched to Hall A					
02/26/11	06:38	Spectrometers changed from Kinematic J to Kinematic I (1888/1889)					
02/26/11	06:40	Target moved from Optics to 4cm LH2 (1888/1889)					
02/26/11	06:42	1889	I	4cm LH2	2.5 uA	360k	optics
02/26/11	06:57	Target moved from 4cm LH2 to 4cm LD2 (1889/1890)					
							Continued on next page

Date	Time	Run	Kin	Target	Current	Events	Comments
02/26/11	06:59	1890	I	4cm LD2	2.5 uA	380k	optics
02/26/11	07:17	Target moved from 4cm LD2 to Optics (1890/1891)					
02/26/11	07:19	1891	I	Optics	2.5 uA	3.6k	optics
02/26/11	07:20	1892	I	Optics	2.5 uA	260k	optics
02/26/11	07:37	Target moved from Optics to BeO (1892/1893)					
02/26/11	07:39	1893	I	BeO	5 uA	130k	optics
02/26/11	07:48	Target moved from BeO to 4cm Al (1893/1894)					
02/26/11	07:51	1894	I	4cm Al	5 uA	130k	optics
02/26/11	08:27	Controlled Access: Spectrometer Work					
02/26/11	11:10	Target moved from 4cm Al to 15cm Al (1894/1895)					
02/26/11	11:12	1895	I	15cm Al	0 uA	100k	deadtime testing
02/26/11	11:20	1896	I	15cm Al	0 uA	3.0k	deadtime testing
02/26/11	11:25	1897	I	15cm Al	0 uA	2.0k	deadtime testing
02/26/11	11:29	1898	I	15cm Al	0 uA	440	deadtime testing
02/26/11	11:59	1899	I	15cm Al	0 uA	1.5k	deadtime testing
02/26/11	12:01	1900	I	15cm Al	0 uA	650	deadtime testing
02/26/11	12:05	1901	I	15cm Al	0 uA	1.3k	deadtime testing
02/26/11	12:08	1902	I	15cm Al	0 uA	1.2k	deadtime testing
02/26/11	12:10	1903	I	15cm Al	0 uA	???	deadtime testing
02/26/11	12:33	1904	I	15cm Al	0 uA	1.2k	deadtime testing
02/26/11	12:35	1905	I	15cm Al	0 uA	2.0k	deadtime testing
02/26/11	12:43	1906	I	15cm Al	0 uA	58	deadtime testing
02/26/11	12:44	1907	I	15cm Al	0 uA	620	deadtime testing
02/26/11	12:46	1908	I	15cm Al	0 uA	1.5k	deadtime testing
02/26/11	12:49	1909	I	15cm Al	0 uA	170	deadtime testing
02/26/11	12:52	1910	I	15cm Al	0 uA	770	deadtime testing
02/26/11	12:54	1911	I	15cm Al	0 uA	490	deadtime testing
02/26/11	12:56	1912	I	15cm Al	0 uA	1.4k	deadtime testing
02/26/11	13:05	1913	I	15cm Al	0 uA	3.1k	deadtime testing
02/26/11	13:13*	1914	I	15cm Al	0 uA	???	
02/26/11	13:22	1915	I	15cm Al	0 uA	???	deadtime testing
02/26/11	13:23	1916	I	15cm Al	0 uA	???	deadtime testing
02/26/11	13:30	1917	I	15cm Al	0 uA	???	deadtime testing
02/26/11	13:34	1918	I	15cm Al	0 uA	500	deadtime testing
							Continued on next page

Date	Time	Run	Kin	Target	Current	Events	Comments
02/26/11	13:35	1919	I	15cm Al	0 uA	720	deadtime testing
02/26/11	13:37	1920	I	15cm Al	0 uA	820	deadtime testing
02/26/11	14:02	1921	I	15cm Al	0 uA	560	deadtime testing
02/26/11	14:03	1922	I	15cm Al	0 uA	38k	deadtime testing
02/26/11	14:33	1923	I	15cm Al	0 uA	0	deadtime testing
02/26/11	14:39*	1924	I	15cm Al	0 uA	???	deadtime testing
02/26/11	14:45	1925	I	15cm Al	0 uA	2.8k	deadtime testing
02/26/11	14:50	1926	I	15cm Al	0 uA	1.8k	deadtime testing
02/26/11	15:02*	1927	I	15cm Al	0 uA	???	deadtime testing
02/26/11	15:15	1928	I	15cm Al	0 uA	???	deadtime testing
02/26/11	16:03	1929	I	15cm Al	0 uA	???	deadtime testing
02/26/11	16:06	1930	I	15cm Al	0 uA	???	deadtime testing
02/26/11	16:11	1931	I	15cm Al	0 uA	???	deadtime testing
02/26/11	16:16	1932	I	15cm Al	0 uA	???	deadtime testing
02/26/11	16:18	1933	I	15cm Al	0 uA	???	deadtime testing
02/26/11	16:25	1934	I	15cm Al	0 uA	???	deadtime testing
02/26/11	16:31	1935	I	15cm Al	0 uA	???	deadtime testing
02/26/11	16:34	1936	I	15cm Al	0 uA	???	deadtime testing
02/26/11	16:35	1937	I	15cm Al	0 uA	???	deadtime testing
02/26/11	16:36	1938	I	15cm Al	0 uA	???	deadtime testing
02/26/11	16:40	1939	I	15cm Al	0 uA	???	deadtime testing
02/26/11	16:45	1940	I	15cm Al	0 uA	???	deadtime testing
02/26/11	16:50	1941	I	15cm Al	0 uA	530	deadtime testing
02/26/11	16:50	RHRS moved to 14 degrees					
02/26/11	16:55	1942	I	15cm Al	0 uA		deadtime testing
02/26/11	16:58	1943	I	15cm Al	0 uA		deadtime testing
02/26/11	17:01	1944	I	15cm Al	0 uA	860	deadtime testing
02/26/11	17:03	1945	I	15cm Al	0 uA	5.4k	deadtime testing
02/26/11	17:11	1946	I	15cm Al	0 uA		deadtime testing
02/26/11	17:37	1947	I	15cm Al	0 uA	820	deadtime testing
02/26/11	17:39	EDTM disabled starting run 1948					
02/26/11	18:09	Target lost due to radcon rope					
02/26/11	19:16	1948	I	15cm Al	0 uA	700	deadtime testing
02/26/11	19:20	1949	I	15cm Al	0 uA	810	deadtime testing
							Continued on next page

Date	Time	Run	Kin	Target	Current	Events	Comments
02/26/11	19:25	1950	I	15cm Al	0 uA	???	deadtime testing
02/26/11	19:33	Target moved from 15cm Al to Empty (1950/1951)					
02/26/11	19:33	Left and Right Bogie systems repaired (mostly)					
02/26/11	19:35	1951	I	Empty	0 uA	???	deadtime testing
02/26/11	19:39	1952	I	Empty	0 uA	50	deadtime testing
02/26/11	19:45*	1953	I	Empty	0 uA	???	deadtime testing
02/26/11	19:51	1954	I	Empty	0 uA	380	deadtime testing
02/26/11	19:58	1955	I	Empty	0 uA	???	deadtime testing
02/26/11	20:06	1956	I	Empty	0 uA	???	deadtime testing
02/26/11	20:09	1957	I	Empty	0 uA	740	deadtime testing
02/26/11	20:15	1958	I	Empty	0 uA	530	deadtime testing
02/26/11	20:19	1959	I	Empty	0 uA	1.3k	deadtime testing
02/26/11	20:47	Deadtime mystery solved (incorrect)					
Sunday, February 27th, 2011							
02/27/11	12:45	Target cooldown started					
02/27/11	13:17	1960	I	Empty	0 uA	120	deadtime testing
02/27/11	13:18	1961	I	Empty	0 uA	1.3k	deadtime testing
02/27/11	13:23	1962	I	Empty	0 uA	???	deadtime testing
02/27/11	13:30	1963	I	Empty	0 uA	2.2k	deadtime testing
02/27/11	13:38	1964	I	Empty	0 uA	2.1k	deadtime testing
02/27/11	13:48	1965	I	Empty	0 uA	78	deadtime testing
02/27/11	13:50	1966	I	Empty	0 uA	1.4k	deadtime testing
02/27/11	13:58	1967	I	Empty	0 uA	51	deadtime testing
02/27/11	14:00	1968	I	Empty	0 uA	250	deadtime testing
02/27/11	14:07	$bb_ts1.crl$ modified for gating of the scalers					
02/27/11	14:50	1969	I	Empty	0 uA	93k	deadtime testing
02/27/11	15:18	1970	I	Empty	0 uA	51k	deadtime testing
02/27/11	15:33	1971	I	Empty	0 uA	31k	deadtime testing
02/27/11	15:39	1972	I	Empty	0 uA	280k	deadtime testing
02/27/11	16:36	1973	I	Empty	0 uA	18k	deadtime testing
02/27/11	16:44	1974	I	Empty	0 uA	29k	deadtime testing
02/27/11	16:58	1975	I	Empty	0 uA	15k	deadtime testing
02/27/11	17:09	1976	I	Empty	0 uA	17k	deadtime testing
02/27/11	17:13	1977	I	Empty	0 uA	4.0k	deadtime testing
							Continued on next page

Date	Time	Run	Kin	Target	Current	Events	Comments
02/27/11	17:20	1978	I	Empty	0 uA	12k	deadtime testing
02/27/11	17:23	Spectrometers changed from Kinematic I to Kinematic H (1978/1979)					
02/27/11	17:40	1979	H	Empty	0 uA	170k	deadtime testing
02/27/11	17:43	ROC8 flag added to THREEARM configuration					
02/27/11	17:47	S0 physically added to LHRS					
02/27/11	18:06	1980	H	Empty	0 uA	710	deadtime testing
02/27/11	18:16	1981	H	Empty	0 uA	280	deadtime testing
02/27/11	18:31	T6 returned to coincidence (after being set to singles)					
02/27/11	18:38	1982	H	Empty	0 uA	570k	deadtime testing
02/27/11	18:40	SIS3800 scaler in ROC5					
02/27/11	19:01	1983	H	Empty	0 uA	720k	deadtime testing
02/27/11	19:32	1984	H	Empty	0 uA	???	deadtime testing
02/27/11	19:42	1985	H	Empty	0 uA	8.5k	deadtime testing
02/27/11	19:50	1986	H	Empty	0 uA	120k	deadtime testing
02/27/11	20:11	HAND scalers enabled in ROC8					
02/27/11	20:14	Preshower 16R fixed, 19R not fixed					
02/27/11	20:32	S0 connected to T4 (incorrectly)					
02/27/11	21:15	MCC can deliver beam					
02/27/11	22:00	Harp scan requested					
02/27/11	22:59	Harp scan in progress					
02/27/11	23:21	Scaler map minor update (S0 AND, left arm)					
02/27/11	23:36	bbts1 server fixed					
Monday, February 28th, 2011							
02/28/11	01:00	Beam position correction requested					
02/28/11	01:00	Harp scan too big, unable to get smaller					
02/28/11	01:05	HAND HV off					
02/28/11	01:19	Target moved from Empty to BeO (1986/1987)					
02/28/11	01:21	1987	H	BeO	5 uA	180k	spot++
02/28/11	01:30	Target moved from BeO to 15cm Al (1987/1988)					
02/28/11	01:33	1988	H	15cm Al	5 uA	32k	test run for rates
02/28/11	01:35	1989	H	15cm Al	5 uA	180k	optics
02/28/11	01:42	Spectrometers changed from Kinematic H to Kinematic G (1989/1990)					
02/28/11	01:45	Target moved from 15cm Al to 4cm LH2 (1989/1990)					
02/28/11	01:47	1990	G	4cm LH2	2.5 uA	410k	optics
							Continued on next page

Date	Time	Run	Kin	Target	Current	Events	Comments
02/28/11	01:55	1991	G	4cm LH2	2.5 uA	500k	optics
02/28/11	02:10	Target moved from 4cm LH2 to 4cm LD2 (1991/1992)					
02/28/11	02:12	1992	G	4cm LD2	2.5 uA	510k	optics
02/28/11	02:23	1993	G	4cm LD2	2.5 uA	500k	optics
02/28/11	02:40	Target moved from 4cm LD2 to Optics (1993/1994)					
02/28/11	02:44	1994	G	Optics	5 uA	???	optics
02/28/11	02:55	1995	G	Optics	5 uA	520k	optics
02/28/11	02:57	Spectrometers changed from Kinematic G to Kinematic F (1994/1996)					
02/28/11	03:15	Target moved from Optics to 4cm LH2 (1995/1996)					
02/28/11	03:17	1996	F	4cm LH2	5 uA	190k	BB HV scan
02/28/11	03:20	1997	F	4cm LH2	5 uA	7.7k	BB HV scan
02/28/11	03:21	1998	F	4cm LH2	5 uA	200k	BB HV scan
02/28/11	03:25	1999	F	4cm LH2	5 uA	200k	BB HV scan
02/28/11	03:30	2000	F	4cm LH2	5 uA	200k	BB HV scan
02/28/11	03:34	2001	F	4cm LH2	5 uA	200k	BB HV scan
02/28/11	03:38	2002	F	4cm LH2	5 uA	200k	BB HV scan
02/28/11	03:42	2003	F	4cm LH2	5 uA	280k	optics
02/28/11	03:50	Target moved from 4cm LH2 to 4cm LD2 (2003/2004)					
02/28/11	03:52	2004	F	4cm LD2	5 uA	260k	optics
02/28/11	04:00	Target moved from 4cm LD2 to Optics (2004/2005)					
02/28/11	04:06	2005	F	Optics	5 uA	260k	optics
02/28/11	04:18	2006	F	Optics	5 uA	260k	optics
02/28/11	04:27	Target moved from Optics to 4cm LD2 (2006/2007)					
02/28/11	04:30	Removed left arm sieve					
02/28/11	04:31	2007	F	4cm LD2	5 uA	310k	optics
02/28/11	04:38	Target moved from 4cm LD2 to 4cm LH2 (2007/2008)					
02/28/11	04:41	2008	F	4cm LH2	5 uA	250k	optics
02/28/11	04:48	2009	E	4cm LH2	5 uA	510k	optics
02/28/11	04:48	Spectrometers changed from Kinematic F to Kinematic E (2008/2009)					
02/28/11	04:56	FPP HV channel trip					
02/28/11	04:58	2010	E	4cm LH2	5 uA	510k	optics
02/28/11	05:10	Target moved from 4cm LH2 to 4cm LD2 (2010/2011)					
02/28/11	05:13	2011	E	4cm LD2	5 uA	510k	optics
02/28/11	05:23	2012	E	4cm LD2	5 uA	510k	optics
							Continued on next page

Date	Time	Run	Kin	Target	Current	Events	Comments
02/28/11	05:37	Target moved from 4cm LD2 to Optics (2012/2013)					
02/28/11	05:40	2013	E	Optics	5 uA	500k	optics
02/28/11	05:53	Target moved from Optics to 15cm Al (2013/2014)					
02/28/11	05:55	2014	E	15cm Al	5 uA	530k	optics
02/28/11	06:06	Target moved from 15cm Al to 4cm Al (2014/2015)					
02/28/11	06:08	2015	E	4cm Al	5 uA	510k	optics
02/28/11	06:22	Target moved from 4cm Al BeO (2015/2016)					
02/28/11	06:26	2016	E	BeO	5 uA	520k	optics
02/28/11	06:40	2017	E	BeO	10 uA	110k	optics
02/28/11	06:46	Target moved from BeO to 4cm Al (2017/2018)					
02/28/11	06:48	2018	E	4cm Al	10 uA	230k	optics
02/28/11	06:55	Target moved from 4cm Al to 15cm Al (2018/2019)					
02/28/11	06:57	2019	E	15cm Al	10 uA	260k	optics
02/28/11	07:01	Target moved from 15cm Al to Optics (2019/2020)					
02/28/11	07:03	2020	E	Optics	10 uA	110k	optics
02/28/11	07:09	Target moved from Optics to 4cm LH2 (2020/2021)					
02/28/11	07:12	2021	E	4cm LH2	5 uA	110k	optics
02/28/11	07:15	Target moved from 4cm LH2 to 4cm LD2 (2021/2022)					
02/28/11	07:17	2022	E	4cm LD2	5 uA	400k	optics
02/28/11	07:25	Target moved from 4cm LD2 to 4cm LH2 (2022/2023)					
02/28/11	07:27	2023	E	4cm LH2	5 uA	210k	optics
02/28/11	07:35	Target moved from 4cm LH2 to Optics (2023/2024)					
02/28/11	07:37	2024	E	Optics	5 uA	220k	optics
02/28/11	07:43	Spectrometers changed from Kinematic E to Kinematic D (2024/2025)					
02/28/11	08:09	2025	D	Optics	10 uA	320k	junk
02/28/11	08:10	RHRS dipole regulation lost					
02/28/11	08:14	2026	D	Optics	10 uA	440k	optics
02/28/11	08:26	Target moved from Optics to 15cm Al (2026/2027)					
02/28/11	08:30	2027	D	15cm Al	10 uA	280k	optics
02/28/11	08:39	Target moved from 15cm Al to 4cm Al (2027/2028)					
02/28/11	08:41	2028	D	4cm Al	10 uA	270k	optics
02/28/11	08:52	Target moved from 4cm Al to BeO (2028/2029)					
02/28/11	08:55	2029	D	BeO	10 uA	260k	optics
02/28/11	09:04	2030	D	BeO	10 uA	310k	optics
							Continued on next page

Date	Time	Run	Kin	Target	Current	Events	Comments
02/28/11	09:12	Target moved from BeO to 4cm Al (2030/2031)					
02/28/11	09:14	2031	D	4cm Al	10 uA	260k	optics
02/28/11	09:22	Target moved from 4cm Al to 15cm Al (2031/2032)					
02/28/11	09:24	2032	D	15cm Al	10 uA	260k	optics
02/28/11	09:35	Target moved from 15cm Al to 4cm LH2 (2032/2033)					
02/28/11	09:37	2033	D	4cm LH2	10 uA	570k	optics
02/28/11	09:52	Target moved from 4cm LH2 4cm LD2 (2033/2034)					
02/28/11	09:54	2034	D	4cm LD2	10 uA	???	junk
02/28/11	09:58	2035	D	4cm LD2	10 uA	520k	optics
02/28/11	10:11	Spectrometers changed from Kinematic D to Kinematic C (2035/2036)					
02/28/11	10:28	LHRS bogie control rebooted					
02/28/11	10:33	2036	C	4cm LD2	10 uA	570k	optics
02/28/11	10:50	Target moved from 4cm LD2 to 4cm LH2 (2036/2037)					
02/28/11	10:53	2037	C	4cm LH2	10 uA	530k	optics
02/28/11	10:56	RHRS dipole trip					
02/28/11	11:10	Target moved from 4cm LH2 to Optics (2037/2038)					
02/28/11	11:14	2038	C	Optics	10 uA	520k	optics
02/28/11	11:27	Target moved from Optics to Empty (2041/2042)					
02/28/11	11:32	2039	C	Optics	10 uA	14k	short run
02/28/11	11:33	2040	C	Optics	10 uA	40	CHL tripped
02/28/11	11:37	Spectrometers changed from Kinematic C to Kinematic B (2040/2042)					
02/28/11	11:44	CHL trip					
02/28/11	11:53	Move to controlled access, full survey					
02/28/11	11:54	Ramping down LHRS magnets for polarity flip					
02/28/11	12:20	LHRS magnets at zero					
02/28/11	12:30	Hall in controlled access					
02/28/11	13:24	2041	X	Optics	0 uA	78k	cosmics
02/28/11	13:29	2042	B	Empty	0 uA	17k	cosmics
02/28/11	13:50	2043	B	Empty	0 uA	???	cosmics
02/28/11	13:58	2044	B	Empty	0 uA	14k	cosmics
02/28/11	14:18	2045	B	Empty	0 uA	???	cosmics
02/28/11	14:20	Spectrometers changed from Kinematic B to Kinematic A (2045/2047)					
02/28/11	14:20	LHRS dipole polarity changed to positive polarity					
02/28/11	14:36	Lead flows on RHRS dipole turned down due to icing					
							Continued on next page

Date	Time	Run	Kin	Target	Current	Events	Comments
02/28/11	14:38*	2046	X	Empty	0 uA	???	cosmics
02/28/11	14:48	ROC3 slot 22 added to read-out					
02/28/11	14:58	2047	A	Empty	0 uA	7.4k	cosmics
02/28/11	15:04	2048	A	Empty	0 uA	5.4k	cosmics
02/28/11	15:07	RHRS BPM connection loosened					
02/28/11	15:10	2049	A	Empty	0 uA	???	cosmics
02/28/11	15:12	Spectrometers changed from Kinematic A to Kinematic 1 (2049/2050)					
02/28/11	15:48	Update of HRS detectors, new database created					
02/28/11	15:57	T6 changed back to singles					
02/28/11	15:57	2050	1	Empty	0 uA	760	cosmics
02/28/11	16:00	Back to beam permit					
02/28/11	16:01	2051	1	Empty	0 uA	49k	cosmics
02/28/11	16:08	Database change summary					
02/28/11	16:17	2052	1	Empty	1.5 uA	540k	cosmics
02/28/11	16:23	N-Delta timing setup ready					
02/28/11	16:27	DVCSTLAB3 scope setup					
02/28/11	16:28	2053	1	Empty	5 uA	3.5k	calibration
02/28/11	16:38	Beam recovery					
02/28/11	16:40	Target moved from Empty to 4cm LH2 (2053/2054)					
02/28/11	16:43	2054	1	4cm LH2	50 uA	870k	production
02/28/11	16:51	Scope trace for T5					
02/28/11	16:53	2055	1	4cm LH2	50 uA	290k	production
02/28/11	16:56	2056	1	4cm LH2	30 uA	76k	production
02/28/11	17:00	2057	1	4cm LH2	20 uA	180k	production
02/28/11	17:05	Configuration chagned to dThreshold-2Arm					
02/28/11	17:07	2058	1	4cm LH2	20 uA	230k	production
02/28/11	17:12	2059	1	4cm LH2	15 uA	1.0M	production
02/28/11	17:28	Deadtime for kinematic 1 update					
02/28/11	17:47	2060	1	4cm LH2	15 uA	1.4M	production
02/28/11	18:13	Coincidence time spectra					
02/28/11	18:33	2061	1	4cm LH2	15 uA	1.4M	production
02/28/11	18:50	Missing mass spectra					
02/28/11	18:55	All FPP chamber HVs ramped to 0 due to lack of CO2					
02/28/11	19:00	Blip in LHRS HV chassis 7					
							Continued on next page

Date	Time	Run	Kin	Target	Current	Events	Comments
02/28/11	19:06	Coincidence time spectra with EDTM location					
02/28/11	19:19	2062	1	4cm LH2	15 uA	1.3M	production
02/28/11	19:36	CO2 canister empty and replaced					
02/28/11	19:46	RHRS EDTM delay changed (2061/2062)					
02/28/11	19:49	RHRS VDC show multipeaks					
02/28/11	20:03	RHRS dp structure related to S2					
02/28/11	20:04	2063	1	4cm LH2	15 uA	850k	production
02/28/11	20:36	2064	1	4cm LH2	15 uA	1.3M	production
02/28/11	21:20	2065	1	4cm LH2	15 uA	610k	production
02/28/11	21:45	Escorted access taken to disconnect RHRS S2 from trigger					
02/28/11	22:53	Beam requested					
02/28/11	23:15	2066	1	4cm LH2	15 uA	1.8M	production
02/28/11	23:15	Problem with RHRS S2 logic units detected					
02/28/11	23:38	RHRS VDC multipeaks disappear after removal of S2					
02/28/11	23:49	2067	1	4cm LH2	15 uA	1.3M	production
Tuesday, March 1st, 2011							
03/01/11	00:20	Controlled access to replace RHRS S2 logic module					
03/01/11	01:10	Returned to beam permit					
03/01/11	01:14	Replaced 758 logic unit for RHRS S2m odd bars, put S2M back into T1					
03/01/11	01:32	2068	1	4cm LH2	15 uA	82k	test run
03/01/11	01:36	2069	1	4cm LH2	30 uA	1.6M	test run
03/01/11	01:44	RHRS VDC multipeak issue resolved					
03/01/11	02:05	2070	1	4cm LH2	15 uA	8.3k	incorrect prescales
03/01/11	02:07	2071	1	4cm LH2	15 uA	1.1M	production
03/01/11	02:29	2072	1	4cm LH2	15 uA	1.5M	production
03/01/11	03:00	2073	1	4cm LH2	15 uA	1.7M	production
03/01/11	03:32	2074	1	4cm LH2	15 uA	1.5M	production
03/01/11	04:02	2075	1	4cm LH2	15 uA	1.4M	production
03/01/11	04:35	Target moved from 4cm LH2 to 4cm Al (2075/2076)					
03/01/11	04:37	2076	1	4cm Al	15 uA	1.6M	dummy run
03/01/11	05:40	Target moved from 4cm Al to BeO (2076/2077)					
03/01/11	05:43	2077	1	BeO	15 uA	76k	optics run
03/01/11	05:55	Target moved from BeO to 4cm LH2 (2077/2078)					
03/01/11	05:58	2078	1	4cm LH2	15 uA	1.6M	production
							Continued on next page

Date	Time	Run	Kin	Target	Current	Events	Comments
03/01/11	06:29	2079	1	4cm LH2	15 uA	1.3M	production
03/01/11	07:00	2080	1	4cm LH2	15 uA	1.6M	production
03/01/11	07:30	2081	1	4cm LH2	15 uA	1.5M	production
03/01/11	08:01	2082	1	4cm LH2	15 uA	1.6M	production
03/01/11	08:33	2083	1	4cm LH2	15 uA	1.5M	production
03/01/11	10:03	Switch to buffered mode					
03/01/11	10:30	Target moved from 4cm LH2 to Empty (2083/2084)					
03/01/11	10:33	2084	1	Empty	0 uA	12k	beam studies
03/01/11	10:44	2085	1	Empty	0 uA	11k	beam studies
03/01/11	10:45	sfi2.crl modified					
03/01/11	10:53	Spectrometers changed from Kinematic 1 to Kinematic 2 (2085/2086)					
03/01/11	10:54	2086	2	Empty	0 uA	94k	beam studies
03/01/11	11:31*	2087	2	Empty	0 uA	???	beam studies
03/01/11	11:59	Change to ROC1 and ROC2 crl					
03/01/11	12:08	2088	2	Empty	0 uA	56k	beam studies
03/01/11	12:20*	2089	2	Empty	0 uA	???	beam studies
03/01/11	12:22	Another change to ROC1 and ROC2 crl					
03/01/11	12:33*	2090	2	Empty	0 uA	???	beam studies
03/01/11	12:34	Target is warming due to ESR problems					
03/01/11	12:35	One further change to ROC1 and ROC2 crl					
03/01/11	12:36	2091	2	Empty	0 uA	3.8k	beam studies
03/01/11	12:38	Lost both HRS magnets					
03/01/11	12:41	2092	2	Empty	0 uA	3.0k	beam studies
03/01/11	12:44	2093	2	Empty	0 uA	3.5k	beam studies
03/01/11	12:50	2094	2	Empty	0 uA	54k	beam studies
03/01/11	12:52	Cryo back to normal					
03/01/11	12:55	2095	2	Empty	0 uA	56k	beam studies
03/01/11	13:04*	2096	2	Empty	0 uA	???	beam studies
03/01/11	13:14	2097	2	Empty	0 uA	41k	beam studies
03/01/11	13:15	Pedestal issue with ROC1/2, CRL code modified					
03/01/11	13:17	2098	2	Empty	0 uA	1.3k	beam studies
03/01/11	13:24	ROC1/2 CRL code changed back					
03/01/11	13:25	2099	2	Empty	0 uA	23k	beam studies
03/01/11	13:36	Major revision to CRL code for ROC1/2					
							Continued on next page

Date	Time	Run	Kin	Target	Current	Events	Comments
03/01/11	13:43	2100	2	Empty	0 uA	3.5k	beam studies
03/01/11	13:49	2101	2	Empty	0 uA	1.8k	beam studies
03/01/11	13:51	2102	2	Empty	0 uA	14k	beam studies
03/01/11	14:09*	2103	2	Empty	0 uA	???	beam studies
03/01/11	14:27	2104	2	Empty	0 uA	53k	beam studies
03/01/11	14:35	Widths changed on T1 and T3					
03/01/11	14:37	T1 delay changed to 32 ns					
03/01/11	15:07	New configuration, BBTS1 crl code changed					
03/01/11	15:12	2105	2	Empty	0 uA	4.8k	beam studies
03/01/11	15:18	New configuration (B2ArmNTS11) changes, $ts_scaler_Left.crl$ changed					
03/01/11	15:35	ROC1/2 CRL reverted again					
03/01/11	16:16	Harp scan results					
03/01/11	16:20	Target moved from Empty to BeO (2105/2106)					
03/01/11	16:26	2106	2	BeO	5 uA	2.1M	spot++
03/01/11	16:39*	2107	2	4cm LH2	15 uA	???	deadtime testing
03/01/11	16:40	Deadtime studies					
03/01/11	16:42	Target moved from BeO to 4cm LH2 (2106/2107)					
03/01/11	16:52	2108	2	4cm LH2	15 uA	37k	deadtime testing
03/01/11	16:56	2109	2	4cm LH2	15 uA	36k	deadtime testing
03/01/11	16:59	2110	2	4cm LH2	15 uA	67k	deadtime testing
03/01/11	17:02	2111	2	4cm LH2	15 uA	67k	deadtime testing
03/01/11	17:04	2112	2	4cm LH2	15 uA	76k	deadtime testing
03/01/11	17:07	2113	2	4cm LH2	15 uA	54k	deadtime testing
03/01/11	17:09	2114	2	4cm LH2	15 uA	120k	deadtime testing
03/01/11	17:18	2115	2	4cm LH2	15 uA	120k	production
03/01/11	17:22	2116	2	4cm LH2	15 uA	1.3M	production
03/01/11	17:56	2117	2	4cm LH2	15 uA	1.0M	production
03/01/11	18:22	2118	2	4cm LH2	15 uA	1.0M	production
03/01/11	18:47	2119	2	4cm LH2	15 uA	1.0M	production
03/01/11	19:15	2120	2	4cm LH2	15 uA	1.1M	deadtime testing
03/01/11	19:19	2121	2	4cm LH2	15 uA	???	deadtime testing
03/01/11	19:21	2122	2	4cm LH2	15 uA	???	deadtime testing
03/01/11	19:24	2123	2	4cm LH2	15 uA	???	deadtime testing
03/01/11	19:30	2124	2	4cm LH2	15 uA	???	deadtime testing
							Continued on next page

Date	Time	Run	Kin	Target	Current	Events	Comments
03/01/11	19:36	2125	2	4cm LH2	15 uA	???	deadtime testing
03/01/11	19:46*	2126	2	4cm LH2	15 uA	???	DAQ crash
03/01/11	19:57	2127	2	4cm LH2	15 uA	450k	test run
03/01/11	20:12	2128	2	4cm LH2	15 uA	200k	test run
03/01/11	20:17	Deadtime tests results					
03/01/11	20:18	2129	2	4cm LH2	15 uA	760k	test run
03/01/11	20:36	2130	2	4cm LH2	15 uA	470k	test run
03/01/11	20:37	Trigger timing crl code changes					
03/01/11	20:50	2131	2	4cm LH2	15 uA	800k	test run
03/01/11	21:08	Controlled access to fix coincidence window					
03/01/11	21:28	Back to beam permit					
03/01/11	21:29	Width on T3 window changed					
03/01/11	21:49	2132	2	4cm LH2	15 uA	55k	test run
03/01/11	21:50	Beam back					
03/01/11	21:53	2133	2	4cm LH2	15 uA	???	junk
03/01/11	21:54	2134	2	4cm LH2	15 uA	1.0M	test run
03/01/11	22:12	2135	2	4cm LH2	15 uA	???	junk
03/01/11	22:14	2136	2	4cm LH2	15 uA	???	junk
03/01/11	22:21*	2137	2	4cm LH2	15 uA	???	junk
03/01/11	22:28	2138	2	4cm LH2	15 uA	???	junk
03/01/11	22:33	2139	2	4cm LH2	15 uA	???	junk
03/01/11	22:39	2140	2	4cm LH2	15 uA	490k	test run
03/01/11	22:55	2141	2	4cm LH2	30 uA	160k	test run
03/01/11	22:58	2142	2	4cm LH2	30 uA	900k	test run
03/01/11	23:11	2143	2	4cm LH2	15 uA	440k	test run
03/01/11	23:21	Escorted access to fix coincidence window again					
03/01/11	23:42	Back to beam permit					
03/01/11	23:45	Coincidence timing spectra					
03/01/11	23:53	Width on T3 window reduced to 70 ns					
03/01/11	23:55	Beam back again					
03/01/11	23:58	2144	2	4cm LH2	15 uA	490k	test run
Wednesday, March 2nd, 2011							
03/02/11	00:01	Test timer library changed					
03/02/11	00:10	2145	2	4cm LH2	15 uA	1.0M	test run?
							Continued on next page

Date	Time	Run	Kin	Target	Current	Events	Comments
03/02/11	00:35	2146	2	4cm LH2	15 uA	1.0M	production
03/02/11	00:48	LHRS VDC HV increased by 1% (to stop alarms)					
03/02/11	00:59	2147	2	4cm LH2	15 uA	1.0M	production
03/02/11	01:27	Target moved from 4cm LH2 to BeO (2147/2148)					
03/02/11	01:30	2148	2	BeO	0.5 uA	???	junk
03/02/11	01:32	2149	2	BeO	0.5 uA	230k	spot++
03/02/11	01:36	2150	2	BeO	0.5 uA	290k	spot++
03/02/11	01:41	2151	2	BeO	0.5 uA	150k	spot++
03/02/11	01:54	2152	2	BeO	15 uA	64k	optics
03/02/11	02:02	Target moved from BeO to 4cm Al (2152/2153)					
03/02/11	02:05	2153	2	4cm Al	15 uA	1.0M	dummy run
03/02/11	03:05	Target moved from 4cm Al to 4cm LH2 (2153/2154)					
03/02/11	03:07	2154	2	4cm LH2	15 uA	???	CODA crashed
03/02/11	03:14	2155	2	4cm LH2	15 uA	1.0M	production
03/02/11	03:38	2156	2	4cm LH2	15 uA	1.0M	production
03/02/11	04:02	2157	2	4cm LH2	15 uA	1.0M	production
03/02/11	04:26	2158	2	4cm LH2	15 uA	1.0M	production
03/02/11	04:49	2159	2	4cm LH2	15 uA	1.0M	production
03/02/11	05:12	2160	2	4cm LH2	15 uA	1.0M	production
03/02/11	05:35	2161	2	4cm LH2	15 uA	1.0M	production
03/02/11	05:58	2162	2	4cm LH2	15 uA	1.0M	production
03/02/11	06:24	2163	2	4cm LH2	15 uA	1.1M	production
03/02/11	06:48	2164	2	4cm LH2	15 uA	1.0M	QE run at start
03/02/11	07:15	2165	2	4cm LH2	15 uA	1.0M	production
03/02/11	07:39	2166	2	4cm LH2	15 uA	1.0M	production
03/02/11	08:04	2167	2	4cm LH2	15 uA	1.1M	production
03/02/11	08:31	2168	2	4cm LH2	15 uA	1.1M	production
03/02/11	08:57	2169	2	4cm LH2	15 uA	???	junk
03/02/11	09:09	2170	2	4cm LH2	15 uA	1.0M	production
03/02/11	09:33	2171	2	4cm LH2	15 uA	1.0M	production
03/02/11	09:57	2172	2	4cm LH2	15 uA	990k	production
03/02/11	10:20	2173	2	4cm LH2	15 uA	480k	production
03/02/11	10:22	DAQ deadtime theory (incorrect again), crl code changed					
03/02/11	10:32	2174	2	4cm LH2	15 uA	74k	junk
							Continued on next page

Date	Time	Run	Kin	Target	Current	Events	Comments
03/02/11	10:36	2175	2	4cm LH2	15 uA	1.0M	production
03/02/11	11:00	2176	2	4cm LH2	15 uA	1.0M	production
03/02/11	11:24	2177	2	4cm LH2	15 uA	1.0M	production
03/02/11	11:38	Target computer reboot					
03/02/11	11:42	FPP HV briefly turned off to check deadtime					
03/02/11	11:49	2178	2	4cm LH2	15 uA	27k	junk
03/02/11	11:51	2179	2	4cm LH2	15 uA	361k	junk
03/02/11	12:02	2180	2	4cm LH2	15 uA	760k	production
03/02/11	12:04	adaql2 system check to check deadtime					
03/02/11	12:07	RHRS Pedestal suppression to check deadtime (2179)					
03/02/11	12:14	Pedestal supression off deadtime theory (incorrect again)					
03/02/11	12:23	2181	2	4cm LH2	15 uA	1.0M	production
03/02/11	12:49	2182	2	4cm LH2	15 uA	1.0M	production
03/02/11	13:15	2183	2	4cm LH2	15 uA	1.0M	production
03/02/11	13:39	2184	2	4cm LH2	15 uA	???	junk
03/02/11	13:43	2185	2	4cm LH2	15 uA	1.0M	production
03/02/11	14:06*	2186	2	4cm LH2	15 uA	???	junk
03/02/11	14:30*	2187	2	4cm LH2	15 uA	???	junk
03/02/11	14:33*	2188	2	4cm LH2	15 uA	???	junk
03/02/11	14:36*	2189	2	4cm LH2	15 uA	???	junk
03/02/11	14:39	2190	2	4cm LH2	15 uA	83k	stopped early
03/02/11	14:46	Beam down					
03/02/11	15:10	Beam back					
03/02/11	15:11	2191	2	4cm LH2	15 uA	1.0M	production
03/02/11	15:34	2192	2	4cm LH2	15 uA	560k	production
03/02/11	15:52	2193	2	4cm LH2	15 uA	21k	junk
03/02/11	15:55	ROC3 error message, ROC3 power cycled					
03/02/11	15:57	2194	2	4cm LH2	15 uA	1.0M	production
03/02/11	16:27	2195	2	4cm LH2	15 uA	???	junk
03/02/11	16:36	2196	2	4cm LH2	15 uA	???	junk
03/02/11	16:39	2197	2	4cm LH2	15 uA	1.0M	production
03/02/11	17:09	2198	2	4cm LH2	15 uA	1.0M	production
03/02/11	17:19	New CODA config unbuffered (UB2ArmNTS11)					
03/02/11	17:33	2199	2	4cm LH2	15 uA	260k	production
							Continued on next page

Date	Time	Run	Kin	Target	Current	Events	Comments
03/02/11	17:35	RHRS Cherenkov #1 HV increase (2200)					
03/02/11	17:35	Switch to unbuffered DAQ (2198)					
03/02/11	17:39	2200	2	4cm LH2	15 uA	1.0M	production
03/02/11	18:01	Deadtime (crl) code added to ROCs 1-4					
03/02/11	18:02	2201	2	4cm LH2	15 uA	840k	production
03/02/11	18:22	2202	2	4cm LH2	15 uA	1.0M	production
03/02/11	18:47	2203	2	4cm LH2	15 uA	1.0M	production
03/02/11	19:10	2204	2	4cm LH2	15 uA	1.0M	production
03/02/11	19:34	2205	2	4cm LH2	15 uA	1.0M	production
03/02/11	19:57	2206	2	4cm LH2	15 uA	1.0M	production
03/02/11	20:30	2207	2	4cm LH2	0 uA	350	cosmics
03/02/11	20:31	Spectrometers changed from Kinematic 2 to Kinematic 3 (2207/2208)					
03/02/11	20:32	2208	3	4cm LH2	0 uA	64k	cosmics
03/02/11	22:00	Target moved from 4cm LH2 to BeO (2208/2209)					
03/02/11	22:02	2209	3	BeO	15 uA	33k	spot++
03/02/11	22:12	2210	3	BeO	15 uA	190k	optics
03/02/11	22:25	Target moved from BeO to 4cm LH2 (2210/2211)					
03/02/11	22:27	2211	3	4cm LH2	15 uA	360k	junk
03/02/11	22:33	2212	3	4cm LH2	15 uA	???	junk
03/02/11	22:42	2213	3	4cm LH2	15 uA	250k	junk
03/02/11	22:44	Readout time for ROCSs 1-4 (problem)					
03/02/11	22:48	2214	3	4cm LH2	30 uA	170k	junk
03/02/11	22:53	2215	3	4cm LH2	20 uA	58k	junk
03/02/11	22:56	2216	3	4cm LH2	25 uA	390k	junk
03/02/11	23:04	2217	3	4cm LH2	25 uA	270k	production
03/02/11	23:09	2218	3	4cm LH2	25 uA	1.0M	production
03/02/11	23:29	2219	3	4cm LH2	25 uA	970k	production
03/02/11	23:49	2220	3	4cm LH2	25 uA	1.0M	production
Thursday, March 3rd, 2011							
03/03/11	00:07	2221	3	4cm LH2	25 uA	1.0M	production
03/03/11	00:28	2222	3	4cm LH2	25 uA	1.0M	production
03/03/11	00:52	Target moved from 4cm LH2 to 4cm Al (2222/2223)					
03/03/11	00:56	2223	3	4cm Al	20 uA	1.2M	dummy run
03/03/11	01:55	Target moved from 4cm Al to 4cm LH2 (2223/2224)					
							Continued on next page

Date	Time	Run	Kin	Target	Current	Events	Comments
03/03/11	01:58	2224	3	4cm LH2	25 uA	1.0M	production
03/03/11	02:19	2225	3	4cm LH2	25 uA	1.0M	production
03/03/11	02:38	2226	3	4cm LH2	25 uA	1.0M	production
03/03/11	02:57	2227	3	4cm LH2	25 uA	1.0M	production
03/03/11	03:16	2228	3	4cm LH2	25 uA	1.0M	production
03/03/11	03:34	2229	3	4cm LH2	25 uA	1.0M	production
03/03/11	03:54	2230	3	4cm LH2	25 uA	1.1M	production
03/03/11	03:55	RF Feedback on standby					
03/03/11	04:15	2231	3	4cm LH2	25 uA	1.0M	production
03/03/11	04:34	2232	3	4cm LH2	25 uA	1.0M	production
03/03/11	04:35	RF Feedback restored					
03/03/11	04:53	2233	3	4cm LH2	25 uA	1.0M	production
03/03/11	05:13	2234	3	4cm LH2	25 uA	1.0M	production
03/03/11	05:32	2235	3	4cm LH2	25 uA	1.0M	production
03/03/11	05:51	2236	3	4cm LH2	25 uA	1.0M	production
03/03/11	06:09	2237	3	4cm LH2	25 uA	940k	production
03/03/11	06:33	2238	3	4cm LH2	25 uA	1.1M	production
03/03/11	06:53	2239	3	4cm LH2	25 uA	1.0M	production
03/03/11	07:13	2240	3	4cm LH2	25 uA	1.0M	production
03/03/11	07:32	2241	3	4cm LH2	25 uA	1.0M	production
03/03/11	07:51	2242	3	4cm LH2	25 uA	1.1M	production
03/03/11	08:13	2243	3	4cm LH2	25 uA	1.1M	production
03/03/11	08:32	2244	3	4cm LH2	25 uA	1.0M	production
03/03/11	08:51	2245	3	4cm LH2	25 uA	1.0M	production
03/03/11	09:10	2246	3	4cm LH2	25 uA	1.2M	production
03/03/11	09:33	2247	3	4cm LH2	25 uA	1.0M	production
03/03/11	09:44	TS deadtime update					
03/03/11	09:53	2248	3	4cm LH2	25 uA	1.0M	production
03/03/11	10:13	2249	3	4cm LH2	25 uA	1.0M	production
03/03/11	10:16	$bb_ts1.crl$ modified					
03/03/11	10:32	2250	3	4cm LH2	25 uA	1.0M	production
03/03/11	10:53	2251	3	4cm LH2	25 uA	1.1M	production
03/03/11	12:20	Target moved from 4cm LH2 to Empty (2251/2252)					
03/03/11	12:27	2252	3	empty	?? uA	20k	BCM calibration
		Continued on next page					

Date	Time	Run	Kin	Target	Current	Events	Comments
03/03/11	13:23	2253	3	empty	?? uA	16k	BCM calibration
03/03/11	14:12	2254	3	empty	?? uA	35k	BCM calibration
03/03/11	14:16	locftm added to config string for pedrun					
03/03/11	15:00	Target moved from Empty to 4cm LH2 (2254/2255)					
03/03/11	15:03	$bb_sfi1.crl$ modified, readout time for ROC10 added					
03/03/11	15:06	2255	3	4cm LH2	25 uA	1.2M	production
03/03/11	15:30	HRS timing calibration done					
03/03/11	15:39	2256	3	4cm LH2	25 uA	???	pedestal run
03/03/11	15:42	2257	3	4cm LH2	25 uA	1.0M	production
03/03/11	16:00	2258	3	4cm LH2	25 uA	1.0M	production
03/03/11	16:16	Pedestal supression fixed					
03/03/11	16:20	2259	3	4cm LH2	25 uA	580k	production
03/03/11	17:43	2260	3	4cm LH2	20 uA	180k	deadtime testing
03/03/11	17:47	Hall A beam size puzzle					
03/03/11	17:48	2261	3	4cm LH2	15 uA	7.4k	deadtime testing
03/03/11	17:49	2262	3	4cm LH2	15 uA	150k	deadtime testing
03/03/11	17:51	2263	3	4cm LH2	15 uA	25k	deadtime testing
03/03/11	17:52	2264	3	4cm LH2	15 uA	130k	deadtime testing
03/03/11	17:54	2265	3	4cm LH2	15 uA	120k	deadtime testing
03/03/11	17:56	2266	3	4cm LH2	15 uA	71k	deadtime testing
03/03/11	17:57	2267	3	4cm LH2	15 uA	32k	deadtime testing
03/03/11	18:02	2268	3	4cm LH2	15 uA	1.0M	production
03/03/11	18:10	Deadtime test results					
03/03/11	18:41	2269	3	4cm LH2	15 uA	1.0M	production
03/03/11	19:22	2270	3	4cm LH2	20 uA	1.0M	production
03/03/11	19:49	2271	3	4cm LH2	25 uA	1.3M	production
03/03/11	20:14	2272	3	4cm LH2	25 uA	1.3M	production
03/03/11	20:39	2273	3	4cm LH2	25 uA	400k	high rate check
03/03/11	20:42	2274	3	4cm LH2	25 uA	???	junk
03/03/11	20:53	2275	3	4cm LH2	25 uA	1.2M	production
03/03/11	21:18	2276	3	4cm LH2	25 uA	1.2M	production
03/03/11	21:41	2277	3	4cm LH2	25 uA	1.3M	production
03/03/11	22:06	2278	3	4cm LH2	25 uA	1.0M	production
03/03/11	22:26	2279	3	4cm LH2	25 uA	1.3M	production
							Continued on next page

Date	Time	Run	Kin	Target	Current	Events	Comments
03/03/11	22:54	2280	3	4cm LH2	25 uA	1.0M	production
03/03/11	23:14	Spectrometers changed from Kinematic 3 to Kinematic 1 (2280/2281)					
Friday, March 4th, 2011							
03/04/11	00:00	Target moved from 4cm LH2 to BeO (2280/2281)					
03/04/11	00:06	2281	1	BeO	15 uA	78k	optics
03/04/11	00:15	Target moved from BeO to 4cm LH2 (2281/2282)					
03/04/11	00:19	2282	1	4cm LH2	15 uA	1.0M	production
03/04/11	00:38	Shower and preshower maps okay					
03/04/11	00:50	2283	1	4cm LH2	15 uA	1.0M	production
03/04/11	01:21	2284	1	4cm LH2	15 uA	1.0M	production
03/04/11	01:51	2285	1	4cm LH2	15 uA	1.0M	production
03/04/11	02:20	2286	1	4cm LH2	15 uA	1.0M	production
03/04/11	02:49	2287	1	4cm LH2	15 uA	1.0M	production
03/04/11	03:16	2288	1	4cm LH2	15 uA	1.0M	production
03/04/11	03:44	2289	1	4cm LH2	15 uA	???	CODA stalled
03/04/11	03:51*	2290	1	4cm LH2	15 uA	???	junk
03/04/11	03:58*	2291	1	4cm LH2	15 uA	???	junk
03/04/11	04:01	2292	1	4cm LH2	15 uA	1.0M	production
03/04/11	04:29	2293	1	4cm LH2	15 uA	1.0M	production
03/04/11	04:56	2294	1	4cm LH2	15 uA	1.0M	production
03/04/11	05:24	2295	1	4cm LH2	15 uA	1.0M	production
03/04/11	05:51	2296	1	4cm LH2	15 uA	1.0M	production
03/04/11	05:56	Compton EPICS reboot					
03/04/11	06:18	2297	1	4cm LH2	15 uA	950k	production
03/04/11	06:48	2298	1	4cm LH2	15 uA	440k	production
03/04/11	07:02	Spectrometers changed from Kinematic 1 to Kinematic 6 (2298/2299)					
03/04/11	07:08	Controlled access					
03/04/11	08:29	Deadtime tests, loose triggers					
03/04/11	08:30	2299	6	4cm LH2	0 uA	6.3M	cosmics
03/04/11	08:55	EDTM setup changed for new kinematic					
03/04/11	08:58	T1 trigger widened to 50 ns					
03/04/11	09:10	ROC3/4 busy report					
03/04/11	09:30	2300	6	4cm LH2	0 uA	930k	cosmics
03/04/11	09:41	Strobe signals cross-connected					
							Continued on next page

Date	Time	Run	Kin	Target	Current	Events	Comments
03/04/11	09:42*	2301	6	4cm LH2	0 uA	???	cosmics
03/04/11	09:54	2302	6	4cm LH2	0 uA	1.2M	cosmics
03/04/11	09:59	T4 connected properly					
03/04/11	10:08	2303	6	4cm LH2	0 uA	2.6M	cosmics
03/04/11	10:13	Deadtime problem found (ROC10)					
03/04/11	10:26	2304	6	4cm LH2	0 uA	610k	cosmics
03/04/11	10:32	2305	6	4cm LH2	0 uA	17k	cosmics
03/04/11	10:34	2306	6	4cm LH2	0 uA	630k	cosmics
03/04/11	10:44	2307	6	4cm LH2	0 uA	1.2M	cosmics
03/04/11	10:52	$bb_sfi3.crl$ modified					
03/04/11	10:58	Triggers restored					
03/04/11	11:06	2308	6	4cm LH2	0 uA	36k	cosmics
03/04/11	11:12	Right Q1 tripped					
03/04/11	11:30	Deadtime issues resolved					
03/04/11	12:00	Target moved from 4cm LH2 to Empty (2308/2309)					
03/04/11	12:03	2309	6	Empty	0 uA	99	cosmics
03/04/11	12:18	Target moved from Empty to BeO (2309/2310)					
03/04/11	12:21	2310	6	BeO	5 uA	22k	spot++
03/04/11	12:30	Target moved from BeO to 4cm LH2 (2310/2311)					
03/04/11	12:34	2311	6	4cm LH2	20 uA	1.6M	check out
03/04/11	12:46	2312	6	4cm LH2	45 uA	1.5M	test
03/04/11	12:59	2313	6	4cm LH2	40 uA	170k	test
03/04/11	13:02	2314	6	4cm LH2	40 uA	1.0M	production
03/04/11	13:14	2315	6	4cm LH2	40 uA	1.1M	production
03/04/11	13:27	2316	6	4cm LH2	40 uA	1.1M	production
03/04/11	13:40	2317	6	4cm LH2	40 uA	1.4M	production
03/04/11	13:59	2318	6	4cm LH2	40 uA	1.1M	production
03/04/11	14:11	2319	6	4cm LH2	40 uA	100k	ended early
03/04/11	14:19	2320	6	4cm LH2	40 uA	1.0M	production
03/04/11	14:32	2321	6	4cm LH2	40 uA	1.0M	production
03/04/11	14:44	2322	6	4cm LH2	40 uA	???	junk
03/04/11	14:48	2323	6	4cm LH2	40 uA	1.0M	production
03/04/11	15:00	2324	6	4cm LH2	40 uA	1.0M	production
03/04/11	15:06	LHRS Pion Rejector Ch 5 turned on					
		Continued on next page					

Date	Time	Run	Kin	Target	Current	Events	Comments
03/04/11	15:14	2325	6	4cm LH2	40 uA	1.0M	production
03/04/11	15:25	2326	6	4cm LH2	40 uA	1.3M	production
03/04/11	15:40	2327	6	4cm LH2	40 uA	1.0M	production
03/04/11	15:52	2328	6	4cm LH2	40 uA	1.1M	production
03/04/11	16:06	2329	6	4cm LH2	40 uA	1.2M	production
03/04/11	16:19	2330	6	4cm LH2	40 uA	1.2M	production
03/04/11	16:33	2331	6	4cm LH2	40 uA	1.6M	production
03/04/11	16:52	2332	6	4cm LH2	40 uA	1.8M	production
03/04/11	17:13	2333	6	4cm LH2	40 uA	1.1M	production
03/04/11	17:26	2334	6	4cm LH2	40 uA	1.1M	production
03/04/11	17:38	2335	6	4cm LH2	40 uA	1.0M	production
03/04/11	17:50	2336	6	4cm LH2	40 uA	1.1M	production
03/04/11	18:04	2337	6	4cm LH2	40 uA	1.?M	CODA crashed
03/04/11	18:15	2338	6	4cm LH2	40 uA	1.1M	production
03/04/11	18:29	2339	6	4cm LH2	40 uA	1.2M	production
03/04/11	18:44	2340	6	4cm LH2	40 uA	1.1M	production
03/04/11	18:57	2341	6	4cm LH2	40 uA	1.1M	production
03/04/11	19:15	2342	6	4cm LH2	40 uA	1.1M	production
03/04/11	19:28	2343	6	4cm LH2	40 uA	1.0M	production
03/04/11	19:41	2344	6	4cm LH2	40 uA	1.1M	production
03/04/11	19:54	2345	6	4cm LH2	40 uA	1.1M	production
03/04/11	20:08	2346	6	4cm LH2	40 uA	1.1M	production
03/04/11	20:23	2347	6	4cm LH2	40 uA	1.1M	production
03/04/11	20:36	2348	6	4cm LH2	40 uA	1.1M	production
03/04/11	20:52	2349	6	4cm LH2	40 uA	1.1M	production
03/04/11	21:07	2350	6	4cm LH2	40 uA	1.1M	production
03/04/11	21:22	2351	6	4cm LH2	40 uA	1.3M	production
03/04/11	21:37	2352	6	4cm LH2	40 uA	1.2M	production
03/04/11	21:53	2353	6	4cm LH2	40 uA	970k	production
03/04/11	22:10	2354	6	4cm LH2	40 uA	1.0M	production
03/04/11	22:25	2355	6	4cm LH2	40 uA	1.6M	production
03/04/11	22:44	2356	6	4cm LH2	40 uA	1.3M	production
03/04/11	23:00	2357	6	4cm LH2	40 uA	1.0M	production
03/04/11	23:13	2358	6	4cm LH2	40 uA	40k	junk

Date	Time	Run	Kin	Target	Current	Events	Comments
03/04/11	23:17	Target moved from 4cm LH2 to BeO (2358/2359)					
03/04/11	23:20	2359	6	BeO	15 uA	18k	optics
03/04/11	23:30	Target moved from BeO to 4cm Al (2359/2360)					
03/04/11	23:33	2360	6	4cm Al	15 uA	800k	dummy run
Saturday, March 5th, 2011							
03/05/11	00:58	Escorted access					
03/05/11	00:59	Spectrometers changed from Kinematic 6 to Kinematic 7 (2360/2361)					
03/05/11	02:00	Target moved from 4cm Al to 4cm LH2 (2360/2361)					
03/05/11	02:09	2361	7	4cm LH2	40 uA	61k	test run for rates
03/05/11	02:10	FFB turned back on					
03/05/11	02:18	2362	7	4cm LH2	50 uA	60k	test run for rates
03/05/11	02:25	2363	7	4cm LH2	60 uA	58k	test run for rates
03/05/11	02:35	2364	7	4cm LH2	70 uA	29k	test run
03/05/11	02:44	2365	7	4cm LH2	80 uA	590k	test run
03/05/11	02:49	2366	7	4cm LH2	80 uA	2.0M	production
03/05/11	03:07	2367	7	4cm LH2	80 uA	2.0M	production
03/05/11	03:24	2368	7	4cm LH2	80 uA	2.0M	production
03/05/11	03:42	2369	7	4cm LH2	80 uA	2.0M	production
03/05/11	04:04	Target moved from 4cm LH2 to 4cm Al (2369/2370)					
03/05/11	04:06	2370	7	4cm Al	20 uA	710k	dummy run
03/05/11	05:10	Target moved from 4cm Al to BeO (2370/2371)					
03/05/11	05:12	2371	7	BeO	20 uA	60k	optics
03/05/11	05:22	Target moved from BeO to 4cm LH2 (2371/2372)					
03/05/11	05:24	2372	7	4cm LH2	80 uA	2.0M	production
03/05/11	05:43	2373	7	4cm LH2	80 uA	2.0M	production
03/05/11	06:04	2374	7	4cm LH2	80 uA	2.0M	production
03/05/11	06:33	2375	7	4cm LH2	80 uA	2.4M	production
03/05/11	06:54	2376	7	4cm LH2	80 uA	2.0M	production
03/05/11	07:15	2377	7	4cm LH2	80 uA	2.0M	production
03/05/11	07:34	2378	7	4cm LH2	80 uA	2.2M	production
03/05/11	08:03	2379	7	4cm LH2	80 uA	2.0M	production
03/05/11	08:23	2380	7	4cm LH2	80 uA	2.0M	production
03/05/11	08:47	2381	7	4cm LH2	80 uA	2.0M	production
03/05/11	09:07	2382	7	4cm LH2	80 uA	2.0M	production
							Continued on next page

Date	Time	Run	Kin	Target	Current	Events	Comments
03/05/11	09:24	2383	7	4cm LH2	80 uA	2.0M	production
03/05/11	09:46	2384	7	4cm LH2	80 uA	2.0M	production
03/05/11	10:04	2385	7	4cm LH2	80 uA	2.0M	production
03/05/11	10:23	2386	7	4cm LH2	80 uA	2.0M	production
03/05/11	10:48	2387	7	4cm LH2	80 uA	2.0M	production
03/05/11	11:06	2388	7	4cm LH2	80 uA	2.0M	production
03/05/11	11:25	Spectrometers changed from Kinematic 7 to Kinematic 5 (2388/2389)					
03/05/11	11:56	2389	5	4cm LH2	80 uA	69k	changed prescales
03/05/11	12:10	2390	5	4cm LH2	60 uA	71k	test run
03/05/11	12:14	2391	5	4cm LH2	70 uA	110k	test run
03/05/11	12:18	2392	5	4cm LH2	70 uA	58k	test run
03/05/11	12:22	2393	5	4cm LH2	70 uA	2.0M	production
03/05/11	12:43	2394	5	4cm LH2	80 uA	2.0M	production
03/05/11	12:55	2395	5	4cm LH2	80 uA	2.0M	production
03/05/11	13:07	2396	5	4cm LH2	80 uA	2.0M	production
03/05/11	13:18	2397	5	4cm LH2	80 uA	2.0M	production
03/05/11	13:34	2398	5	4cm LH2	80 uA	2.0M	production
03/05/11	13:47	2399	5	4cm LH2	80 uA	2.0M	production
03/05/11	14:10	Target moved from 4cm LH2 to 4cm Al (2399/2400)					
03/05/11	14:14	2400	5	4cm Al	20 uA	380k	dummy run
03/05/11	14:48	Target moved from 4cm Al to BeO (2400/2401)					
03/05/11	14:51	2401	5	BeO	20 uA	???	junk
03/05/11	14:59	2402	5	BeO	20 uA	61k	optics
03/05/11	15:20	Target moved from BeO to 4cm LH2 (2402/2403)					
03/05/11	15:23	2403	5	BeO	20 uA	11k	junk
03/05/11	15:26	2404	5	4cm LH2	80 uA	2.0M	production
03/05/11	15:39	2405	5	4cm LH2	80 uA	2.0M	production
03/05/11	15:51	2406	5	4cm LH2	80 uA	2.0M	production
03/05/11	16:04	2407	5	4cm LH2	80 uA	2.0M	production
03/05/11	16:18	2408	5	4cm LH2	80 uA	970k	production
03/05/11	16:26	Spectrometers changed from Kinematic 5 to Kinematic 11 (2408/2409)					
03/05/11	16:50	Controlled access to mark 22 degrees (RHRS)					
03/05/11	17:30	Back to beam					
03/05/11	17:40	2409	11	15 cm LH2	10 uA	490k	test run
		Continued on next page					

Date	Time	Run	Kin	Target	Current	Events	Comments
03/05/11	17:45	2410	11	15 cm LH2	30 uA	1.0M	test run
03/05/11	17:50	2411	11	15 cm LH2	20 uA	500k	test run
03/05/11	18:01	2412	11	4cm LH2	20 uA	73k	test run
03/05/11	18:08	2413	11	4cm LH2	40 uA	76k	test run
03/05/11	18:12	2414	11	4cm LH2	60 uA	1.3M	test run
03/05/11	18:33	2415	11	4cm LH2	55 uA	430k	test run
03/05/11	18:40	2416	11	4cm LH2	55 uA	???	junk
03/05/11	18:43	2417	11	4cm LH2	55 uA	2.1M	production
03/05/11	19:10	2418	11	4cm LH2	55 uA	2.3M	production
03/05/11	19:43	2419	11	4cm LH2	55 uA	2.0M	production
03/05/11	20:09	2420	11	4cm LH2	55 uA	2.0M	production
03/05/11	20:37	2421	11	4cm LH2	55 uA	2.0M	production
03/05/11	21:03	2422	11	4cm LH2	55 uA	2.2M	production
03/05/11	21:36	Target moved from 4cm LH2 to BeO (2422/2423)					
03/05/11	21:40	2423	11	BeO	20 uA	18k	production
03/05/11	21:49	Target moved from BeO to 4cm Al (2423/2424)					
03/05/11	21:52	2424	11	4cm Al	20 uA	190k	production
03/05/11	22:30	Target moved from 4cm Al to 4cm LH2 (2424/2425)					
03/05/11	22:35	2425	11	4cm LH2	55 uA	2.1M	production
03/05/11	23:02	2426	11	4cm LH2	55 uA	2.0M	production
03/05/11	23:33	2427	11	4cm LH2	55 uA	2.0M	production
03/05/11	23:59	2428	11	4cm LH2	55 uA	2.0M	production
Sunday, March 6th, 2011							
03/06/11	00:25	2429	11	4cm LH2	55 uA	2.0M	production
03/06/11	00:50	2430	11	4cm LH2	55 uA	2.0M	production
03/06/11	01:16	2431	11	4cm LH2	55 uA	???	CODA froze
03/06/11	01:23	2432	11	4cm LH2	55 uA	???	killed CODA
03/06/11	01:31	2433	11	4cm LH2	55 uA	2.0M	production
03/06/11	01:57	2434	11	4cm LH2	55 uA	2.0M	production
03/06/11	02:23	2435	11	4cm LH2	55 uA	2.0M	production
03/06/11	02:53	Spectrometers changed from Kinematic 11 to Kinematic 12 (2435/2436)					
03/06/11	03:31	2436	12	4cm LH2	80 uA	1.3M	production
03/06/11	03:56	2437	12	4cm LH2	80 uA	1.0M	production
03/06/11	04:15	2438	12	4cm LH2	80 uA	1.0M	production
							Continued on next page

Date	Time	Run	Kin	Target	Current	Events	Comments
03/06/11	04:40	2439	12	4cm LH2	10 uA	50k	boiling test run
03/06/11	04:47	2440	12	4cm LH2	20 uA	63k	boiling test run
03/06/11	04:54	2441	12	4cm LH2	30 uA	85k	boiling test run
03/06/11	05:01	2442	12	4cm LH2	40 uA	110k	boiling test run
03/06/11	05:10	2443	12	4cm LH2	50 uA	20k	boiling test run
03/06/11	05:13	2444	12	4cm LH2	50 uA	150k	boiling test run
03/06/11	05:20	2445	12	4cm LH2	60 uA	170k	boiling test run
03/06/11	05:28	2446	12	4cm LH2	70 uA	210k	boiling test run
03/06/11	05:40	2447	12	4cm LH2	80 uA	290k	boiling test run
03/06/11	05:49	Target moved from 4cm LH2 to BeO (2447/2448)					
03/06/11	05:52	2448	12	BeO	20 uA	47k	optics
03/06/11	06:00	Target moved from BeO to 4cm Al (2448/2449)					
03/06/11	06:03	2449	12	4cm Al	20 uA	350k	dummy run
03/06/11	06:43	RF Zone 2L15 down, no beam					
03/06/11	07:01	2450	12	4cm Al	20 uA	200k	dummy run
03/06/11	07:01	Zone recovered					
03/06/11	07:27	Target moved from 4cm Al to 4cm LH2 (2450/2451)					
03/06/11	07:30	2451	12	4cm LH2	80 uA	1.0M	production
03/06/11	07:48	2452	12	4cm LH2	80 uA	1.0M	production
03/06/11	08:07	2453	12	4cm LH2	80 uA	1.0M	production
03/06/11	08:29	2454	12	4cm LH2	80 uA	1.1M	production
03/06/11	08:50	2455	12	4cm LH2	80 uA	1.1M	production
03/06/11	09:08	2456	12	4cm LH2	80 uA	1.0M	production
03/06/11	09:28	2457	12	4cm LH2	80 uA	1.0M	production
03/06/11	09:47	2458	12	4cm LH2	80 uA	1.0M	production
03/06/11	10:06	2459	12	4cm LH2	80 uA	1.0M	production
03/06/11	10:25	2460	12	4cm LH2	80 uA	1.0M	production
03/06/11	10:46	2461	12	4cm LH2	80 uA	600k	production
03/06/11	11:00	Spectrometers changed from Kinematic 12 to Kinematic 8 (2461/2462)					
03/06/11	11:05	Target moved from 4cm LH2 to 15cm LH2 (2461/2462)					
03/06/11	11:10	2462	8	15 cm LH2	20 uA	620k	beam current test
03/06/11	11:30	2463	8	15 cm LH2	40 uA	1.0M	production
03/06/11	11:38*	2464	8	15 cm LH2	30 uA	???	junk
03/06/11	11:46	2465	8	15 cm LH2	30 uA	1.1M	production
							Continued on next page

Date	Time	Run	Kin	Target	Current	Events	Comments
03/06/11	11:55	Incorrect Angle Data (2463)					
03/06/11	11:58	2466	8	15 cm LH2	35 uA	1.0M	production
03/06/11	12:05	2467	8	15 cm LH2	35 uA	1.0M	production
03/06/11	12:13	2468	8	15 cm LH2	35 uA	1.1M	production
03/06/11	12:25	2469	8	15 cm LH2	40 uA	2.0M	production
03/06/11	12:37	2470	8	15 cm LH2	40 uA	2.0M	production
03/06/11	12:48	2471	8	15 cm LH2	40 uA	2.0M	production
03/06/11	13:00	2472	8	15 cm LH2	40 uA	2.0M	production
03/06/11	13:24	Target moved from 15cm LH2 to 15cm Al (2472/2473)					
03/06/11	13:28	2473	8	15cm Al	20 uA	590k	dummy run
03/06/11	14:02*	2474	8	4cm Al	20 uA	???	junk
03/06/11	14:05	Target moved from 15cm Al to 4cm Al (2473/2474)					
03/06/11	14:10	iocha22 problems					
03/06/11	14:37*	2475	8	4cm Al	20 uA	???	junk
03/06/11	14:40*	2476	8	4cm Al	20 uA	???	junk
03/06/11	14:43*	2477	8	4cm Al	20 uA	???	junk
03/06/11	14:45	iocha22 fixed					
03/06/11	14:46	Run 2478, Kinematic 8, 4cm Al, 20 uA 310k events					dummy run
03/06/11	15:20	Target moved from 4cm Al to BeO (2478/2479)					
03/06/11	15:25	2479	8	BeO	20 uA	51k	optics
03/06/11	15:40	Target moved from BeO to 4cm LH2 (2479/2480)					
03/06/11	15:44	2480	8	4cm LH2	80 uA	2.0M	production
03/06/11	16:10	2481	8	4cm LH2	80 uA	2.0M	production
03/06/11	16:35	2482	8	4cm LH2	80 uA	2.0M	production
03/06/11	16:48*	2483	8	4cm LH2	80 uA	???	junk
03/06/11	17:02	2484	8	4cm LH2	80 uA	2.2M	production
03/06/11	17:32	2485	8	4cm LH2	80 uA	2.2M	production
03/06/11	17:59	2486	8	4cm LH2	80 uA	1.8M	production
03/06/11	18:22	Spectrometers changed from Kinematic 8 to Kinematic 9 (2486/2487)					
03/06/11	18:47	Target moved from 4cm LH2 to 15cm LH2 (2486/2487)					
03/06/11	18:51	2487	9	15 cm LH2	40 uA	570k	test
03/06/11	18:54	2488	9	15 cm LH2	30 uA	1.5M	production
03/06/11	19:03	2489	9	15 cm LH2	25 uA	2.4M	production
03/06/11	19:21	2490	9	15 cm LH2	30 uA	37k	junk
							Continued on next page

Date	Time	Run	Kin	Target	Current	Events	Comments
03/06/11	19:22	2491	9	15 cm LH2	30 uA	2.2M	production
03/06/11	19:35	2492	9	15 cm LH2	30 uA	3.3M	production
03/06/11	19:53	2493	9	15 cm LH2	30 uA	2.3M	production
03/06/11	20:06	2494	9	15 cm LH2	30 uA	2.0M	production
03/06/11	20:18	2495	9	15 cm LH2	30 uA	2.1M	production
03/06/11	20:30	2496	9	15 cm LH2	30 uA	2.0M	production
03/06/11	20:32	Decision to only take 85% of Kinematic 9					
03/06/11	20:41	2497	9	15 cm LH2	30 uA	2.2M	production
03/06/11	20:54	2498	9	15 cm LH2	30 uA	2.2M	production
03/06/11	21:06	2499	9	15 cm LH2	30 uA	2.2M	production
03/06/11	21:19	2500	9	15 cm LH2	30 uA	2.0M	production
03/06/11	21:31	2501	9	15 cm LH2	30 uA	2.1M	production
03/06/11	21:42	2502	9	15 cm LH2	30 uA	2.2M	production
03/06/11	21:55	2503	9	15 cm LH2	30 uA	2.3M	production
03/06/11	22:08	2504	9	15 cm LH2	30 uA	13k	junk
03/06/11	22:13	Target moved from 15cm LH2 to 15cm Al (2504/2505)					
03/06/11	22:16	2505	9	15cm Al	20 uA	240k	dummy run
03/06/11	22:33	Target moved from 15cm Al to BeO (2505/2506)					
03/06/11	22:36	2506	9	BeO	20 uA	13k	optics
03/06/11	22:48	Target moved from BeO to 15cm LH2 (2506/2507)					
03/06/11	22:51	2507	9	15 cm LH2	30 uA	2.2M	production
03/06/11	23:04	2508	9	15 cm LH2	30 uA	2.5M	production
03/06/11	23:18	2509	9	15 cm LH2	30 uA	2.0M	production
03/06/11	23:29	2510	9	15 cm LH2	30 uA	3.3M	production
03/06/11	23:47	2511	9	15 cm LH2	30 uA	2.3M	production
03/06/11	23:59	2512	9	15 cm LH2	30 uA	2.0M	production
Monday, March 7th, 2011							
03/07/11	00:11	2513	9	15 cm LH2	30 uA	2.0M	production
03/07/11	00:23	2514	9	15 cm LH2	30 uA	2.0M	production
03/07/11	00:36	2515	9	15 cm LH2	30 uA	2.2M	production
03/07/11	00:48	2516	9	15 cm LH2	30 uA	2.0M	production
03/07/11	01:00	2517	9	15 cm LH2	30 uA	2.0M	production
03/07/11	01:14	2518	9	15 cm LH2	30 uA	2.1M	production
03/07/11	01:25	2519	9	15 cm LH2	30 uA	2.1M	production
						Continued on next page	

Date	Time	Run	Kin	Target	Current	Events	Comments
03/07/11	01:37	2520	9	15 cm LH2	30 uA	2.0M	production
03/07/11	01:49	2521	9	15 cm LH2	30 uA	2.0M	production
03/07/11	02:02	Spectrometers changed from Kinematic 9 to Kinematic 10 (2521/2522)					
03/07/11	02:27	2522	10	15 cm LH2	50 uA	25k	test for 50 uA
03/07/11	02:29	2523	10	15 cm LH2	50 uA	4.0M	production
03/07/11	02:51	2524	10	15 cm LH2	50 uA	4.0M	production
03/07/11	03:14	2525	10	15 cm LH2	50 uA	2.4M	production
03/07/11	03:28	2526	10	15 cm LH2	50 uA	2.0M	production
03/07/11	03:39	2527	10	15 cm LH2	50 uA	2.0M	production
03/07/11	03:50	2528	10	15 cm LH2	50 uA	2.0M	production
03/07/11	04:05	2529	10	15 cm LH2	50 uA	2.0M	production
03/07/11	04:16	2530	10	15 cm LH2	50 uA	2.0M	production
03/07/11	04:28	2531	10	15 cm LH2	50 uA	2.0M	production
03/07/11	04:44	Target moved from 15cm LH2 to BeO (2531/2532)					
03/07/11	04:47	2532	10	BeO	20 uA	44K	optics
03/07/11	04:55	Target moved from BeO to 15cm Al (2532/2533)					
03/07/11	04:57	2533	10	15cm Al	20 uA	280K	dummy run
03/07/11	05:20	Target moved from 15cm Al to 15cm LH2 (2533/2534)					
03/07/11	05:25	2534	10	15 cm LH2	50 uA	2.0M	production
03/07/11	05:36	2535	10	15 cm LH2	50 uA	2.0M	production
03/07/11	05:47	2536	10	15 cm LH2	50 uA	2.0M	production
03/07/11	05:59	2537	10	15 cm LH2	50 uA	2.0M	production
03/07/11	06:10	2538	10	15 cm LH2	50 uA	2.0M	production
03/07/11	06:27	2539	10	15 cm LH2	50 uA	2.0M	production
03/07/11	06:39	2540	10	15 cm LH2	50 uA	2.0M	production
03/07/11	06:46*	2541	10	15 cm LH2	50 uA	???	junk
03/07/11	06:54*	2542	10	15 cm LH2	50 uA	???	junk
03/07/11	06:57	2543	10	15 cm LH2	50 uA	2.0M	production
03/07/11	07:11	2544	10	15 cm LH2	50 uA	2.2M	production
03/07/11	07:26	2545	10	15 cm LH2	50 uA	2.4M	production
03/07/11	07:41	2546	10	15 cm LH2	50 uA	2.1M	production
03/07/11	07:57	Spectrometers changed from Kinematic 10 to Kinematic 13 (2546/2547)					
03/07/11	08:50	Target moved from 15cm LH2 to BeO (2546/2547)					
03/07/11	08:53	2547	13	BeO	5 uA	2.8K	optics
		Continued on next page					

Date	Time	Run	Kin	Target	Current	Events	Comments
03/07/11	08:57	2548	13	BeO	5 uA	54K	optics
03/07/11	09:01	2549	13	BeO	20 uA	38K	optics
03/07/11	09:06	Target moved from BeO to 15cm Al (2549/2550)					
03/07/11	09:08	2550	13	15cm Al	20 uA	580K	dummy run
03/07/11	09:32	Target moved from 15cm Al to 15cm LH2 (2550/2551)					
03/07/11	09:38	2551	13	15 cm LH2	35 uA	2.0M	production
03/07/11	09:50	2552	13	15 cm LH2	35 uA	2.0M	production
03/07/11	10:03	2553	13	15 cm LH2	35 uA	2.0M	production
03/07/11	10:16	2554	13	15 cm LH2	35 uA	2.2M	production
03/07/11	10:29	2555	13	15 cm LH2	35 uA	2.0M	production
03/07/11	10:42	2556	13	15 cm LH2	35 uA	2.0M	production
03/07/11	10:54	2557	13	15 cm LH2	35 uA	2.0M	production
03/07/11	11:06	2558	13	15 cm LH2	35 uA	2.1M	production
03/07/11	11:18	2559	13	15 cm LH2	35 uA	2.1M	production
03/07/11	11:34	2560	13	15 cm LH2	35 uA	2.0M	production
03/07/11	11:46	2561	13	15 cm LH2	35 uA	2.3M	production
03/07/11	12:02	Spectrometers changed from Kinematic 13 to Kinematic 14 (2561/2562)					
03/07/11	12:30	Target moved from 15cm LH2 to BeO (2561/2562)					
03/07/11	12:38	2562	14	BeO	20 uA	54K	optics
03/07/11	12:44	Target moved from BeO to 15cm Al (2562/2563)					
03/07/11	12:45	2563	14	15cm Al	20 uA	1.4K	junk
03/07/11	12:49	2564	14	15cm Al	20 uA	530K	dummy run
03/07/11	13:10	Target moved from 15cm Al to 15cm LH2 (2564/2565)					
03/07/11	13:12	2565	14	15 cm LH2	35 uA	2.0M	production
03/07/11	13:20	Created B3NArmNTS11 configuration					
03/07/11	13:25	2566	14	15 cm LH2	35 uA	2.3M	production
03/07/11	13:38	2567	14	15 cm LH2	35 uA	2.0M	production
03/07/11	13:51	2568	14	15 cm LH2	35 uA	2.0M	production
03/07/11	14:03	2569	14	15 cm LH2	35 uA	2.0M	production
03/07/11	14:15	2570	14	15 cm LH2	35 uA	2.3M	production
03/07/11	14:27	2571	14	15 cm LH2	35 uA	2.0M	production
03/07/11	14:39	2572	14	15 cm LH2	35 uA	2.2M	production
03/07/11	14:51	2573	14	15 cm LH2	35 uA	2.0M	production
03/07/11	15:04	Spectrometers changed from Kinematic 14 to Kinematic Z (2573/2574)					
		Continued on next page						

Date	Time	Run	Kin	Target	Current	Events	Comments
03/07/11	15:30	Target moved from 15cm LH2 to BeO (2573/2574)					
03/07/11	15:43	2574	Z	BeO	0 uA	???	spot++
03/07/11	15:47	2575	Z	BeO	0 uA	???	spot++
03/07/11	16:16	2576	Z	BeO	0 uA	280k	spot++
03/07/11	16:24	Escorted access, fixed T7					
03/07/11	16:31	TS11 crl code modified					
03/07/11	16:34	Escorted access, reset Loop 1 fan controller					
03/07/11	17:11	2577	Z	BeO	3 uA	810k	spot++
03/07/11	17:26	Target moved from BeO to 4cm LD2 (2577/2578)					
03/07/11	17:28	2578	Z	4cm LD2	5 uA	460k	junk
03/07/11	17:43	2579	Z	4cm LD2	5 uA	5.6k	short run
03/07/11	17:47	2580	Z	4cm LD2	5 uA	250k	calibration runs
03/07/11	17:50	UBTHREEARM configuration updated					
03/07/11	18:00	2581	Z	4cm LD2	5 uA	270k	calibration runs
03/07/11	18:16	2582	Z	4cm LD2	5 uA	330k	calibration runs
03/07/11	18:19	EDTM disabled					
03/07/11	18:32	2583	Z	4cm LD2	5 uA	61k	short run
03/07/11	18:38	2584	Z	4cm LD2	10 uA	400k	calibration runs
03/07/11	18:58	2585	Z	4cm LD2	5 uA	770k	calibration runs
03/07/11	19:35	2586	Z	4cm LD2	5 uA	470k	calibration runs
03/07/11	19:59	2587	Z	4cm LD2	5 uA	480k	calibration runs
03/07/11	20:24	2588	Z	4cm LD2	5 uA	480k	calibration runs
03/07/11	20:47	2589	Z	4cm LD2	5 uA	430k	calibration runs
03/07/11	21:08	2590	Z	4cm LD2	5 uA	440k	calibration runs
03/07/11	21:30	2591	Z	4cm LD2	5 uA	580k	calibration runs
03/07/11	22:01	2592	Z	4cm LD2	5 uA	700k	calibration runs
03/07/11	22:58	2593	Z	4cm LD2	5 uA	680k	calibration runs
03/07/11	23:31	2594	Z	4cm LD2	5 uA	400k	calibration runs
03/07/11	23:52	Target moved from 4cm LD2 to BeO (2594/2595)					
Tuesday, March 8th, 2011							
03/08/11	00:30	Target warmup started					
03/08/11	01:03	Vacuum pressure spike					
03/08/11	02:05	2595	Z	BeO	5 uA	34k	
03/08/11	02:15	Target moved from BeO to Slanted Carbon (2595/2596)					
							Continued on next page

Date	Time	Run	Kin	Target	Current	Events	Comments
03/08/11	02:17	2596	Z	Slanted Carbon	5 uA	350k	
03/08/11	02:24	2597	Z	Slanted Carbon	5 uA	310k	
03/08/11	02:30	2598	Z	Slanted Carbon	5 uA	310k	
03/08/11	02:44	2599	Z	Slanted Carbon	5 uA	1.2M	
03/08/11	03:10	2600	Z	Slanted Carbon	5 uA	7.6k	
03/08/11	03:14	2601	Z	Slanted Carbon	5 uA	280k	
03/08/11	03:42	2602	Z	Slanted Carbon	10 uA	1.0M	
03/08/11	03:56	LHRS S1 HV adjustment					
03/08/11	04:32	2603	Z	Slanted Carbon	10 uA	520k	
03/08/11	05:03	2604	Z	Slanted Carbon	5 uA	28k	
03/08/11	05:08	2605	Z	Slanted Carbon	5 uA	26k	
03/08/11	05:12	2606	Z	Slanted Carbon	10 uA	860k	
03/08/11	05:59	2607	Z	Slanted Carbon	10 uA	1.3M	
03/08/11	07:00	Beam off, move to restricted access					

Table A.1: Run List

Bibliography

[1] N. Sparveris, S. Gilad, D.W. Higinbotham, A. Sarty (Spokesperson), *Measurement of the Coulomb quadrupole amplitude in the $\gamma^* p \to \Delta(1232)$ in the low momentum transfer region.* Jefferson Lab Hall A Proposal E08-010, 14p, 2007. (`http://www.jlab.org/exp_prog/proposals/08/PR-08-010.pdf`)

[2] S.L. Glashow, Physica **A 96**, 27 (1979)

[3] A.J. Buchmann and E.M. Henley, Phys. Rev. **C63**, 015202 (2000)

[4] C. Mistretta *et al.*, Phys. Rev. **184**, 1487 (1969)

[5] N. Isgur, G. Karl, and R. Koniuk, Phys. Rev. **D 25**, 2394 (1982)

[6] T. Sato and T.-S.H. Lee, Phys. Rev. **C63**, 055201 (2001)

[7] R. Roché, Ph.D. thesis, Florida State University (2003)

[8] C. Amsler *et al.*, Phys. Lett. **B 667**, 1 (2008)

[9] D. Dreschel and L. Tiator, J. Phys. **G18**, 449 (1992)

[10] Z. Chai, Ph.D. thesis, Massachusetts Institute of Technology (2003)

[11] J.J. Kelly, *et al.*, Phys. Rev. **C75**, 025201 (2007)

[12] J.J. Kelly, EPIPROD: program to calculate pseudoscaler meson production by electron-nucleon scattering, (`http://hallaweb.jlab.org/experiment/E91-011/EPIPROD/epiprod.html`), July 22, 2005.

[13] A. de Rujula, H. Georgi and S.L. Glashow *et al.*, Phys. Rev. **D12**, 147 (1975)

[14] W. Albrecht *et al.*, Nucl. Phys. **B25**, 1 (1970); Nucl. Phys. **B27**, 615 (1971); J.C. Alder *et al.*, Nucl. Phys. **B46**, 573 (1972)

[15] R. Siddel *et al.*, Nucl. Phys. **B35**, 93 (1971)

[16] F. Kalleicher *et al.*, Z. Phys. **A359**, 201 (1997)

[17] G. Blanpied *et al.*, Phys. Rev. Lett. **79**, 4337 (1997)

[18] R. Beck *et al.*, Phys. Rev. Lett. **78**, 606 (1997)

[19] V.V. Frolov *et al.*, Phys. Rev. Lett. **82**, 45 (1999)

[20] C. Mertz *et al.*, Phys. Rev. Lett. **86**, 2963 (2001)

[21] Th. Pospischil *et al.*, Phys. Rev. Lett. **86**, 2959 (2001)

[22] K. Joo *et al.*, Phys. Rev. Lett. **88**, 122001 (2002)

[23] J.J. Kelly, *et al.*, Phys. Rev. Lett. **95**, 102001 (2005)

[24] N.F. Sparveris *et al.*, Phys. Rev. Lett. **94**, 022003 (2005)

[25] D. Elsner *et al.*, Eur. Phys. J. **A 27**, 91-97, (2006)

[26] S. Stave *et al.*, Eur. Phys. J. **A 30**, 471 (2006)

[27] N.F. Sparveris *et al.*, Phys. Lett. **B 651**, 102 (2007)

[28] J. Alcorn *et al.*, Nucl. Instrum. Methods **A 522**, 294 (2004)

[29] D. Dreschel *et al.*, Nulc. Phys. **A645**, 145 (1999)

[30] D. Dreschel *et al.*, A Unitary Isobar Model for Pion Photo- and Electroproduction on the Nucleon, (`http://wwwkph.kph.uni-mainz.de/MAID//maid2007/`)

[31] R.A. Arndt, I.I. Strakovsky, R.L. Workman, Phys. Rev. **C53**, 430 (1996)

[32] W.J. Briscoe *et al.*, CNS Data Analysis Center, (`http://gwdac.phys.gwu.edu/`)

[33] S.S. Kamalov and S.N. Yang, Phys. Rev. Lett. **83**, 4494 (1999)

[34] V. Pascalutsa and M. Vanderhaegen *et al.*, Phys. Rev. Lett. **95**, 232001 (2005); Phys. Rev. **D73**, 034003 (2006)

[35] C. Alexandrou *et al.*, Phys. Rev. **D69**, 114506 (2004); Phys. Rev. Lett. **94**, 021601 (2005)

[36] E. Stiliaris and C.N. Papanicolas, AIP Conf. Proc. **904**, 257 (2007)

[37] E. Stiliaris and C.N. Papanicolas, arXiv:nucl-ex/0703031

[38] J. Glister, Ph.D. thesis, Dalhousie University (2009)

[39] R. Michaels, *et al.*, Jefferson Lab HALL A Logbook - Full Listing, (`http://hallaweb.jlab.org/halog/log/html/logdir.html`)

[40] Hall A Target Configuration, (`http://hallaweb.jlab.org/experiment/E07-006/target_info.pdf`), March 10, 2011

[41] The Aluminum Association, International Alloy Designations and Chemical Composition Limits for Wrought Aluminum and Wrought Aluminum Alloys, (`http://www.aluminum.org/sites/default/files/Teal_Sheets.pdf`), February 2009

[42] J.-O. Hansen, Hall A High Resolution Spectrometers General Characteristics, (`http://hallaweb.jlab.org/equipment/high_resol.html`), September 25, 2001

[43] J.-O. Hansen, Hall A C++ Analyzer Documentation, (`http://hallaweb.jlab.org/podd/doc/index.html`), December 10, 2009

[44] B.E. Norum *et al.*, *Exclusive Study of Deuteron Electrodisintegration near Threshold.* Jefferson Lab Hall A Proposal E08-008. (`http://hallaweb.jlab.org/collab/PAC/PAC33/PR-08-008:DeepThreshold.pdf`)

[45] E. Piasetzky *et al.*, *Studying Short-Range Correlations in Nuclei at the Repulsive Core Limit via the Triple Coincidence (e, e'pN) Reaction.* Jefferson Lab Hall A Proposal E07-006. (`http://hallaweb.jlab.org/collab/PAC/PAC31/PR-07-006-SRC.pdf`)

[46] J. Arrington, *et al.*, *Three-nucleon short range correlations studies in inclusive scattering for $0.8 < Q^2 < 2.8$ $(GeV/c)^2$.* Jefferson Lab Hall A Proposal E08-014. (`http://hallaweb.jlab.org/collab/PAC/PAC33/PR-08-014:xgt2.pdf`)

[47] E.A. Chudakov, *et al.*. JLab Hall A General Operations Manual. (`http://hallaweb.jlab.org/news/minutes/OSP/osp-27feb2011.pdf`) February 27, 2011.

[48] J. Dahlberg, Jefferson Lab Alignment Group Data Transmittal. (`https://www.jlab.org/accel/survalign/documents/dthalla/A1379.pdf`) February 17, 2011.

[49] J. Dahlberg, Jefferson Lab Alignment Group Data Transmittal. (`https://www.jlab.org/accel/survalign/documents/dthalla/A1376.pdf`) February 15, 2011.

[50] (`http://pdgusers.lbl.gov/~sbl/pp_total.dat`) June 29, 2004

[51] HAPPEX Collaboration Homepage. (`http://hallaweb.jlab.org/experiment/HAPPEX/index.html`) March 8, 2012.

[52] P.E. Ulmer, `http://hallaweb.jlab.org/publications/Technotes/files/2005/05-064.ps`

[53] Thermophysical Properties of Fluid Systems. (`http://webbook.nist.gov/chemistry/fluid/`) September 23, 2013.

[54] P.E. Ulmer. MCEEP: Monte Caro for (e,e'p) experiments. (`http://hallaweb.jlab.org/software/mceep/mceep.html`) June 14, 2006.

[55] R.C.E. Devenish and D.H. Lyth, Nucl. Phys. **B43** (1972)

[56] P. Breeuwsma. Cubic interpolation. (`http://www.paulinternet.nl/?page=bicubic`)